Department of Electrical Engineering

Measuring Picosecond Flashover in Pressurized Sulfur Hexafluoride (SF6)

Joni Viljami Klüss

Aalto University

DOCTORAL DISSERTATIONS

Aalto University publication series
DOCTORAL DISSERTATIONS 53/2011

Measuring Picosecond Flashover in Pressurized Sulfur Hexafluoride (SF6)

Joni Viljami Klüss

Doctoral dissertation for the degree of Doctor of Science in Technology to be presented with due permission of the School of Electrical Engineering for public examination and debate in Auditorium S1 at the Aalto University School of Electrical Engineering (Espoo, Finland) on the 29th of July 2011 at 12:00.

Aalto University
School of Electrical Engineering
Department of Electrical Engineering
High Voltage Engineering

Supervisor
Prof. Matti Lehtonen

Instructor
Dr. Petri Hyvönen

Preliminary examiners
Prof. Steffen Grossmann, TU Dresden, Germany
Prof. Ali Harlin, VTT, Finland

Opponents
Prof. Steffen Grossmann, TU Dresden, Germany
Dr. Kari Luoma, Merinova, Finland

Aalto University publication series
DOCTORAL DISSERTATIONS 53/2011

ISBN 978-952-60-4170-4 (pdf)
ISBN 978-952-60-4169-8 (printed)
ISSN-L 1799-4934
ISSN 1799-4942 (pdf)
ISSN 1799-4934 (printed)

Aalto Print
Helsinki 2011

Finland

The dissertation can be read at http://lib.tkk.fi/Diss/

Author
Joni Klüss

Name of the doctoral dissertation
Measuring Picosecond Flashover in Pressurized Sulfur Hexafluoride (SF6)

Publisher School of Electrical Engineering

Unit Department of Electrical Engineering

Series Aalto University publication series DOCTORAL DISSERTATIONS 53/2011

Field of research High Voltage Engineering

Manuscript submitted 12 January 2011 **Manuscript revised** 6 June 2011

Date of the defence 29 July 2011 **Language** English

☒ **Monograph** ☐ **Article dissertation (summary + original articles)**

Abstract

The exceedingly fast speed of breakdown in gas presents numerous challenges for measurement systems. Data integrity and analysis of recorded results are considerably affected by the measurement setup. In efforts to remove the effect of the measuring system and verify observations pertaining to the physical phenomenon of breakdown, two systems are compared. In addition, issues concerning the design, manufacturing and operation of high voltage pressurized spark gaps are discussed.

Risetime of voltage collapse is measured in a pressurized SF6 spark gap using D-dot sensors and oscilloscopes with analogue bandwidth ranging from 6 to 30 GHz. Results from a 50 GHz series sampling oscilloscope are also presented. Inter-electrode distance is varied between 0.1 and 0.9 mm and pressure is increased from 1 to 19 bar. Breakdown voltages are measured ranging from c. 10 to 180 kV.

Risetime values ranging from 50 to 800 ps and distinct variations in the voltage collapse waveform are observed. Measurements are documented and significant variables affecting the breakdown process and risetime analysis are identified. Risetime dependency to pressure, gap distance and electric field strength are presented using several analysis methods and compared to known theory. Methods to overcome or compensate the identified variables are discussed. Finally, optimal solutions for measurement systems and future research are presented.

Keywords high voltage, breakdown, flashover, sulfur hexafluoride, spark gap, risetime

ISBN (printed) 978-952-60-4169-8 **ISBN (pdf)** 978-952-60-4170-4

ISSN-L 1799-4934 **ISSN (printed)** 1799-4934 **ISSN (pdf)** 1799-4942

Location of publisher Espoo **Location of printing** Helsinki **Year** 2011

Pages 153 **The dissertation can be read at** http://lib.tkk.fi/Diss/

Tekijä
Joni Klüss

Väitöskirjan nimi
Pikosekuntiluokan ylilyönnin mittaaminen paineistetussa rikkiheksafluoridikaasussa (SF6)

Julkaisija Sähkötekniikan korkeakoulu

Yksikkö Sähkötekniikan laitos

Sarja Aalto University publication series DOCTORAL DISSERTATIONS 53/2011

Tutkimusala Suurjännitetekniikka

Käsikirjoituksen pvm 12.01.2011 **Korjatun käsikirjoituksen pvm** 06.06.2011

Väitöspäivä 29.07.2011 **Kieli** Englanti

☒ **Monografia** ☐ **Yhdistelmäväitöskirja (yhteenveto-osa + erillisartikkelit)**

Tiivistelmä

Kaasussa tapahtuvan erittäin nopean läpilyönnin tutkiminen asettaa lukuisia haasteita mittausjärjestelmille. Mittauskokoonpanolla on ratkaiseva vaikutus saadun mittausdatan eheyteen ja edelleen tulosten analysointiin. Tässä tutkimuksessa pyritään vähentämään tätä riippuvuutta ja vahvistamaan itse läpilyönti-ilmiön erottamista mittaustuloksista kahdella erillisellä mittausjärjestelmällä. Lisäksi työssä käsitellään paineistetun suurjännitekytkimen suunnitteluun, rakentamiseen ja käyttöön liittyviä seikkoja.

Jännitteen romahduksen nousuaika mitattiin paineistetussa SF6-kipinävälissä käyttäen derivoivia antureita ja reaaliaikaoskilloskooppeja, joiden todellinen kaistanleveys vaihteli välillä 6 GHz - 30 GHz. 50 GHz sarjanäytteistysmittalaitteella saadut tuloksia ovat myös esitetty. Elektrodien välistä avausta säädettiin 0.1 mm ja 0.9 mm välillä ja kaasun painetta nostettiin askelittain 19 bar asti. Mitatut ylilyöntijännitteet olivat välillä 10 kV - 180 kV. Nousuaikoja mitattiin väliltä 50 ps - 800 ps. Mittaustulokset dokumentoitiin ja muuttujat, jotka merkittävästi vaikuttivat kaasun läpilyöntiprosessiin ja nousuajan analyysiin, identifioitiin.

Nousuajan riippuvuus paineesta, kipinävälin avauksesta ja sähkökentänvoimakkuudesta esitetään käyttäen useita eri analyysimenetelmiä. Tehtyjä havaintoja verrataan tunnettuun teoriaan ja identifioitujen muuttujien vaikutuksen kompensointia pohditaan eri menetelmin. Lopuksi esitetään optimaalinen mittausjärjestelmäratkaisu ilmiön tutkimiseksi.

Avainsanat suurjännite, läpilyönti, ylilyönti, rikkiheksafluoridi, kipinäväli, nousuaika

ISBN (painettu) 978-952-60-4169-8 **ISBN (pdf)** 978-952-60-4170-4

ISSN-L 1799-4934 **ISSN (painettu)** 1799-4934 **ISSN (pdf)** 1799-4942

Julkaisupaikka Espoo **Painopaikka** Helsinki **Vuosi** 2011

Sivumäärä 153 **Luettavissa verkossa osoitteessa** http://lib.tkk.fi/Diss/

Preface

When attending a high voltage engineering course in 2006, lecturer Jari Hällström approached me with a Master's thesis topic concerned with measuring high speed flashover in pressurized gas. After initially declining politely several times due to schedule conflicts, Hällström's persistence paid off and I joined the joint project between TKK and PvTT which had originally commenced in 2003. Following thousands of pulses and a successful thesis, I was stricken by the vast number of unanswered questions which had risen from tackling this query. Hence, after filling the appropriate paper work to register as a post graduate student and obtaining financial grants I began my Doctoral thesis early 2008 hoping to ratify earlier observations and gain comprehensible insight into the ultra fast breakdown phenomenon in insulation gases.

Acknowledgements

Gratitude needs to be expressed to Dr. Jari Hällström for initially involving me with this project which has grown to expand into so many interesting areas of research. Furthermore, he has consistently been open to discussion and developing this research topic. I am grateful to my supervisor Professor Matti Lehtonen for enabling my post graduate research at the Helsinki University of Technology TKK (currently Aalto University) and ensuring I have all the necessary research tools.

Fortum Foundation and the Finnish Cultural Foundation are greatly acknowledged for their financial grants without which this research would not be possible. Also, the state of the art measurement equipment provided by Orbis, PvTT and Jari Viiala from Onninen and materials from Ensto are immensely appreciated.

The personnel at the Department of Electrical Engineering have been more than helpful. Thanks are in order to Jouni Mäkinen for helping me acquire all the necessary materials needed for this research and sacrificing weekends spent measuring; Veli-Matti Niiranen for fixing all my hundreds of hardware and software problems that have come along the way; Dr. Petri Hyvönen for his guidance and insight throughout my post-graduate studies; Eero Saarijärvi, Tatu Nieminen and all the rest for making my time here at the lab memorable.

Finally, I would like to thank my wife, Tanja, for always having the time to listen to my theories and knowing the right answer even though it might not have anything to do with the research.

Contents

Preface ..... **vii**

Acknowledgements ..... **viii**

List of Abbreviations ..... **xi**

List of Symbols ..... **xii**

1. Introduction **1**

1.1 Research Problem 2
1.2 Aim of Research 2
1.3 Research Methods 2
1.4 Scientific Contribution 3
1.5 Organization of the Thesis 3

2. Breakdown in Gases **5**

2.1 Ionization 5
2.2 Townsend Mechanism 6
2.2.1 Townsend's First Ionization Coefficient 7
2.2.2 Townsend's Second Ionization Coefficient 8
2.3 Paschen's Law 12
2.4 Streamer Mechanism 14
2.5 Channel Formation 16
2.5.1 Braginskii Model 16
2.5.2 Toepler Model 17
2.6 Overview 18

3. Sulfur Hexafluoride **19**

3.1 Electron Attachment Process and Electronegative Gases 19
3.2 Decomposition Products 22
3.3 Greenhouse Effect 22

4. Previous Research **23**

5. Test Setups **25**

5.1 General 25
5.2 Coaxial System – Setup 1 25
5.2.1 Spark Gap 25
5.2.2 Homogeneous Field 26
5.2.3 *D*-dot Probe 26
5.2.4 Oscilloscope 28
20 GHz Tektronix DSA72004 (prototype) 28
16 GHz Tektronix DSA72004 (retail) 28
50 GHz Tektronix TDS8200/80E01 28
5.2.5 Measurement System 28
5.3 Conical System – Setup 2 30
5.3.1 Spark Gap 30
Mechanical Failure 33
5.3.2 Homogeneous Field 35
Homogeneous Field vs. Fixed Impedance 36
5.3.3 *D*-Dot Probe 39
D-dot Probe Functionality 39
5.3.4 Oscilloscope 42

5.3.5 Measurement System....42
Gap Distance Accuracy....42
Measurement Bandwidth....42
Measurement Setup....44

6. Results....45

6.1 Coaxial System – Setup 1 Results....45
6.1.1 Breakdown Voltage....45
Conditioning Effect....46
Steepness....47
6.1.2 Breakdown Waveform....48
Region I....48
Transition Region....48
Region II....48
6.1.3 Risetime....48
6.2 Conical System – Setup 2 Results....50
6.2.1 Breakdown Voltage....50
Gap Distance Compensation Based on Simulation....52
Gap Distance Compensation Based on Theory....53
Gap Distance Compensation Based on Simulation and Theory....56
Gap Distance Compensation Based on Measurements....58
6.2.2 Breakdown Waveform....62
Type I....62
Type II....63
Type III....64
6.2.3 Risetime....65
Raw Data....65
Cropped Data....67
Line Fitting....69

7. Discussion....71

7.1 Reflections Analysis....72
7.1.1 Type I and III....75
Side Flashover....79
7.1.2 Type II....81
7.1.3 Overview of All Types....88
7.2 Interference....94
7.3 Bandwidth and Sampling....96
7.4 System Development....99
7.4.1 Optimal Impedance Matching at the Expense of Field Homogeneity....99
7.4.2 Sensor Selection....101
7.4.3 Measurement Cables....101
7.4.4 Gap Distance Uncertainty....101
7.4.5 Digital Signal Analyzer....102

8. Conclusions....103

References....109

Appendix 1 – Complete Tables....111

Appendix 2 – Four-Boundary Analysis....115

Appendix 3 – Side Flashover Analysis....118

Appendix 4 – Side Flashover Coordinates....121

Appendix 5 – Measured Waveforms....124

List of Abbreviations

2D	Two Dimensional
3D	Three Dimensional
BW	Band Width
DSA	Digitizing Signal Analyzer
DSP	Digital Signal Processing
EMP	Electromagnetic Pulse
FEM	Finite Element Method
FGB	Fiberglass Boundary
GND	Ground
HV	High Voltage
MMF	Multiple Multiplicative Factor
MTS	Haefely Multi Test Set impulse generator
NTP	Normal Temperature and Pressure
p.u.	Per Unit (pu)
PvTT	Finnish Defence Forces Technical Research Centre
PW	Pulse Width
RMS	Root Mean Square
SF_6	Sulfur Hexafluoride, Sulphur-hexafluoride
SI	Système International d'Unités, International System of Units
SK	Standard K 2.92 mm connector type (2.92, SMK, K)
SMA	Connector type SubMiniature version A
SNR	Signal to Noise Ratio (S/N)
TKK	Teknillinen Korkeakoulu, Helsinki University of Technology
UV	Ultraviolet
UWB	Ultra Wide Band
WWII	World War 2

List of Symbols

A	Atom
A^+	Positive ion
A_s	Cross sectional area of discharge [m²]
α, $\alpha(E)$	Townsend's first ionization coefficient
B_1, B_2	Impedance discontinuity boundary
c	Speed of light ($3 \cdot 10^8$ m/s)
d, d_o	Gap distance (mm)
Δd	Change in gap distance
$\dot{D}$	D-dot probe
D	Electric displacement density, electric flux density
dB	Decibel
d_{comp}	Compensated gap distance
dn	Number of new electrons
dV/dt	Derivative of voltage over time
dx	Distance travelled by electrons in an avalanche
ΔE	Change in electric field distribution
e^-	Electron
E, E_o	Electric field (kV/mm)
E/p	Electric field over pressure (kV/mm·bar)
$(E/p)_{comp}$	Electric field over pressure using gap distance compensation
E_b, $(E/p)_{crit}$	Breakdown field strength, critical field strength
ε_r	Relative permittivity (for SF_6 $\varepsilon_r = 1$)
η	Attachment coefficient
f	Frequency
γ	Townsend's second ionization coefficient
I, i, $i(t)$	Current
I_o	Initial current at cathode
K	Kelvin
k_k	Constant equal to 24.7
kN	Kilo Newton
k_t	Toepler's constant
λ_E	Free path of electrons
λ_m	Mean free path of electrons
m_e	Mass of electron
m_i	Mass of ion
M	Molecular weight
N	Number of collisions per primary electrode
n_o	Primary number of electrons

n_o'	Number of secondary (γ) electrons
n_o''	Total number of electrons leaving the cathode
Ω	Ohm
p, p_o	Pressure
p_{max}	Maximum operational pressure
pd	Product of pressure and gap distance [bar·mm]
$(pd)_{comp}$	Product of pressure and compensated gap distance
$(pd)_{min}$	Paschen's minimum
pVs	Picovolt second
q_e, e	Charge of electron
q_i	Charge of ion
R	Ratio of digitizer bandwidth in relation to the input signal frequency
$r(t)$	Radius of discharge
R_t	Spark resistance
ρ	Reflection coefficient
ρ_o	Air density at atmospheric pressure (1.29×10^{-3} g/cm^3)
t	Time
T_1	Front time, $1.67(t_{90\%} - t_{30\%})$
T_2	Time to half-value
t_r	Risetime
τ	Transmission coefficient
θ	Half angle of conical electrode [°]
U	Voltage
U_a	Applied voltage
U_b	Breakdown voltage
U_i	Ionization voltage
u_r	Reflecting wave u
u_t	Transmitting wave u
W_i	Ionization energy
Z	Impedance
∞	Infinity

1. Introduction

> "High voltage pulse technology involves a capacitive storage of energy at high voltage and its rapid release to deliver a pulse of energy to a load." [Far94].

The presence of electricity has been acknowledged throughout history in one form or the other – from electric eels in Ancient Egypt, to Greek electrostatic experiments with amber, to high voltage (HV) impulses in the form of lightning. It was not until Benjamin Franklin's experiments (1751) and James Lind's demonstrations (1773) of lightning's destructive power, that interest in reproducing such surges in the laboratory commenced [Far94]. The invention of the Leyden Jar (1745) along with Volta's early battery (1800) advanced the topic of electricity from a natural philosophy to a more quantitative science [Lin07]. By the late 1800s, Townsend had provided knowledge on the process of ionization using modern physics and consequently the concept of an electric field became well established [All04]. By now, electricity distribution systems were developing, setting new standards involving lightning surges and overvoltages and as such, impulse generators needed to be developed to test equipment.

In 1920, techniques for generating HV pulses by switching a charged capacitor onto a load progressed with the development of the multistage Marx generator [Far94]. Pulsed power experienced further development during WWII when great efforts were spent in developing the radar [Wik09]. Advances in material and switching technologies stimulated the development of a wide variety of new designs for impulse generators which strived to surpass earlier limitations such as pulse risetime, peak voltage and energy content [Far94]. For the production of fast plasma closing switches, which are significant components in many high-power systems such as UWB radar and laser drives, insight into the processes related to ultrafast electrical breakdown involving small gap distances and highly pressurized gaseous dielectrics is required [Dic02, Fro02]. Along with the previously mentioned applications, ultrafast gas switches can function as UWB impulse simulators producing electromagnetic environments appropriate for particle accelerators, pollution control systems, mineral extraction, high speed imaging, EMP testing, bioelectromagnetic studies, and for basic studies of gas breakdown physics [Fro02, Far94].

1.1 Research Problem

Essentially, the research problem addressed here is valid measurement of extremely fast breakdown in gas. Identified risetimes have developed from microseconds to nanoseconds to picoseconds as measuring technology and spark gap designs have progressed. Currently, recorded risetimes are under certain conditions c. 50 ps and extended research is required to validate this data and the dependant factors leading to such results.

1.2 Aim of Research

Once data integrity has been established and significant parameters pertaining to the breakdown process identified, an independent relation could possibly be established to provide calculable breakdown speeds which are applicable to differing systems. In order to achieve this, the effect of the measuring system must be removed from the results ensuring that observed data pertains to the physical breakdown process and not a result of the test setup. Thus, this research aims at identifying problems related to measuring fast breakdown pulses, presenting methods to overcome or compensate these issues, approximate results, and present an optimal measurement setup for successfully measuring such pulses.

1.3 Research Methods

Measurements are conducted using alternative measurement systems to study the reproducibility of the observed phenomena. Two different test gaps were designed using FEM simulations and theoretical analysis. The first switch has a coaxial structure with a biconical spark gap and was built for a previous project where its characteristics were studied. In this text, the first test gap is used as a comparison. More details concerning its construction and results can be found at [Klü07]. The second switch has a conical design. In both cases the electrodes have been designed to produce a homogeneous electric field in the spark gap.

A steep impulse is fed into the spark gap. One electrode is grounded while the other is fed with increasing voltage until breakdown occurs in the insulating gas. A conducting channel with low resistance forms, equalizing the potentials, until the gas regains its insulating properties and the channel is extinguished. The breakdown pulse propagating from the spark gap is measured using derivating probes, *D*-dot probe ($\dot{D}$ probe), which measure the change in voltage over the change in time *dV/dt*. The integral of the measured pulse provides the voltage collapse waveform from which risetime can be calculated.

Parameters affecting the measured pulse are varied in order to determine their interdependent relations. Such parameters include pressure of gas inside the spark gap, inter-electrode distance, steepness of applied voltage, and frequency of sequential breakdown.

1.4 Scientific Contribution

Improving on previous measurements systems [Klü07], a new test gap was designed in efforts to attain more accurate data. The transmission line of the test gap strives to maintain constant impedance to reduce the impact of superimposed signals on recorded samples. The large volume of insulation gas also minimizes the possibility of contaminated breakdown by-products influencing the recorded phenomena. Multiple uniform sensors enable simultaneous data collection using varying equipment and thus, provide comparable data which improves measurement integrity. The state of the art equipment used in this study with its increased resolution has provided greater insight into the observed breakdown phenomenon. In the past results have been limited by the sample acquisition rate of measuring devices. Risetimes observed in this thesis are also operating at the limit of the current measurement equipment, suggesting that the voltage collapse might be faster than reported here. Despite limited measurement tools, the experimental series are supported through theoretical consideration and modeling of the phenomena.

Since two different test gaps are used, a more uniform relationship could be established which could be possibly applicable to other measurement setups. In addition, notable fluctuation in signal waveforms was recorded. Significant controllable components as well as variable factors influencing the observed outcomes are identified enabling the noted fluctuations to be documented and constrained to certain conditions.

1.5 Organization of the Thesis

The thesis is organized as follows:

- Chapter 2 provides an overview of different factors and mechanisms pertaining to breakdown in gases. Topics covered include the Townsend and Streamer mechanism, Paschen's law and channel formation.
- Chapter 3 presents properties and applications for Sulfur Hexafluoride as an insulating gas.
- Chapter 4 outlines previous and current research by various authors related to the topic of measuring voltage collapse in pressurized spark gaps.

- Chapter 5 describes the test setups and measurement processes for both gaps.
- Chapter 6 presents observed data, including measured breakdown voltages, waveforms and risetimes. Several analysis methods are also introduced which deal with gap distance compensation and waveform interpretation.
- Chapter 7 discusses the implications of observed results and their interdependent relations. The effect of reflections along the transmission line is discussed in greater detail. Improvements and ideas for future development are also presented
- Chapter 8 summarizes the previous sections and presents concluding remarks.
- Appendix 1 displays full tables with complete calculations of compensation values used in Chapter 6.
- Appendix 2 considers the non-ideality of the transmission line using the "Four-Boundary Analysis".
- Appendix 3 presents the effect of side flashover (Side Flashover Analysis).
- Appendix 4 considers the role of varying flashover location on measured and modeled waveforms (Side Flashover Coordinates).
- Appendix 5 shows measured waveforms for referencing throughout the text.

2. Breakdown in Gases

Gas in its normal state is an insulator. However, when sufficiently high voltage is applied between two electrodes separated by a gaseous medium, discharge may occur. During electrical discharge, a dielectric loses its insulating properties and an ionized channel forms conducting a large current and causing voltage to collapse. In other words, a short circuit is created between two conducting electrodes. "The maximum voltage applied to the insulation at the moment of breakdown is called the breakdown voltage," U_b [Nai96].

Discharges in gases are of two types – non-sustaining discharge and self-sustaining discharge. The first type, consisting of local or corona discharge, occurs around conductors with sufficiently high potentials but does not extend to the opposite electrode or to earth to complete a conducting path. The second type transitions from a non-sustaining discharge into a self-sustaining discharge forming a complete electrical breakdown in the gaseous media between electrodes.

Insulators are not ideal and some degree of leakage current is always present. This current is caused by charge carriers – the movement of electrons and positive and negative ions in an electric field [Aro03]. The rapid "build up of high currents in breakdown is due to the process known as ionization in which electrons and ions are created from neutral atoms or molecules, and their migration to the anode and cathode respectively." [Nai96].

The most important types of charge carriers are [Kin85, Råd01, Wik10a]:

Electrons	Elementary particle with a negative charge. Charge $q_e = -e = -1.6022 \cdot 10^{-19}$ C Mass $m_e = 9.1095 \cdot 10^{-31}$ kg
Ions	Atom or molecule with the total number of electrons not equal to the number of protons, giving it a net positive or negative electrical charge. Charge (when singly ionized) $q_i = \pm e$ Mass $m_i \approx \mathrm{M} \cdot 2836 m_e$ (≈ molecular weight M times proton mass)
Large ions	Formation by attachment of electrons or ions on dust particles, water droplets and macroscopic particles.

2.1 Ionization

"The process of liberating an electron from a gas molecule with the simultaneous production of a positive ion is called ionization" [Nai96].

Ionization may occur by collision, photo-ionization and secondary ionization processes.

When ionization by collision occurs, a free electron collides with a neutral gas molecule and a new electron and positive ion is released. In order for ionization to happen, the energy gained traveling between collisions needs to exceed the ionization voltage U_i (the energy required to free an electron from its atomic shell) [Nai96].

$$e^- + A \xrightarrow{\varepsilon > U_i} e^- + A^+ + e^- \qquad (2.1)$$

A is the atom, A^+ is the positive ion, e^- is the electron and ε represents energy.

Photo-ionization involves an interaction of radiation with matter and occurs when the amount of radiation energy absorbed by an atom or molecule exceeds its ionization potential causing a photon to eject one or more electrons called photoelectrons.

In secondary ionization processes secondary electrons are produced to sustain a discharge (discussed later in Section 2.2.2).

The ionization process is influenced by numerous factors such as gas properties, pressure, temperature, electrode configurations and material, thereby making the breakdown development hard to predict and model. Two theories have been generally accepted in the scientific society for explaining the breakdown mechanism under different conditions – Townsend theory and Streamer theory.

2.2 Townsend Mechanism

As mentioned before, ionization is possible if the amount of energy caused by collisions or electromagnetic radiation exceeds the ionization voltage. The ionization condition can be expressed in terms of electric field strength E and average ionizing free path λ_E which is the distance a charge carrier travels on average between collisions under the influence of electric field E as shown in Figure 1,

$$E\lambda_E > U_i = \frac{W_i}{e}. \qquad (2.2)$$

Here U_i is ionization voltage, W_i is ionization energy and e is the charge of an electron [Aro03, Kin85]. Ionization voltages of some selected gases are listed in Table 2.1.

Table 2.1. *Ionization voltages of gas [Kin85].*

Type of Gas	N_2	O_2	Hg	Cs	$SF_6 \rightarrow SF_5^+$
U_i [V]	15.8	12.8	10.4	3.9	15.9

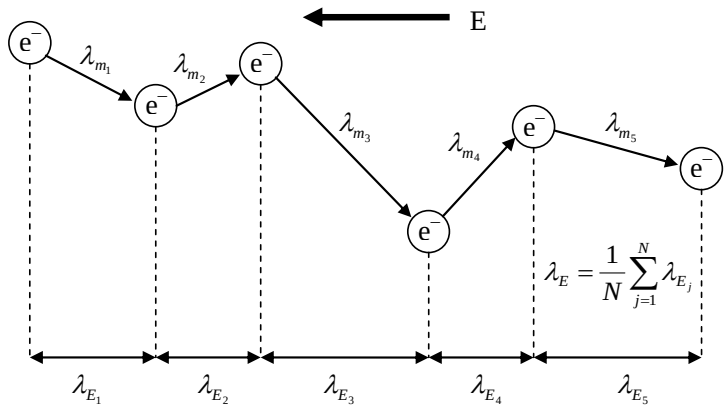

Figure 1. *The free path of electrons in an electric field [Aroo3].*

2.2.1 Townsend's First Ionization Coefficient

If the ionization condition is fulfilled, a multiplicative process of electron growth by collision commences. Depending upon local field strength, the number of new electrons *dn* produced over the distance *dx* is expressed as,

$$dn = \alpha n(x)dx\,. \tag{2.3}$$

Here, $\alpha = \alpha(E)$ is called the ionization coefficient of electrons (*Townsend's first ionization coefficient*). For a primary electron number n_o (number of electrons leaving cathode) and *inhomogeneous* field,

$$n(x) = n_0 e^{\int_0^x \alpha dx}\,. \tag{2.4}$$

In a *homogeneous* field, where α is constant, this relation simplifies to

$$n(x) = n_0 e^{\alpha x}. \tag{2.5}$$

This exponential increase of the electron number is called an electron avalanche (Figure 2) and can also be expressed in terms of current *I*,

$$I = I_0 e^{\alpha x}, \tag{2.6}$$

where I_o is the initial current at the cathode.

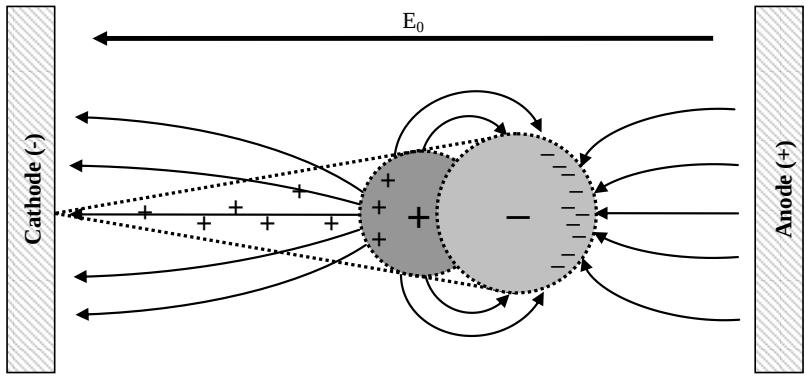

Figure 2. *Electron avalanche in a homogeneous field.*

Consider ionization caused by an electron with mean free path λ_m over a distance x. The average number of collisions across this distance x is x/λ_m. The probability that an electron travels a free path λ_E without colliding with other atoms is $e^{-\lambda_E/\lambda_m}$. Hence, over a distance x, the amount of ionization (successful collisions) is

$$\alpha x = \frac{x}{\lambda_m} e^{-\frac{\lambda_E}{\lambda_m}}. \tag{2.7}$$

Replacing λ_E by inserting equation (2.2) and further simplifying the above equation (2.7) gives Townsend's first ionization coefficient α as

$$\alpha = \frac{1}{\lambda_m} e^{-\frac{U_i}{E\lambda_m}}. \tag{2.8}$$

Since the mean free path λ_m is inversely proportional to pressure p at constant temperature,

$$\alpha = Ape^{-\frac{Bp}{E}}, \tag{2.9}$$

where A and B are constants. From the above equation it is evident that α/p is a function of E/p. However, this is valid only for an experimentally determined range for each gas [Aro03, Kin85].

Referring back to Figure 2 depicting the electron avalanche, electrons may be very densely packed at the head of the avalanche causing a considerable concentration of electric field. Positive ions remain behind the head of the avalanche and as these move towards the cathode they may liberate secondary electrons under certain conditions [Kin85], which is discussed next.

2.2.2 Townsend's Second Ionization Coefficient

The breakdown process discussed thus far can be illustrated using a current-voltage curve (Figure 3) where voltage is applied between two electrodes and slowly increased.

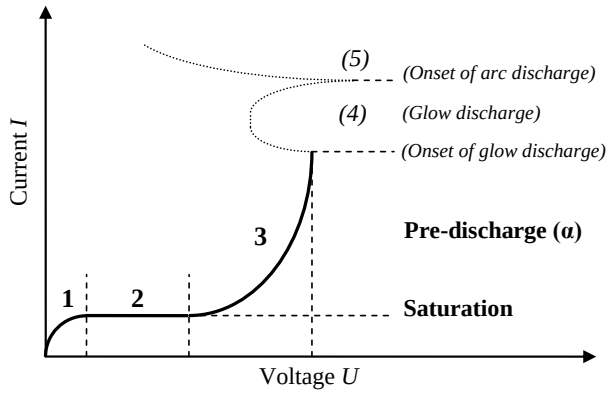

Figure 3. *First stages of the current – voltage curve for gas. Edited from [Aro03].*

"In the absence of electric field the rate of electron and positive ion generation in an ordinary gas is counterbalanced by decay processes and a state of equilibrium exists. This state of equilibrium will be upset upon the application of a sufficiently high field." [Kuf00]. At first, when voltage is increased, current increases proportionally (zone 1). This increase is brought on by an external electric field causing charge carriers in the gas to migrate to the electrodes. Current growth is arrested when the electric field is strong enough to cause all free electrons and ions present in the gas to migrate to the electrodes before recombination occurs (zone 2) causing current to remain at nearly constant value (saturation current/background current). The magnitude of this saturation area is solely dependent on external sources and corresponds to the number of carriers generated by external ionizations [Kin85] (i.e. if the cathode is radiated with UV light, the saturation current level would give the emitted photocurrent [Kuf00]). As voltage is increased further, current begins to increase exponentially (zone 3). Here, the free electrons in the gas gain enough energy between collisions to ionize atoms or molecules. [Aro03].

The single avalanche process described in Section 2.2.1 becomes complete once the initial set of electrons reaches the anode. However, this exponential growth of electrons and hence, current, does not necessarily lead to a complete breakdown. Assume, N is the number of ionized collisions per primary electron leaving the cathode and i_0 is initial current at the cathode. Discharge current then becomes,

$$i = i_0(1+N). \tag{2.10}$$

Mathematically, current can grow infinitely large only if N or i_0 is infinite [Aro03]. Therefore, Townsend's first ionization coefficient α explains mainly so-called "dark" pre-discharge current which may be observed in gas discharges following the current saturation phase and prior to the onset of glow discharge (zone 3 in Figure 3). For breakdown to occur, additional ionization mechanisms are required. These mechanisms include [Nai96, Aro03]:

(i) The positive ions liberated may have sufficient energy to cause liberation of electrons from the cathode when they impinge on it.

(ii) Excited atoms or molecules in avalanches may emit photons, resulting in the emission of electrons due to photo-emission.

(iii) Metastable particles may diffuse back causing electron emission (particles in a delicate equilibrium may fall into lower-energy states with minor interactions).

(iv) Thermal ionization may occur due to the high temperatures in the plasma channel.

Electrons produced by these processes are called secondary electrons. The secondary ionization coefficient γ is defined the same way as α – the net number of secondary electrons produced per incident positive ion, photon,

excited or metastable particle. The total value of γ is the sum of all individual coefficients due to the secondary processes introduced above and is called the *Townsend's second ionization coefficient*. The coefficient is a function of gas pressure p and electric field E/p [Nai96] and experimental values for γ have been determined to range $10^{-8}...10^{-1}$ [Kin85].

The Townsend model is based on the assumption that an avalanche produced by n_0 primary initial electrons in the vicinity of the cathode (Figure 4 – I), on traversing the spacing x, generates a total of $n_0(e^{\alpha x} - 1)$ ions (Figure 4 – II). On striking the cathode, these ions release $\gamma n_0(e^{\alpha x} - 1)$ secondary electrons through secondary emission (Figure 4 – III) [Kin85].

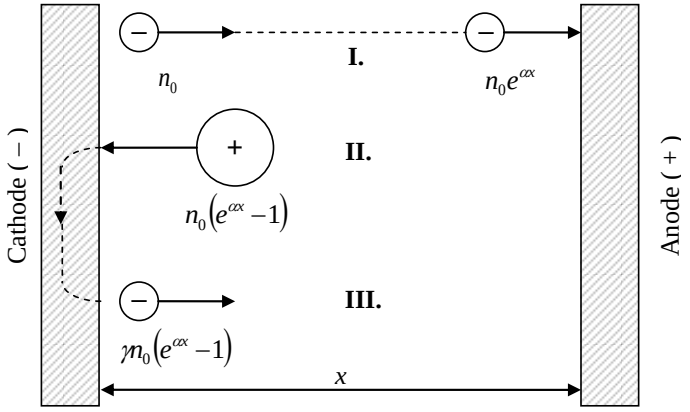

Figure 4. *Electron generation according to the Townsend mechanism [Kin85].*

Assume n_0' is the number of secondary electrons produced due to secondary processes (γ) and n_0'' is the total number of electrons leaving the cathode. Then,

$$n_0'' = n_0 + n_0'. \tag{2.11}$$

The total number of electrons n reaching the anode becomes

$$n = n_0'' e^{\alpha x} = (n_0 + n_0')e^{\alpha x}. \tag{2.12}$$

n_0' considers all secondary processes $\gamma = \gamma_1 + \gamma_2 + ... + \gamma_n$. Hence,

$$n_0' = \gamma n - \gamma n_0'' = \gamma(n - n_0'') = \gamma[n - (n_0 + n_0')] \tag{2.13}$$

Eliminating n_0' by inserting equation (2.13) into equation (2.12) gives,

$$n = \frac{n_0 e^{\alpha x}}{1 - \gamma(e^{\alpha x} - 1)} \tag{2.14}$$

or expressed in terms of current,

$$I = \frac{I_0 e^{\alpha x}}{1 - \gamma(e^{\alpha x} - 1)}. \tag{2.15}$$

Referring back to equation (2.10), it is now possible for current to become infinite (limited only by the resistance of the power supply and external

circuit) when equation (2.15) has zero denominator. In other words, when

$$\gamma\left(e^{\alpha x}-1\right)=1. \tag{2.16}$$

This is known as *Townsend's breakdown criterion* and can also be derived logically considering breakdown is possible only if the number of secondary electrons $\gamma n_0(e^{\alpha x}-1)$ is larger than the initial electrons n_0,

$$\gamma n_0\left(e^{\alpha x}-1\right)> n_0, \tag{2.17}$$

which simplifies to

$$\gamma\left(e^{\alpha x}-1\right)>1. \tag{2.18}$$

Townsend's criterion is also often presented in the form [Aro03, Kin85]

$$\alpha x=\ln\left(\frac{1}{\gamma}+1\right). \tag{2.19}$$

For homogeneous fields, "the right-hand side of the equation hardly changes in the usual ranges of γ" [Kin85] so that the breakdown criterion can be expressed as

$$\alpha x \geq k. \tag{2.20}$$

Values of k have been reported as ranging 2.5...18 [Kin85]. For inhomogeneous fields, the ionization coefficient α is dependent on location and can be given as [Aro03]

$$\int_0^x \alpha dx \geq k. \tag{2.21}$$

In both cases, α depends on field strength E, whose value on attaining the ignition condition is known as the breakdown (critical) field strength E_b. For homogeneous fields, E_b can be calculated if breakdown voltage U_b and electrode gap d distance is known,

$$E_b=\frac{U_b}{d}. \tag{2.22}$$

Continuing the analysis first presented in Figure 3, further increasing voltage will dramatically increase the conductivity of the gas and breakdown will occur (Figure 5).

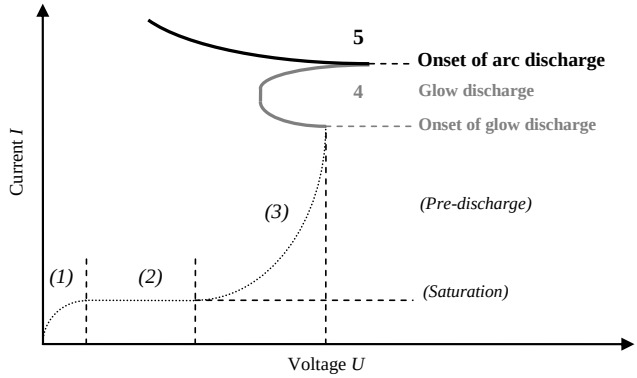

Figure 5. *Last stages of the current – voltage curve for gas. Edited from [Aro03].*

Breakdown will give way to arcing (zone 5). Arcing causes the voltage between the electrodes to collapse and current settles at a value determined by the impedance of the feeding circuit. At small pressures or inhomogeneous fields, arcing can be preceded by glow discharge (zone 4). "An electric arc differs from glow discharge in that the current density is quite high, and the voltage drop within the arc is low" [Wik10]. In this case, the discharge current can be uncorrelated to voltage and greatly affected by voltage losses (cathode drop). In practice, it is important to know the peak voltage at zone 3, since this is the onset (ignition) voltage for discharge. In some cases, the voltage peak between zone 4 and 5 does not occur at all [Aro03].

2.3 Paschen's Law

Townsend's breakdown criterion can also be expressed in terms of electric field or voltage making its practical interpretation easier to understand. Consider a homogeneous field where E is constant ($E = U/d$). Expressing Townsend's first ionization coefficient α (equation (2.9)) in terms of breakdown voltage gives,

$$\alpha = Ape^{-\frac{Bp}{E}} = Ape^{-\frac{Bpd}{U_b}}. \tag{2.23}$$

Also, Townsend's breakdown criterion (equation (2.19)), where $x = d$ gives,

$$\alpha x = \ln\left(\frac{1}{\gamma}+1\right) \Rightarrow \alpha = \frac{1}{d}\ln\left(\frac{1}{\gamma}+1\right) \tag{2.24}$$

Hence,

$$\frac{1}{d}\ln\left(\frac{1}{\gamma}+1\right) = Ape^{-\frac{Bpd}{U_b}}. \tag{2.25}$$

Solving for U_b gives,

$$U_b = \frac{Bpd}{\ln\dfrac{Apd}{\ln\left(\dfrac{1}{\gamma}+1\right)}}. \tag{2.26}$$

Equation (2.26) is called Paschen's law and expresses breakdown voltage as a function of pressure and inter-electrode (gap) distance,

$$U_b = f(pd) \tag{2.27}$$

and achieves a minimum value (Paschen's minimum, $(pd)_{\min}$) when,

$$\ln\frac{Apd}{\ln\left(\dfrac{1}{\gamma}+1\right)} = 1, \tag{2.28}$$

under which breakdown is theoretically not possible (Figure 6). Naidu [Nai96] explains the existence of a minimum sparking potential in Paschen's law as follows:

$pd > (pd)_{min}$	Electrons migrating across the gap collide more frequently with gas molecules than at $(pd)_{min}$, but the energy gained between collisions is lower. In order to maintain the desired ionization applied voltage has to be increased.
$pd < (pd)_{min}$	Electrons may migrate across the gap without a single collision (or fewer number of collisions). Hence, applied voltage has to be increased for breakdown to occur.

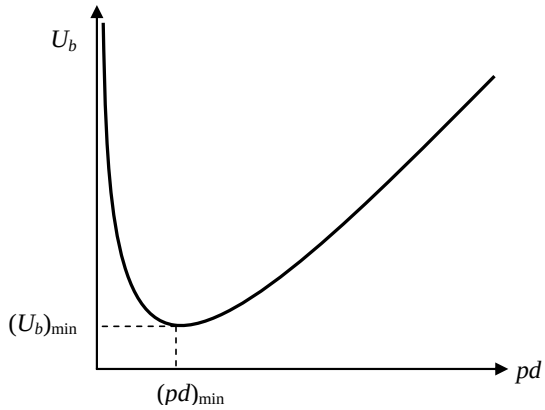

Figure 6. *Schematic representation of Paschen's curve.*

Paschen's law follows Townsend's breakdown criteria and is applicable to homogeneous electric fields in gas where breakdown occurs according to the Townsend mechanism. However, Townsend's mechanism has been found to have certain inconsistencies when compared to experimental observations.

Townsend explains current growth as a result of ionization only, when in practice, breakdown voltages were found to depend on other factors as well. It has been observed experimentally that as applied voltage, gap distance or gas pressure is sufficiently large, even in a homogeneous field, discharge advances from one electrode to another at speeds which cannot be explained by Townsend's mechanism [Aro03]. Time lags (the difference between the application of sufficient voltage to cause breakdown and the occurrence of breakdown itself) predicted in theory are c. 10^{-5} s while actual breakdown was observed to occur at very short times of the order of 10^{-8} s [Nai96]. Also, while the Townsend mechanism predicts a diffused form of discharge, in practice, discharge was found to be filamentary (narrow) and irregular (branching) [Aro03]. The Townsend mechanism failed to explain all these observed phenomena and as a result, around 1940 Raether, Loeb and Meek independently proposed the Streamer theory [Nai96].

2.4 Streamer Mechanism

For uniform electric fields the growth of charge carriers in an avalanche is described as $e^{\alpha x}$. Raether, Loeb and Meek explained that this exponential growth of an avalanche cannot be increased at will since the avalanche becomes unstable at a critical length [Kin85]. This growth is valid only as long as the electric field of the space charges can be neglected compared to the original uniform field E_o [Kuf00].

The focal mechanism behind streamer discharge is the formation of an inhomogeneous field produced around the advancing discharge (Figure 7) [Aro03]. The theory predicts "the development of a spark discharge directly from a single avalanche in which the space charge developed by an avalanche is said to transform the avalanche into a plasma streamer." [Nai96]

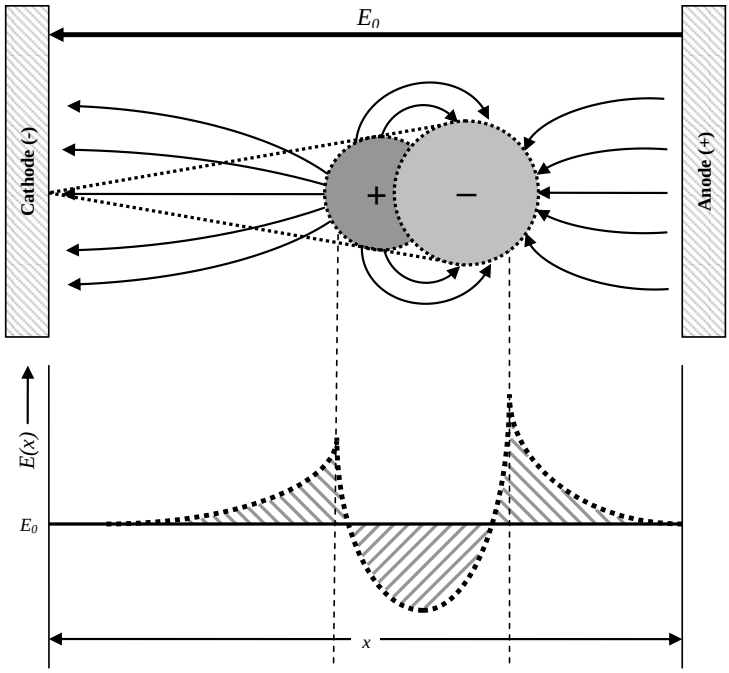

Figure 7. *Field distortion caused by space charges in electron avalanche. Edited from [Kuf00].*

Consider a single electron starting at the cathode builds up an avalanche by ionization. Electrons have higher mobility and migrate very fast compared to the positive ions in the avalanche. As electrons propagate towards the anode the positive ions are virtually in their original positions and form positive space charges at the anode [Nai96]. At the head of the avalanche where the electric field is enhanced, recombination and excitation of electrons and positive ions takes place causing photo-

ionization in the gas. Photo-ionization may trigger new avalanches in the positive space charge region at the anode (Figure 8) [Aro03, Nai96].

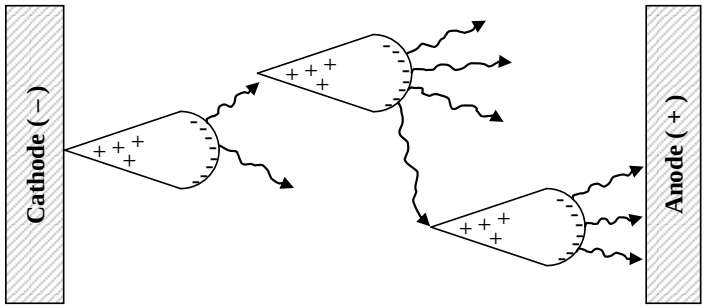

Figure 8. *Photo-ionization causing secondary electron avalanches. Edited from [Aro03].*

The electrons produced by the radiation migrate to the still positive area behind the head of the avalanche and a weakly conducting streamer is formed. As soon as the streamer tip approaches the cathode, a cathode spot is formed and a stream of electrons flow from the cathode to neutralize the positive space charge in the streamer [Nai96]. Once these streamers have established contact between the electrodes, current heats up a low-resistance plasma channel [Kin85].

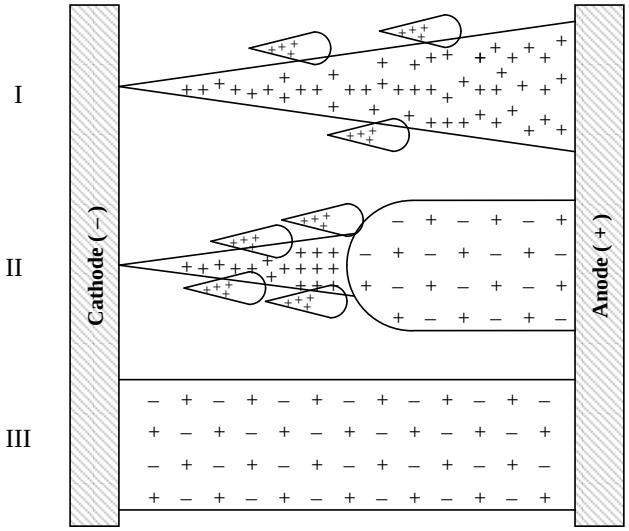

Figure 9. *Cathode directed streamer. Edited from [Nai96].*

The streamer development stages are illustrated in Figure 9. At stage I, the avalanche has crossed the gap. At stage II, the streamer has crossed half the gap length and at stage III the gap has been bridged by a conducting channel [Nai96]. The channel is caused by a synergy of photon radiation (photo-ionization) and collision ionization. Hence, secondary emission at the electrodes (as predicated by Townsend) is not essential [Aro03].

2.5 Channel Formation

An early model for exploring the dynamics of channel formation during breakdown was proposed by Rompe and Weitzel [Rom44]. They assumed that the entire energy resulting from Joule heating (ohmic heating) goes into temperature increase, which in turn increases the conductivity of the channel. In this model channel expansion was neglected. Later, Drabkina [Dra51] proposed that energy goes mainly into channel expansion. This expansion, together with thermal conduction and radiation, keeps the temperature approximately unvarying and electrical conductivity remains roughly constant. Drabkina's proposal was further refined by Braginskii [Bra58].

2.5.1 Braginskii Model

According to Braginskii a hot and ionized conducting channel forms in the gas beginning from a single point where breakdown occurs. Once breakdown takes place, the gas begins to conduct and heat up. Joule heating in the channel causes an increase in temperature from which follows an increase in pressure and rapid growth of channel cross sectional area. The electrical conductivity of the gas increases rapidly with temperature. Since the channel expansion is faster than the speed of sound, an audible shock wave forms and advances along the channel. The temperature in the vicinity of the shock is much higher than in the gas at rest. Also, the temperature in the channel itself is many times higher than that of the shockwave. Consequently, the density of the gas in the channel is very low and the major part of the moving gas is displaced from it. The growth is limited by temperature transferring from the channel into its surrounding and the expansion of the heated area as pressure increases. In this model, Braginskii makes the following assumptions:

> The channel is assumed to end once temperature falls low enough to significantly decrease ionization.
>
> The model neglects inertia of the moving gas in the channel.
>
> Electric and thermal conductivity is neglected. Hydrodynamic cooling associated with expansion, together with radiative cooling are assumed to be sufficient to maintain the temperature (conductivity) of the channel constant.

Hussey *et al.* [Hus99] contested Braginskii's last assumption, claiming that radiative and thermal cooling is not sufficient to maintain constant conductivity during channel expansion. Instead, during the first pico- to nanoseconds both density and temperature increase significantly. Referring to an experiment performed by Sorensen and Risti, Hussey stated that the Braginskii model is successful at qualitatively describing the experiment. However, the experimental conductivity increases more rapidly than the

model, which could be understood if the channel temperature were to increase with time, rather than remain constant, as Braginskii proposes.

In a more recent study, Singha [Sin03] stated that, from all previous literature concerning calculations for the instantaneous spark channel resistance, the only two relations that agree with experimental data over short time intervals (ns) are Rompe and Weitzel's model which was mentioned earlier, and Toepler's model.

2.5.2 Toepler Model

During the formation of the conducting plasma channel bridging the electrodes and equalizing their potentials, the spark resistance drops from a high value (>> 10^6 Ω) to a very low value of ~5 Ω [Bog82, Osm92]. According to Toepler, the instantaneous value of the spark resistance R_t is inversely proportional to the charge conducted through the spark channel [And66],

$$R_t = d\,\frac{k_t}{\int_0^t i\,dt}, \tag{2.29}$$

where d is the length of the discharge gap in cm, i is the discharge current in amperes and k_t is the Toepler's constant in Vs/cm.

Engel *et al.* [Eng89] compared Toepler's equation and several other published equations predicting time dependant variation of the spark resistance. According to Engel, the equation predicting resistance per unit length of the spark channel over the entire length of the current pulse is one published by Kushner *et al.* [Kus85] and is given as,

$$R(t) = k_k\left(\frac{p_0^3}{A_s^2 i(t)^6}\right)^{1/5}, \tag{2.30}$$

where k_k is a constant equal to 24.7, A_s is the cross sectional area of the discharge in m^2, p_o is the pressure in Pa and $i(t)$ is the discharge current given in amperes. The cross section of the discharge channel varies with the current and it can be obtained from the following formula, derived by Braginskii [Bra58], which shows how the time-dependent radius of the discharge channel, $r(t)$, varies with time,

$$r(t) = 0.93\cdot 10^{-3}\rho_0^{-1/6} i^{1/3} t^{1/2}, \tag{2.31}$$

where $r(t)$ is given in m, time t in μs, instantaneous current i in kA and ρ_o is air density at atmospheric pressure (1.29 kg/m^3 at 273.15 K). "Braginskii's derivation is valid for a linearly increasing current, which means that the results may be applicable in the rising part of the discharge current which can be approximated by a linear ramp" [Eng89].

2.6 Overview

The Townsend mechanism involves the exponential growth of an electron avalanche triggered by collision ionization. Secondary emission from the cathode is needed to supply additional electrons to bridge the gap and form a complete breakdown. The Streamer theory predicts that secondary emission is not essential in the breakdown process. Instead, due to photo-ionization brought on by field distortion, additional avalanches are triggered closer to the anode which are then bridged by streamers and eventually form a conducting channel at speeds significantly faster than those predicted by Townsend. Paschen's law explains breakdown voltage as a function of pressure and gap distance and is based on the Townsend mechanism. However, limitations and deviations from this theory have been observed including:

Paschen's law is satisfied well for static breakdown (not too rapidly changing stress) empirically up to a certain value of *pd*. For impulse voltage stress this *pd* value decreases with increasing stress gradient [Kin85].

It is generally assumed that for *pd* values below 1000 – 2000 torr·cm (~13.3 – 26.7 bar·mm) and gas pressures varying from 0.01 to 300 torr (~ 13 µbar to 0.4 bar), the Townsend's mechanism dominates the breakdown process while higher pressure and *pd* values apply to the Streamer theory. However, controversy still exists on these statements [Nai96].

At higher *pd* values the breakdown voltage (in non-attaching gases) is found to be somewhat higher than at smaller spacing for the same value of *pd*. This departure is probably associated with the transition from the Townsend breakdown mechanism to the Streamer mechanism, as the product of *pd* is increased above a certain value [Kuf00]. Naidu [Nai96] attributes higher breakdown voltages for a given *pd* value at larger gap distances to the loss of electrons from the gap due to diffusion.

Divergence from Paschen's law occurs not only for excessively high, but also for exceedingly low pressure levels. Below c. 10^{-6} bar the laws of vacuum breakdown is applicable [Kin85]. Here, the breakdown mechanism ceases to be influenced by the gas particles and becomes electrode dominated [Kuf00].

Dielectric strength of a gas is dependent on electrode distance. If the gap is very short, ionization mechanisms do not have enough time to operate resulting in increased electric field strength (Figure 10) [Aro03, Kin85].

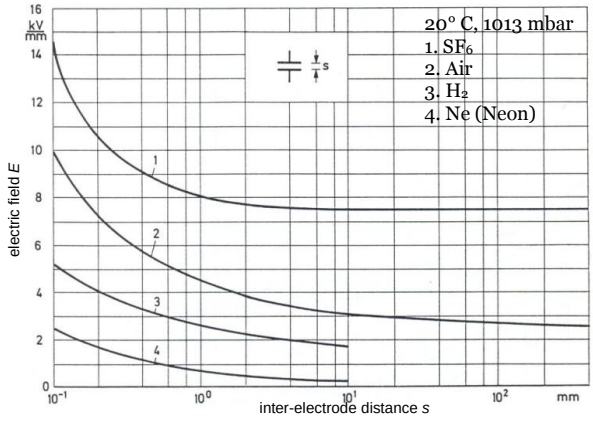

Figure 10. *Breakdown field strength for homogeneous plate electrodes [Kin85].*

3. Sulfur Hexafluoride

Under standard conditions, sulfur hexafluoride is a chemically stable, colorless, odorless, non-toxic and non-flammable gas. SF_6 consists of six fluorine atoms attached to a central sulfur atom (Figure 11). As gas, it is approximately 5 times denser than air with a density of 6.27 kg/m³ at 1.013 bar and 288.15 K[1] [Wik09a, Air11].

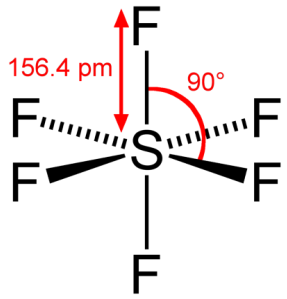

Figure 11. *Octahedral geometry of SF_6 [Wik09a].*

SF_6 is mainly used as a gaseous dielectric medium in the electrical industry. Pressurized SF_6 has notably higher dielectric strength compared to air and nitrogen and thus enables significant reductions in electrical equipment size. However, SF_6 can only be pressurized to 20 bar before it turns into liquid at room temperature (SF_6 liquefies at 5 bar in 243.15 K) [Kin85]. Its high dielectric strength and excellent arc-quenching properties can be attributed to its attaching nature.

3.1 Electron Attachment Process and Electronegative Gases

Free electrons play a significant role in the breakdown process. Free electrons and ions are constantly created and removed through different mechanisms. Recombination can rejoin free electrons with positive ions. Diffusion can cause electrons to migrate under Coulombs forces. Free electrons can also be seized by electronegative atoms by attachment to form negative ions [Aro03]. This process of electron attachment has been recognized in giving high breakdown strengths to gas. Similar to positive ions, negative ions are too massive to produce ionization due to collision as they are significantly slower than electrons, and as such, “attachment represents an effective way of removing electrons which otherwise would have led to current growth and breakdown at low voltages” [Nai96].

[1] Non SI units are used in this text in place of *Pascal* as the meter gauges used during measurements present the pressure in *bar*.

Gases in which this attachment process plays an active role are called electronegative gases. All electrically insulating gases, such as O_2, CO_2, Cl_2, F_2, and SF_6 exhibit this property. In attaching or insulating gases, the atoms or molecules have vacancies in their outermost shells and, therefore, have an affinity for electrons [Nai96].

Common attachment process observed in gases are (a) "direct attachment in which an electron directly attaches to form a negative ion", and (b) "dissociative attachment in which the gas molecules split into their constituent atoms and the electronegative atom forms a negative ion" [Nai96].

(a) Direct attachment $AB + e^- \longrightarrow AB^-$

(b) Dissociative attachment $AB + e^- \longrightarrow A^- + B$

With attaching gases, an attachment coefficient η needs to be considered along with the ionization coefficient α. The attachment coefficient η is defined as the number of attaching collisions made by one electron drifting one centimeter in the direction of the field [Nai96]. Hence, the breakdown mechanism is governed by the net ionization $\alpha - \eta$ which is a balance between ionization and attachment. Now, Townsend's equation for current growth (equation (2.5)) becomes [Kuf00, Nai96],

$$I = I_0 \frac{\dfrac{\alpha}{\alpha-\eta}\left(e^{(\alpha-\eta)d} - \dfrac{\eta}{\alpha}\right)}{1 - \dfrac{\alpha\gamma}{\alpha-\eta}\left(e^{(\alpha-\eta)d} - 1\right)}. \qquad (3.1)$$

Now, the breakdown criterion for attaching gases can be expressed as,

$$\frac{\alpha\gamma}{(\alpha-\eta)}\left(e^{(\alpha-\eta)d} - 1\right) = 1. \qquad (3.2)$$

For $\alpha > \eta$, breakdown is always possible irrespective of the values of α, η, and γ. In other words, the net ionization coefficient needs to be positive for breakdown to occur. On the other hand when $\alpha < \eta$, attachment dominates over ionization and discharge growth is not possible. With an increasing value of d equation (3.2) approaches an asymptotic form,

$$\gamma \frac{\alpha}{(\alpha-\eta)} = 1 \quad \text{or} \quad \alpha = \frac{\eta}{(1-\gamma)}. \qquad (3.3)$$

Typically γ is very small and the above equation can be written as $\alpha = \eta$ [Nai96]. This condition puts a limit for E/p below which breakdown is not possible regardless of the value of d. This limit value is called the critical E/p (referred in text as $(E/p)_{crit}$).

The relationship between $\alpha - \eta$ and pressure p is linear for SF_6 compared to a rather exponential relation in air (Figure 12). The steepness of this linear relation has termed SF_6 as a "brittle" gas [Far04] in that ionization accumulates very rapidly if critical field strength is exceeded.

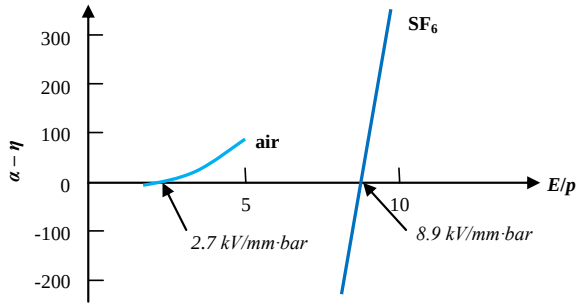

Figure 12. *Effective ionization coefficients in air and SF_6. Edited from [Far04].*

The net ionization coefficient for SF_6 can be expressed as,

$$\frac{\alpha-\eta}{p}=A\left(\frac{E}{p}\right)-B, \tag{3.4}$$

where A = 27.7 kV^{-1} and B = 246 bar^{-1} mm^{-1} [Far04]. Critical field strength ($\alpha-\eta=0$) can now be calculated as,

$$\left(\frac{E}{p}\right)_{crit}=\frac{B}{A}p=8.9kV/mm\cdot bar\,. \tag{3.5}$$

According to Kuffel [Kuf00] the linear relationship shown in Figure 12 is valid for an E/p range of 7.5 to 20 kV/mm·bar. Kuffel gives the breakdown field strength of SF_6 in uniform fields as,

$$\frac{E_b}{p}=\left(\frac{E}{p}\right)_{crit}+\frac{K}{A(pd)}, \tag{3.6}$$

where K = 0...10 for the Townsend mechanism and 18...20 for the streamer mechanism. Removing the constants (K = 18) gives a breakdown field strength [kV/mm] for a pressure p,

$$E_b=8.9+0.65/d\,. \tag{3.7}$$

For a uniform field gap, the Paschen relation can be expressed as,

$$U_b=0.65+8.9(pd), \tag{3.8}$$

where breakdown voltage is given in kV. Kuffel found this dependency to agree well with measured values (Figure 13) for ranges within 1 kV ≤ U_b ≤ 250 kV and 0.4 ≤ pd ≤ 30 bar·mm.

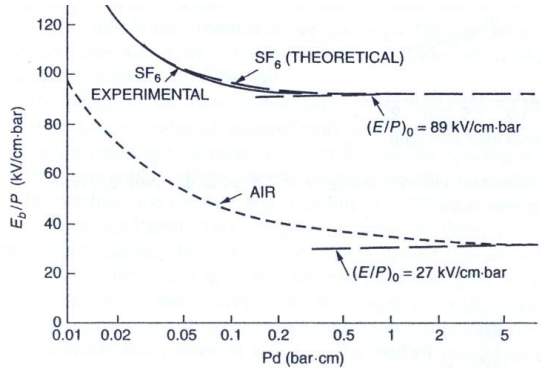

Figure 13. *Breakdown field strength of uniform gap in SF_6 and air [Kuf00].*

3.2 Decomposition Products

As mentioned earlier, in its standard state SF_6 is stable and non-toxic. However, in an impure environment SF_6 can react with different materials to form various compounds. For example, impurities in the environment combine with SF_6 to produce products shown in Table 3.1 [Say09].

Table 3.1. *SF_6 reactions with impurities.*

Impurity		Product
Water (H_2O)	$\Rightarrow$	Hydrofluoric Acid (HF)
Carbon Dioxide (CO_2)	$\Rightarrow$	Carbon Tetrafluoride (CF_4)
Araldite Casting (silicon dioxide SiO_2)	$\Rightarrow$	Silicon Tetrafluoride (SiF_4)

Breakdown in SF_6 also leads to the formation of byproducts. During arcing, temperature is significantly increased creating gaseous and solid decomposition products. The SF_6 gas decomposes into atoms of sulfur (S) and fluorine (F) which then recombine to reform mainly SF_6, but also SF_4 and $SF_5\cdot$ radicals. Of the decomposition products, S_2F_{10} is much more toxic than other products, followed by (in decreasing order) SO_2F_2, SOF_2 and SiF_4 [Gri09]. Solid decomposition products in the form of whitish powder are aggressive when reacting with the humidity of mucous membranes (i.e. nasal and esophageal cavities as well as the hands). However, the volume of decomposed products is microscopic – dangerous levels are rarely reached in part due to the regeneration of decomposed products into pure SF_6 [Say09]. Decomposition products caused by repeated breakdown in SF_6 are shown in Table 3.2.

Table 3.2. *Decomposition products of SF_6 [Gri09, Wik09a].*

Product	Approx. concentration [%]	Comments
SOF_2	0.5	SF_4, which is the major byproduct of SF_6 decomposition, rapidly hydrolyzes to SOF_2
SOF_4	0.085	Forms from the reaction of atomic oxygen with the primary SF_6 breakdown products
SO_2F_2	0.006	
S_2F_{10}	0.026	Combination of two $SF_5\cdot$ radicals. A highly toxic gas, with toxicity similar to phosgene
SO_2	0.002	Forms from hydrolytic reactions of various products
HF	1	
S_2OF_{10}	0.0013	Forms from HF reacting with ceramic insulators
$S_2O_2F_{10}$	0.445	
SiF_4	0.026	

3.3 Greenhouse Effect

SF_6 has been recognized as the most potent greenhouse gas that the Intergovernmental Panel on Climate Change has evaluated. It has a global warming potential of 22 200 time that of CO_2 when compared over a 100 year period. However, "due to its high density relative to air, SF_6 flows to the bottom of the atmosphere which limits its ability to heat the atmosphere". Its atmospheric lifetime is 3200 years [Wik09a].

4. Previous Research

Numerous authors have developed equations for calculating the risetime of discharge in various insulating gases. Several selected formulae describing the observed relationships between risetime, electric field, pressure and impedance found in literature are presented below.

Pécastaing *et al.* [Péc01] report that risetime is strongly dependent on the electric field value. For a given electric field, risetime decreases with gas density. In their report, Pécastaing presents J.C. Martin's equation [Mar81],

$$t_r(ns) = \frac{88}{Z^{1/3}E^{4/3}}\left(\frac{\rho}{\rho_0}\right)^{1/2}, \qquad (4.1)$$

where E is the electric field in kV/mm, Z is the characteristic impedance of the generator, and ρ and ρ_o is the density of the gas used and the density of air at NTP respectively. Equation (4.1) has been shown to produce excessively high risetime. However, the dependencies appear to hold true ($Z^{-1/3}$, $E^{-4/3}$, $(\rho/\rho_o)^{1/2}$).

Martin's equation gives approximately the same risetimes as Sorenson's equation for nitrogen [Sor77],

$$t_r(ns) = \frac{44p^{1/2}}{Z^{1/3}E}, \qquad (4.2)$$

as they are both applied in the same field regions ($E \approx 8$ kV/mm). Sorenson's equations contain pressure p which is not to be confused with density ρ as in Martin's formula. For electric field intensities in the range of 22 to 60 kV/mm, Sorenson presents the following equation for helium,

$$t_r(ns) = \frac{6.4p^{1/3}}{Z^{1/3}E^{1/2}}. \qquad (4.3)$$

Pécastaing [Péc01] determined in his measurements that the influence of the gap is not very great and risetime is dependent solely on the field strength. Using their collected data (Figure 14), the equation for risetime in hydrogen was reformulated into,

$$t_r(ns) = \frac{2.023}{E^{0.807}}. \qquad (4.4)$$

The following equations are collected in Blanchet's [Bla91] report. Ray O'Rourke proposes a proportional risetime as,

$$t_r(ns) \propto \frac{d^{1/3}}{Z^{1/3}E^{4/3}}\left(\frac{\rho}{\rho_0}\right)^{1/3}, \qquad (4.5)$$

where d is inter-electrode distance in mm.

Ian Smith instead offers,

$$t_r(ns) \propto \frac{d^{1/3}}{Z^{1/3}E}\left(\frac{\rho}{\rho_0}\right)^{1/2}. \qquad (4.6)$$

However, Blanchet uses for his own measurements,

$$t_r(ns) = \frac{50d}{Z}\left(\frac{\rho}{\rho_0}\right)^{1/2}. \qquad (4.7)$$

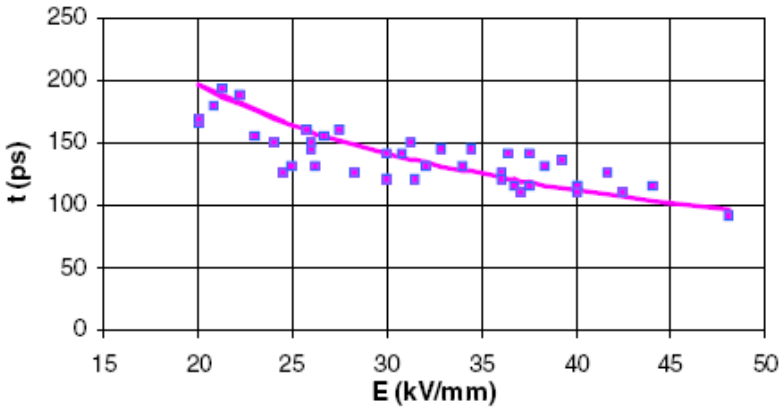

Figure 14. *Pécastaing's risetime plotted against applied electrical field [Péc01].*

5. Test Setups

5.1 General

The test system consists of the test spark gap, an impulse generator and a divider for voltage measurements. An impulse voltage generator (Haefely Multi Test Set, MTS) is used to excite the spark gap and the applied voltage is measured by an impulse voltage divider having a risetime of 20 ns (Figure 15). Components are listed in Table 5.1.

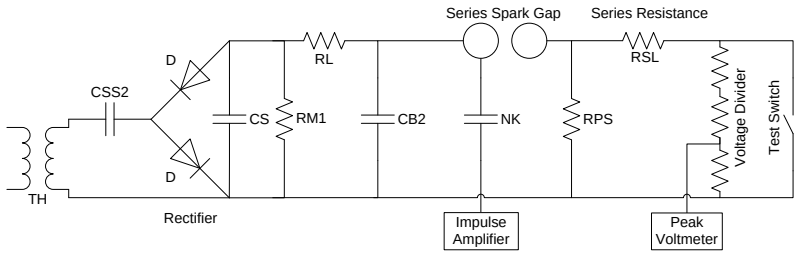

Figure 15. *Impulse source – Haefely MTS setup.*

Table 5.1. *List of MTS components.*

Code	Component	Value
TH	High voltage transformer	100 kV rms, 5 kVA, ≤ 5 pC
CSS2	Coupling capacitor	100 kV DC, 2 nF
D	High voltage diode	100 kV, 20 mA
CS	Smoothing/impulse capacitor	200 kV DC, 15 nF
RM1	Measuring resistor with test jack	200 kV DC, 800 MΩ
RL	Charging resistor	200 kV, 10 MΩ
CB2	Load capacitor	1000 pF, 400 kV impulse
NK	Standard capacitor	100 kV rms, 100 pF
RPS	Tail resistor	100 kV, 84 kΩ
RSL	Lightning impulse front resistor	115 – 1800 Ω

5.2 Coaxial System – Setup 1

5.2.1 Spark Gap

The test gap is a coaxial structure with identical hemispherical stainless steel electrodes facing each other (Figure 16). The characteristic impedance of the coaxial line is c. 30 Ω and is maintained along the entire coaxial structure to the spark gap via a biconical design. The inter-electrode distance can be adjusted and the electrodes are situated in a gas-tight chamber where the insulating gas can be pressurized accordingly. High voltage is applied to one electrode while the other electrode is connected to

the ground via resistance approximately equal to the characteristic impedance of the line. The outer conductor is connected to the ground terminal of the high voltage laboratory floor.

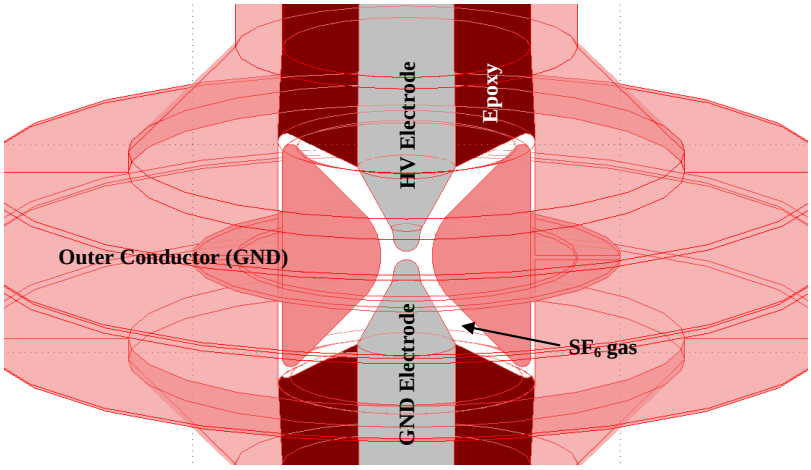

Figure 16. *Test gap geometry. Gray – inner conductor. White – gas. Dark red – epoxy.*

5.2.2 Homogeneous Field

The hemispherical electrodes were designed to maintain a homogeneous field in the spark gap so that the relation $E = U/d$ holds true. Based on simulations the field distribution fluctuates approximately 14 % when gap distance is 1 mm and applied voltage is 200 kV (Figure 17).

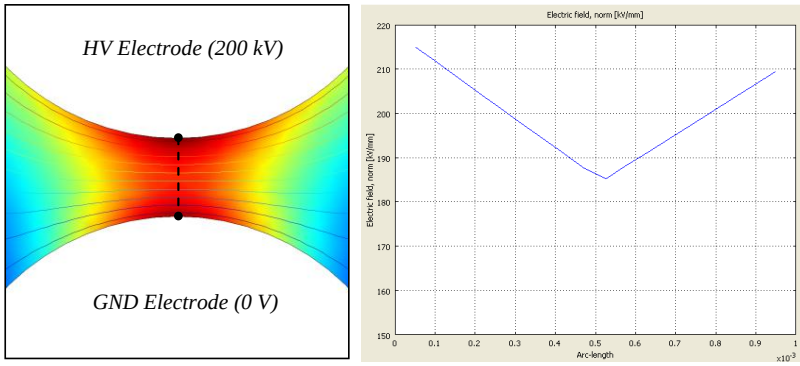

Figure 17. *Left – visualization of electric field distribution at hemispherical electrode tips. Right – electric field deviation $\Delta E \approx 14\%$ at center point of spark gap.*

5.2.3 *D*-dot Probe

Two *D*-dot probes are located on the coaxial line c. 6 cm away from the gap in both directions (supply side and load side). The probe was made from a standard straight bulkhead SMA jack (Huber+Suhner 22-SMA-50-0-12) by cutting off the center conductor to the level of the insulation and mounting it flush with the inner wall of the coaxial line.

Burkhart [Bur85] explains the basic function of such a coaxial probe as follows. “The normal electric field generates a surface charge density on the center conductor of the coax (Figure 18). At zero frequency, the center conductor is held at zero potential through the 50 Ω termination. When E_r, varies, the charge varies linearly, but the current path is through the resistor Z_o with the dissipated power representing the power that is coupled down the coaxial transmission line.”

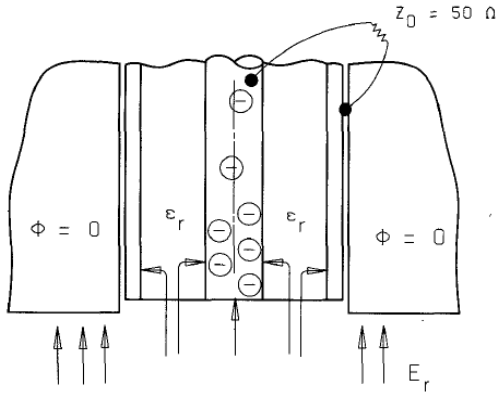

Figure 18. *Working principle of a coaxial sensor [Bur85].*

The output from a *D*-dot probe is proportional to the derivative of the electric field, the change in electric field over change in time *dE/dt*, and is thus recorded by the oscilloscopes as *dV/dt* (more accurately, the probe measures the change in electric displacement (flux) density *D*, hence the name *D*-dot). In order to recover the actual voltage collapse, the signal has to be integrated (Figure 19).

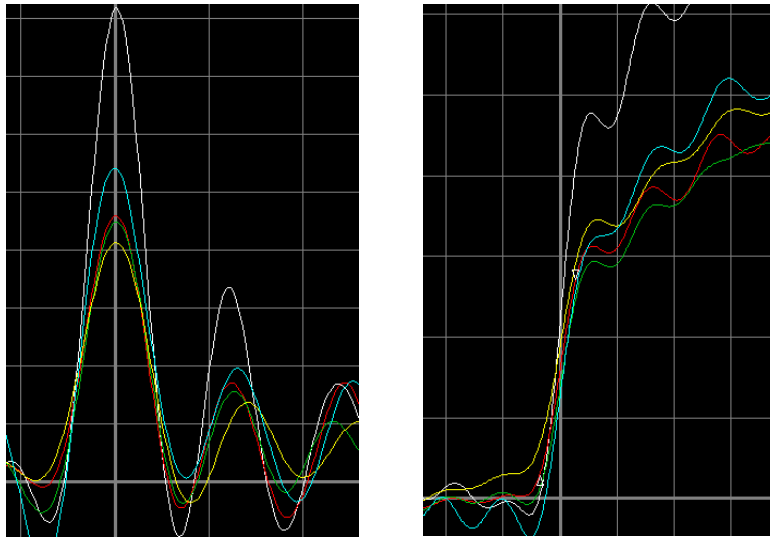

Figure 19. *Digitizer measures dV/dt (left) and voltage collapse is the integral of acquired pulse (right). Scale is arbitrary as the figures are used purely for the sake of visualization.*

5.2.4 Oscilloscope

The coaxial spark gap in Setup 1 was tested using three different measurement systems.

20 GHz Tektronix DSA72004 (prototype)
First measurements of the test gap were conducted using a DSA72004 prototype. The 16 GHz analogue bandwidth was extended using interpolation and frequency response correction of samples to 20 GHz. However, as this was a prototype, the oscilloscope only provided the measured signal after built-in signal processing and the actual raw data samples remained masked.

16 GHz Tektronix DSA72004 (retail)
The retail version of the DSA72004 was equipped with user-selectable DSP enhancement. Therefore, without interpolation, the 16 GHz analogue bandwidth provided raw samples every 20 ps (50 GS/s). Typical risetime (10% to 90%) of the oscilloscope was 22.5 ps and with only a few samples on the rising front of the measured pulse, this system was working at its maximum capacity.

50 GHz Tektronix TDS8200/80E01
A series sampling oscilloscope was used in efforts to improve measurement integrity by increasing the number of samples per pulse. The Tektronix TDS8200 Series Sampling Oscilloscope with 80E01 Sampling Module enables bandwidth exceeding 50 GHz. Impulses were fed at 2 Hz and 500 samples were collected (one from each applied pulse) to form the final waveform with a time resolution of 2 ps.

Unlike the DSA single-shot oscilloscopes measuring both load side and supply side signals simultaneously, the series sampling oscilloscope requires an external trigger. The load-side *D*-dot probe was connected to the trigger channel via a 2.4 m Sucotest ST18 cable. The supply-side probe was connected to the sampling module using a 10 m Sucoflex SF106 cable. In this manner, the load signal informed the oscilloscope to commence sampling while the measured signal arrived with a c. 30 ns delay (due to the extended cable length).

5.2.5 Measurement System

Considerable disturbances were present during testing. The high voltage supply feeder from the impulse generator acts as an antenna propagating inference throughout the measurement laboratory resulting in the acquired data being masked within disturbances. Previous attempts to increase distance between the test gap and measurement equipment proved to be

futile as the increased measurement cable length attenuated and deformed the picosecond breakdown signal to an unrecognizable level. Hence, shorter cables were acquired and measuring equipment was moved to the neighboring high voltage hall while the test gap and supply remained in the original hall. A 10 cm thick grounded steel door was used as electromagnetic shielding and furthermore the shorter distance between the test gap and measuring equipment enables all devices to be grounded at the same point. The impulse generator and voltage divider setup was controlled remotely using a private network as depicted in Figure 20 and Figure 21.

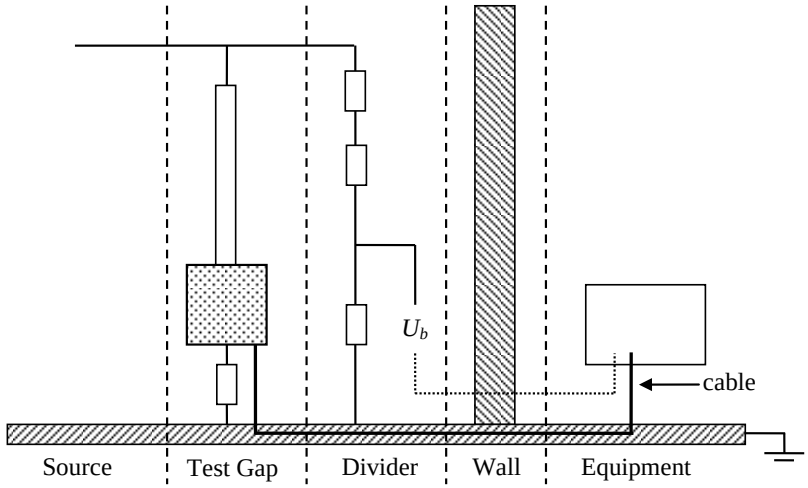

Figure 20. *Data acquisition setup. MTS source coupled with test gap and voltage divider. Measurement cables connect source and test device with measurement equipment in neighboring hall.*

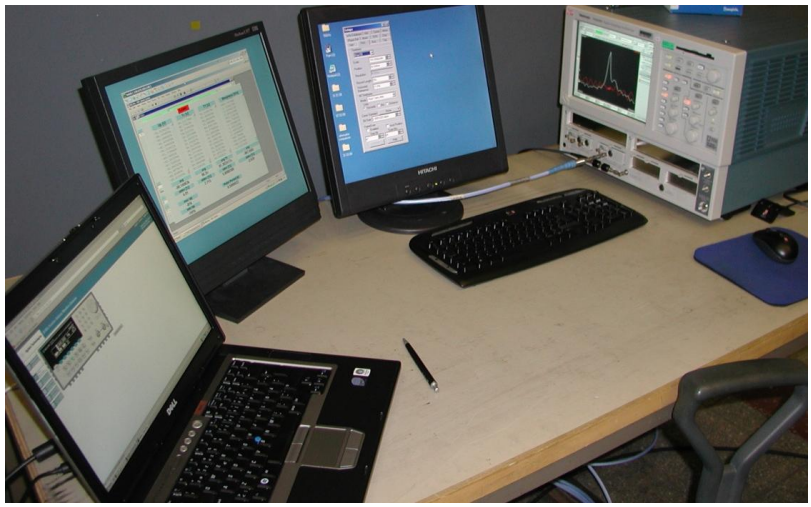

Figure 21. *Measurement equipment behind steel door. From left to right – remote control for source trigger; remote control for voltage divider measurement system; control for series sampling oscilloscope; series sampling oscilloscope.*

5.3 Conical System – Setup 2

The second test gap was made to be comparable with its previous version. Hence, key properties remained fixed, such as:

Insulation gas (SF_6)

Applied voltage range and source (200 kV Marx generator, Haefely MTS)

Pressure range (1 – 19 bar)

Electrode material (stainless steel)

Gap distance (0.1 – 0.9 mm)

Impedance (c. 30 Ω)

Measurement probes (standard straight bulkhead SMA jack)

Homogeneous field distribution at spark gap

However, improvements to prior test gap design include:

Larger volume of gas chamber – percentage of contaminated gas with poorer insulation properties following excessive breakdown is decreased. In addition, migration distance for any conducting impurities to bridge the spark gap is also increased.

Conical construction – fixed angle maintains constant impedance along the transmission line resulting in reduced superpositioning of propagating signals.

Additional probes allowing up to four simultaneous measurements to be obtained from a single breakdown pulse – improves validity of comparable data since subsequent breakdown pulses are statistically deviant and therefore cannot be directly compared with each other.

Improved operability of test gap – ease of maintenance and mobility

5.3.1 Spark Gap

A conical design was implemented to allow fixed impedance along a constant angle of 60 degrees (giving an impedance of approximately 30 Ω) for a distance of 17.5 cm (Figure 22). Since the sensors are located 2 cm from the gap midpoint, the measured pulse can propagate unobstructed for a distance of 15.5 cm before it is reflected back towards the sensor. Hence, reflections will be observed with a delay of approximately 1 n after the initial breakdown pulse is recorded. The dimensions of the test gap were determined using electric field FEM simulations (Figure 23). Distance between the upper conducting plate (high voltage) and the lower plate (ground) had to be sufficient to ensure that breakdown occurs in the spark gap and not in the form of flashover in the air between the plates or as surface discharge along the insulating poles holding the structure together.

Once the dimensions of the geometry were set, it was necessary to conduct structural mechanics simulations to ensure that the design can withstand its intended stress (20 bar of pressure). From simple 2D

simulations it became evident that increasing pressure causes displacement of the high voltage electrode and the ground plate resulting in the augmentation of inter-electrode distance. Hence, the structured needed to be strengthened.

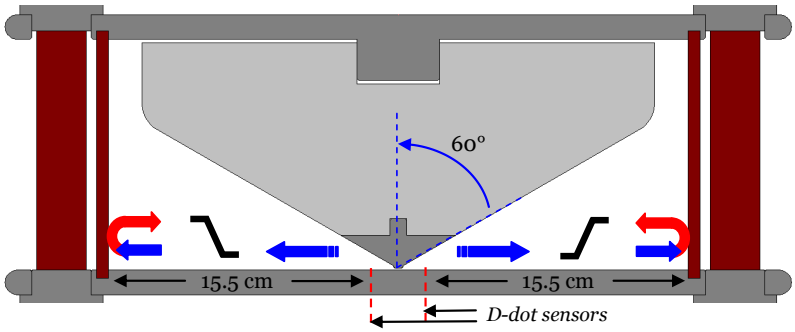

Figure 22. *Conical test gap dimensions. Red = fiberglass; light grey = aluminum; dark grey = steel.*

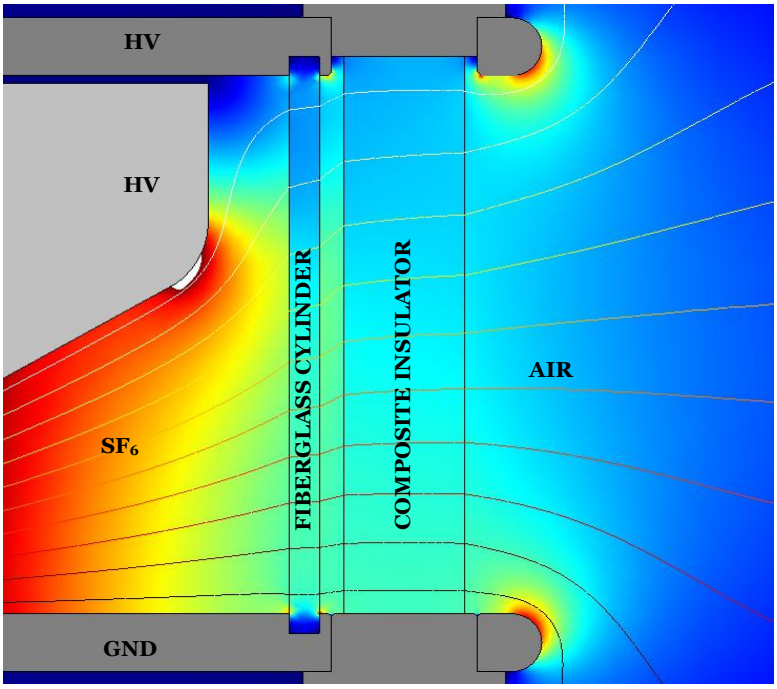

Figure 23. *2D electric field simulation. Red = high electric field concentration c. 2.5 kV/mm; white > 3 kV/mm (critical withstand strength of air).*

3D simulations were carried out to determine the placement of I-frames to support the structure (Figure 24). The optimum construction was established having a maximum gap displacement of c. 0.17 mm at 20 bar (Figure 25 and Figure 26). Further improvements to the design proved to be insignificant due to the restricted accuracy of the simulation caused by the complexity of the structure and processing limitations. “Coarse”

simulations were performed using a 64 bit VISTA, 8 GB RAM computer. Significantly higher processing power would be required to simulate micrometer deformation of a 0.125 m^3 structure in greater detail.

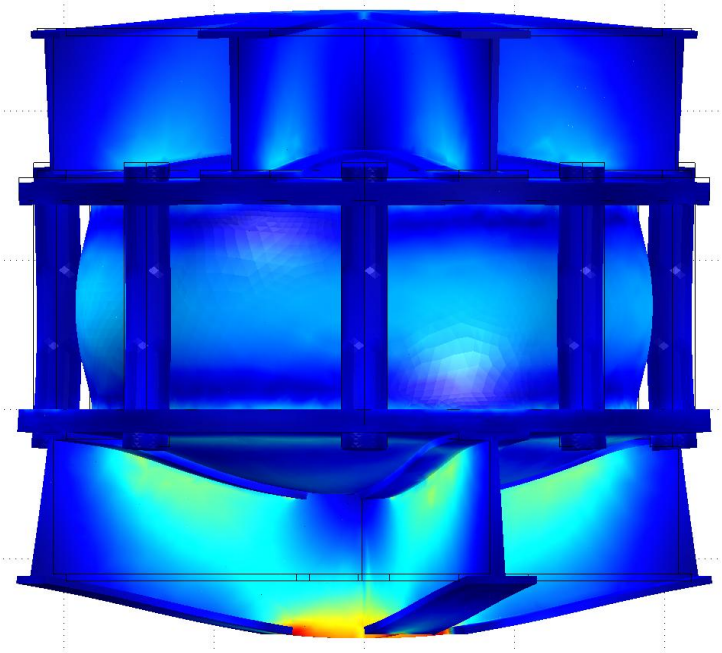

Figure 24. *3D simulation of von Mises stress (red ≈ 175 MPa) and structural deformation*

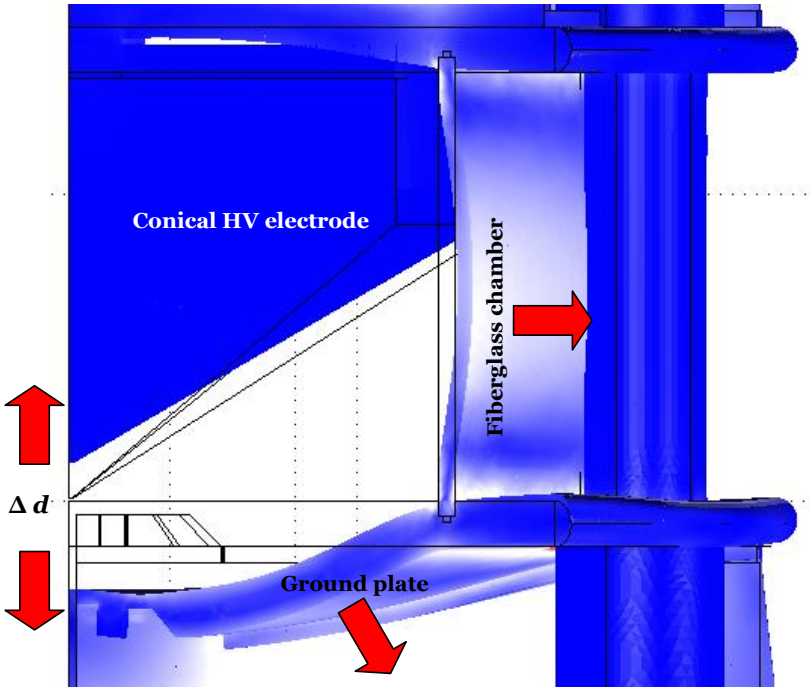

Figure 25. *Gap distance increasing due to mechanical expansion under the influence of pressure. Direction of deformation shown by red arrows.*

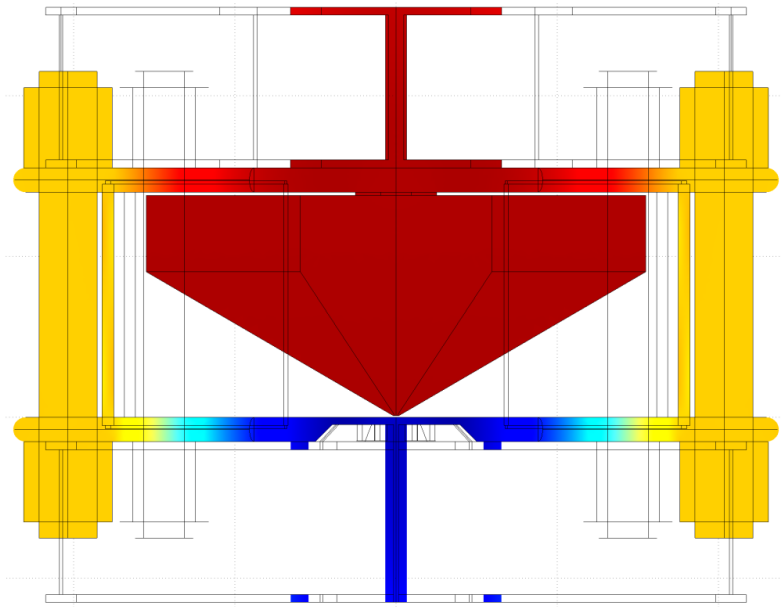

Figure 26. *Z-displacement. Red = 0.0475 mm, blue = -0.124 mm.*

Furthermore, mechanical withstand tests using pressurized water up to 26 bar ($1.3p_{max}$, maximum operational pressure) were carried out successfully to ensure that the final construction was stable and safe (Figure 27).

Figure 27. *Pressure test.*

Mechanical Failure

Several mechanical designs failed due to inadequate simulation methodology and limited knowledge of the insulation material constitution. For the first attempt, mechanical simulation was conducted with simplified

assumptions which proved to be lacking since the consequence of screw threading was not considered (Figure 28a). In the second attempt, a more detailed geometry was simulated to accurately determine the stresses involved (including tightening torque and friction). Fiberglass/epoxy insulation rods provided sufficient tensile strength to withstand the simulated stresses. However, once threads were inserted into the rod, its mechanical properties deteriorated as the strong fiber bonds were broken and the insulation fractured as pressure was applied (Figure 28b). Similar problems would arise if outer threads were to be implemented. Furthermore, the forces involved in pressurizing the spark gap over 20 bar were undervalued as simple spot welds were not sufficient to hold the I-frames onto the steel plate (Figure 28c). Consequently, all welds were strengthened and symmetrically distributed to allow even distribution of force.

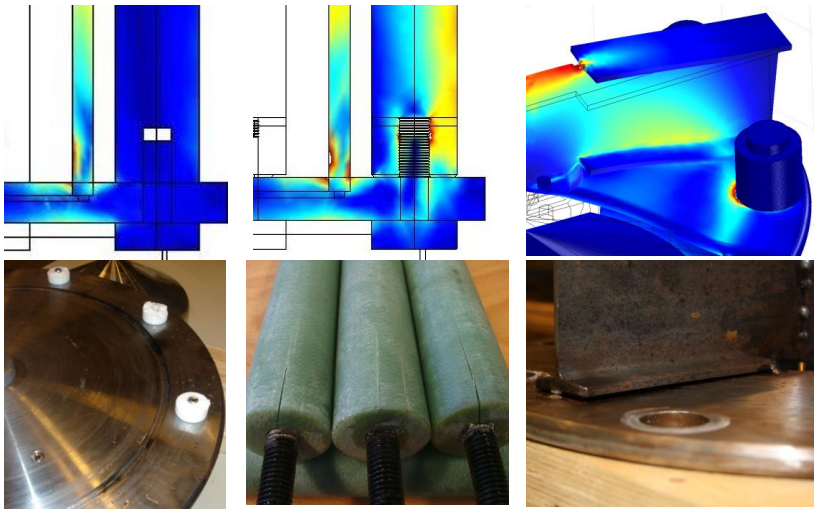

a.) Ertalyte plastic b.) G Entronax EP 11 c.) 10 cm steel I-frame

Figure 28. *Failed mechanical designs.*

It soon became apparent that any alteration to the original insulation rod structure destroyed its mechanical strength. Hence, the solution was found by attaching the rods to the steel plate at a metal to metal interface. This was accomplished using standard overhead line composite tension insulators. These insulators are manufactured to withstand a routine test load of 35 kN (per insulator) which, based on simulations, is sufficient. The loops at the steel end fittings were removed, outer threads were implemented and the silicone rubber sheds were cut off to allow better fitting. Thus, the fiberglass central rod remained untouched and thereby retained its original mechanical properties (Figure 29).

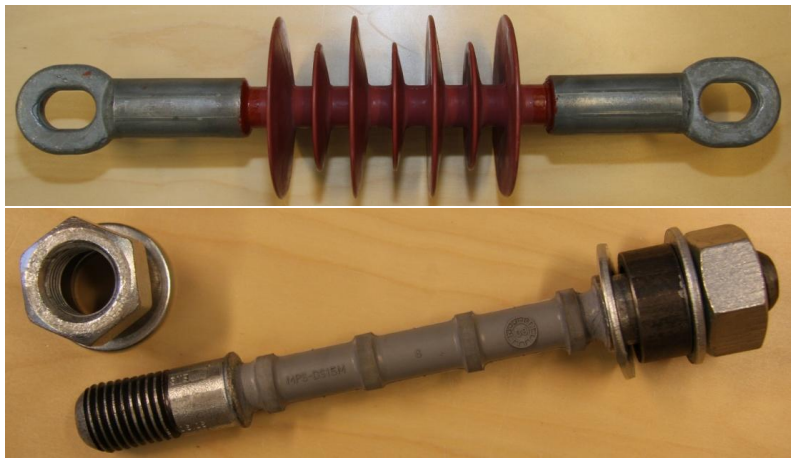

Figure 29. *Composite tension insulator. Top – original structure. Bottom – modified to fit test gap.*

5.3.2 Homogeneous Field

Several profiles were considered when designing the spark gap electrodes, such as Rogowski and Bruce profiles [Tri80]. However, considering the vast number of pulses needed for measurements, a simple plane profile was chosen since more detailed profiles would lose their homogeneous field properties relatively fast due to consequent deterioration from frequent breakdown. The plane profile was achieved with a 2 mm flat stainless steel surface terminated with 2 mm radii (Figure 30).

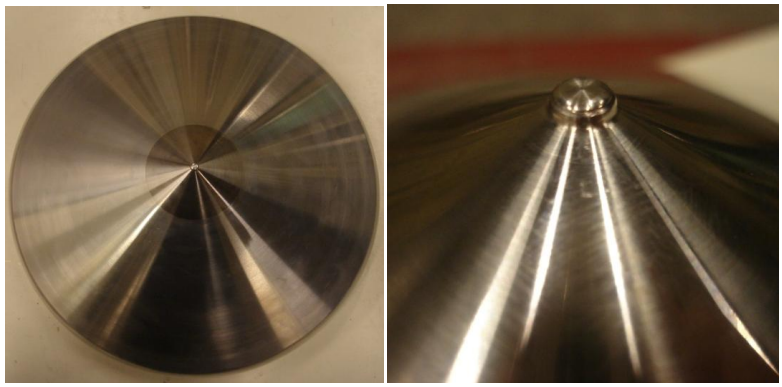

Figure 30. *Conical electrode with plane profile tip. Darker area is stainless steel and lighter region is aluminum.*

The electric field distribution is most uniform at the center of the electrode (Figure 31 a) where field fluctuation between the high voltage electrode and the ground plate is c. 2%. This is maintained along the 2 mm flat area. Electric field is enhanced at the termination of this plane area (Figure 31 b) where the electric field is increased by 7%. This percentage is also influenced by the accuracy of the simulation. Overall, homogeneity of

the spark gap was improved compared to the previous test gap structure (Section 5.2.2).

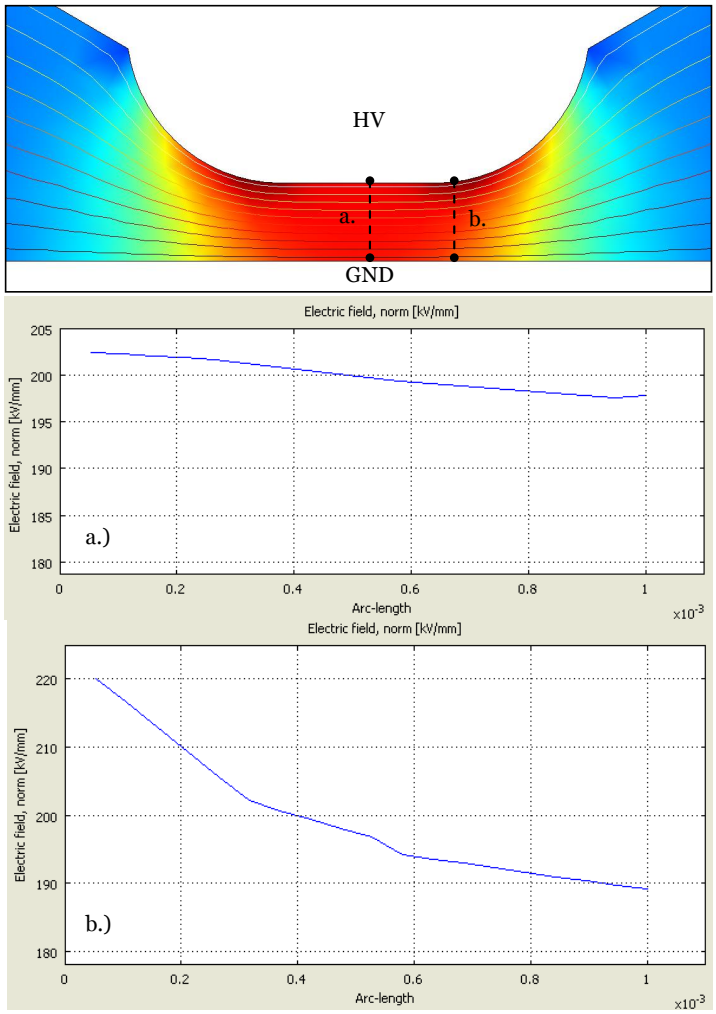

Figure 31. *Electric field distribution at the plane profile electrode tip, a.) center ΔE ≈ 2%, b.) 2 mm radii round-off termination ΔE ≈ 7%.*

Homogeneous Field vs. Fixed Impedance

A compromise between impedance matching and electric field homogeneity was made when designing the electrode. For a conical structure, impedance is maintained constant over a fixed angle and given as [Dic02],

$$Z = \frac{60}{\sqrt{\varepsilon_r}} \ln\left[\cot\left(\frac{\theta}{2}\right)\right]. \qquad (5.1)$$

For a homogeneous field, the conical electrode is terminated using a plane profile with a 2 mm radii curvature. This termination alters the impedance as θ changes along the curvature before settling to a fixed angle along the conical electrode (Figure 32).

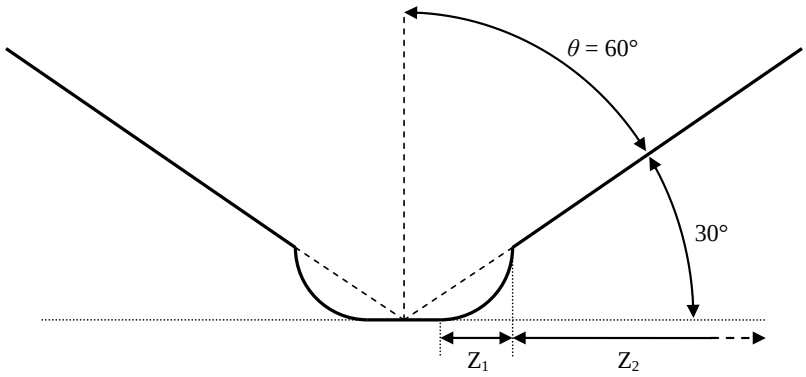

Figure 32. *Impedance variation caused by plane profile termination of conical electrode.*

Consider a simple case of changing impedance along a transmission line. When a propagating wave u reaches an impedance discontinuity region (from Z_1 into Z_2), the resulting reflected wave u_r can be given as [Aro03],

$$u_r = \frac{Z_2 - Z_1}{Z_2 + Z_1} u = \rho \cdot u \,, \tag{5.2}$$

while the transmitted wave u_t can be expressed as,

$$u_t = \frac{2Z_2}{Z_2 + Z_1} u = \tau \cdot u \,. \tag{5.3}$$

Figure 33 studies the change in impedance along the curvature at different points. It is assumed that the curvature is an ideal arc with a constant radius of 2 mm.

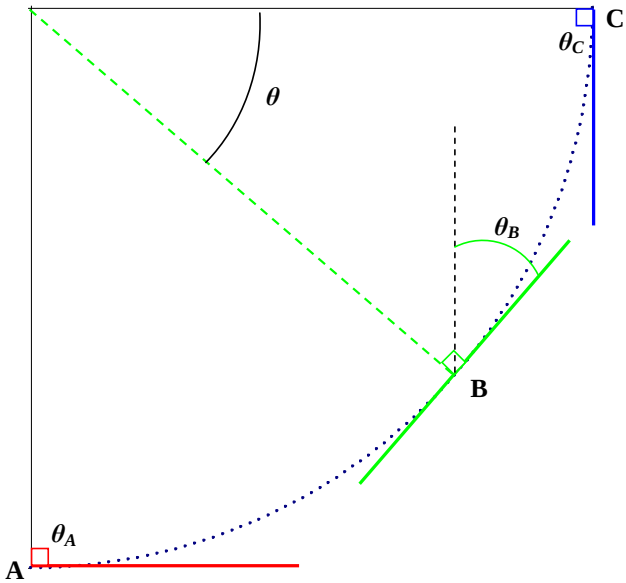

Figure 33. *Change in angle along plane profile termination.*

At point A, the half angle θ of the conical electrode is $\theta_A = 90°$ giving an impedance $Z_1 = 0$. Moving along the arc will constantly decrease θ until point C, where $\theta_C = 0$. As the angle approaches zero, impedance becomes infinitely large. Table 5.2 calculates the reflection and transmission coefficients using equations (5.2) and (5.3) when the arc in Figure 33 is approximated using 90 points with respective angles to calculate a string of impedances connected in series. From Table 5.2 it becomes evident that each subsequent point along the arc has very low reflection coefficients while transmission coefficients are approximately 1. If infinite points are applied along the arc (ideally rounded arc), reflection and transmission coefficients would converge to 0 and 1 respectively since the change in angle between two subsequent points would be negligible (an ideal transmission line).

Table 5.2. *Impedance matching along curvature.*

Point	Angle θ [°]	Z_1 [Ω]	Z_2 [Ω]	Reflection Coefficient	Transmission Coefficient
A	90	0	1	1	2
A+1	89	1.0	2.1	0.33	1.33
	88	2.1	3.1	0.20	1.20
	87	3.1	4.2	0.14	1.14
	86	4.2	5.2	0.11	1.11
	85	5.2	6.3	0.09	1.09
	84	6.3	7.3	0.08	1.08
	83	7.3	8.4	0.07	1.07
	82	8.4	9.5	0.06	1.06
	81	9.5	10.5	0.05	1.05
	80	10.5	11.6	0.05	1.05
	79	11.6	12.7	0.04	1.04
	78	12.7	13.7	0.04	1.04
⋮	⋮	⋮	⋮	⋮	⋮
	50	45.8	47.2	**0.01**	**1.01**
	49	47.2	48.6	**0.01**	**1.01**
	48	48.6	50.0	**0.01**	**1.01**
	47	50.0	51.4	**0.01**	**1.01**
	46	51.4	52.9	**0.01**	**1.01**
B	45	52.9	54.4	**0.01**	**1.01**
B+1	44	54.4	55.9	**0.01**	**1.01**
	43	55.9	57.4	**0.01**	**1.01**
	42	57.4	59.0	**0.01**	**1.01**
	41	59.0	60.6	**0.01**	**1.01**
	40	60.6	62.3	**0.01**	**1.01**
⋮	⋮	⋮	⋮	⋮	⋮
	10	146.2	152.5	0.02	1.02
	9	152.5	159.6	0.02	1.02
	8	159.6	167.7	0.02	1.02
	7	167.7	176.9	0.03	1.03
	6	176.9	187.9	0.03	1.03
	5	187.9	201.3	0.03	1.03
	4	201.3	218.6	0.04	1.04
	3	218.6	242.9	0.05	1.05
	2	242.9	284.5	0.08	1.08
C	1	284.5	∞	1	2
C+1	0	∞	32.9	-1	0

Assuming an ideal structure, where point A and C have a respective half angle of 90° and 0° in respect to the conical electrode, the termination of the arc will produce a reflection factor $\rho = 1$ and a transmission factor $\tau = 2$ (i.e. an open transmission line discontinuity where Z_1 is finite and $Z_2 = \infty$). For this ideal case, at point C+1 where the arc (having infinite impedance) joins the conical electrode with a fixed impedance of 32.9 Ω, equations (5.2) and (5.3) would imply that a full negative reflection occurs completely impeding the propagating signal (i.e. comparable to a short circuit discontinuity where Z_1 is finite and $Z_2 = 0$).

However, a more realistic analysis of signal propagation can be carried out by assuming that some angle is present at the coupling of the arc and conical electrode. For example, with a half angle of 15°, $Z_1 = 146.2\ \Omega$ and $Z_2 = 32.9\ \Omega$, reflection and transmission coefficients can be calculated as

$$\rho = -0.57 \quad \text{and} \quad \tau = 0.43,$$

implying that only c. 40 % of the pulse propagates past this point towards the measurement sensors. The exact extent of transmission and reflection caused by impedance mismatching cannot be defined accurately. However, the time period can be estimated and as such, the impact on measured data can be approximated (Section 7.1). Furthermore, an ideally matched impedance termination for a conical electrode is discussed in Section 7.4.1.

5.3.3 *D*-Dot Probe

Four standard straight bulkhead SMA jacks located 2 cm from the spark gap and displaced 90° from each other are used as *D*-dot probes (Figure 34). The center conductor is cut to the level of the insulation and mounted flush with the ground plate. The probes enable up to four oscilloscopes to simultaneously measure a single breakdown pulse improving validity of comparable data.

D-*dot Probe Functionality*

Trial measurements were conducted using a magnetic field sensor and *D*-dot probes, enabling the characteristics of the sensors to be compared. In contrast to the *D*-dot sensors measuring a changing electric field and requiring additional integration to yield the voltage collapse waveform (integral of *dV/dt* given as arbitrary picovolt second scale since the sensor is uncalibrated), the magnetic field probe directly provides the oscilloscope with a signal (in volts) proportional to current.

Both probes are connected to a 6 GHz LeCroy WaveMaster 8600A oscilloscope via 10 m Sucoflex 106 cables and use the same attenuators (20 dB, Huber+Suhner 6620 SMA 50-1, 18 GHz). Results are shown in Figure 35 where the *D*-dot probe is shown in blue (integral of the *D*-dot in green) and the magnetic field sensor measurements in pink.

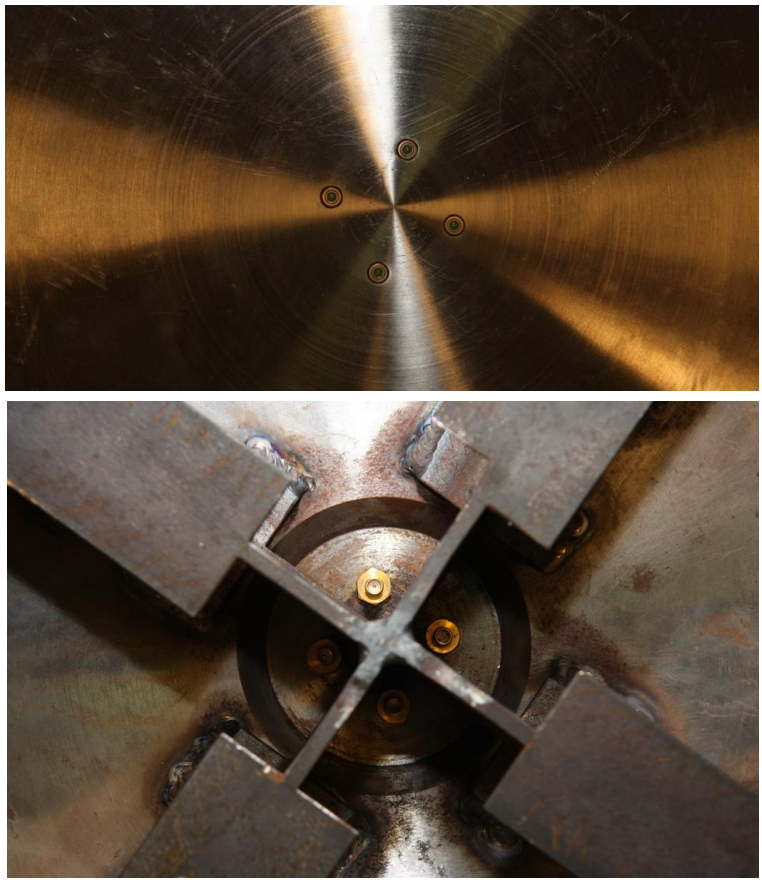

Figure 34. *D-dot probes mounted on the ground plate. Top – sensors flush with ground plate (interior view). Bottom – cable connection under lower plate (exterior view).*

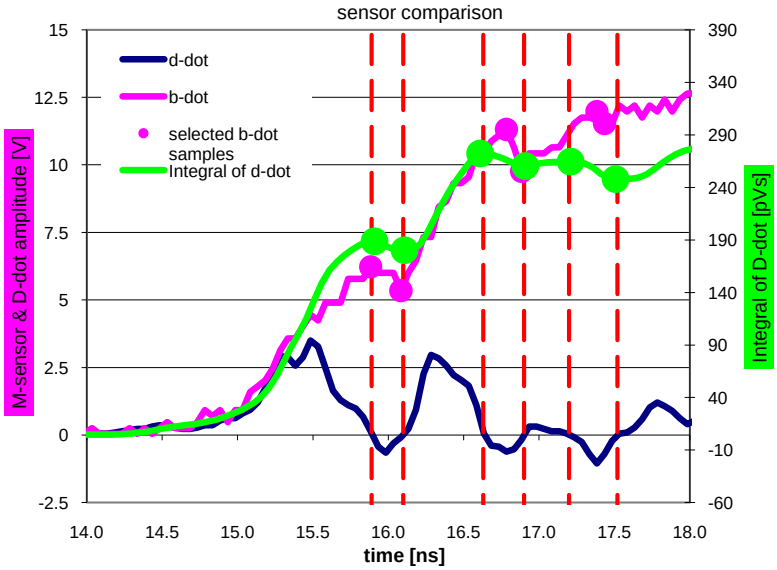

Figure 35. *Electric field versus magnetic field measurements.*

The magnetic field sensor was estimated to have a bandwidth of c. 1 – 3 GHz while the *D*-dot probe bandwidth exceeds 18 GHz. Hence, the sensitivity of the sensors (magnitude and time) differs somewhat. Nevertheless, selected samples are easily distinguishable. For example, when the *dV/dt* pulse falls below the zero-level y-axis, it measures a negative change in the electric field. Hence, its integral has peaked and starts to decrease with time. In contrast, when the *dV/dt* pulse once again is positive, its integral begins to increase. By identifying these corresponding *dV/dt* polarity shifts in the observed integral peaks and dips and comparing with the measured magnetic field samples, a correlation between the two different probes can be made. However, since neither magnetic field probe nor *D*-dot sensor is calibrated, a direct proportionality between pVs and V values cannot be determined. As this research concentrates mainly on measuring the speed of the breakdown phenomenon, normalized values are used and as such, the arbitrary magnitude scale of the integral pulses are of minor importance. Nevertheless, the applicability of *D*-dot probes for field measurements has been established.

In addition, Figure 36 shows a comparison between the commercially available standard Huber+Suhner SMA connector used in this research as a *D*-dot probe (red), a *D*-dot probe designed for an unrelated EMP testing project (yellow) and the previously introduced magnetic field sensor (green). As is evident from the figure, all sensors detect relatively identical waveform (amplitudes of pulses are variably scaled to allow better comparison).

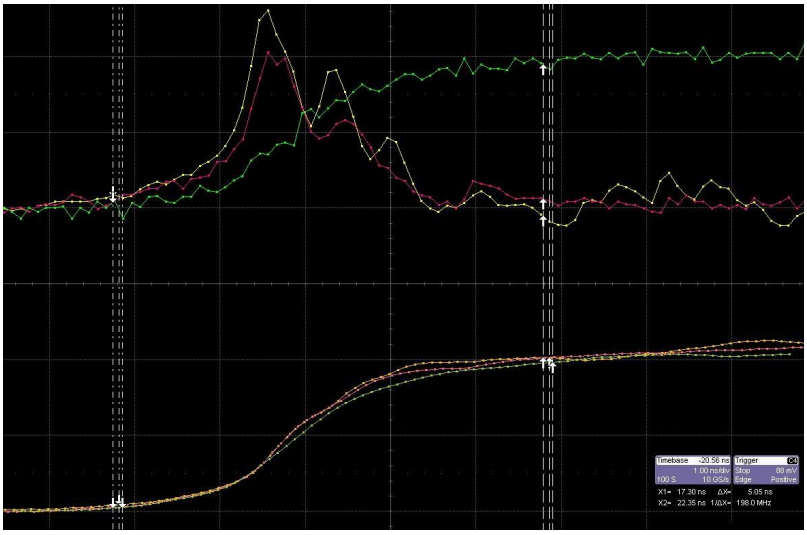

Figure 36. *Sensor comparison. Red – D-dot probe 1 (Huber+Suhner SMA connector). Yellow – D-dot probe 2. Green – magnetic field sensor. Horizontal scale 1 ns/div.*

5.3.4 Oscilloscope

Table 5.3 lists the digitizers used for testing the conical spark gap (Setup 2). At the time of this research[2], SDA 830Zi was the world's fastest real-time oscilloscope [Lec09] sampling every 12.5 ps with a 30 GHz analogue bandwidth. All oscilloscopes use single-shot (real-time) acquisition and are manufactured by LeCroy.

Table 5.3. *Digitizer list.*

LeCroy	Analogue Bandwidth	Risetime [10-90%][3]	Samples	
WaveMaster 8600A	6 GHz	75 ps	20 GS/s	S / 50 ps
SDA 11000	11 GHz	40 ps	40 GS/s	S / 25 ps
SDA 830Zi	30 GHz	15.5 ps	80 GS/s	S / 12.5 ps

5.3.5 Measurement System

Gap Distance Accuracy

Considering the combined uncertainty of all tools used for measuring clearance between the HV electrode and ground plate (including levelness of the plates), inter-electrode distance can be given as d ± 0.01 mm. Additional uncertainty caused by structural deformation as a function of pressure cannot be directly determined using FEM simulation as computational accuracy is limited. Furthermore, only basic material properties (average and typical benchmark values) were used for simulating mechanical strength, whereas, the actual components may have considerably different characteristics (i.e. density, Young's modulus, Poisson's ratio). Estimating the actual gap distance is discussed in more detail in 6.2.1.

Measurement Bandwidth

The data acquisition and data transfer system in the measurement setups consists of *D*-dot sensors, attenuators, cables and oscilloscopes.

The *D*-dot probe functions as a derivative sensor for electric field. "When frequencies become too high, the *D*-dot probe loses its derivative properties and it becomes a monopole antenna. This happens when the length of the *D*-dot probe approaches a quarter wavelength of the incident wave" [And03]. Hence, the original SMA connector with a 4.4 mm center conductor has a cut-off frequency of 18 GHz. However, since the probe is inserted flush with the ground plate, its bandwidth is significantly increased.

$$l = \frac{\lambda}{4} = \frac{c}{4f} \Leftrightarrow f = \frac{c}{4l}. \qquad (5.4)$$

[2] Measurements conducted in November 2009

[3] Note: LeCroy calculates risetime as $t_r = 0.45$ / bandwidth.

Equation (5.4) implies that a 1 mm center conductor would have a cut-off frequency of 75 GHz. Consequently, a *D*-dot probe inserted flush at ground level will still operate as a derivative sensor for frequencies exceeding 75 GHz. Conversely, sensor sensitivity is decreased as the conductor length is shortened.

Both SMA and 2.92 mm (SK) attenuators are used. The SMA attenuators operate up to 18 GHz while the SK attenuators have a cut-off frequency of 44 GHz. Properties of the measurement cables are listed in Table 5.4.

Table 5.4. *Cable properties [from manufacturer's data sheet].*

Cable	Length [m]	Impedance [Ω]	Signal delay [ns/m]	Maximum operating frequency	Nominal attenuation at f_{max} [dB]
Sucoflex 106	10	50	4.3	18 GHz	7.6
Sucotest 18[4]	1.2	50	4.3	18 GHz	3.9

The highest analogue bandwidth is provided by the 30 GHz LeCroy SDA 830Zi oscilloscope. In contrast, the lowest cut-off frequency is limited by the 18 GHz cables. "Theoretical amplitude error of a measured signal can be calculated from the ratio of the digitizer's bandwidth in relation to the input signal frequency" [Nat09].

$$Error(\%) = \left(1 - \frac{R}{\sqrt{1+R^2}}\right) \cdot 100\,. \qquad (5.5)$$

Hence, for a maximum 18 GHz input signal measured by a 30 GHz digitizer, the ratio R = 30/18 = 1.67. As a result, the amplitude error is approximately 56%. Amplitude is not an issue since risetime is calculated from the 30% and 90% coordinates of the normalized pulse. However, the step response of the data acquisition components is a concern.

Risetime is given as[5],

$$Risetime = \frac{0.35}{Bandwidth}\,, \qquad (5.6)$$

and, "it is recommended that the risetime of the digitizer input path be 1/3 to 1/5 the risetime of the measured signal to capture the signal with minimal risetime error" [Nat09]. To fulfill this recommendation, for example, a 20 ps risetime signal would require a digitizer and sensor to have a risetime of c. 4 – 7 ps. A 4 ps risetime correlates to a bandwidth of 87.5 GHz. Such bandwidths are attainable using sampling oscilloscopes, however, this would not be practical for breakdown measurements since scatter is significant (evident in results for Setup 1 shown later in Section 6.1).

[4] Two Sucotest 18 cables were coupled together to form a 2.4 m cable. Nominal attenuation is given for the total cable length (2.4 m).

[5] Note: This relationship is valid only for a one-pole model (i.e. RC low pass filter) [Tek10]. This rule of thumb equation is used here to estimate the order of magnitude.

Measurement Setup

The same measurement setup was utilized as for the coaxial spark gap system presented earlier in Section 5.2.5. Sensitive measurement equipment was situated in the neighboring high voltage hall separated from the test gap and impulse generator by a grounded steel door (Figure 37 – Figure 39).

Figure 37. *Measurement and control equipment situated in the large high voltage hall behind grounded steel door.*

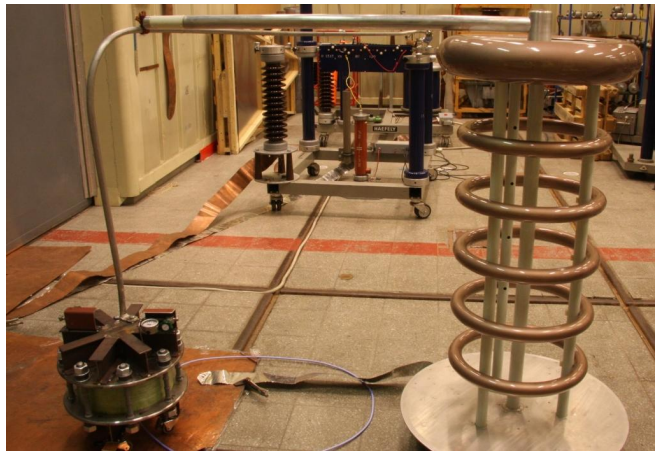

Figure 38. *Test gap, voltage divider and MTS source in the small high voltage hall.*

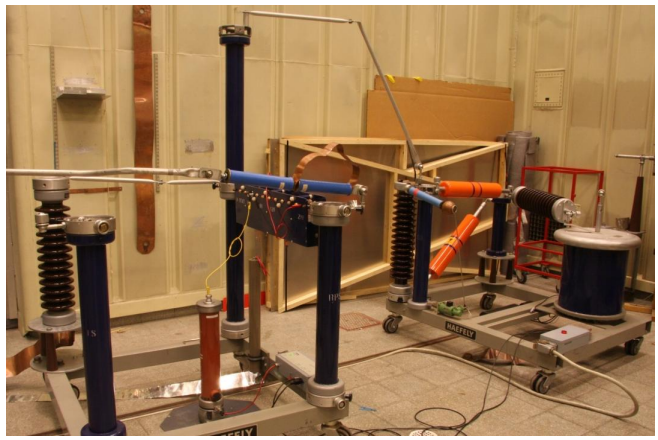

Figure 39. *MTS source: transformer, rectifier, series spark gap and RC circuit.*

6. Results

6.1 Coaxial System – Setup 1 Results

6.1.1 Breakdown Voltage

For each submillimeter gap spacing applied pressure was increased from 1 to 19 bar. Breakdown voltage ranged from 10 kV to 120 kV and followed a rather linear relationship with pressure as described by theory (Figure 40).

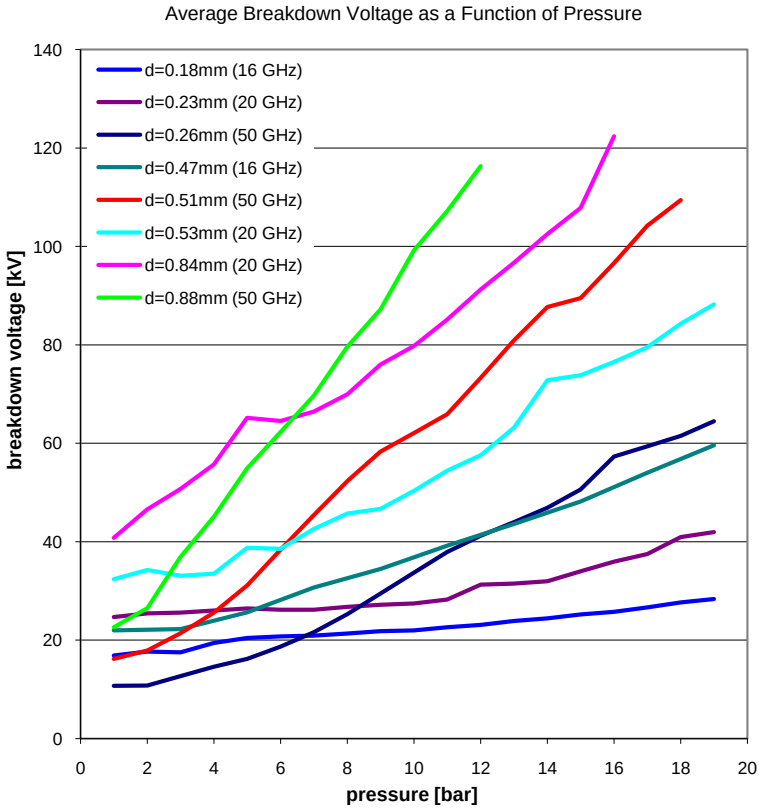

Figure 40. *Breakdown voltage plotted against pressure.*

The correlation between breakdown voltage U_b, electric field strength E/p and the product of pressure and gap distance pd, is shown in Figure 41. Significant deviation from Paschen's law at lower values of pd (corresponding to E/p values exceeding approximately 15 kV/mm·bar) was observed which agrees relatively well with Kuffel's results displayed in Figure 13 of Section 3.1. Here, E is electric field strength in kV/mm, p is pressure in bar and d is gap distance in millimeters.

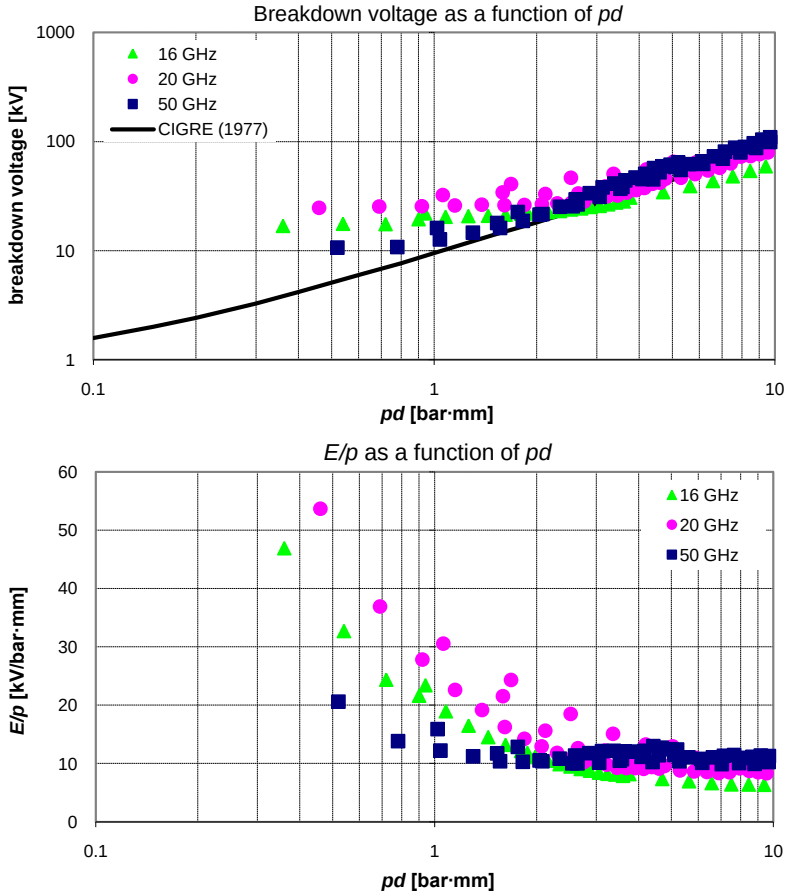

Figure 41. *Top – Measured breakdown voltages plotted along the Paschen's curve [Cig77]. Bottom – E/p plotted against pd values.*

Conditioning Effect

For each gap spacing the test gap was opened and cleaned to avoid contaminating the SF_6 insulation gas. Considerable scatter was observed in breakdown voltages and measured pulse shapes for the first 1000 triggers. As the series sampling oscilloscope collects a number of samples from which it builds a pulse, this scatter significantly hinders measurements.

When measuring with the series sampling oscilloscope it was necessary to trigger the test gap numerous times until subsequent pulses became more unified and scatter was decreased to an acceptable level within a measurement series. Malik and Qureshi [Mal87] refer to this as the "conditioning effect" where weak points of the gap are destroyed by repetitive breakdown pulses. Figure 42 displays 10 000 sequential breakdown voltages (measured in sets of 1000 pulses due to trigger setting restrictions) where the maximum observed increase in linear gradient is approximately 0.3.

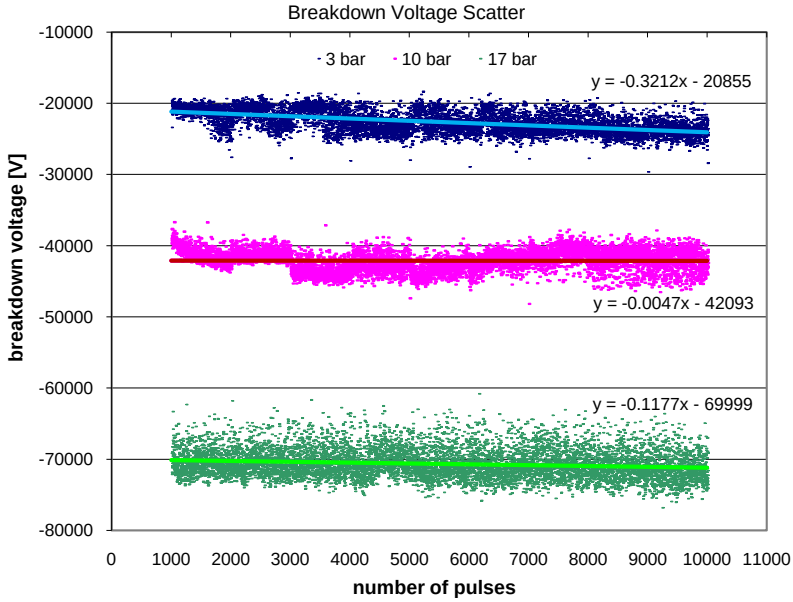

Figure 42. *10 000 successive pulses for d = 0.29 mm at p = 3, 10 and 17 bar.*

Steepness

The steepness of the high voltage impulse exciting the spark gap ranged from 400 to 1200 kV/µs. Previous research [Klü07] has shown that for this setup applied voltages below c. 1400 kV/µs will not influence breakdown voltages as shown in Figure 43 (i.e. a steeper impulse will result in higher breakdown voltage levels).

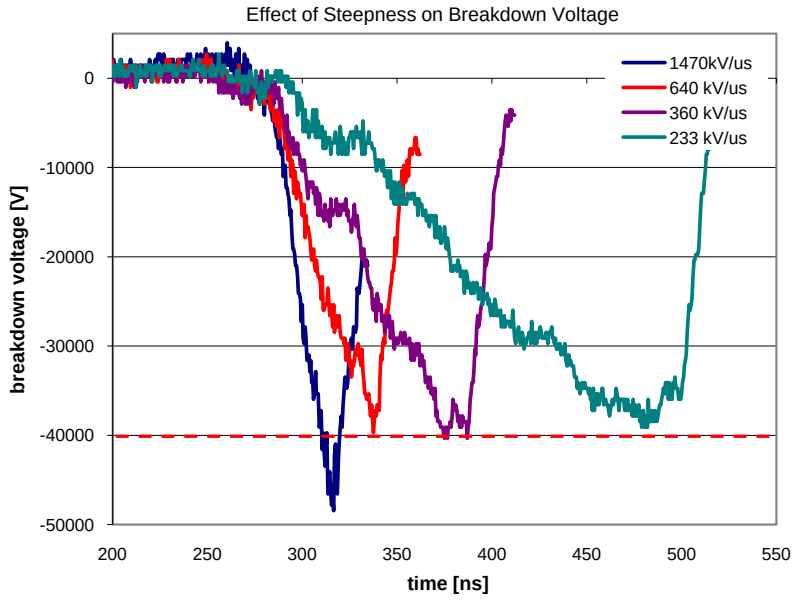

Figure 43. *Effect of applied voltage steepness on breakdown voltage.*

6.1.2 Breakdown Waveform

Two distinct *dV/dt* pulse shapes were observed which allowed the measured waveforms to be grouped into three categories – region I, transition region, and region II.

Region I

Region I is characterized by a rather symmetrical *dV/dt* pulse with a linear rising front, distinct amplitude peak, and clear return to zero-level as shown in Figure 44. The integral of this pulse provides a discrete point at which the voltage collapse settles and from which an accurate risetime value can be calculated.

Transition Region

The transition region occurs when moving from region I to region II. Each successive pulse varies greatly and linear fronts and single amplitude peaks are rare. Measured pulse shapes included double peaks, pyramid shaped pulses and arbitrary fluctuations of amplitude as shown in Figure 45. Integrals of such measured *dV/dt* pulses, from which risetime is to be calculated, are severely varying in nature. At times, several pulse shapes pertaining to region I or region II were observed. However, a consistent waveform representative of this region was not acquired.

Region II

Observed pulse shapes are most uniform in region II. Acquired *dV/dt* pulses once again have a clear linear rise and distinguishable peak amplitude. However, the pulse does not immediately return to zero-level. Instead, the tail of the *dV/dt* pulse plateaus as seen in Figure 46. In turn, the integral of such a measured pulse changes gradient at this "plateau" region and hence risetime is increased until the voltage collapse settles at a constant value (*dV/dt* pulse settles at zero-level).

6.1.3 Risetime

Each aforesaid region can be correlated with a specific *E/p* range and respective risetime (Figure 47). Here, risetime t_r refers to front time T_1 [IEC89],

$$t_r = T_1 = 1.67\left(t_{90\%} - t_{30\%}\right). \qquad (6.1)$$

In region II, where *E/p* values are just above the critical field strength of SF_6 (8.9 kV/mm·bar), risetime was measured as a relatively constant value between 200 and 250 ps regardless of the further increase of pressure from 10 to 19 bar. In region I, where *E/p* exceeds 30 kV/mm·bar, measured risetime was mostly c. 50 ps. Calculated risetimes in the transition region, where $10 < E/p < 30$ kV/mm·bar, were inaccurate as the unstable pulse did not provide a distinguishable waveform. This is summarized in Table 6.1.

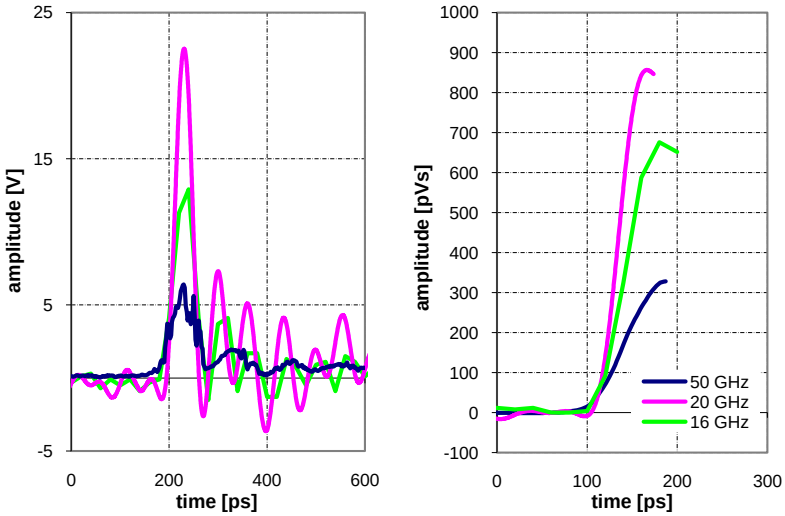

Figure 44. *Region I pulse shape – left: dV/dt waveform, right: integral of measured dV/dt pulse.*

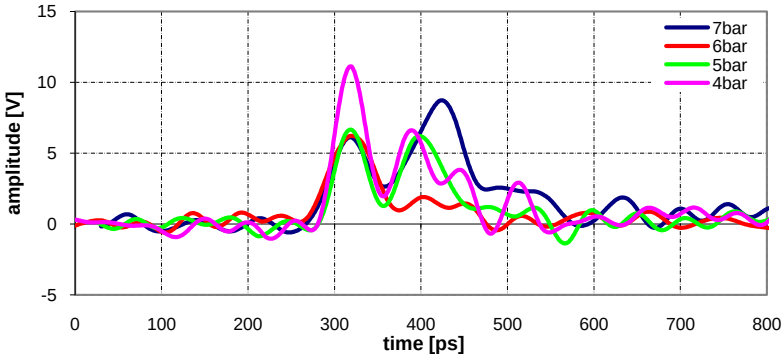

Figure 45. *Typical transition region dV/dt pulse shape.*

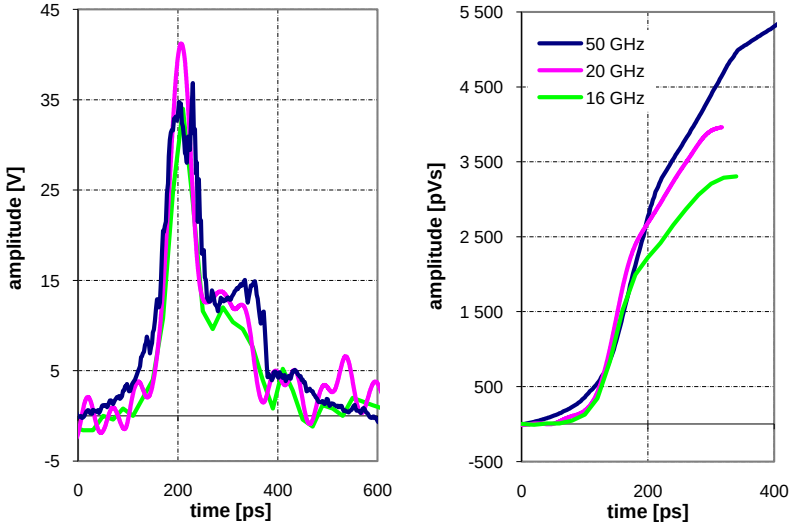

Figure 46. *Region II pulse shape – left: dV/dt, right: integral of dV/dt.*

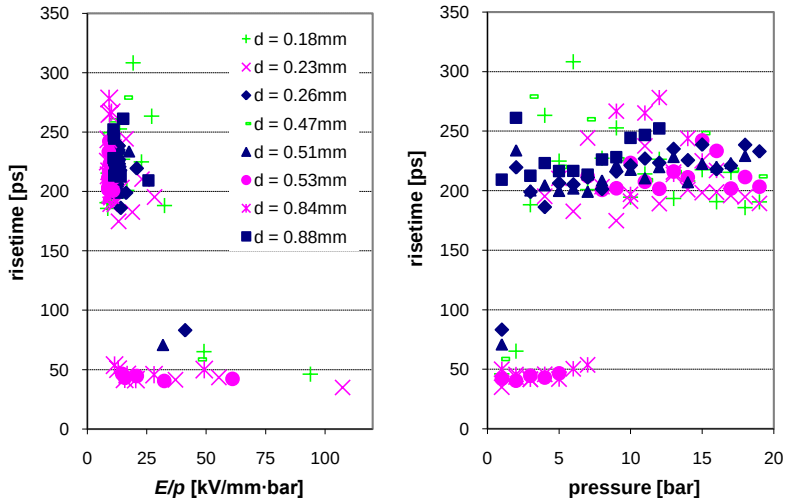

Figure 47. *Risetime of measured breakdown (Note – transition region values not included).*

Table 6.1. *Pulse regions.*

Region	Pressure Range [bar]	*E/p* [kV/mm·bar]	Risetime [ps]
I	1 – 3	> 30	50
Transition	4 – 9	10 – 30	N/A
II	> 10	~ 10	200 – 250

The deviation from Paschen's law shown in Section 6.1.1 is also consistent with the shift from region I to region II where *pd* values below c. 2.6 mm·bar (corresponding to *E/p* values observed in region I) do not follow theory. It is not until region II, where *pd* values are above 2.6 mm·bar and *E/p* is approximately 10 kV/mm·bar, that measured data coincides with Paschen's law (refer to Figure 41).

6.2 Conical System – Setup 2 Results

6.2.1 Breakdown Voltage

A set of ten impulses was measured for each pressure and gap distance ranging from 1 to 18 bar and 0.17 mm to 0.77 mm respectively. Measured average breakdown voltages are shown for each inter-electrode distance in Figure 48. The dashed lines portray the theoretical increase of breakdown voltage U_b relative to pressure,

$$U_b = E_{crit}(pd), \tag{6.2}$$

where E_{crit} = 8.9 kV/mm, p is pressure in bar and d is gap distance in mm.

Compared to CIGRE's values [Cig77] in Figure 49, it is evident that measured data deviates considerably although the general trend between breakdown voltage and the product of pressure and distance is still visible.

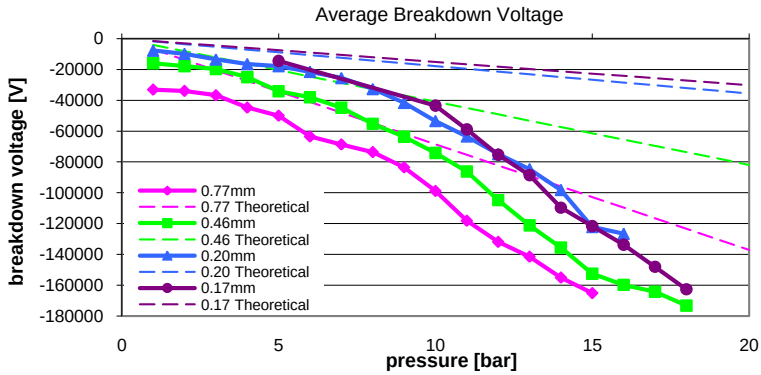

Figure 48. *Average measured breakdown voltage (solid lines) and theoretical breakdown voltage (dashed lines) as a function of pressure.*

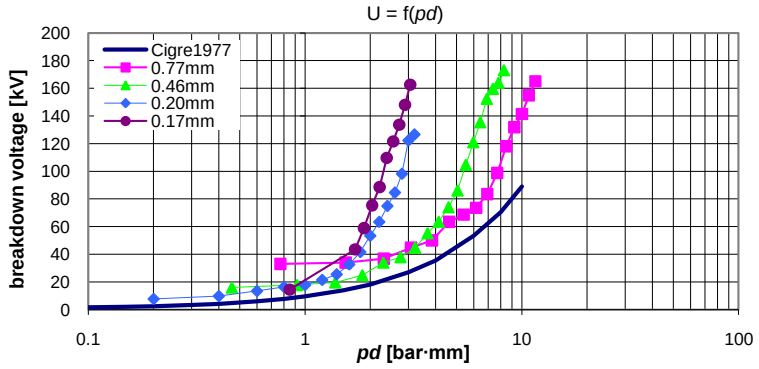

Figure 49. *Measured breakdown voltage as a function of pressure and gap distance.*

The divergence between measurement and theory is even more evident in Figure 50 where the relation between electric field strength (*E/p*) and *pd* is rather U-shaped and appears to grow as *pd* increases. The results suggest that, as pressure increases, the voltage withstand level (critical electric field limit) is developing to values greater than those proposed by theory. Breakdown voltage and pressure can be measured fairly accurately. Thus, the remaining variable influencing these values is inter-electrode distance.

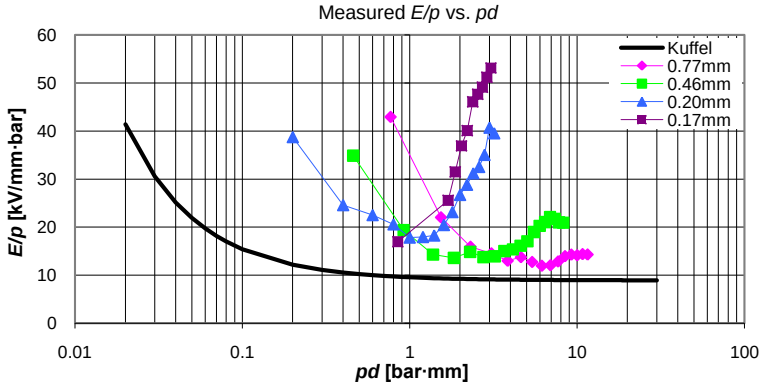

Figure 50. *Electric field strength (E/p) plotted against pd.*

Gap Distance Compensation Based on Simulation

Using Comsol Multiphysics, z-displacement (vertical displacement) of the test gap was simulated with increasing pressure up to 20 bar. As previously stated in Section 5.3.1, maximum displacement at 20 bar is approximately 0.17 mm. Displacement as a function of pressure is shown in Table 6.2.

Table 6.2. *Simulated z-displacement of test gap.*

p [bar]	HV electrode (+z) [mm]	Δ	Ground plate (-z) [mm]	Δ	Σ z	Δ
1	0.00238		0.00619		**0.00856**	
2	0.00475	0.0024	0.01240	0.0062	**0.01715**	0.0086
3	0.00713	0.0024	0.01860	0.0062	**0.02573**	0.0086
4	0.00950	0.0024	0.02470	0.0061	**0.03420**	0.0085
5	0.01190	0.0024	0.03090	0.0062	**0.04280**	0.0086
6	0.01430	0.0024	0.03710	0.0062	**0.05140**	0.0086
7	0.01660	0.0023	0.04330	0.0062	**0.05990**	0.0085
8	0.01900	0.0024	0.04950	0.0062	**0.06850**	0.0086
9	0.02140	0.0024	0.05570	0.0062	**0.07710**	0.0086
10	0.02380	0.0024	0.06190	0.0062	**0.08570**	0.0086
11	0.02610	0.0023	0.06810	0.0062	**0.09420**	0.0085
12	0.02850	0.0024	0.07420	0.0061	**0.10270**	0.0085
13	0.03090	0.0024	0.08040	0.0062	**0.11130**	0.0086
14	0.03330	0.0024	0.08660	0.0062	**0.11990**	0.0086
15	0.03560	0.0023	0.09280	0.0062	**0.12840**	0.0085
16	0.03800	0.0024	0.09900	0.0062	**0.13700**	0.0086
17	0.04040	0.0024	0.10500	0.0060	**0.14540**	0.0084
18	0.04280	0.0024	0.11100	0.0060	**0.15380**	0.0084
19	0.04510	0.0023	0.11800	0.0070	**0.16310**	0.0093
20	0.04750	0.0024	0.12400	0.0060	**0.17150**	0.0084
Avg.		**0.0024**		**0.0062**		**0.0086**

Thus, based on simulations, the actual gap distance is,

$$d_{comp(sim)} = 0.0086\,p + d_0, \qquad (6.3)$$

where d_o is the original inter-electrode distance at zero pressure (atmospheric pressure). Corresponding gap distances using this formula are shown in Figure 51 as a linear function of pressure.

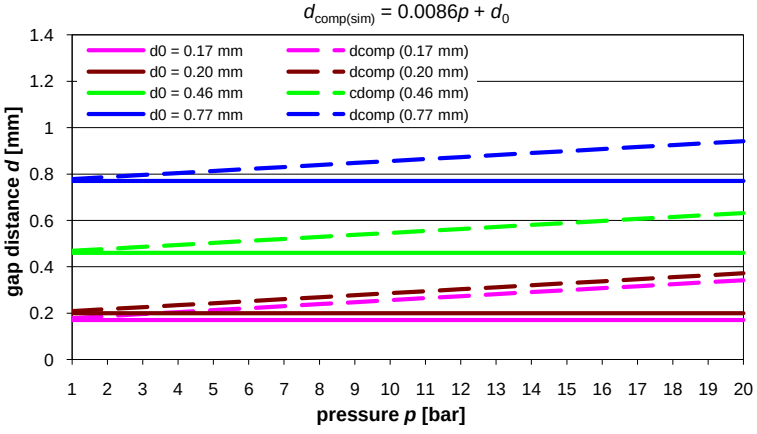

Figure 51. *Simulated gap expansion (dotted lines) under the influence of pressure.*

Application of these simulated gap distances to measured breakdown data is shown in Figure 52 and Figure 53.

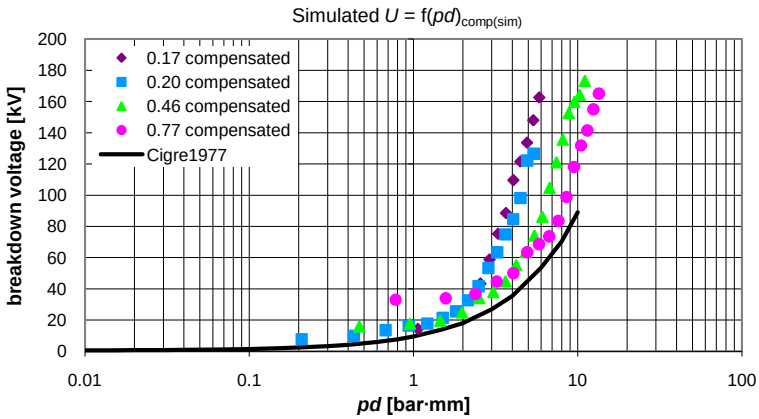

Figure 52. *Breakdown voltage as a function of pressure and simulated gap distance.*

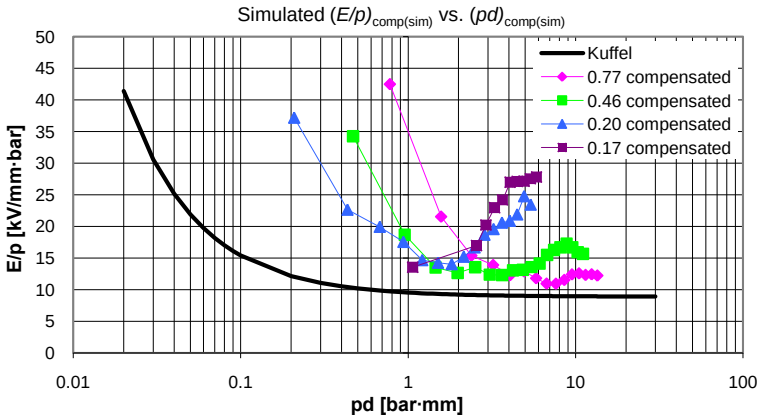

Figure 53. *Field strength as a function of pressure and simulated gap distance.*

Some improvement relative to known theory is evident in these figures. However, significant deviation still remains. Since simulation calculates ideal situations and homogeneous material properties, this analysis is not very accurate. Simulation uses standard properties for common steel and fiberglass which can differ significantly from the actual material used in the test gap. Thus, another method for gap compensation is considered.

Gap Distance Compensation Based on Theory

Assuming critical electric field strength E_{crit} = 8.9 kV/mm, the following analysis can be made. Using measured breakdown voltage values, gap distance can be calculated as,

$$d = U / E(p). \qquad (6.4)$$

Such theoretically acquired values for gap distance d = 0.46 mm are shown in Table 6.3 and the full range of data is plotted in Figure 54. The table also shows the deviation (Δd) from the original gap distance d_o.

Table 6.3. *Calculated gap distance based on theory*[6].

d_o [mm]	p [bar]	E [kV/mm]	$E \cdot p$ [kV·bar/mm]	U_b [kV]	$d = U_b/E \cdot p$ [mm]	Δd [mm]	Δd [%]
0.46	1	8.9	8.9	16.05	**1.80**	1.34	392
0.46	2	8.9	17.8	17.82	**1.00**	0.54	218
0.46	3	8.9	26.7	19.70	**0.74**	0.28	160
0.46	4	8.9	35.6	24.98	**0.70**	0.24	153
0.46	5	8.9	44.5	34.10	**0.77**	0.31	167
0.46	6	8.9	53.4	37.99	**0.71**	0.25	155
0.46	7	8.9	62.3	44.83	**0.72**	0.26	156
0.46	8	8.9	71.2	55.26	**0.78**	0.32	169
⋮	⋮	⋮	⋮	⋮	⋮	⋮	⋮
0.46	17	8.9	151.3	164.16	**1.09**	0.63	236
0.46	18	8.9	160.2	173.20	**1.08**	0.62	235

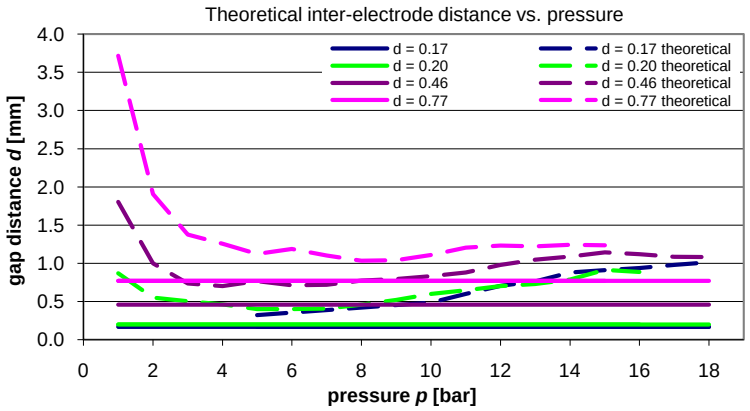

Figure 54. *Inter-electrode spacing (d) expanding under the influence of pressure (p).*

From Figure 54, a somewhat linear growth in gap distance as pressure increases is evident for pressure exceeding approximately 6 bar. The significantly larger values observed at lower pressures are comparable to Kind's and Kuffel's experimentally acquired values shown earlier in Figure 10 and Figure 13 where higher breakdown levels are observed for smaller gap spacing and *pd* values.

This analysis assumes that low-pressure (c. 1 – 5 bar) calculated gap distance values shown in Figure 54 are not predominately related to mechanical expansion (insufficient stress to cause deformation of structure) and therefore these values are left unaltered. The pressure region with the onset of the linear rise is taken as a reference and only gap distances exceeding this pressure is compensated. In other words, gap distances corresponding to pressures below the reference value remain constant (i.e. $d = d_o$ = 0.17, 0.20, 0.46, or 0.77 mm) and gap distances corresponding to pressures exceeding the reference value are compensated using the corresponding normalized Δd values shown in Table 6.3. The compensated values for d = 0.46 mm are given in Table 6.4 and results of this compensation method are plotted in Figure 55 and Figure 56.

[6] Complete tables for all compensation methods are shown in Appendix 1.

Table 6.4. *Compensated gap distance using reference onset.*

d_o [mm]	d (theory) [mm]	Δd [mm]	d (compensated) [mm]	p [bar]	pd [bar·mm]	U_b [kV]	E/p [kV/mm·bar]
0.46				1	0.46	16.05	34.88
0.46				2	0.92	17.82	19.37
0.46				3	1.38	19.70	14.27
0.46				4	1.84	24.98	13.58
0.46				5	2.30	34.10	14.83
0.46				6	2.76	37.99	13.76
0.46	**0.72**	**0.00**	**0.46**	**7**	**3.22**	44.83	13.92
0.46	0.78	0.06	**0.52**	8	4.13	55.26	13.37
0.46	0.79	0.07	**0.53**	9	4.81	63.62	13.22
0.46	0.83	0.11	**0.57**	10	5.73	74.12	12.93
0.46	0.88	0.16	**0.62**	11	6.83	86.24	12.62
0.46	0.98	0.26	**0.72**	12	8.65	104.76	12.10
0.46	1.05	0.33	**0.79**	13	10.23	121.10	11.84
0.46	1.09	0.37	**0.83**	14	11.60	135.56	11.69
0.46	1.14	0.42	**0.88**	15	13.25	152.55	11.52
0.46	1.12	0.40	**0.86**	16	13.79	159.71	11.58
0.46	1.09	0.37	**0.83**	17	14.03	164.16	11.70
0.46	1.08	0.36	**0.82**	18	14.79	173.20	11.71

= reference

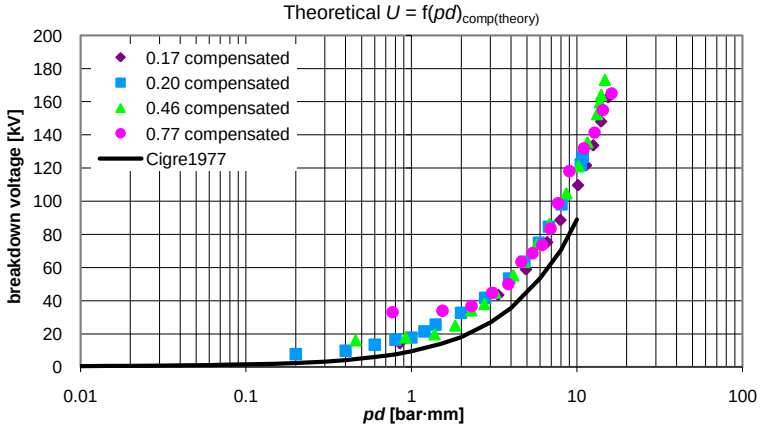

Figure 55. *Breakdown voltage as a function of pressure and compensated gap distance.*

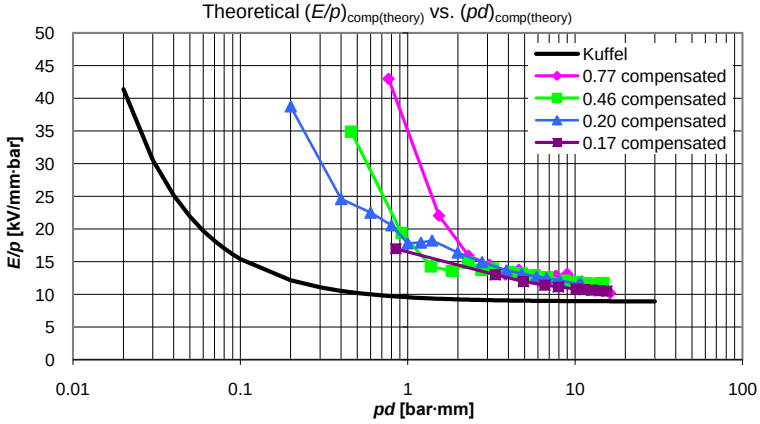

Figure 56. *Electric field strength (E/p) versus pressure and compensated gap distance.*

Recall that the prior method only compensates high-pressure data (pressure exceeding c. 6 bar) where mechanical displacement is more significant. As Kuffel has shown that critical field strength fluctuates for lower *pd* values, low-pressure data should also be compensated for a more accurate compensation model.

Gap Distance Compensation Based on Simulation and Theory

Simulation provided a linear correlation between pressure and gap distance. This linear relation can be applied to the theoretically derived gap distances in Figure 54 to extend a trendline from the high-pressure data (Figure 57) to include low-pressure data compensation.

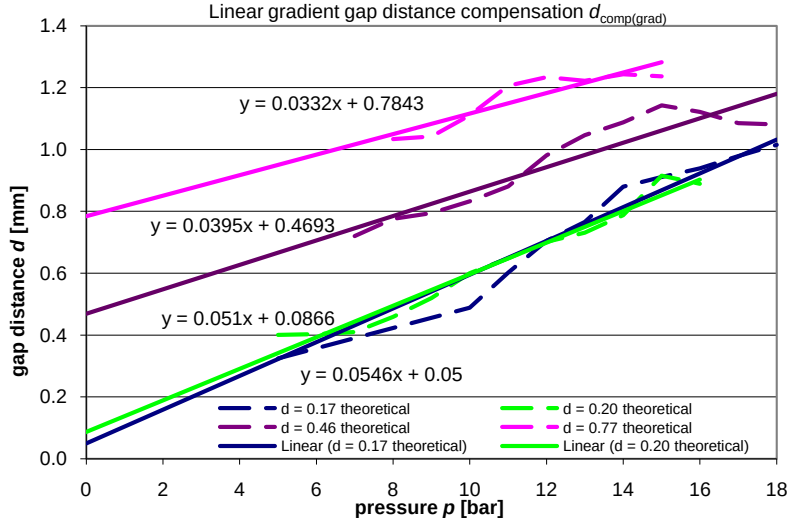

Figure 57. *Linear gradient for gap expansion under increasing pressure.*

The extended trendlines for gap distances d = 0.77 mm and d = 0.46 mm appear to be quite suitable when considering gap distance d_o at p = 0 bar where mechanical displacement is yet to occur – constant b (y-intercept) in the linear equation $y = ax + b$ should be equal to gap distance d. However, for smaller gap spacings (d = 0.17 mm and d = 0.20 mm), the trendline gives excessively small values (b < d). The original linear gradient for d = 0.17 mm gives a negative value for constant b (not shown in Figure 57), signifying a closed circuit inside the test gap. This is obviously not the case, since c. 10 kV breakdown voltages were measured at this distance when p = 1 bar. Nevertheless, this would imply that the smallest gap openings are in fact, even smaller. This is quite plausible as such minimal distances are difficult to achieve in practice when accounting for all the non-idealities of the test gap design and measurement error. Since data for d = 0.17 mm is limited, the offset is estimated to be 0.05 mm. The compensated gap distance values for d = 0.46 mm are shown in Table 6.5 and respective results are plotted in Figure 58.

Table 6.5. *Compensated gap distance using linear gradient.*

d_o [mm]	p [bar]	$d = 0.0395p + 0.4693$	$(pd)_{comp}$ [bar·mm]	Measured U_b [kV]	E/p [kV/mm·bar]
0.46	1	0.51	0.51	16.05	31.54
0.46	2	0.55	1.10	17.82	16.25
0.46	3	0.59	1.76	19.70	11.17
0.46	4	0.63	2.51	24.98	9.96
0.46	5	0.67	3.33	34.10	10.23
0.46	6	0.71	4.24	37.99	8.96
0.46	7	0.75	5.22	44.83	8.59
0.46	8	0.79	6.28	55.26	8.80
0.46	9	0.82	7.42	63.62	8.57
0.46	10	0.86	8.64	74.12	8.58
0.46	11	0.90	9.94	86.24	8.67
0.46	12	0.94	11.32	104.76	9.25
0.46	13	0.98	12.78	121.10	9.48
0.46	14	1.02	14.31	135.56	9.47
0.46	15	1.06	15.93	152.55	9.58
0.46	16	1.10	17.62	159.71	9.06
0.46	17	1.14	19.39	164.16	8.46
0.46	18	1.18	21.25	173.20	8.15

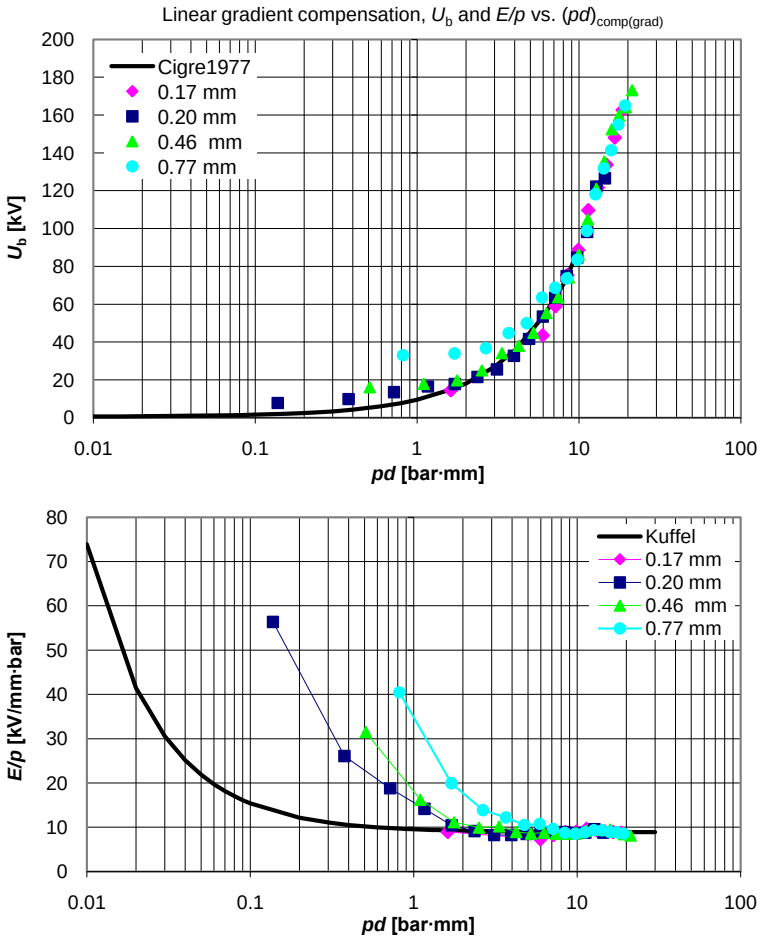

Figure 58. *Breakdown voltage (top) and E/p (bottom) as a function of pd using linear gradient compensation.*

Gap Distance Compensation Based on Measurements

All previously discussed gap compensation methods are based on a primary assumption upon which a compensated value is derived using either simulation or theory. In order to improve the integrity of measured data and strengthen the validly of the discussed compensation methods, measurements which consider the actual test device in question needed to be conducted. As it is impossible to measure the inter-electrode displacement directly from the electrode tips enclosed within the pressurized gas chamber, three locations on the outside of the test spark gap were selected. Micrometer dial gauges were used to measure the displacement of the lower plate (d_1 – as close as possible to the center of the ground plate), displacement of the upper plate (d_2 – as close to the center as possible) and the displacement of the upper I-frame (d_3 – located directly in the center of the upper plate) as shown in Figure 59. The additional dial gauge was employed to measure d_3 since the other gauge (d_2) cannot extend exactly to the center coordinate of the upper plate. The test spark gap was placed on a stable platform upon which the dial gauges where attached using magnets. Displacement was measured with increasing pressure up to 18 bar. After releasing pressure, the dial gauges returned relatively close to zero (± 0.025 mm) signifying that the test device has remained fairly fixed in its original position. Measurements were repeated twice.

Several models were used to determine the most appropriate representation of the measured trend including the Hoerl model, Multiple Multiplicative Factor MMF model (Figure 60) and a third degree polynomial[7]. All models provided an adequate fit for the measured data with correlation coefficients r = 0.99. However, an average of the above mentioned models was taken as the best representation of all measured data as shown in Figure 61 – "Average Model".

Implementing this "Average Model", the inter-electrode displacement (compensated gap distance) based on measured values could be calculated as a function of pressure as shown in Figure 62.

[7] The Hoerl and MMF models were calculated using CurveExpert ver. 1.4 and the polynomial function was derived using Microsoft Office Excel 2003.

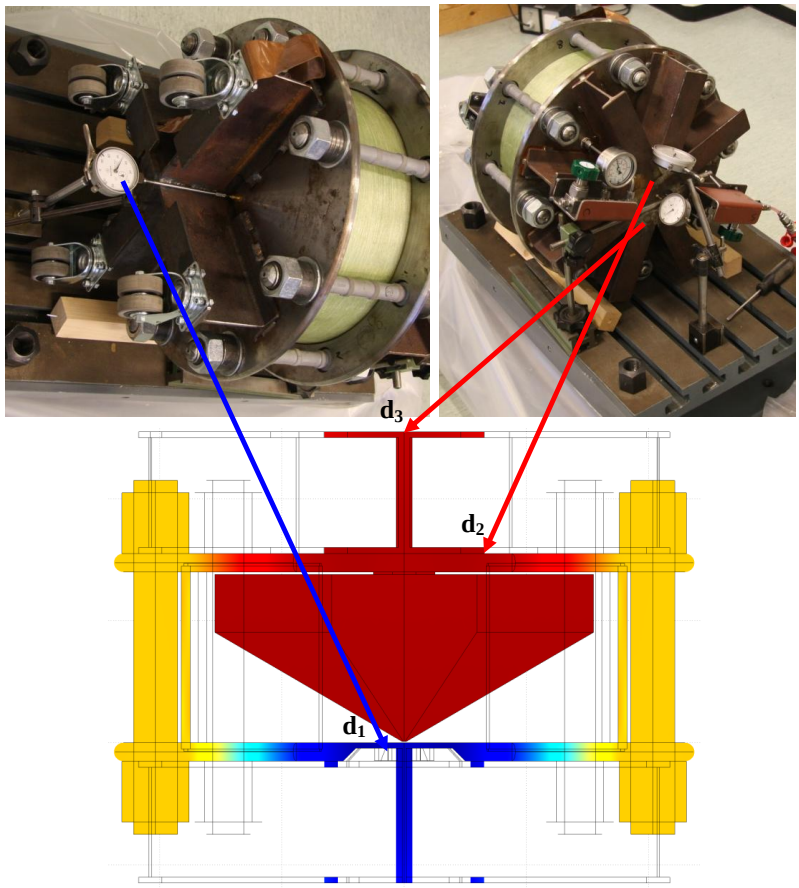

Figure 59. *Dial gauge placement for gap displacement measurements.*

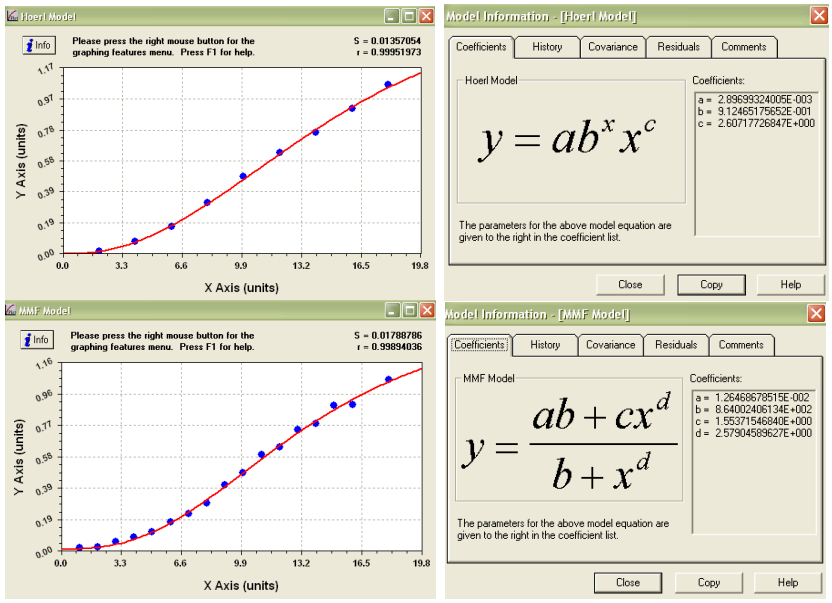

Figure 60. *Line fitting models (Hoerl, MMF) for measured data.*

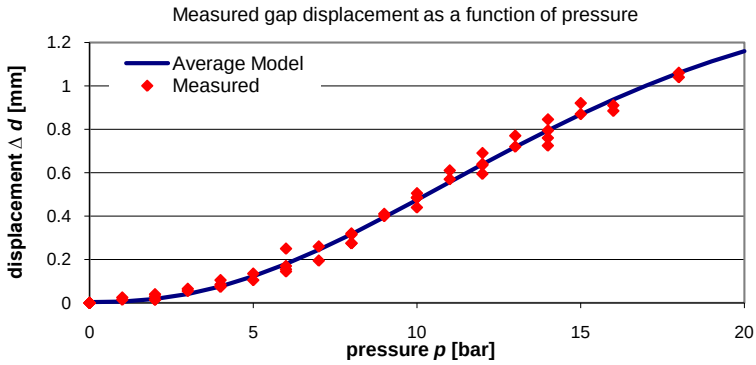

Figure 61. *Model for measured displacement as a function of pressure.*

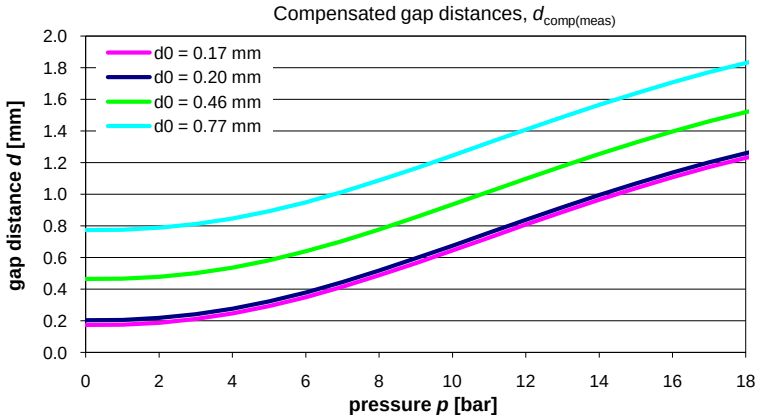

Figure 62. *Compensated inter-electrode distance as a function of pressure based on measurements.*

Contrary to the initial simulated linear relationship, the onset of deformation was observed to be gradual up until approximately 6 bar after which the gradient of displacement remains quite constant. The absence of fixed linearity throughout the entire measurement range (1 – 18 bar) can be explained by the differing materials providing mechanical support in the structure. For example, it is very likely that small voids are present between the supporting I-frames and the plates. As pressure is increased, the plate will deform and fill these cavities after which a firm contact between the plate and I-frame is achieved. Subsequently, after all boundaries have been compressed and individual deformations of material interfaces have saturated, a constant displacement can be observed with increasing pressure. As already previously mentioned, the simulated linear relationship between displacement and pressure is derived using homogeneous materials and ideal coupling conditions and can therefore differ from empirical scenarios.

Now, the relationship between electric field and breakdown voltage as a function of pressure and inter-electrode distance can be calculated and

compared with theory using compensated values based on measurements (Figure 63). The entire series of data for measured gap compensation distances are given in Appendix 1.

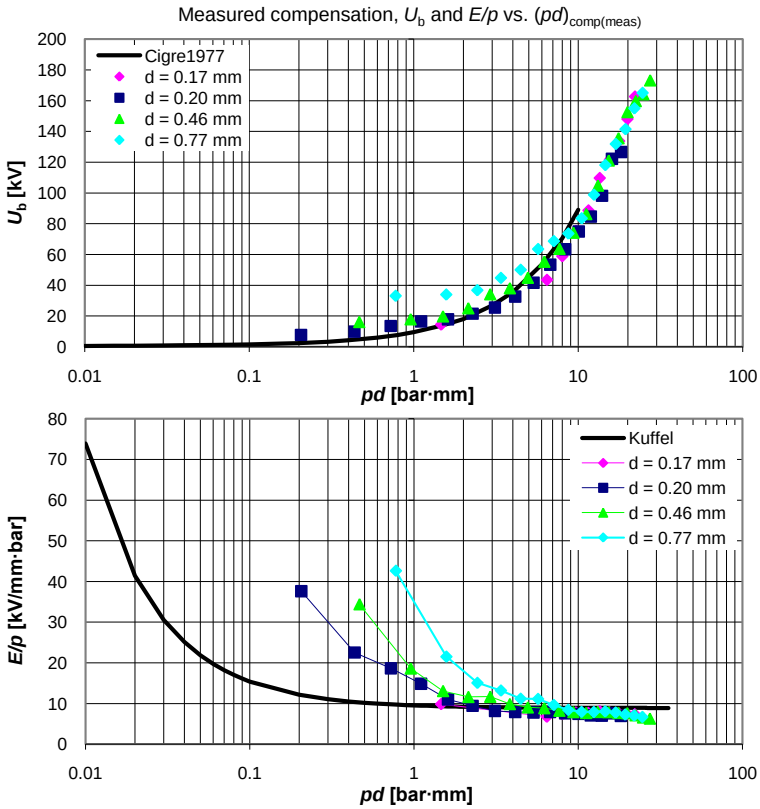

Figure 63. *Breakdown voltage (top) and electric field (bottom) as a function of pressure and compensated gap distance based on measurements.*

As is the case with all measurement setups, non-idealities exist that can influence the integrity of the data. The weak point of this setup is the fact that gap distance cannot be measured directly from the tip of the electrode. Thus, in order to derive the inter-electrode distance, it is assumed that displacement measured from the outside surface of the HV plate and the ground plate is equal to the displacement of the electrode tips. In addition, even though the relation for increasing displacement with increasing pressure has been established, the original gap spacing d_o upon which this compensation is implemented is to be assumed correct (d_o is exactly equal to 0.17, 0.20, 0.46 or 0.77 mm). Nevertheless, compared with the previous gap compensation method (based on theory and simulation), measured displacement provides very similar results. Therefore, the measured results can be considered reasonable and as such, data integrity is conserved. Thus, the compensated gap distances presented in Figure 62 shall be used hereafter when referring to *gap spacing compensation*.

6.2.2 Breakdown Waveform

Measured *dV/dt* waveforms can be categorized by their shape (rising front, tail, pulse width, etc.). The following section displays typical measured pulse shapes recorded by the different oscilloscopes. All three oscilloscopes measure the same breakdown pulse simultaneously for a given pressure and gap distance[8].

Type I

Type I pulses are characterized by a distinct peak value and narrow symmetrical pulse shape as shown in Figure 64.

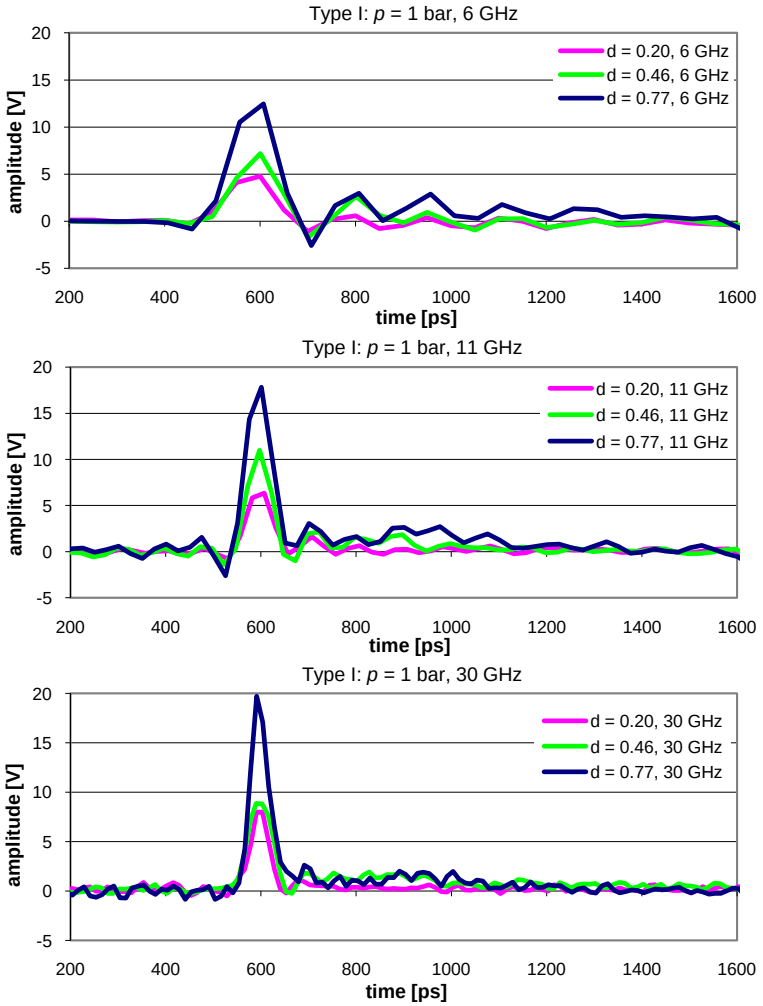

Figure 64. *Typical Type I dV/dt waveforms recorded with 6, 11, and 30 GHz oscilloscopes.*

[8] Recalling Section 5.3.3, the sensors are uncalibrated resulting in an arbitrary vertical scale. However, the relative amplitudes of the pulses are consistent in reference to each other (i.e. all oscilloscopes have the same attenuation and can therefore be compared with one another)

Type II

Type II *dV/dt* pulses have two distinct crests separated by a plateau area where peak separation is related to gap distance (larger gap distance equates to a longer plateau region) as shown in Figure 65.

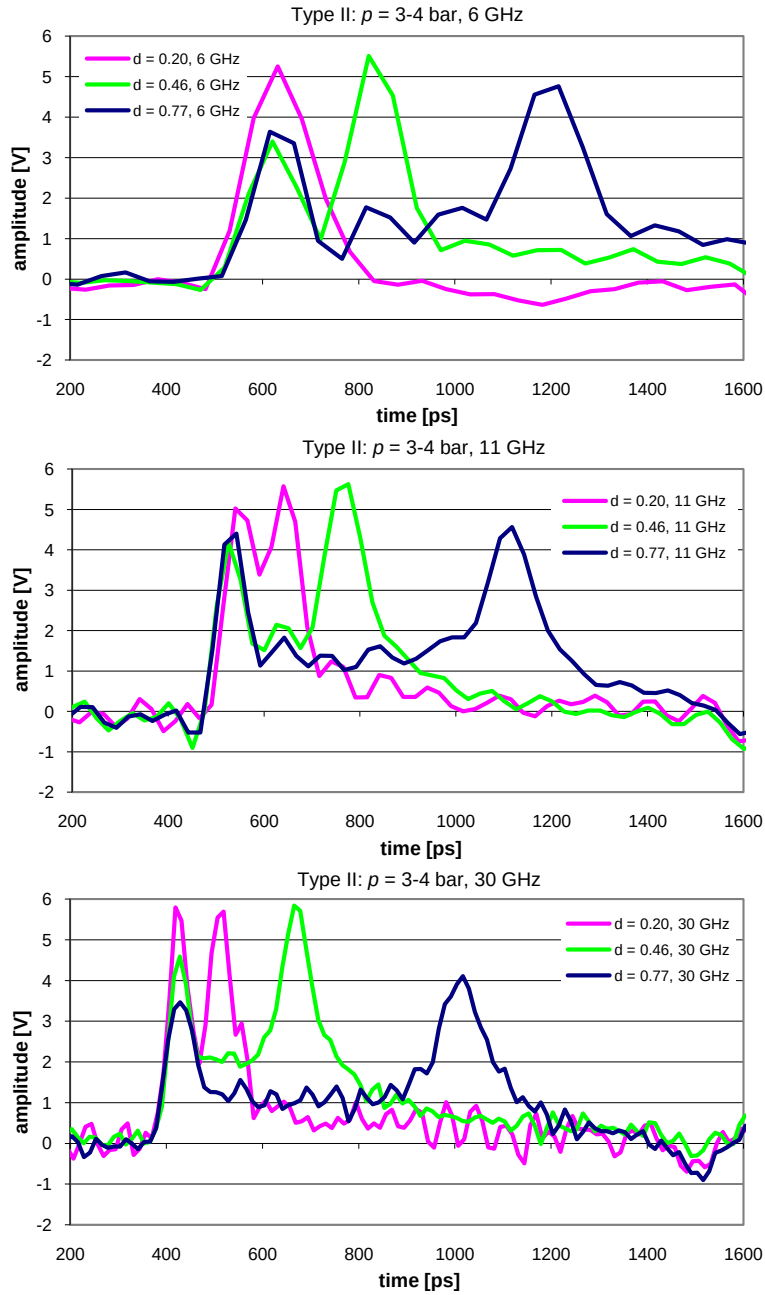

Figure 65. *Typical Type II dV/dt waveforms recorded with 6, 11, and 30 GHz oscilloscopes.*

Type III

Type III *dV/dt* pulses, once again, have a single distinct peak. In contrast to type I waveforms, now the tail of the pulse can be significantly longer than its rising front (Figure 66)

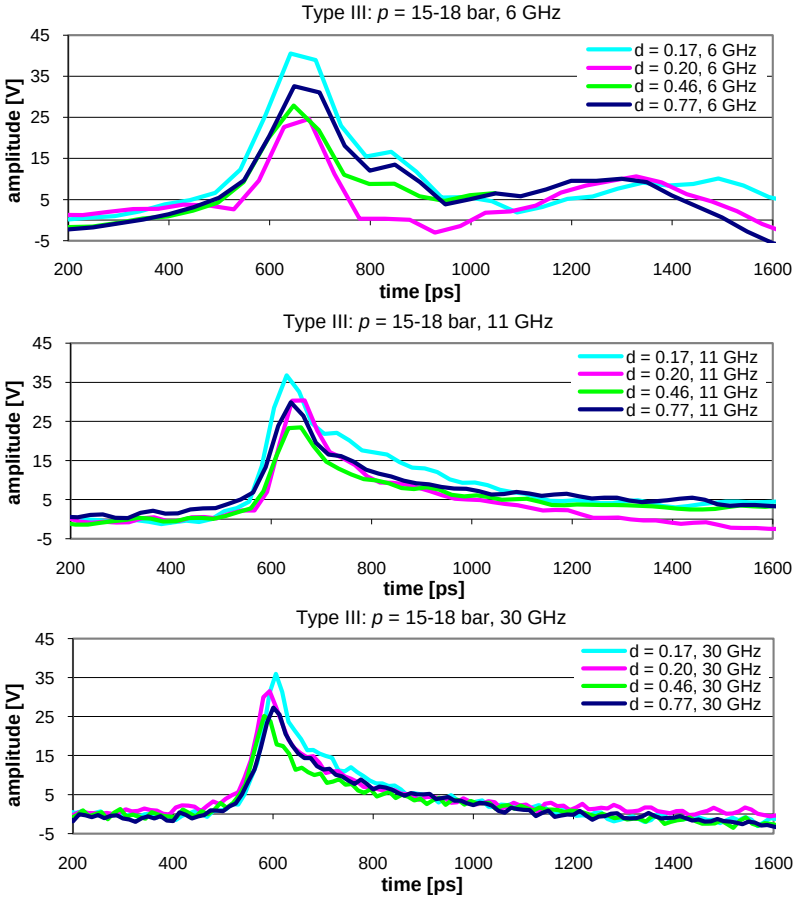

Figure 66. *Typical Type III dV/dt waveforms recorded with 6, 11, and 30 GHz oscilloscopes.*

The coaxial spark gap (Setup 1) produced very similar pulses as those observed with the conical spark gap (Setup 2). However, type II waveforms (Setup 2) are significantly more consistent than those observed in the transition region (Setup 1), thus allowing a more definite classification of the process. As such, both systems have separate classifiers. Nevertheless, the categorizations of the breakdown waveform for both systems are parallel as shown in Table 6.6.

Table 6.6. *Classification of pulse shapes.*

Coaxial Spark Gap SETUP 1		Conical Spark Gap SETUP 2
Region I	⇔	Type I
Transition Region	⇔	Type II
Region II	⇔	Type III

6.2.3 Risetime

Risetime[9] analysis is hindered by varying issues such as interference, limited sampling and pulse interpretation, where the latter was found to have a significant impact on the final risetime value. The following section is divided into several parts where the first presents original raw data, followed by several analysis methods striving to remove factors not related to the physical phenomena of breakdown.

Raw Data

Software developed at the Department of Electrical Engineering at Aalto University was used for calculating the integral of the measured *dV/dt* pulses and its respective parameters (Figure 67). The software plots the recorded data (input files include time and amplitude data) and calculates the peak amplitude ("Up"), front time ("T1"), time to half value ("T2") and pulse width ("P50-N50") of the *dV/dt* pulse. In addition, the software computes the integral of the *dV/dt* pulse and provides its risetime information ("T1" in the integral column) along with its peak value ("MAX") and cut-off point ("LAST"). Additional filtering ("MeanSmooth points") is available but was not applied for any data presented in this text.

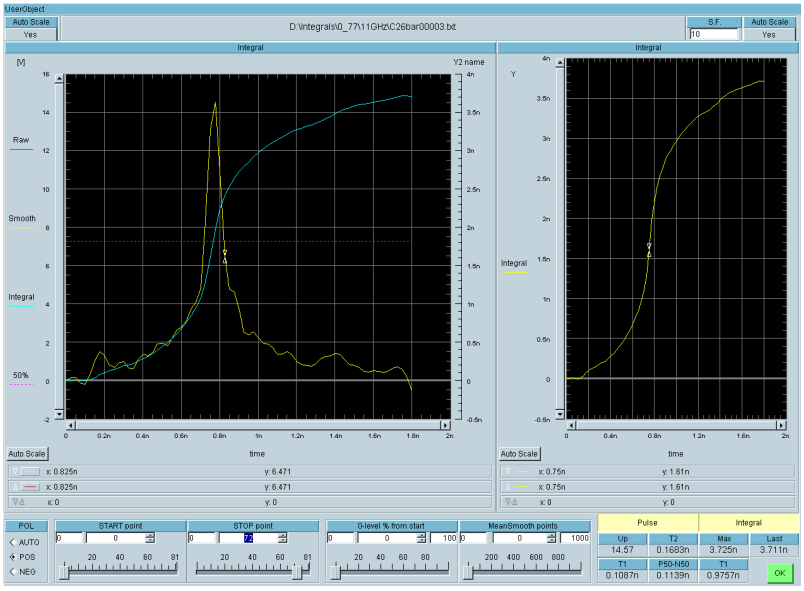

Figure 67. *Software used for calculating pulse parameters.*

Risetime values calculated from measured raw data are shown in Figure 68 and risetime values including gap distance compensation are given in Figure 69. The extent of disassociation between measured samples, electric field strength, pressure and distance is quite notable. However, correlation

[9] Note: Risetime refers to T_1 as defined in Section 6.1.3.

is considerably improved when compensating the gap distance as a function of pressure. In addition, there is prominent disparity between values recorded by the different oscilloscopes (i.e. data recorded by the 30 GHz digitizer gives faster risetimes compared to the 6 GHz oscilloscope).

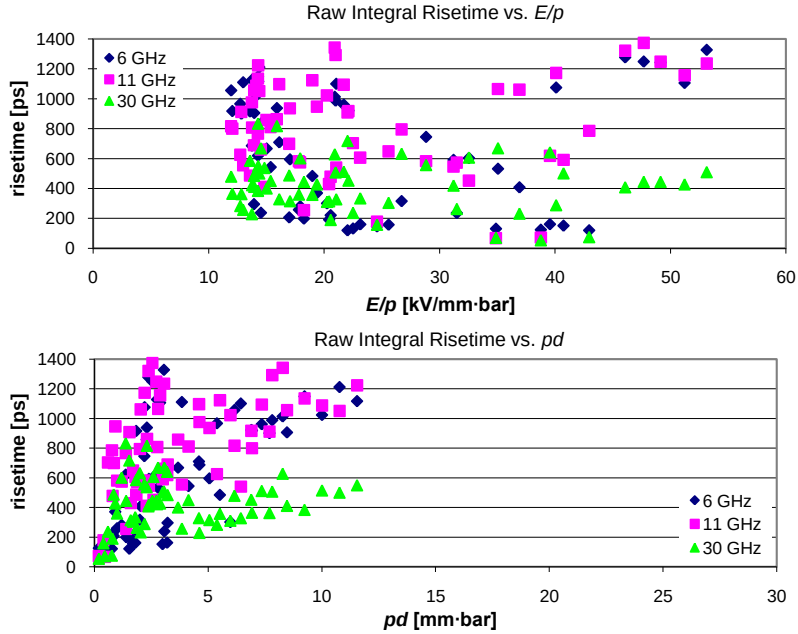

Figure 68. *Measured pulse risetime plotted against electric field strength (top) and the product of pressure and gap distance (bottom).*

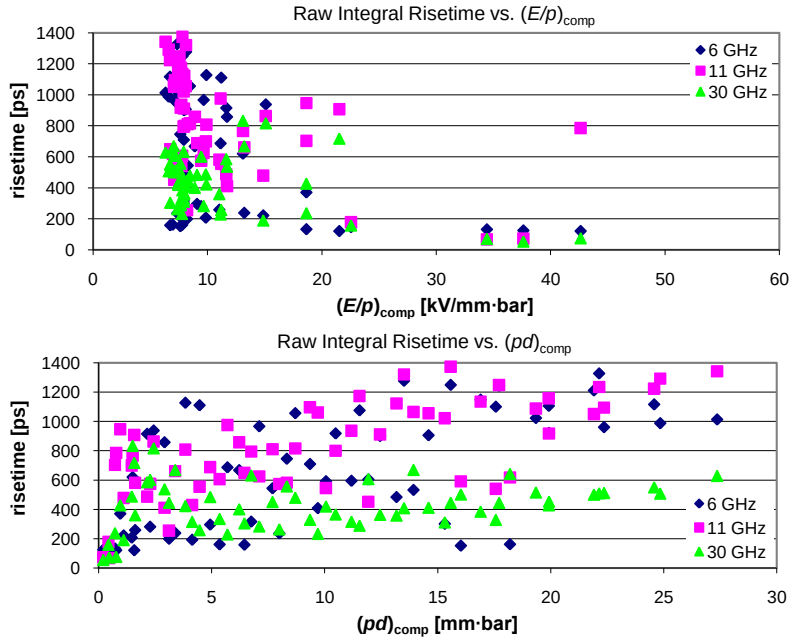

Figure 69. *Measured pulse risetime including gap compensation.*

Cropped Data

As pressure is increased, higher breakdown voltages are recorded. These larger breakdown pulses cause coupling of interference into the oscilloscope inputs, for example via grounding, measurement cables, leakage current between adjacent input channels or via airborne radiation. Thus, the observed waveform can include numerous interference components superimposed onto the actual breakdown signal. An example of such an occurrence is shown in Figure 70, where the 6 GHz oscilloscope experiences significant sinusoidal zero-level fluctuation making it impossible to determine where the signal ends.

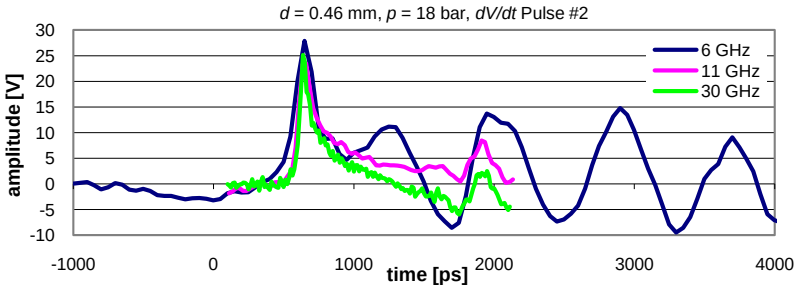

Figure 70. *Example of sinusoidal zero-level fluctuations observed with the 6 GHz oscilloscope (dark blue).*

In order to minimize the effect of such undesired signal components, cropping of the pulse can be used. Cropping deletes the samples which are considered noise and calculates pulse parameters using only valid samples. This is done in practice by setting the onset and offset points manually in the software previously shown in Figure 67 ("START point" and "STOP point"). An example of pulse cropping is presented in Figure 71 where the oscillating post-pulse zero-level oscillation is disregarded.

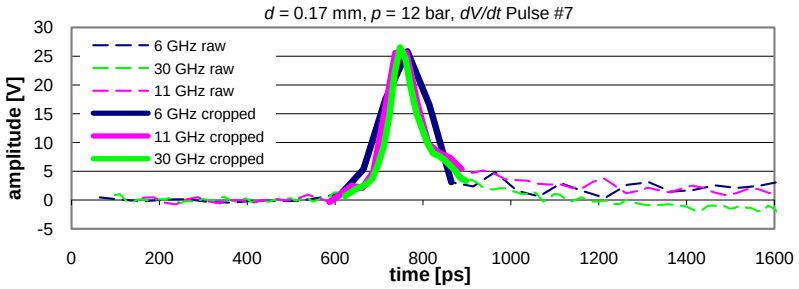

Figure 71. *Example of cropping dV/dt pulse. Dotted samples are disregarded.*

As a result, the peak value of voltage collapse is significantly altered as shown in Figure 72 where the solid line represents the valid samples and the dashed line portrays the disregarded data. Implementation of this cropping method and its influence on derived risetime values is shown in Figure 73 in relation to *E/p* and *pd*. Gap spacing compensation is included in Figure 74.

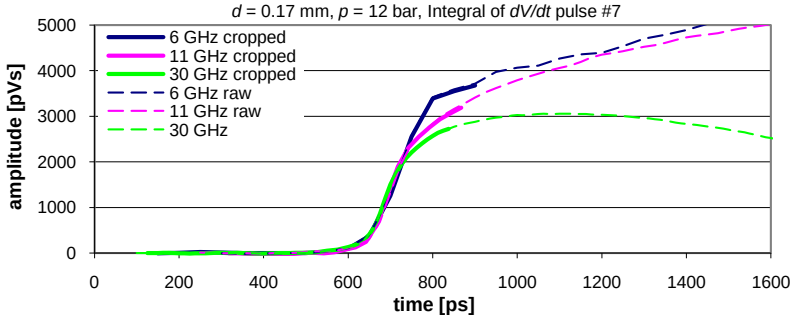

Figure 72. *Corresponding integrals of the cropped dV/dt pulse.*

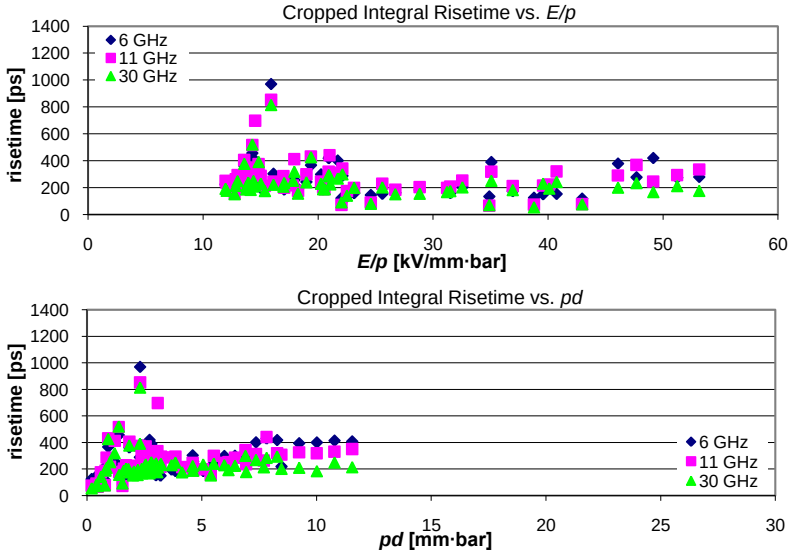

Figure 73. *Risetime of cropped pulses versus field strength (top) and pd (bottom).*

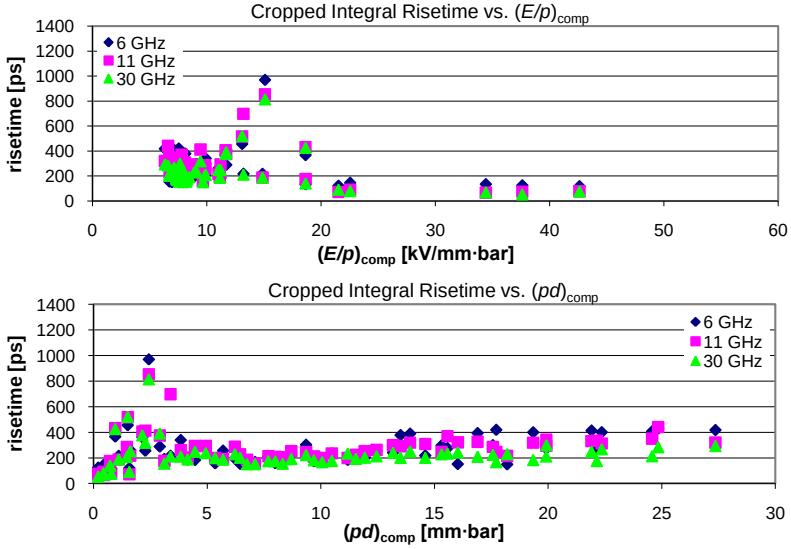

Figure 74. *Risetime of cropped pulses including gap compensation.*

Line Fitting

Since cropping significantly shortens the *dV/dt* pulse and does not allow the pulse to return to zero-level, the integral from which risetime is calculated is misleading. Thus, line fitting is used to extend the pulse. In this approach, the valid samples are used to find a model which best correlates to the measured pulse (Figure 75). A comparison between the fitted model and the measured data along with the corresponding integrals is shown in Figure 76. Integrals of all cropped and line fitted *dV/dt* pulses (when applicable) are shown in Appendix 5.

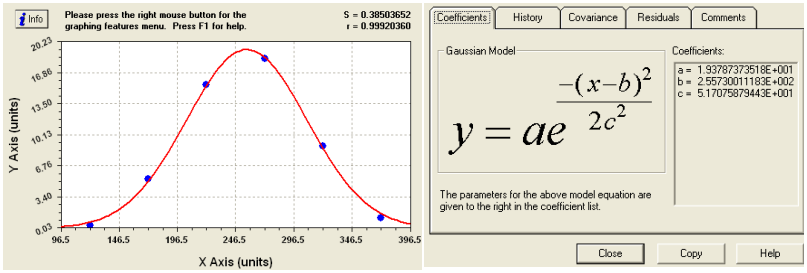

Figure 75. *Example of line fitting using CurveExpert (version 1.4)*

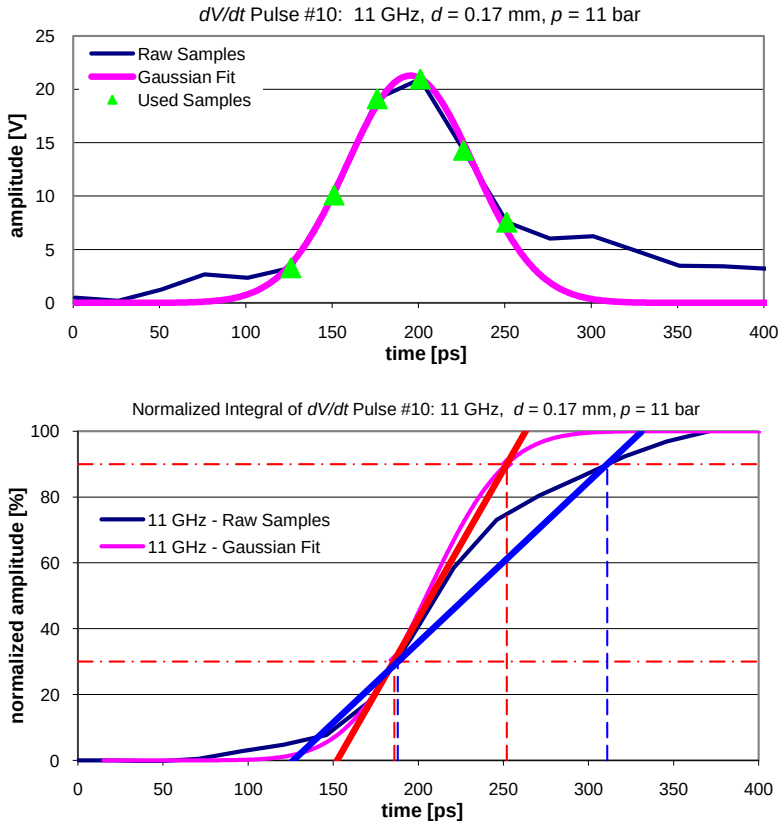

Figure 76. *Sample selection from measured data and application of appropriate model.*

Risetimes of these fitted models are shown in Figure 77 as a function of electric field strength (E/p) and as a function of pressure and gap distance (pd) in Figure 78.

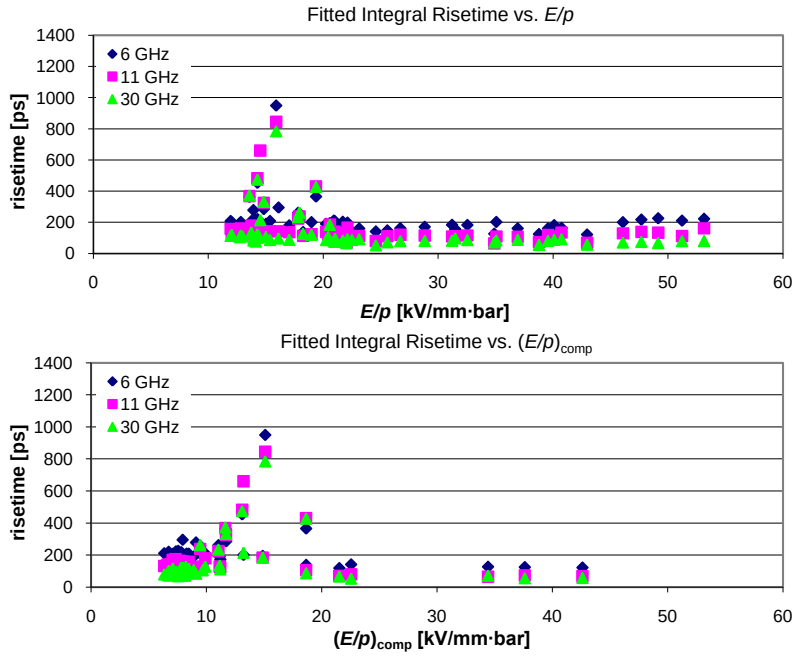

Figure 77. *Risetime of fitted models versus electric field strength. Top – without gap compensation. Bottom – including gap compensation.*

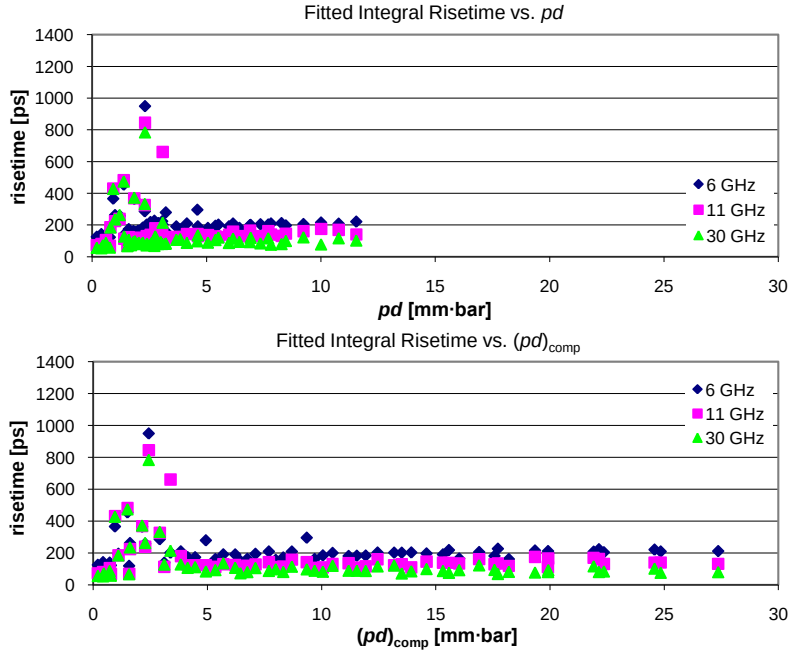

Figure 78. *Risetime of fitted models versus pressure and gap distance. Top – no gap compensation. Bottom – including gap compensation.*

7. Discussion

The variation in observed waveforms measured by the coaxial test gap (Setup 1) suggests an alteration in the breakdown phenomenon within confined pressure ranges corresponding to certain *E/p* values with relatively constant risetime. However, these consistently uniform risetimes are somewhat questionable. It could be possible that the geometry of the spark gap is affecting measured data. By calculating the velocity of a propagating pulse through the different insulating media within the structure, it was estimated that the first reflecting signal due to impedance mismatching at the closest boundary between insulation materials arrives at the *D*-dot sensor approximately 200 ps after the measured pulse (Figure 79). The breakdown signal takes 300 ps to propagate from the spark gap to the *D*-dot sensor which is located 6 cm from the spark gap center. Meanwhile, a reflecting pulse arrives at t = 500 ps. This pulse then continues to reflect and attenuate within the boundaries with a time period of 200 ps. Reflections from more distant boundaries arrive at the sensor at approximately t = 1100 ps and 1430 ps.

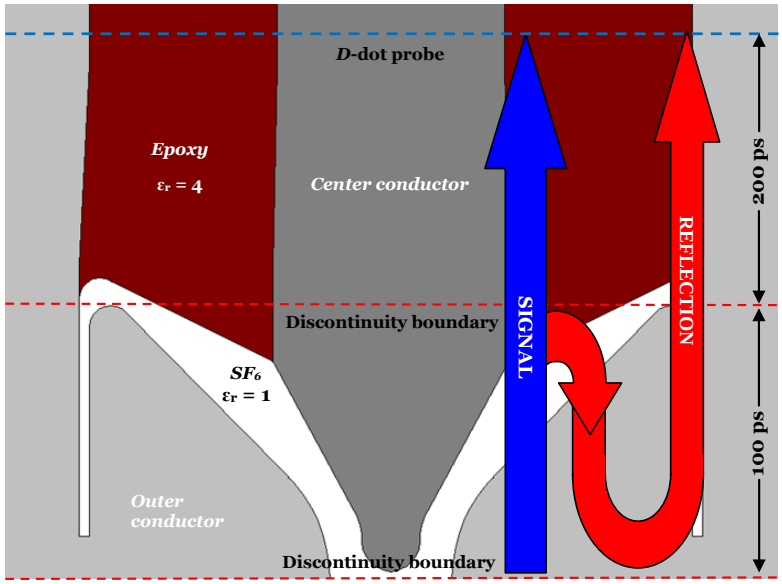

Figure 79. *Impedance mismatch along the transmission line of the first test gap (coaxial setup).*

This would imply that measured data succeeding the onset of voltage collapse by 200 ps will be superimposed with reflections as visualized in Figure 80.

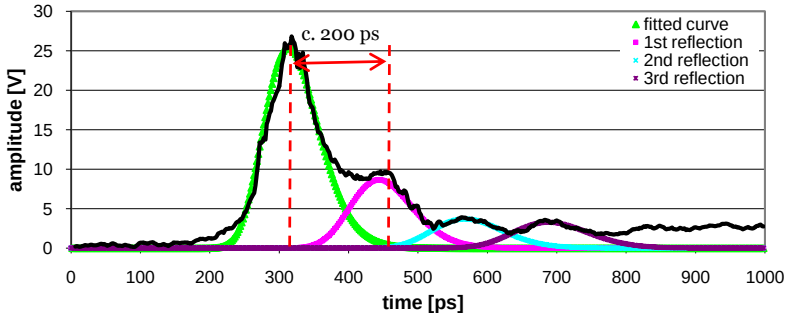

Figure 80. *Superimposed signals within the measured dV/dt signal (0.26 mm, 19 bar).*

In order to verify this claim, the second test gap (conical design, Setup 2) was designed to take into consideration the onset of reflections by having a longer consistent transmission line with fixed impedance. However, as results for the second test gap show relatively similar behavior, the consequence of reflections on measured data once again becomes a concern. The following sections discuss how the possible impact of reflecting waveforms is taken into account.

7.1 Reflections Analysis

By studying the geometry of the test gap a simple lattice diagram is constructed, as shown in Figure 81. This analysis assumes flashover occurs at the center of the electrode. The *D*-dot sensors are located 2 cm from the center point and are identified in the figure as black dashed lines. Reflection boundaries are identified by the green and red dashed lines.

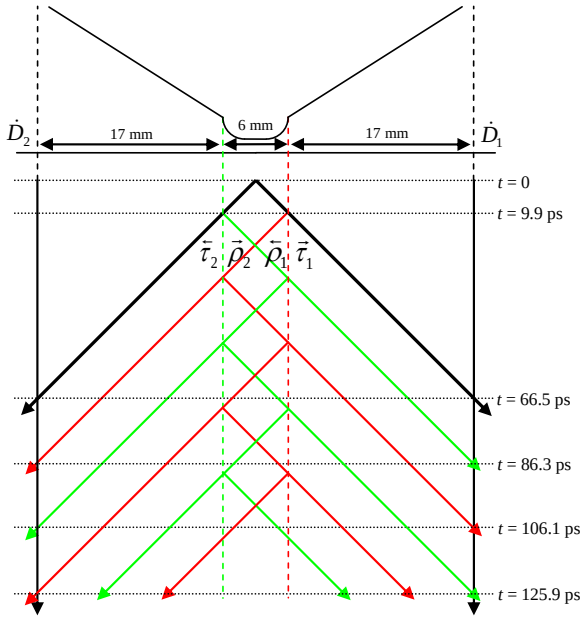

Figure 81. *Lattice diagram of wave propagation from the center of the spark gap.*

Implementing the approximate values determined earlier in Section 5.3.2 (Homogeneous Field vs. Fixed Impedance), impedance divergence along the transmission line can be portrayed as in Figure 82 where B_1 and B_2 are the discontinuity boundaries (as identified in the previous figure). Point A refers to the center of the spark gap (electrode tip)

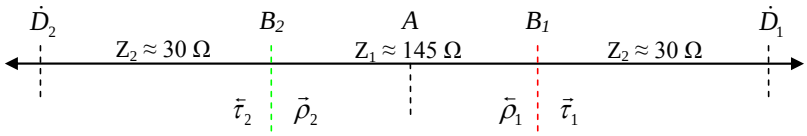

Figure 82. *Impedance mismatching along the transmission line.*

Reflected waveform u_r and transmitted waveform u_t are given as,

$$u_r = \frac{Z_2 - Z_1}{Z_2 + Z_1} u = \rho \cdot u \qquad u_t = \frac{2Z_2}{Z_2 + Z_1} u = \tau \cdot u,$$

where transmission coefficients τ and reflection coefficients ρ are approximated as,

$$\tau_1 = \tau_2 = \frac{2Z_2}{Z_2 + Z_1} = \frac{2(30)}{30+145} = 0.34 \qquad \rho_1 = \rho_2 = \frac{Z_2 - Z_1}{Z_2 + Z_1} = \frac{30-145}{30+145} = -0.65$$

The amplitude of each reflection corresponding to their respective reflection time is given in Table 7.1. Following the onset of flashover at t_o = 0, the first reflection arrives at the sensor after a delay of 66.5 ps (assuming signal propagation velocity as the speed of light, $c = 3 \cdot 10^8$ m/s) with an amplitude of 34% relative to the normalized flashover signal.

Table 7.1. *Reflection amplitudes as a function of time*

time [ps]		*D*-dot sensor output	
t_o	0	0	0
t_1	66.5	τ_1	0.340
t_2	86.3	$\rho_2\tau_1$	- 0.221
t_3	106.1	$\rho_1\rho_2\tau_1$	0.144
t_4	125.9	$\rho_1(\rho_2)^2\tau_1$	- 0.093
t_5	147.5	$(\rho_1)^2(\rho_2)^2\tau_1$	0.061
t_6	167.3	$(\rho_1)^2(\rho_2)^3\tau_1$	- 0.039
t_7	187.1	$(\rho_1)^3(\rho_2)^3\tau_1$	0.026
t_8	206.9	$(\rho_1)^3(\rho_2)^4\tau_1$	- 0.017

As the signal propagates along the transmission line, it reflects at a period of 19.8 ps while attenuating at each boundary. This analysis only considers the first 8 reflections, as the signal at t_8 has already diminished to only 1.7% of the original pulse and, as such, subsequent transmission coefficients can be considered negligible. Each of the reflected pulses are then summed together to represent the pulse observed by the *D*-dot sensor. For simplicity, a symmetrical triangular *dV/dt* pulse is considered. Figure 83 displays a 120 ps triangular breakdown pulse ("Input") and the resulting waveform observed by the *D*-dot sensor ("*D*-dot") which is formed by combining the individual reflections shown in the figure as dashed lines.

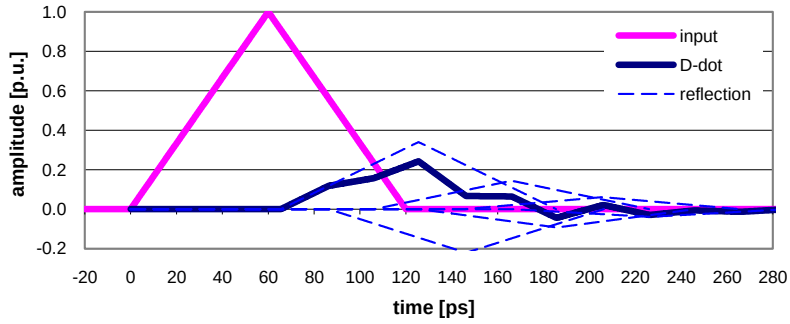

Figure 83. *Input signal (pink) and corresponding sensor output (blue).*

Implementing this same process, Figure 84 displays waveforms observed by the *D*-dot for varying triangular input pulse durations ranging from 40 ps to 300 ps.

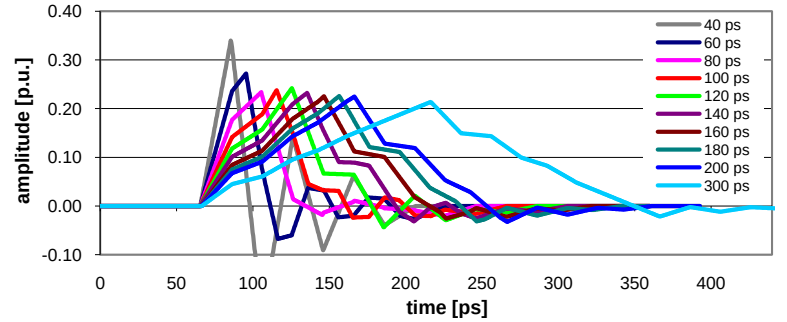

Figure 84. *Waveforms observed by the D-dot sensor for varying input durations. Note: only one input (40 ps) visualized in this figure.*

A comparison between measured pulses and calculated waveforms based on the aforesaid method of superimposed reflections is show in Figure 85. Type I and Type III waveform characteristics are noticeable in the modeled pulse. However, the time scale is inconsistent with measured data.

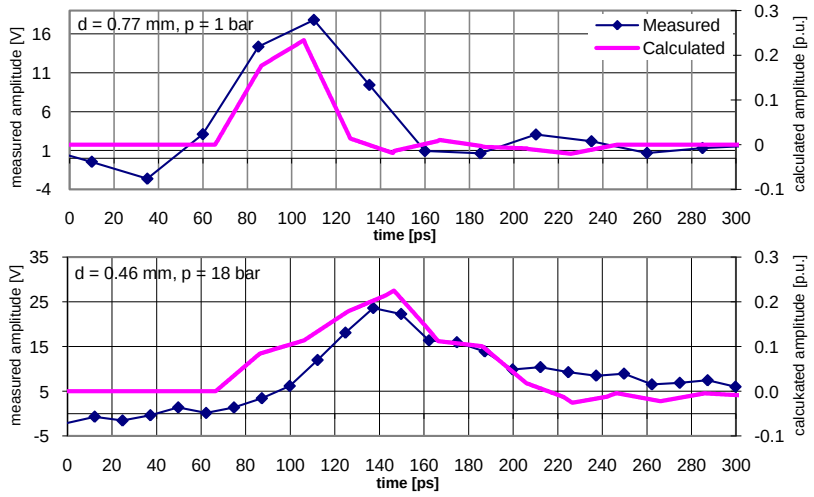

Figure 85. *Calculated waveform (pink) compared to measured waveform (blue).*

To attain more accurate models, an iterative process was implemented in which the measured waveform is compared with a modeled waveform (Model Output) which takes into account the previously introduced transmission and reflection coefficients and propagation time parameters (τ, ρ, *t*) as shown in Figure 86. The model input waveform is modified until the output waveform (*D*-dot sensor reading) coincides with the measured signal. As a result, a modeled waveform describing breakdown at the center spark gap prior to the onset of superimposing signals is achieved (Modeled Breakdown Waveform = Model Input when Measured Waveform = Model Output).

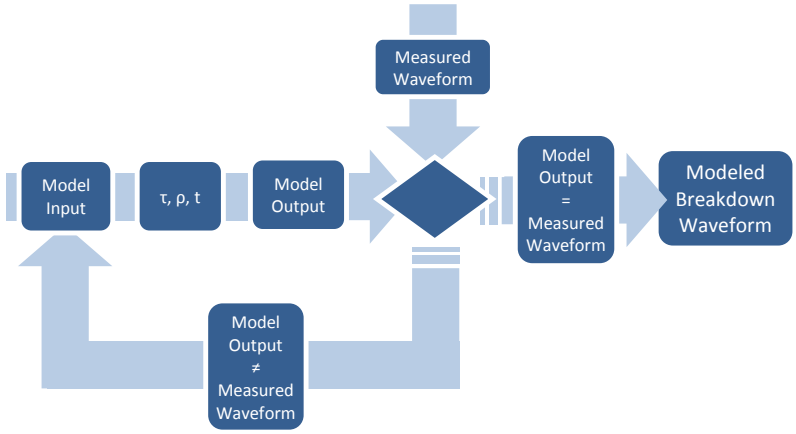

Figure 86. *Iterative modeling process.*

Non-idealities during the construction of the electrode such as surface roughness and inconsistencies along the curvature of the electrode tip can all affect impedance matching along the transmission line. In efforts to make the analysis more accurate, the geometry of the electrode was studied in greater detail. Steps taken in this non-ideality analysis (Four-Boundary Analysis) are shown in Appendix 2. Consequently, it became apparent that symmetrical triangular input pulses do not reproduce the measured waveform. The rising front is a fairly good representation of measured signals. However, the falling tail does not have the appropriate time scale. Therefore, further analysis is required in order to determine the pulse shape of flashover in the gap which coincides with measured data from the sensors.

7.1.1 Type I and III

When normalizing the typical measured type I and type III waveforms (acquired by the 30 GHz oscilloscope) it becomes evident that the rising front is approximately constant while the falling tail elongates as pressure is increased (Figure 87).

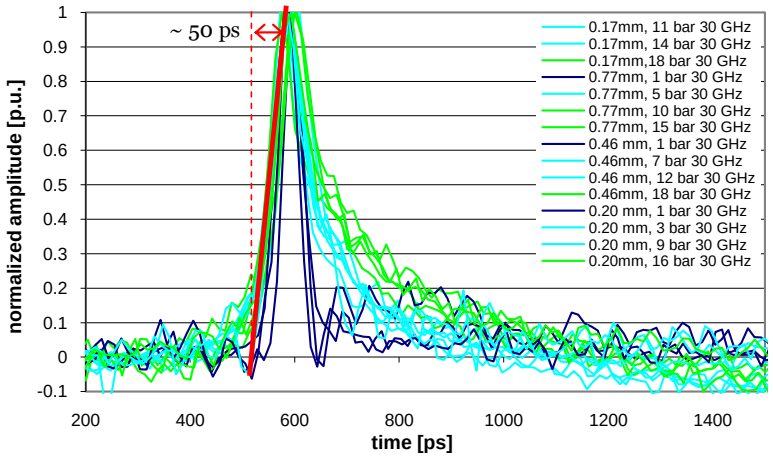

Figure 87. *Typical type I and type III normalized dV/dt waveforms.*

Using the previously mentioned Four-Boundary Analysis (detailed in Appendix 2) and iterative input parameter fine-tuning, equivalent waveforms were modeled, of which two examples are shown in Figure 88.

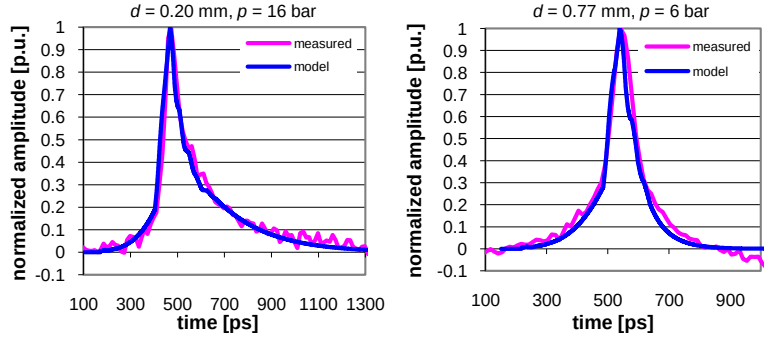

Figure 88. *Modeling equivalent waveforms.*

The corresponding calculated waveforms (model output) for the selected measured pulses shown in Figure 87 are displayed below, in Figure 89.

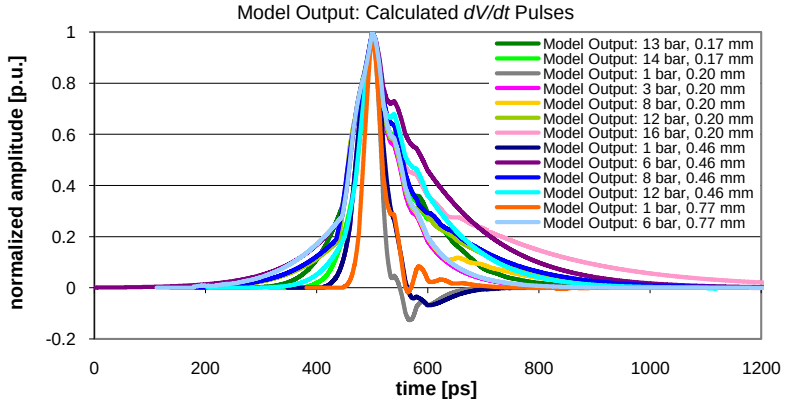

Figure 89. *Equivalent waveforms observed by the D-dot sensors (model output).*

Taking into account the properties of the test gap (geometry, pulse propagation velocity and impedance variation along the transmission line), for the sensors to record such equivalent waveforms (model output) shown in the previous figure, flashover pulses occurring at the center of the spark gap (model input) will have the shape as depicted in Figure 90.

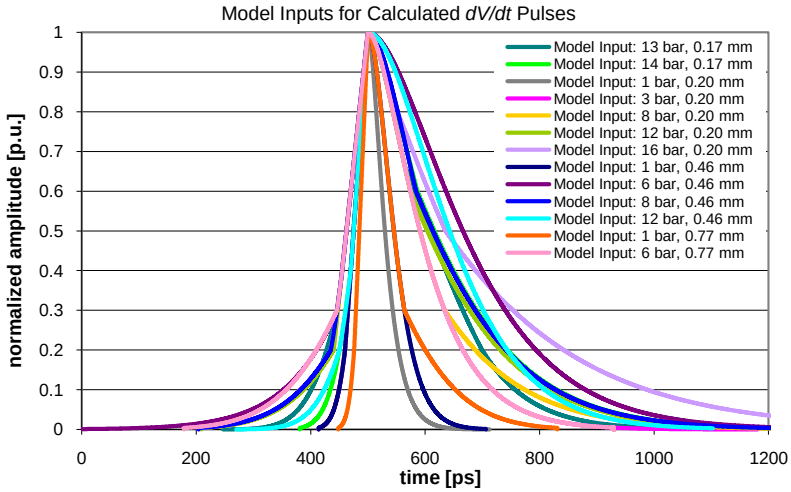

Figure 90. *Equivalent modeled waveforms for center flashover in spark gap (model input).*

Now, risetime can be calculated from the integral of the modeled *dV/dt* flashover pulses (model input). Voltage collapse waveforms are shown in Figure 91 and respective parameters in Table 7.2.

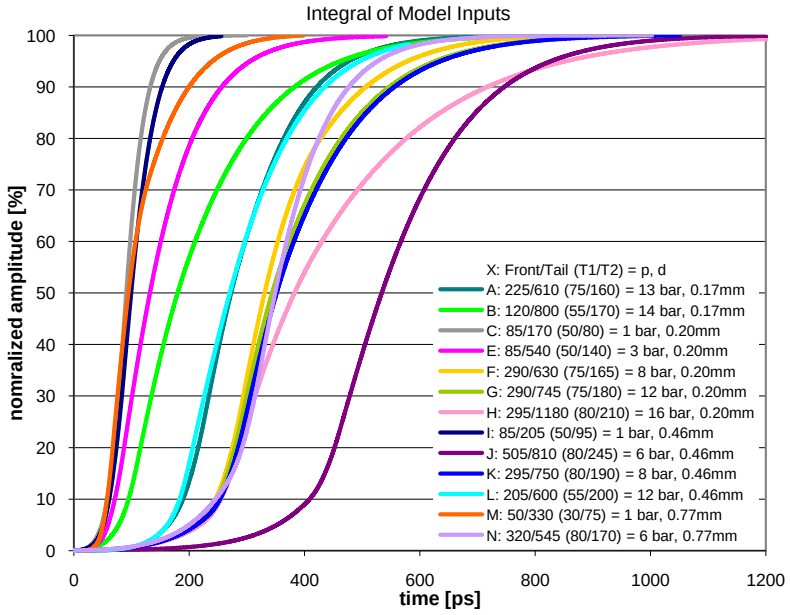

Figure 91. *Voltage collapse calculated from integral of model input.*

Table 7.2. *Parameters of voltage collapse.*

	p	d_o	d_{comp}	pd_o	pd_{comp}	U_b	E/p	$(E/p)_{comp}$	dV/dt input		Integral of dV/dt	
	[bar]	[mm]		[bar·mm]		[kV]	[kV/bar·mm]		Front/Tail [ps]	T1/T2 [ps]	Model T1 [ps]	Meas. T1 [ps]
A	13	0.17	0.89	2.21	11.57	88.61	40.10	7.66	225/610	75/160	312.3	288.5
B	14	0.17	0.96	2.38	13.44	109.7	46.08	8.16	120/800	55/170	414.2	408.1
C	1	0.20	0.21	0.20	0.21	7.75	38.75	36.90	85/170	50/80	91.65	54.04
D	3	0.20	0.24	0.60	0.72	13.50	22.50	18.75	85/540	50/140	259.5	237.1
E	8	0.20	0.52	1.60	4.16	32.69	20.43	7.86	290/630	75/165	354.7	314.4
F	12	0.20	0.84	2.40	10.08	74.90	31.21	7.43	290/745	75/180	413.1	419.5
G	16	0.20	1.14	3.20	18.24	126.6	39.56	6.94	295/1180	80/210	671.9	641.2
H	1	0.46	0.47	0.46	0.47	16.05	34.89	34.15	85/205	50/95	116.8	70.95
I	6	0.46	0.64	2.76	3.84	37.99	13.76	9.89	505/810	80/245	447.3	422.3
J	8	0.46	0.78	3.68	6.24	55.26	15.02	8.86	295/750	80/245	416.5	400.5
K	12	0.46	1.10	5.52	13.20	104.8	18.98	7.94	205/600	55/200	348.0	357.8
L	1	0.77	0.78	0.77	0.78	33.08	42.96	42.41	50/330	30/75	207.1	75.15
M	6	0.77	0.95	4.62	5.70	63.49	13.74	11.14	320/545	80/170	271.7	228.7

For comparison, risetime dependency of selected measured data and modeled waveforms on electric field strength, pressure and gap distance is shown in Figure 92.

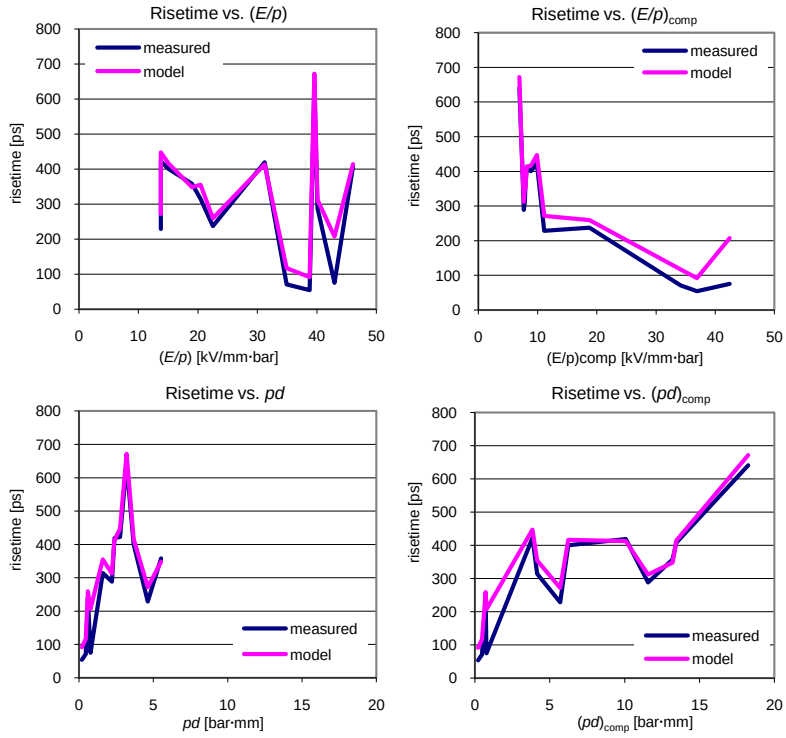

Figure 92. *Risetime of type I and III waveforms in relation to field strength (top) and as a function of pressure and distance (bottom). The impact of gap compensation is also shown.*

Recall, the analysis thus far is consistent when flashover is assumed to occur at the center of the spark gap (directly at the tip of the electrode).

Side Flashover

It was observed that the same waveform was recorded differently by the various oscilloscopes. Obviously, the bandwidth and sampling rate of the oscilloscope influence the waveform. However, another reason was also discovered when examining the electrode surface following numerous measurement trials. Instead of forming a discharge channel directly in the center of the electrode, some flashover occurred at the curvatures of the plane profile electrode tip as shown in Figure 93. When adjusting the gap distance between measurement series, the threads of the electrode structure deteriorate (due to its large mass) and as a result, the electrode tilts slightly. Thus, one side of the electrode tip may be closer to the ground plate than its opposite side.

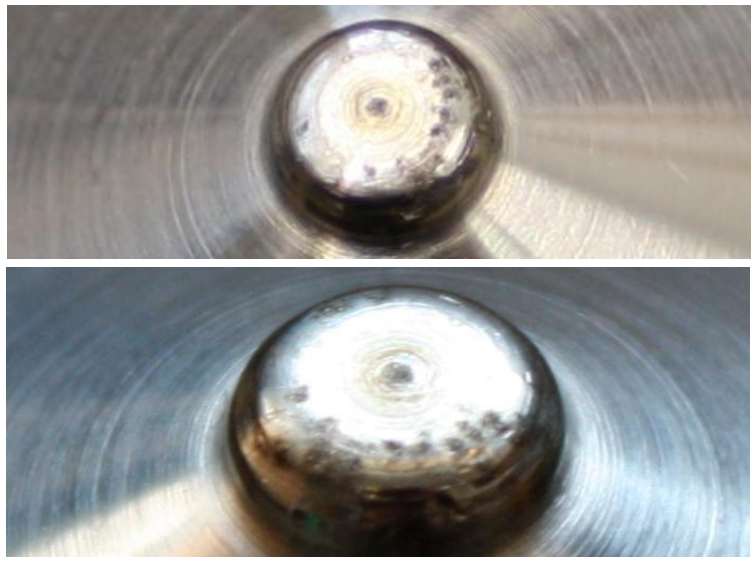

Figure 93. *Photograph of electrode tip after measurements.*

To account for this "side flashover", the Four-Boundary Analysis lattice diagram is modified to calculate the effect of reflections occurring from such discharge. This analysis considers how the sensor closest to the flashover point ($\dot{D}_1$) will record a different waveform than that observed by the farthest sensor ($\dot{D}_2$). The side flashover lattice diagram and respective reflection coefficients are presented in Appendix 3.

From Figure 94, it is evident that the farthest sensor from the flashover point will observe a smaller (-10 %) peak amplitude compared to the closer sensor while also displaying a dissimilar pulse shape. For example, as input signal duration is increased, the peak of the farthest sensor signal ("D_2") begins to plateau and overall pulse width increases compared to the closer sensor signal ("D_1"). For better comparison, the model input signal and both sensor signals ("D1", "D2") are shown in the same figure in Figure 95.

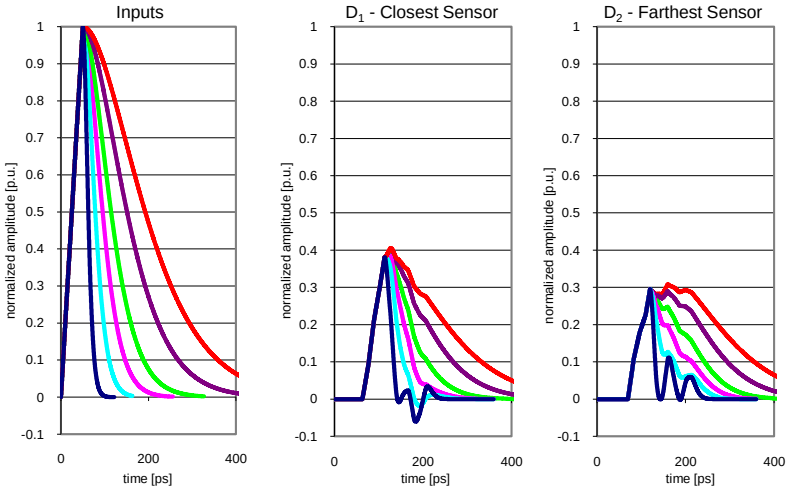

Figure 94. *Probe reading disparity for side flashover.*

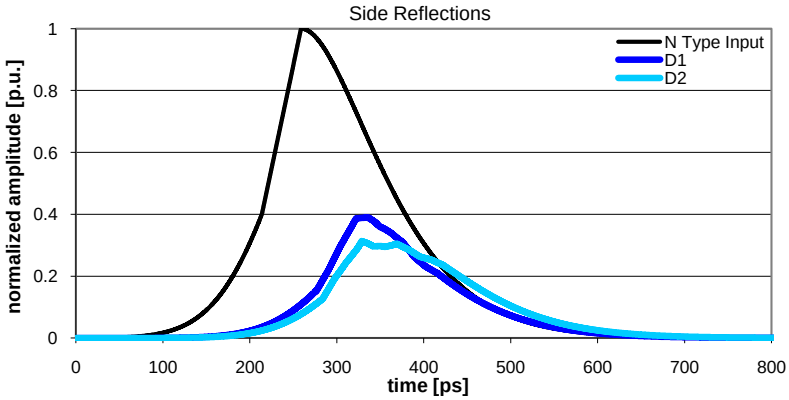

Figure 95. *Input and sensor waveforms for side flashover.*

A comparison between modeled side flashover waveforms and measured data is shown in Figure 96. Modeled deviations between sensors (calculated side reflections) agree quite well with measured sensor variation (measured side reflections).

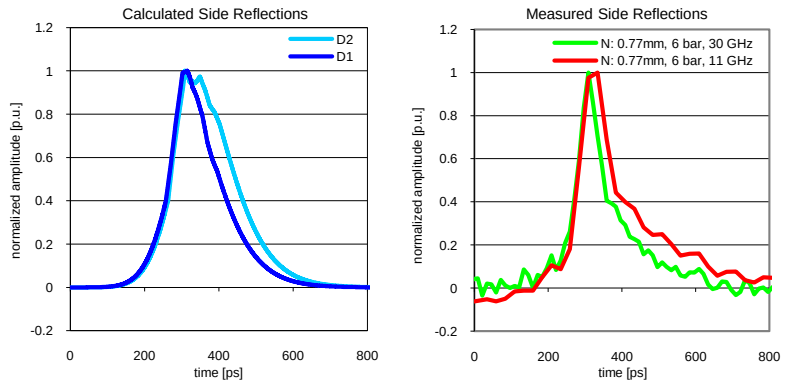

Figure 96. *Measured and calculated waveforms portraying side flashover.*

Thus, waveforms can differ significantly depending on where flashover is assumed to take place. Appendix 4 considers the impact of varying side reflection coordinates on the waveform observed by respective sensors.

7.1.2 Type II

Type II waveforms are observed between the low pressure region (1 – 3 bar) and high pressure region ($p \geq 6$ bar). Prior to the typical onset of type II pulses, a smaller second crest is observed following the first major *dV/dt* peak. In contrast, as pressure is further increased past the typical double peak type II waveform, the smaller crest is now observed before the major peak. Thus, type II pulses can be further subcategorized into "pre" and "post" type II waveforms. This development is shown in Figure 97[10].

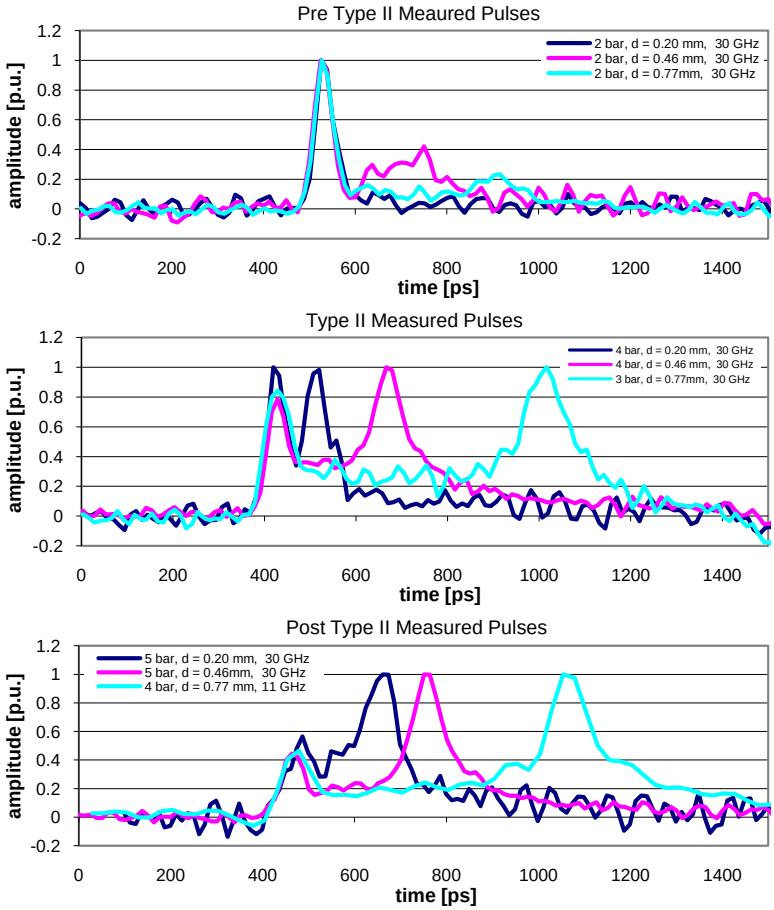

Figure 97. *Top – pre type II measured dV/dt waveforms. Middle – typical double peak type II waveforms. Bottom – post type II waveforms (30 GHz oscilloscope).*

[10] Note: Bottom of Figure 97 shows an 11 GHz pulse (p = 4 bar, d = 0.77mm). The trigger level of the 30 GHz oscilloscope was set excessively high and was unable to record a complete pulse (the initial smaller peak was omitted). Thus, the 30 GHz pulse is replaced in this figure by its corresponding 11 GHz waveform.

Type II waveforms are undeniably a physical phenomenon and not simply a result of superimposed reflections because the waveform has a noticeable dependency on gap distance. A larger gap distance results in a longer time interval between the two distinct peaks of the waveform. Reflections do play some role in modifying the signal as was discussed in the side flashover analysis in the previous section. However, the most noticeable double peaks resulting from such modeled side reflections (Figure 98) are not significant enough to be comparable with actual measured type II pulses.

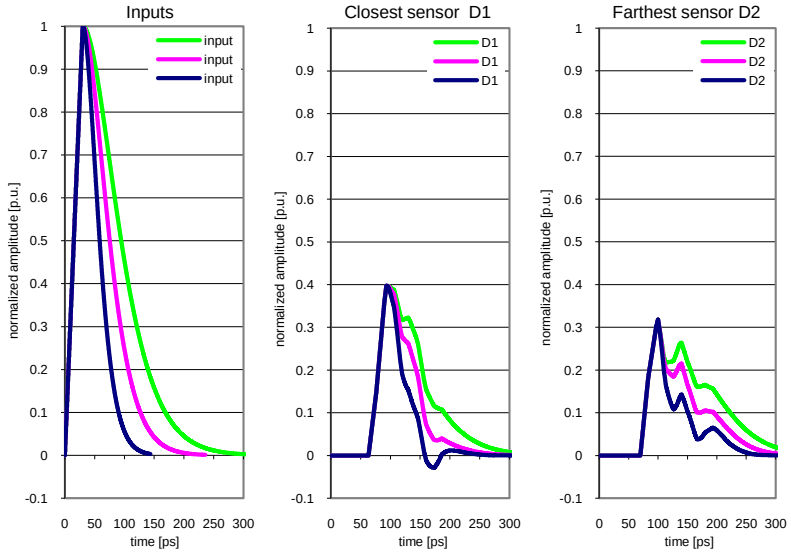

Figure 98. *Modeled double peaks caused by side flashover.*

Thus, using the same analysis method as for earlier four-boundary center flashover, the input model signal is iteratively modified until a comparable sensor reading is obtained. The following figures show the measured waveforms, equivalent calculated waveforms (model output) and their respective model inputs for pre type II (Figure 99), type II (Figure 100), and post type II (Figure 101) pulses.

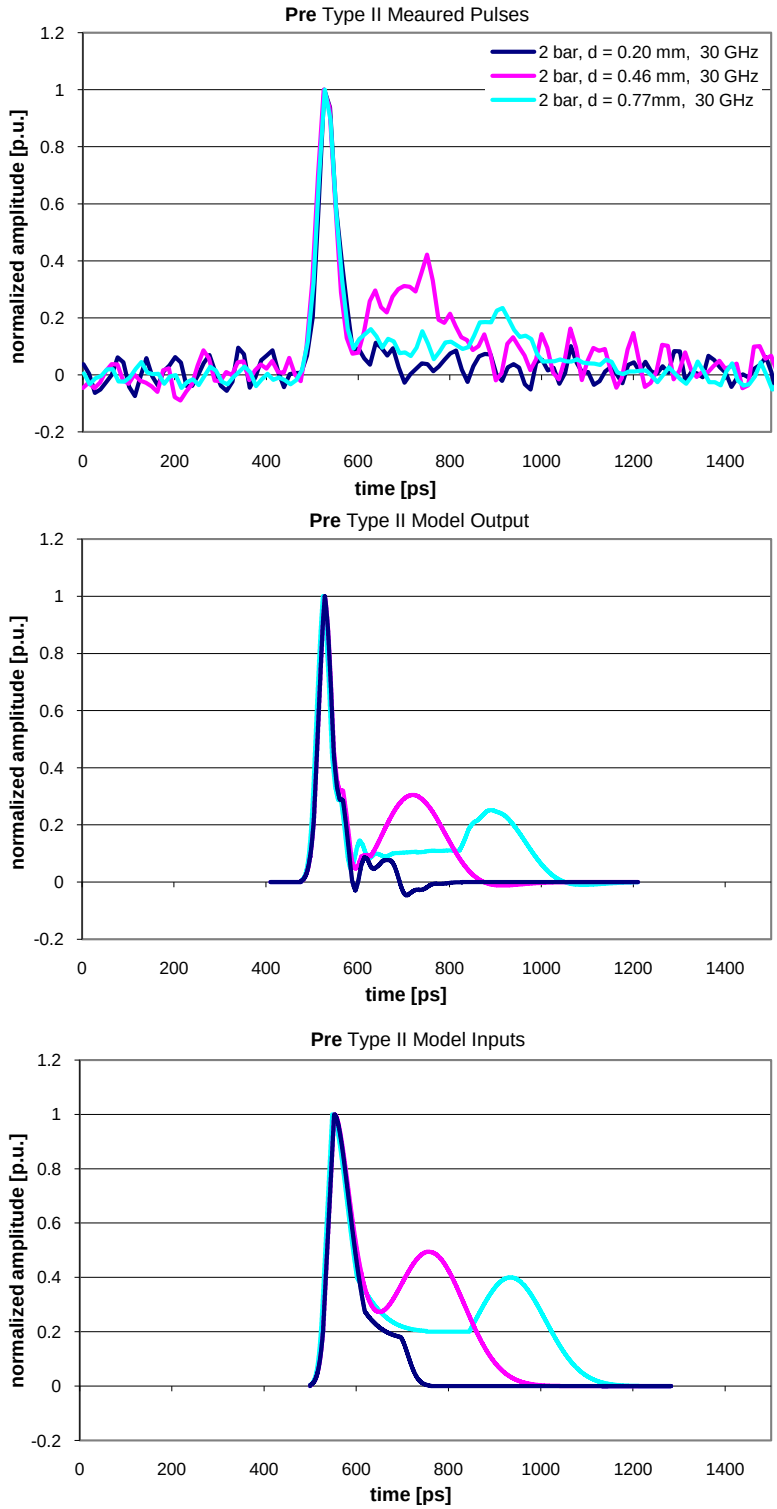

Figure 99. *Pre type II. Top – measured dV/dt data. Middle – model output data. Bottom – corresponding model input data.*

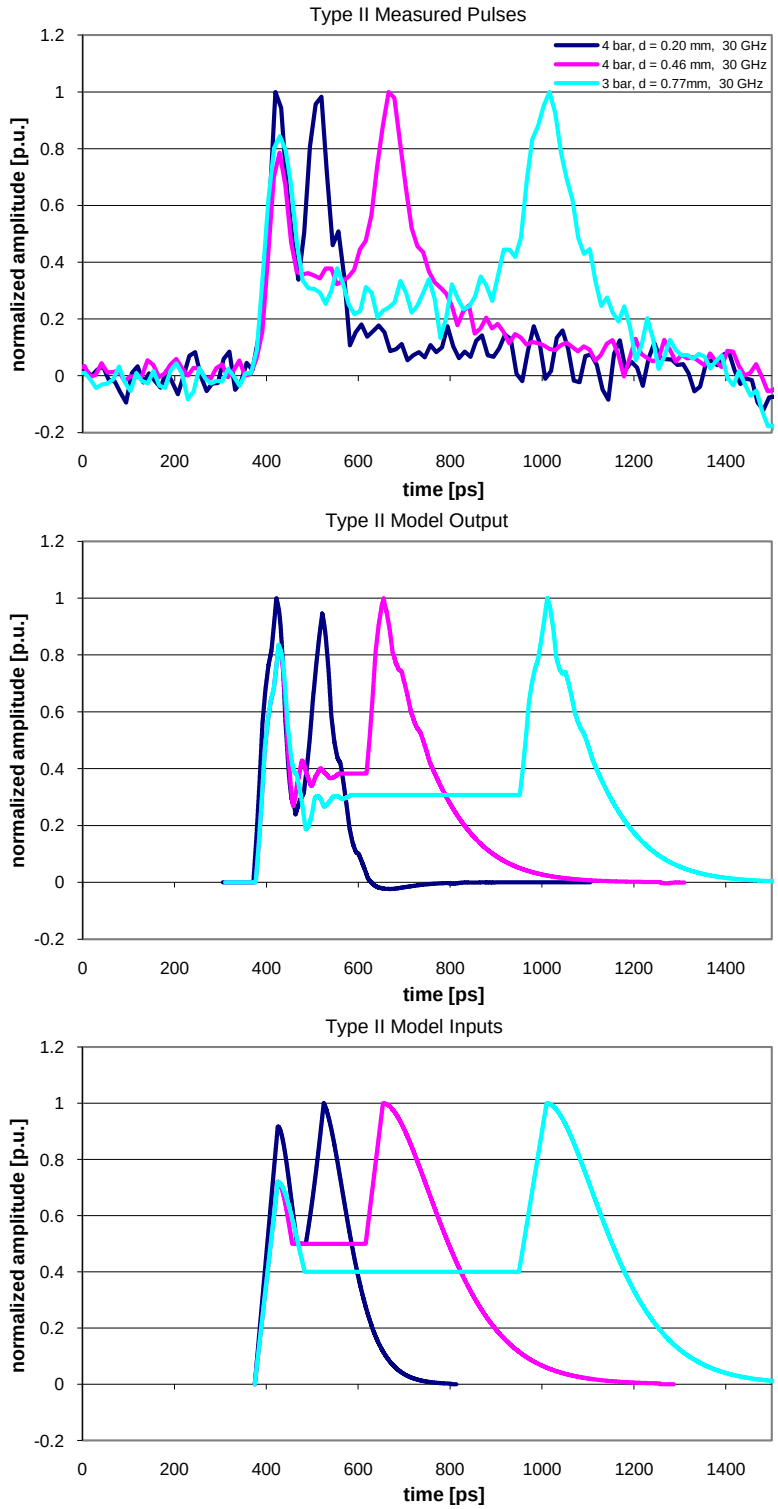

Figure 100. *Type II. Top – measured dV/dt data. Middle – model output data. Bottom – corresponding model input data.*

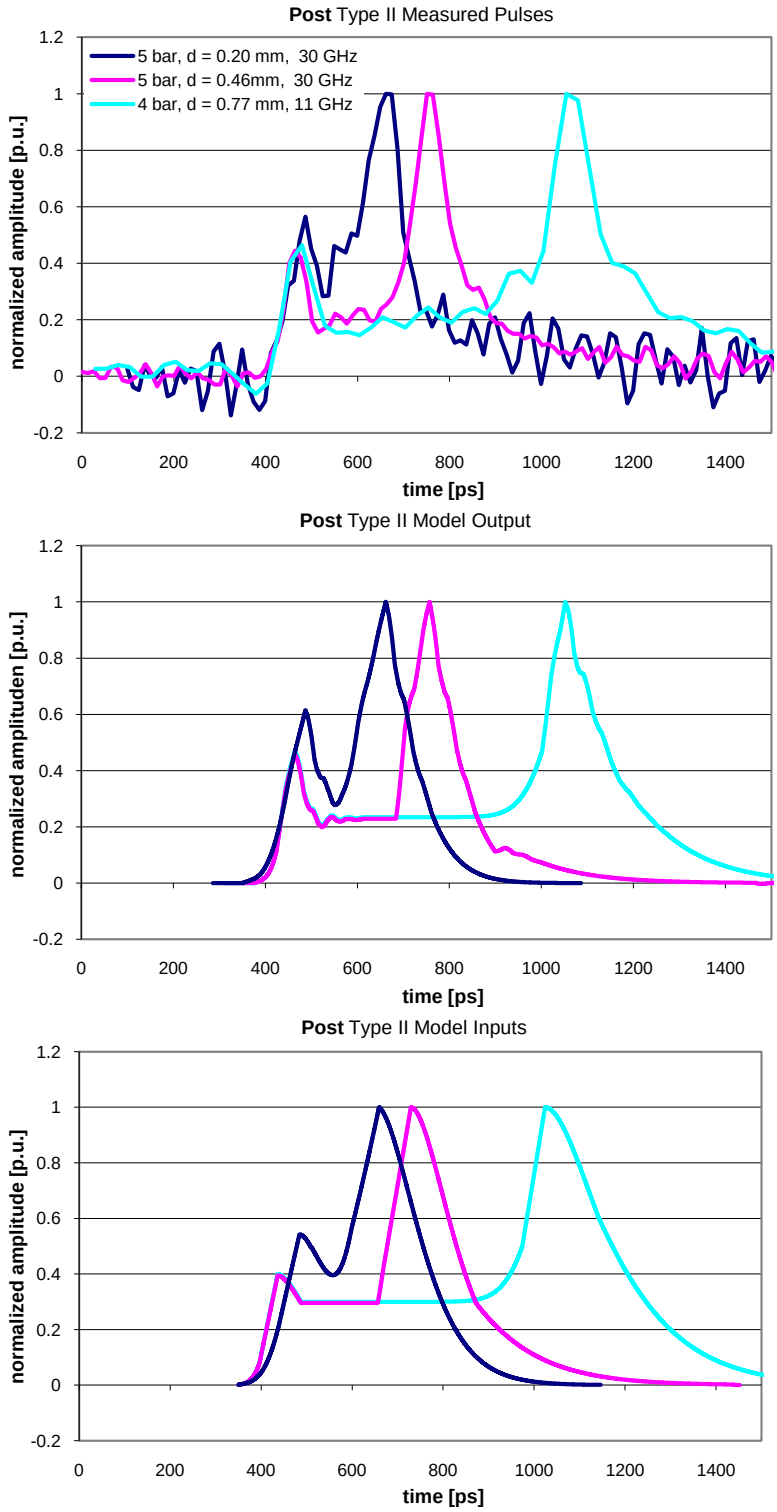

Figure 101. *Post type II. Top – measured dV/dt data. Middle – model output data. Bottom – respective model input data.*

Properties of the typical type II waveforms shown in the previous figures are given in Table 7.3 and respective modeled voltage collapse is shown in Figure 102.

Table 7.3. Type II waveform parameters.

Type II	*p* [bar]	*d* [mm]	Pulse Duration [ps]	Model Input Risetime T1 [ps]	Measured Risetime T1 [ps]
PRE	2	0.20	262	191.0	158.0
PRE	2	0.46	529	402.5	427.4
PRE	2	0.77	706	652.8	717.6
MID	4	0.20	438	241.1	190.0
MID	4	0.46	911	467.4	585.4
MID	3	0.77	1209	803.3	816.8
POST	5	0.20	818	330.9	359.6
POST	5	0.46	1099	437.5	537.2
POST	4	0.77	1460	742.3	668.3

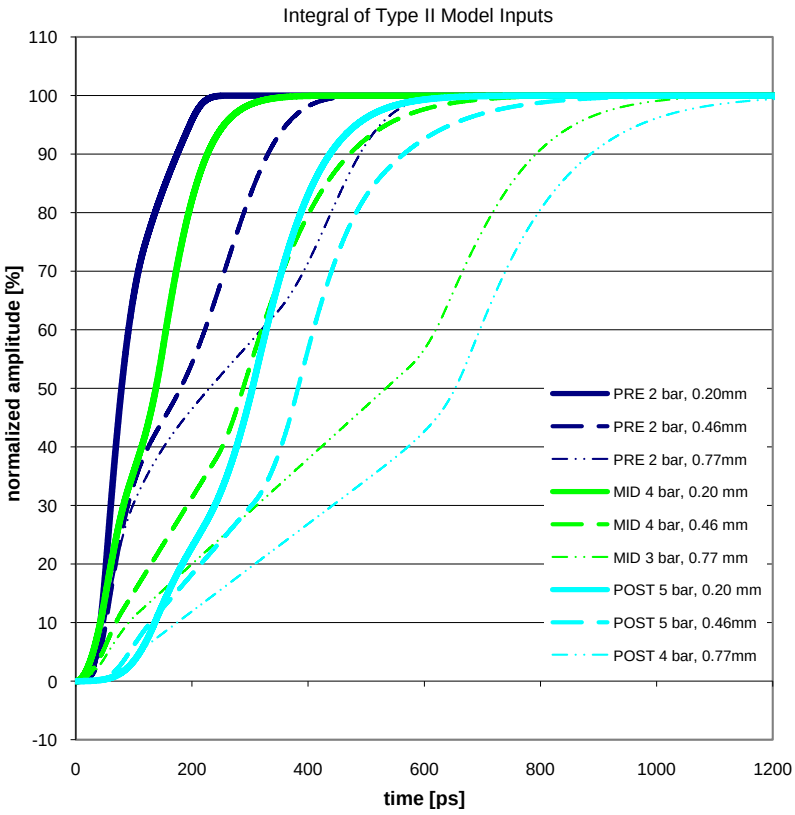

Figure 102. *Voltage collapse of type II model input waveforms.*

A comparison between measured and modeled type II data is shown in Figure 103, where risetime is given as a function of pressure and gap distance and as a function of electric field strength in Figure 104. Gap compensation is also included.

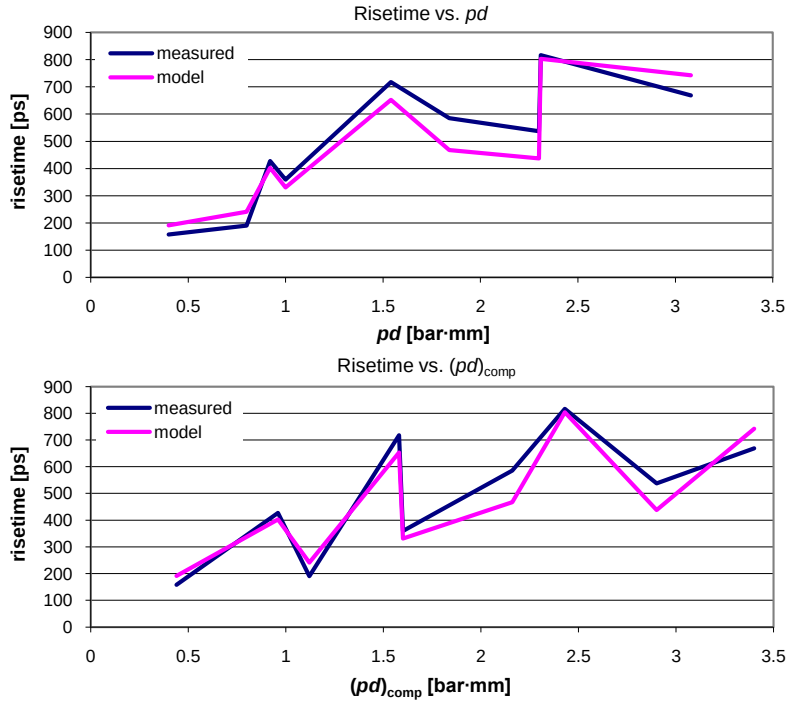

Figure 103. *Risetime dependency of Type II waveforms on pressure and gap distance. Top – without gap compensation. Bottom – including gap compensation.*

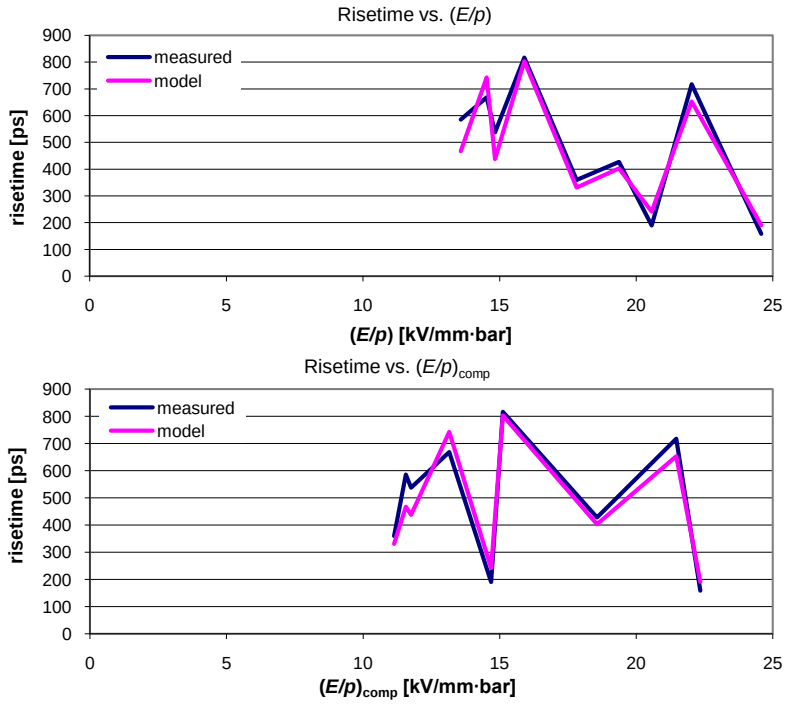

Figure 104. *Risetime dependency of Type II waveforms on field strength. Top – without gap compensation. Bottom – including gap compensation.*

7.1.3 Overview of All Types

Table 7.4 presents risetime values from both measured data and modeled voltage collapse pulses. Most of the calculated waveforms agree relatively well with measured values (deviation is typically under 10 %). However, some measured waveforms have significantly larger risetimes compared to the model input waveform. This is due to the poor signal to noise ratio (SNR) which causes considerable zero level fluctuation post discharge. This additional ripple, which is not accounted for in the reflection analysis, causes the integral of the measured pulses to extend past its peak value, which in turn, results in a larger risetime.

Table 7.4. *Risetime comparison between modeled and measured voltage collapse.*

p **[bar]**	***d*** **[mm]**	**Integral T1**				**Comment**
		Modeled	**Measured**	**Δ [ps]**	**Δ [%]**	
13	0.17	260.4	288.5	28.1	9.7	
14	0.17	375.8	408.1	32.3	7.9	
1	0.2	55.87	54.04	-1.83	-3.4	
2	0.2	149.5	158.0	8.50	5.4	
3	0.2	190.5	237.1	46.6	19.7	*poor SNR*
4	0.2	213.2	190.0	-23.2	-12.2	*poor SNR*
5	0.2	300.7	359.6	58.9	16.4	*very poor SNR*
8	0.2	322.6	314.4	-8.20	-2.6	
12	0.2	370.1	419.5	49.4	11.8	
16	0.2	649.2	641.2	-8.00	-1.2	
1	0.46	75.16	70.95	-4.21	-5.9	
2	0.46	390.0	427.4	37.4	8.8	
4	0.46	445.0	585.4	140.4	24.0	*FGB reflection*
5	0.46	398.2	537.2	139.0	25.9	*FGB reflection*
6	0.46	409.2	422.3	13.1	3.1	
8	0.46	374.5	400.5	26.0	6.5	
12	0.46	304.0	357.8	53.8	15.0	
1	0.77	67.06	75.15	8.09	10.8	
2	0.77	658.6	717.6	59.0	8.2	
3	0.77	784.8	816.8	32.0	3.9	
4	0.77	723.5	668.3	-55.2	-8.3	*11 GHz pulse*
6	0.77	206.9	228.7	21.8	9.5	

In addition, a major reflection is recorded at approximately 1.2 ns following the onset of discharge. This is the reflecting signal propagating back from the fiberglass cylinder enclosing the gas chamber (Fiberglass Boundary FGB in Table 7.4). For some measured type III waveforms with long gradual falling tails and wide type II pulses, this FGB reflection is superimposed into the tail of the signal, notably increasing risetime compared to the modeled waveforms which do not account for this reflection. Overall, the calculated *dV/dt* (model output) waveforms can be considered a fair representation of the measured data and assuming the approximated reflection coefficients are reasonable, the flashover waveform occurring at center spark gap can thus be obtained from the model input.

Modeled voltage collapse is shown in Figure 105 grouped by type. As an overview, a simplified trend representation of the observed waveform types is shown in Figure 106.

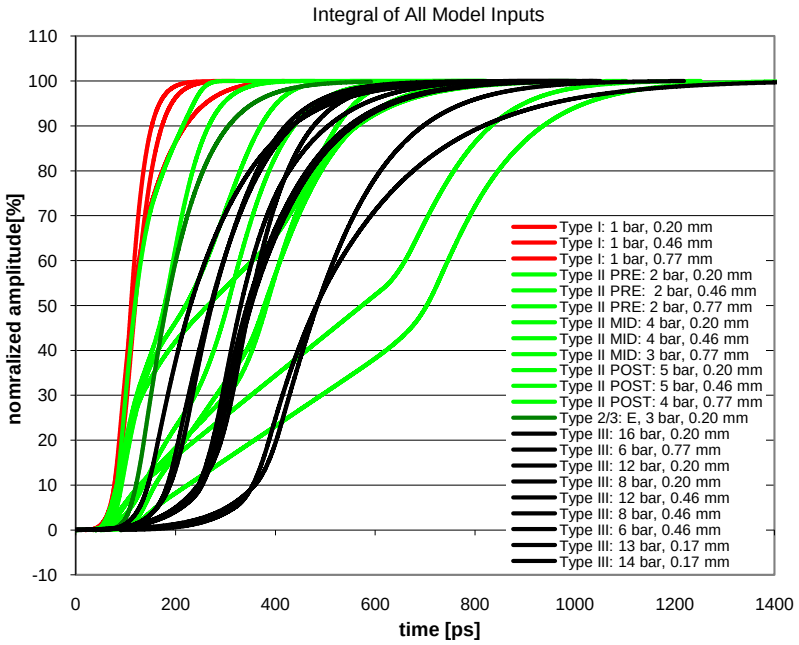

Figure 105. *Voltage collapse for all model waveform types.*

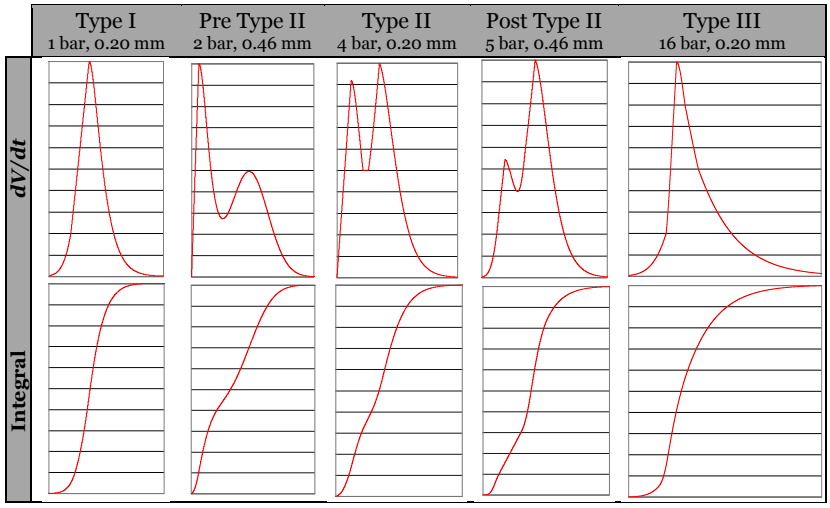

Figure 106. *Simplified trend for modeled waveforms.*

Finally, all the modeled (input) data can be compared with measured waveforms. Risetime dependency throughout each pulse type is plotted against electric field strength and the product of pressure and gap distance in Figure 107 and Figure 108.

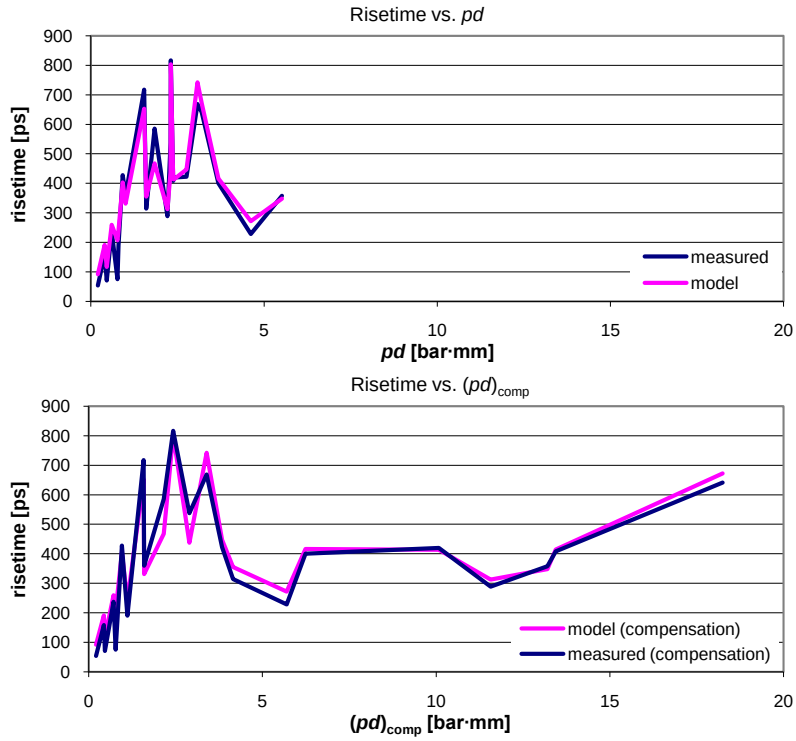

Figure 107. *All modeled results compared against measured risetime as a function of pd.*

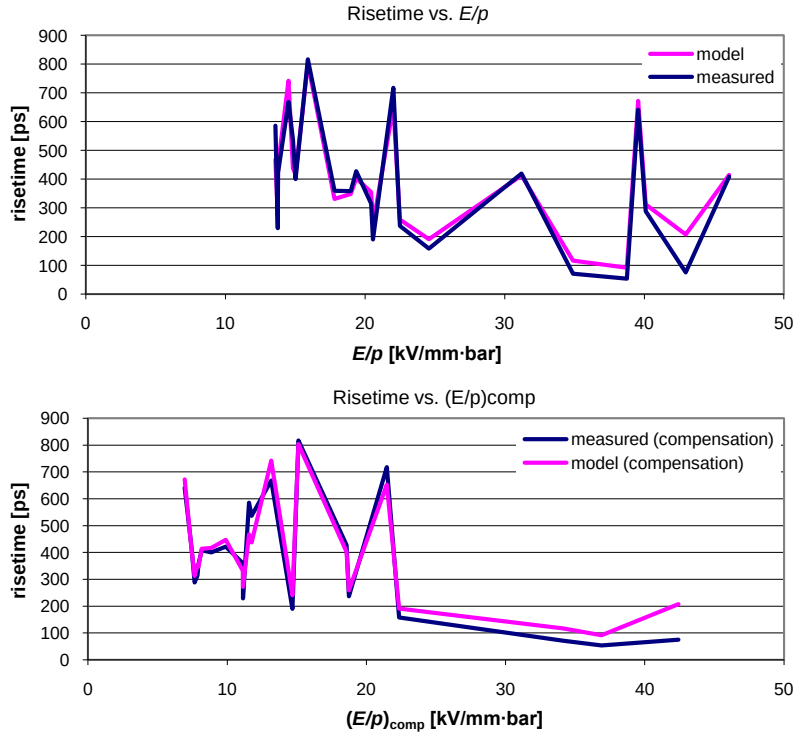

Figure 108. *All modeled results compared against measured risetime as a function of E/p.*

In order to observe how each type of waveform affects risetime dependency, the data is sorted by pulse type and presented in Figure 109 including unaltered measurement data, gap distance compensation and modeled data.

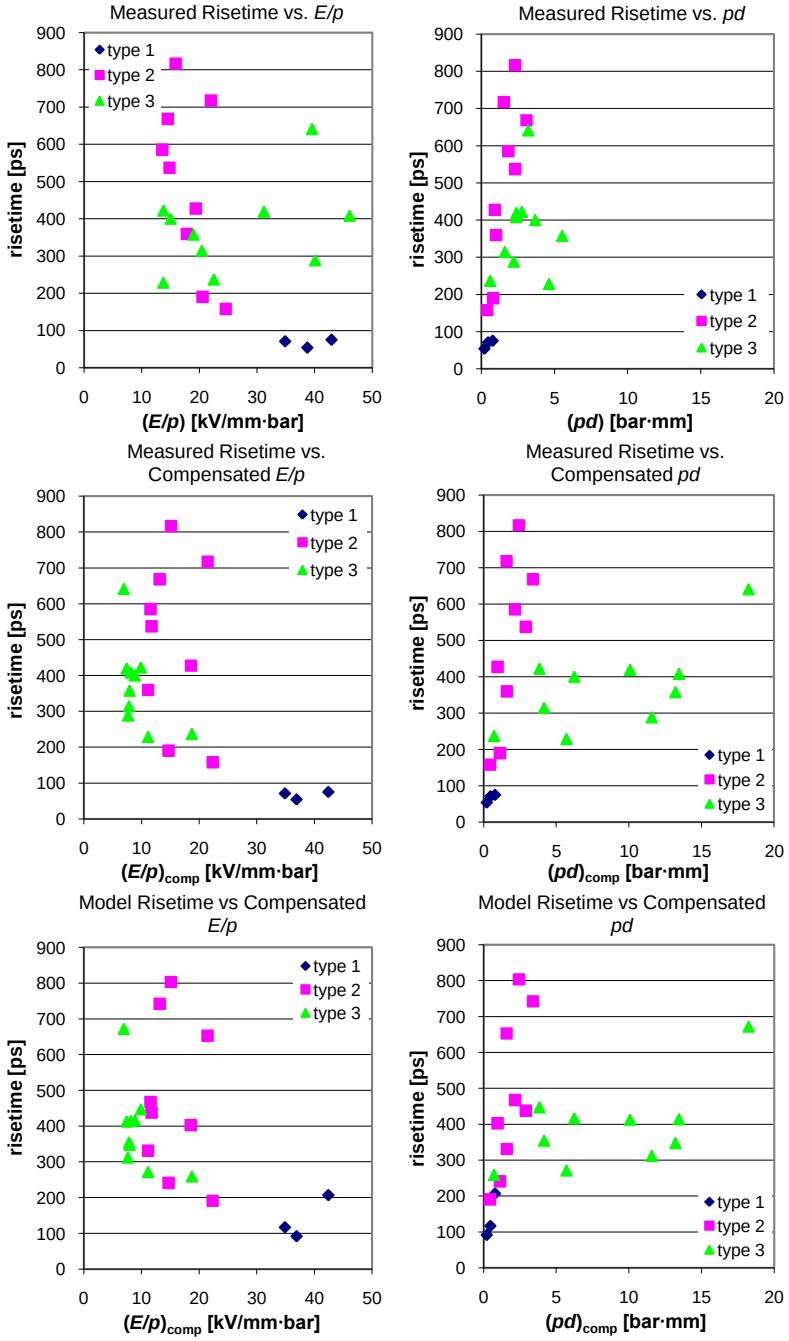

Figure 109. *Risetime dependency sorted by type. Top – raw measured data, middle – measured data and compensated gap distance, bottom – modeled data and compensated gap distance.*

Examining modeled risetime in relation to compensated *E/p* suggests a strong relation between field strength and pulse type (Figure 109, bottom left). Type III pulses are shown to have a relatively constant field strength approximately equal to the critical electric field strength of SF_6, $(E/p)_{crit}$ = 8.9 kV/mm (the one green data sample at $E/p \approx 18$ kV/mm·bar is a borderline case between type III and type II and can be grouped in either category depending on one's interpretation of the pulse shape). At this critical field strength, type III pulses have a large scatter of risetime values ranging from 250 to 700 ps. The same can be stated for type II pulses with *E/p* values ranging from 10 to 25 kV/mm·bar and risetimes varying between 200 and 800 ps. In contrast, type I waveforms consistent with *E/p* values exceeding 30 kV/mm·bar are shown to give rather uniform risetimes of approximately 100 – 200 ps.

As such, risetime dependency is more visible when studying its relation to pressure and gap distance (Figure 109, bottom right). Type I pulses with *pd* values under 1 bar·mm produce the fastest risetimes increasing from 100 to 200 ps as *pd* is increased. Type II pulses are dominant for *pd* values between 1 and 4 bar·mm. A similar increase in risetime from 200 to 800 is observed as *pd* increases within this range. Type III pulses are evident when *pd* exceeds 4 bar·mm. Here, risetime is first relatively constant between 300 and 400 ps before increasing to 700 ps at $pd \approx 18$ bar·mm. Observations are summarized in Table 7.5.

Table 7.5. *Risetime relations with waveform type*

Type	*E/p* [kV/mm·bar]	*pd* [bar·mm]	Risetime [ps]
I	> 30	< 1	100 – 200
II	10 – 25	1 – 4	200 – 800
III	≈ 8.9	> 4	300 – 700

As can be derived from the previous figures (Figure 107 - Figure 109), risetime values do not drastically deviate between measured and modeled data. Thus, for visualization's sake all measured data points (acquired by the 30 GHz digitizer) are shown in Figure 110 to portray the risetime development with greater resolution. Note that values may slightly vary from Table 7.5 since the figure displays the entire range of unaltered measurement data (with the exception of gap compensation) while the table is compiled from typical modeled waveforms where the effect of superimposing signals is removed. Nevertheless, the consistent trends in regards to pressure, inter-electrode distance, and electric field are visible.

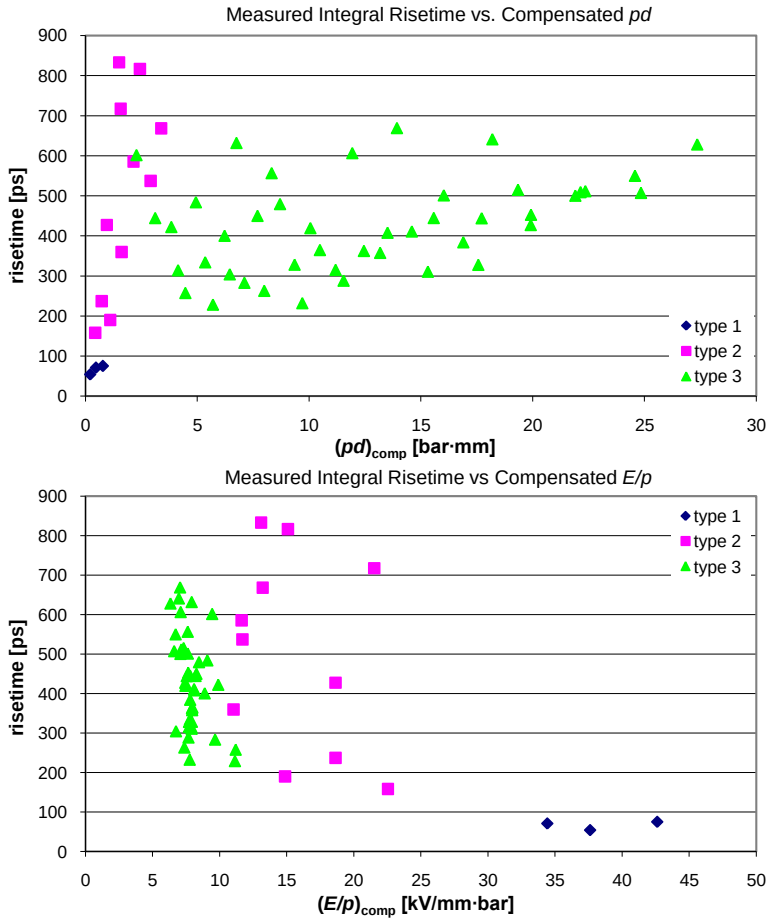

Figure 110. *All measured data plotted against gap compensated pd (top) and E/p (bottom).*

Referring back to the risetime dependencies presented in Chapter 4, type I risetime values are relatively consistent with Pécastaing's measurements using hydrogen but only within the constrained E/p range. Moreover, Pécastaing's data was collected using a 3 GHz (10 GS/s) direct sampling (real-time) oscilloscope and 6 GHz series sampling oscilloscopes where the limited bandwidth (along with the scatter of series sampling) can severely alter such fast pulses as is evident when comparing 6 GHz and 30 GHz data presented in this text (i.e. Figure 64). As such, Pécastaing's data should be viewed with a certain degree of reservation. Martin's and Sorenson's equations present a weakly comparable development for risetime as a function of pressure and electric field. However, risetime values deviate considerably. The other relationships presented in Chapter 4 do not provide similar trends for risetime signifying that most likely the equations are confined to their respective measurement setups and are not applicable to differing systems.

7.2 Interference

As mentioned in Section 5.2.5, significant interference was present in the measurement system. In addition to reflections modifying the measured signal, accompanying disturbances can seriously hinder the accurate measurement of risetime. Figure 111 shows an example of measured interference using the 6 GHz oscilloscope. Channels 1 (yellow), 3 (blue) and 4 (green) are open (no signal cable attached) and channel 2 (red) measures the *dV/dt* pulse observed by the *D*-dot probe via a 10 meter cable. All channels record a c. 15 ns noise signal with peak to peak amplitude of approximately 20% of the measured breakdown *dV/dt* pulse.

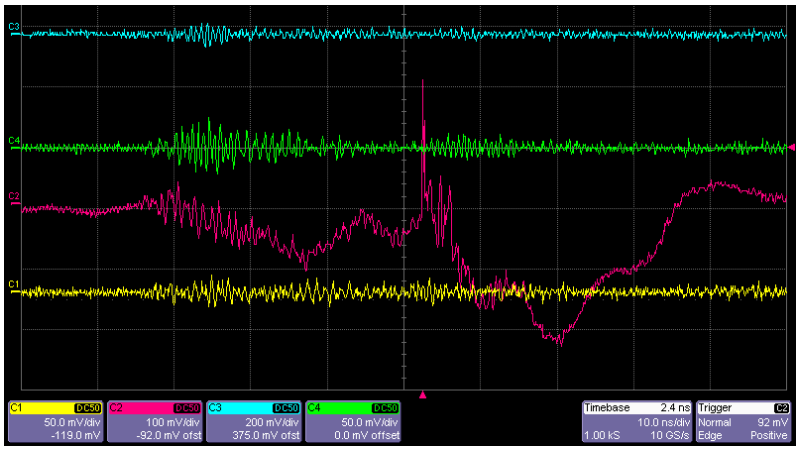

Figure 111. *Example of interference. Horizontal scale 10 ns/div.*

The noise signal is first observed before the actual onset of the *dV/dt* pulse. Therefore, interference reaches the oscilloscope faster than the signal travelling along the cables. Noise propagating through air at the speed of light over a distance of approximately 2 meters (distance between spark gap and measurement device) will reach the input channels of the oscilloscope 6.7 ns following the onset of discharge in the test gap. In contrast, the signal travelling along the measurement cables (propagation velocity 77% speed of light; value from manufacturer's data sheet) over a distance of 10 meters will arrive at the oscilloscope 43.3 ns after the onset of flashover in the test gap. In addition, the open channels also record a smaller noise signal approximately at the same time as the *dV/dt* pulse is recorded. This suggests that during the onset of breakdown, some of the noise propagating through the air couples into the measurement cables and thus propagates at the same speed as the measured *dV/dt* pulse. Alternatively, leakage current may be present between the oscilloscope channels. Consequently, the signal at the oscilloscope input is a sum of the measured *dV/dt* signal, interference propagating in the air, interference coupling into cables, possible interference via grounding, and possible internal noise of the oscilloscope.

Figure 111 represents the worst case scenario where adjacent measurement channels are open, grounding is two point (in contrast to single point grounding for all devices) and the oscilloscope has the weakest shielding (compared to the novel higher bandwidth digitizers – SDA 11000 and SDA 830Zi). The situation is significantly improved when the adjacent channels are short circuited to avoid leakage current into the measurement inputs and grounding is made more effective. In efforts to shield the measurement cables, they are inserted directly though the grounded copper sheet overlaying the measurement area as shown in Figure 112.

Figure 112. *Cable shielding.*

Overall, disturbances can be outlined in Figure 113, where discharge in the test gap results in interference propagating through the air (red) merging with the measured *dV/dt* signal (blue) at the oscilloscope input.

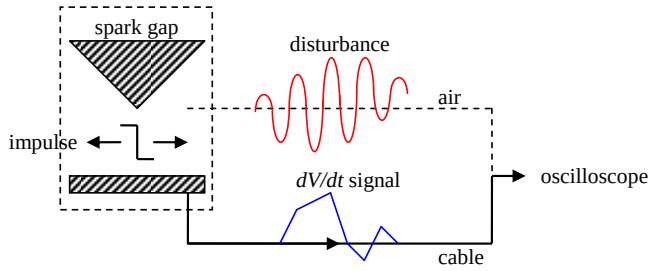

Figure 113. *Disturbances present in the measurement setup.*

Figure 114 describes the various components which are measured by the oscilloscope. Discharge in the test gap occurs at t = 0. After 6.7 ns the first noise signal (lasting approximately 15 ns) is observed by the oscilloscope. This signal eventually attenuates but maintains zero-level fluctuations of smaller amplitude. At t = 43.3 ns the *dV/dt* pulse arrives at the oscilloscope

input via the measurement cable along with some additional noise coupled into the cable. After the onset of discharge in the test gap, the signal advancing along the conical transmission line is reflected back from the inner wall of the fiber glass gas chamber. This is observed as a noticeable peak approximately 1.2 ns following the initial *dV/dt* signal.

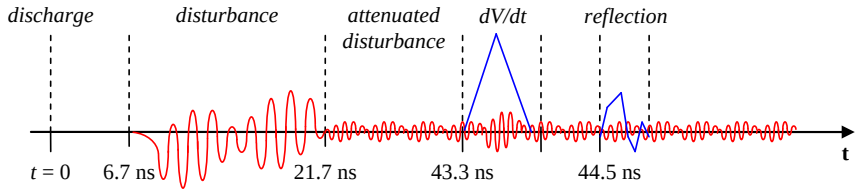

Figure 114. *Signal components measured by the oscilloscope.*

Since the *dV/dt* pulse duration of interest is typically under 1 ns, in order to view all these disturbances a significantly longer measurement time period (time/div) is needed. When selecting a longer time range, the resolution is decreased (fewer samples per second, due to the limited record length of the oscilloscope) making the disturbances less distinguishable. Consequently, measuring the fast breakdown pulse while simultaneously monitoring disturbances is not feasible. This is especially problematic, when a measured waveform exhibits noticeable zero-level fluctuation prior to the onset of the distinct *dV/dt* pulse, as it is impossible to determine the definite starting point and end of the signal. Furthermore, since only a limited number of samples are acquired on the rising front of the *dV/dt* pulse, a fluctuation in offset which shifts a single sample in either direction can result in a 25 ps deviation in the final risetime calculation. Thus, interpretation of the oscilloscope output has a significant effect on the final outcome.

7.3 Bandwidth and Sampling

Based on the reflection analyses presented earlier, the influence of impedance mismatching along the transmission line is most prominent in type I pulses. As significant reflections were calculated to last for approximately 50 – 100 ps following the onset of discharge, this accounts for a large portion of the type I pulse. Therefore, reflections severely modify the falling tail of the pulse (i.e. duration) and consequently, the peak of the integrals from which risetime is calculated. In contrast, type III pulses were observed to have pulse durations spanning up to 1 ns. As a result, the calculated reflections are seen as a minor change in the gradient of the falling tail but are not as significant since calculated reflection coefficients have attenuated by then to relatively small values. Accordingly, the pulse

duration of type III waveforms is not considerably altered by these reflections and most importantly the termination point (zero-level crossing) of the signal remains unchanged. This is evident in Figure 115. Pulse characteristics are outlined in Table 7.6.

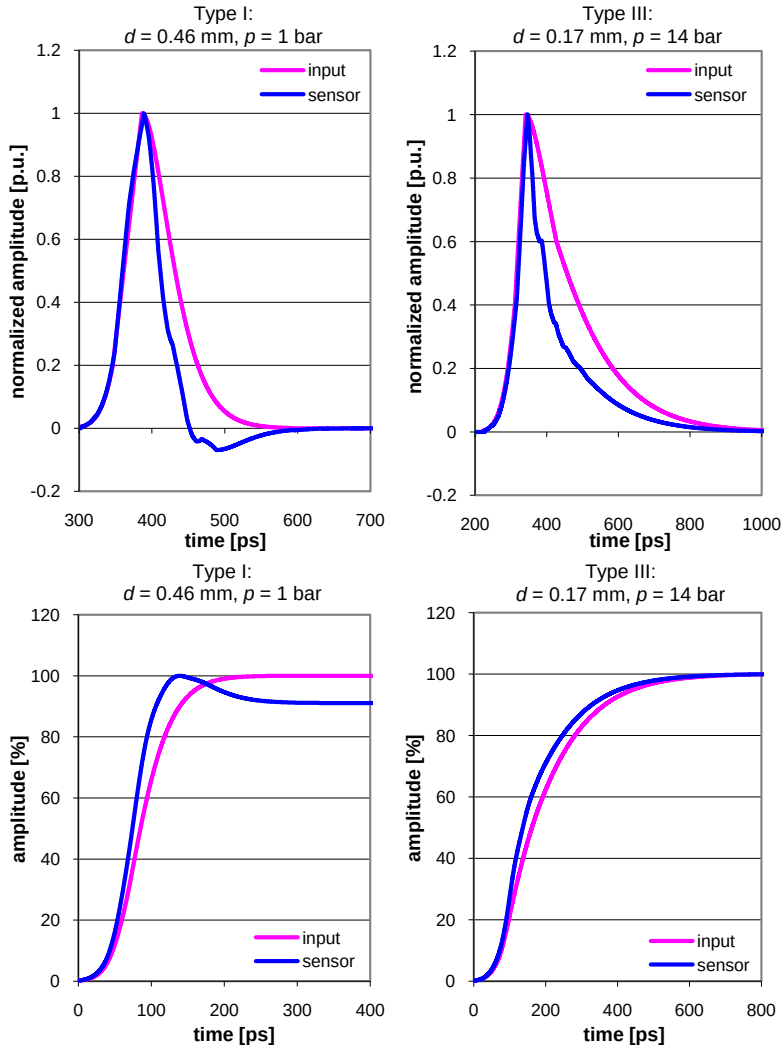

Figure 115. *Effect of reflections. Measured dV/dt pulses on top and voltage collapse (integral) on bottom. Input = without reflections, sensor = including reflections.*

Table 7.6. *Comparison between flashover pulse (model input) and sensor reading (model output).*

		dV/dt				Integral
		T1 [ps]	T2 [ps]	Pulse width [ps]	Pulse duration [ps]	T1 [ps]
Type I	Input	50.1	95.4	70.34	300	116.8
	Sensor	50.6	75.24	50.21	150	75.16
Type III	Input	56.7	171.7	143.3	900	414.2
	Sensor	57.47	108.9	80.18	900	375.8

Although both type I and type III sensor readings (model outputs) have a risetime approximately 40 ps faster than the actual flashover pulse (model input), risetime measured by the sensor for type III is only 10% smaller, while for type I sensor readings risetime is decreased by c. 35%. Thus, before the pulse arrives at the oscilloscope channel, the sensors record a pulse modified to appear faster by superimposed reflections.

In addition, even though the center conductor of the probe is cut flush with the ground plane, giving it a bandwidth significantly higher than the original 18 GHz specified by the manufacturer (Section 5.3.5), the measurement cables are limited to 18 GHz. Hence, the oscilloscope measuring 1 sample every 12.5 ps at 30 GHz bandwidth will record a signal modified by the transmission line and limited by the cable bandwidth.

When considering the applicability of the measurement system for such fast pulses, one is most concerned with the rising front of the *dV/dt* pulse since this is the fastest parameter recorded by the system. From Table 7.7, the fastest *dV/dt* front times (0 – 100%) are approximately 50 ps.

Table 7.7. *Model input waveform parameters.*

		dV/dt						Integral
p **[bar]**	***d*** **[mm]**	**T1 [ps]**	**T2 [ps]**	**PW [ps]**	**Front [ps]**	**Tail [ps]**	**Duration [ps]**	**T1 [ps]**
1	0.20	50.1	79.7	54.7	86.3	169.3	255.6	91.7
1	0.46	50.1	95.4	70.3	86.3	206.2	292.5	116.8
2	**0.20**	**30.1**	**75.4**	**60.4**	**51.9**	**210.1**	**262.0**	**191.0**
1	**0.77**	**30.1**	**75.4**	**60.4**	**51.9**	**331.1**	**383.0**	**207.1**
4	0.20	54.6	210.7	183.4	N/A	N/A	437.9	241.1
3	0.20	50.1	141.1	116.0	86.3	536.1	622.4	259.5
6	0.77	77.6	168.3	129.5	321.3	545.9	867.2	271.7
13	0.17	77.6	158.9	147.1	223.9	610.7	834.6	312.3
5	0.20	326.4	402.9	239.7	309.1	509.2	818.3	330.9
12	0.46	56.7	198.6	170.3	204.4	602.8	807.2	348.0
8	0.20	74.9	165.6	128.1	290.9	629.8	920.7	354.7
2	**0.46**	**30.2**	**79.8**	**64.7**	**52.0**	**476.9**	**528.9**	**402.5**
12	0.20	75.2	178.9	141.3	291.0	743.1	1034.1	413.1
14	0.17	56.7	171.7	143.3	120.2	795.5	915.7	414.2
8	0.46	77.5	190.8	152.1	295.8	752.0	1047.8	416.5
5	0.46	491.9	552.6	306.7	379.2	719.7	1098.9	437.5
6	0.46	77.6	243.2	204.4	505.1	807.6	1312.7	447.3
4	0.46	418.5	526.1	316.8	N/A	N/A	911.3	467.4
2	**0.77**	**30.0**	**75.4**	**60.4**	**47.8**	**658.6**	**706.4**	**652.8**
16	0.20	77.5	212.9	174.1	295.7	1182.0	1477.7	671.9
4	0.77	986.0	1044.0	550.7	674.2	785.8	1460.0	742.3
3	0.77	1009.0	1059.0	554.5	N/A	N/A	1209.0	803.3

These pulses propagate along the transmission line to the sensors, via the measurement cable and into the oscilloscope channel where they are recorded as a shorter superimposed signal compiled from the actual flashover signal, reflections and noise, and further time warped by the limited bandwidth cables. These factors appear to considerably limit the

accuracy of the measurement system. Implementing an ideal transmission line, improving shielding from external noise, and purchasing higher bandwidth measurement cables would alleviate these problems. However, the 50 ps rising front of the *dV/dt* pulse would still be recorded by the 30 GHz oscilloscope as consisting of only 4 – 5 samples. Thus, as expressed earlier, the interpretation of the observed signal is of most importance since an offset of ±1 sample will significantly alter the final risetime calculation, more so than the above mentioned limitations.

The 50 ps rising *dV/dt* fronts have risetimes of approximately 30 ps. The recommended risetime of a measurement system for such a pulse is approximately 3 – 5 times faster (Section 5.3.5), making the required system risetime 6 – 10 ps. This equates to a system bandwidth ranging from 35 – 60 GHz. Considering a situation where the transmission line is lossless and system bandwidth is limited only by the 30 GHz oscilloscope, the system is still short of the recommended specifications. Thus, even for an ideal lossless system operating at is maximum capacity, the measurement bandwidth is not sufficient to measure the fastest signal components.

7.4 System Development

Numerous factors affecting the final observed waveform recorded by the oscilloscope have been presented. Next, further improvements in system accuracy are discussed.

7.4.1 Optimal Impedance Matching at the Expense of Field Homogeneity

As explained earlier, slight impedance mismatching can cause reflected signals to propagate along the transmission line and modify the waveform observed by the sensors. The plane region at the tip of the electrode was selected to ensure a homogeneous electric field at the discharge location. However, in order to achieve a higher transmission coefficient and consequently reduce the effect of reflections, the following modification to the electrode tip can be made.

Impedance of a conical transmission line remains constant along a fixed angle θ. Section 5.3.2 (Homogeneous Field vs. Fixed Impedance) considered issues arising from terminating a conical electrode with a plane profile – impedance mismatching at the coupling of the profile with the conical electrode. For ideal matching, the conical electrode with a constant angle should be terminated with a hemisphere at the point where the tangent of the arc is at the same angle (point A in Figure 116). Here, $Z_1 = Z_2$ giving respective reflection and transmission coefficients as 0 and 1.

For an ideal sphere with a consistent finite radius, impedance will remain

constant along the arc (as was shown in Table 5.2). Hence, if a signal propagates from the center axis, the impedance along the entire transmission line (including the hemisphere and conical electrode) is fixed and reflections will be avoided.

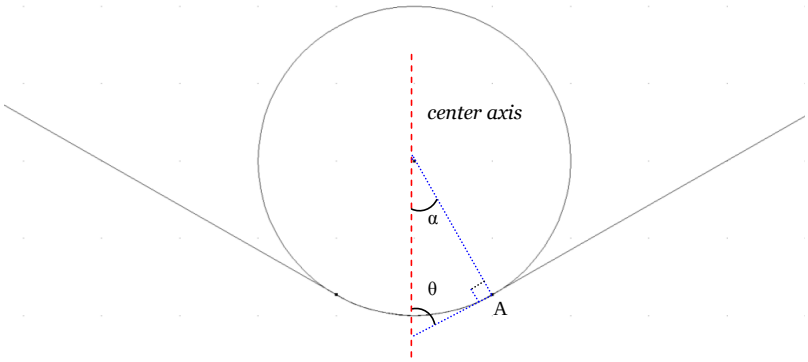

Figure 116. *Coupling of hemisphere termination with conical electrode.*

Figure 117 shows the electric field distribution for the suggested geometry while Figure 118 displays field fluctuation along the center axis of the spark gap between the two electrodes.

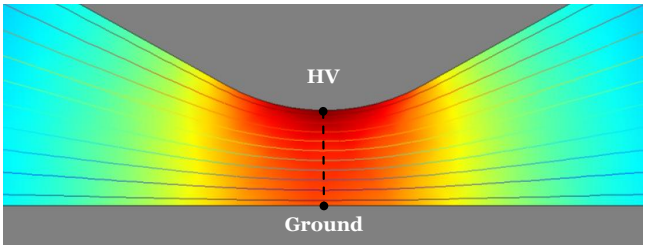

Figure 117. *Electric field distribution of spark gap (d = 1 mm, HV = 200 kV).*

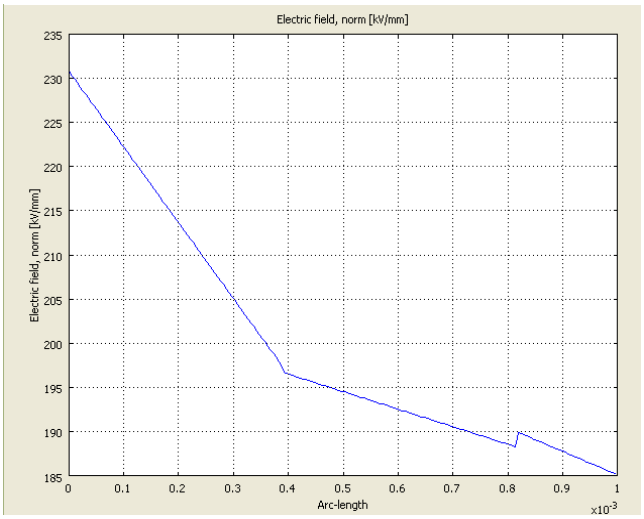

Figure 118. *Electric field fluctuation between electrodes.*

Based on FEM simulations, the electric field fluctuates c. 20 % between the high voltage electrode and grounded plate. Hence, an ideally matched hemisphere termination provides a less homogeneous electric field compared to a plane profile which was shown to have field fluctuations of c. 7% (Figure 31 in Section 5.3.2). As homogeneity is decreased, the probability of side flashover is also decreased since discharge is more likely to occur at the point where electric field concentration is greatest. Thus, the sensors distributed around the discharge area are more likely to measure similar waveforms making the inter-comparison of oscilloscope performance more accurate. However, this matched termination will lose its ideality as continuous discharges corrode its finite profile. Therefore, its functionality is limited by the number of desired breakdown pulses.

7.4.2 Sensor Selection

The implemented *D*-dot sensors measure the time derivative of voltage collapse. The risetime of the flashover pulse is then calculated from the integral of the measured pulse. Thus, any misinterpretation of the *dV/dt* pulse (offset, starting point, end point) will be amplified in the final integral. To remove this factor from the system, probes with built-in integrators (such as the magnetic field probe in Section 5.3.3) could be utilized to observe risetime directly from the measured pulse without additional manipulation (i.e. integration) of data. However, the response and bandwidth of such probes would need to be sufficient to guarantee feasible representation of the fast phenomena.

7.4.3 Measurement Cables

Improving electromagnetic shielding would enable the use of shorter measurement cables. Currently, the shortest practical measurement distance is approximately 2 m. If economical issues were not a limiting factor, high bandwidth SK-connector (2.92 mm) cables could be purchased to increase the cable bandwidth up to 44 GHz.

7.4.4 Gap Distance Uncertainty

One of the major uncertainties in the measurement setup was introduced by the inter-electrode distance varying as a function of pressure. This was caused by the large gas chamber introducing extremely high mechanical stress to the structure. In order to improve the mechanical withstand strength of the test gap, a similar coaxial structure could be used as in section 5.2. The improved structure is shown in Figure 119 where transmission line length is increased to avoid reflections and the metal to metal outer conductor interfaces allow for higher mechanical strength.

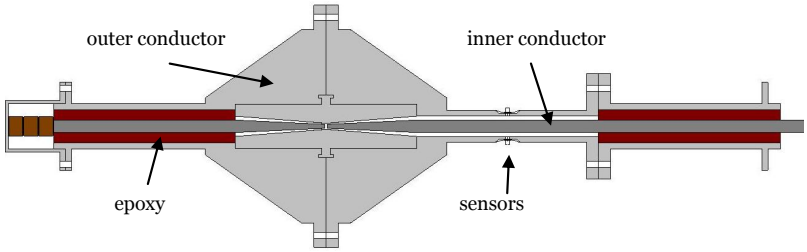

Figure 119. *Prototype for test gap 3.*

According to simulations (Figure 120), mechanical stress is significantly decreased (under 16 MPa) due to the smaller gas chamber and thus gap fluctuation as a function of pressure is limited to approximately 3 µm. The only drawback is its large size (over 1.5 m in length) and its structural complexity which increases material and manufacturing expenses.

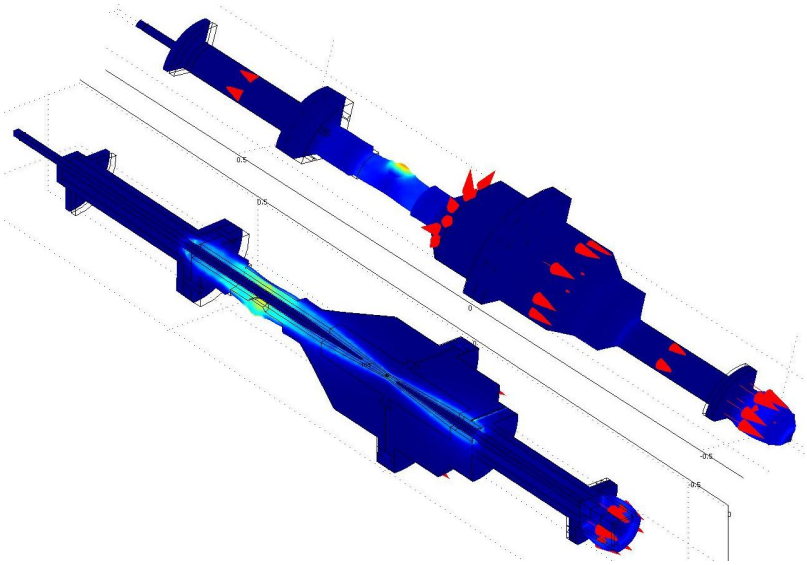

Figure 120. *Mechanical simulations of test gap 3 prototype.*

7.4.5 Digital Signal Analyzer

As technology is rapidly advancing, higher bandwidth oscilloscopes will no doubt be available in the near future. As previous analysis showed, the 30 GHz oscilloscope is borderlining the recommended measurement bandwidth and any improvements in sampling rates will enable the verification of results presented in this research. However, increases in measurement technique will enhance the effect of any non-idealities in the system (i.e. microscopic irregularities of the electrode will cause more notable ripple in measured pulses). Thus, advances in measurement devices require parallel advances in structural design of test equipment.

8. Conclusions

Breakdown of sulfur hexafluoride was measured in pressurized submillimeter spark gaps. Flashover characteristics were studied most accurately with Setup 2 (conical spark gap), utilizing a 30 GHz digitizer and post-processing to account for the non-ideality of the measurement system (impedance mismatching, mechanical expansion, and discharge location).

Both measurement systems discussed in this research provided very similar trends. In both cases, measured waveforms could be categorized into different groups with calculated risetimes confined to specific electric field and pressure constraints. However, differences in recording equipment and post-processing methods resulted in notable digression of calculated values. Setup 1 are presents purely raw measured data. Built-in digital signal processing of the oscilloscopes, reflections, and other such influential factors are not considered. As such, Setup 2 verifies the trends observed in the first setup and in addition, provides further insight and greater accuracy into the phenomenon of voltage collapse in gas.

Results can be summarized by the observed relations between risetime and the variables shown in Figure 121 (E/p and pd). Cropping and line fitting methods disregard a significant amount of measured data and as such cannot be considered a truly accurate depiction of the process. Thus, incorporating reflection and transmission coefficients to model voltage collapse prior to the onset of transmission line non-idealities, along with compensated gap distance accounting for structural deformation as a function of pressure, is selected as the most suitable representation.

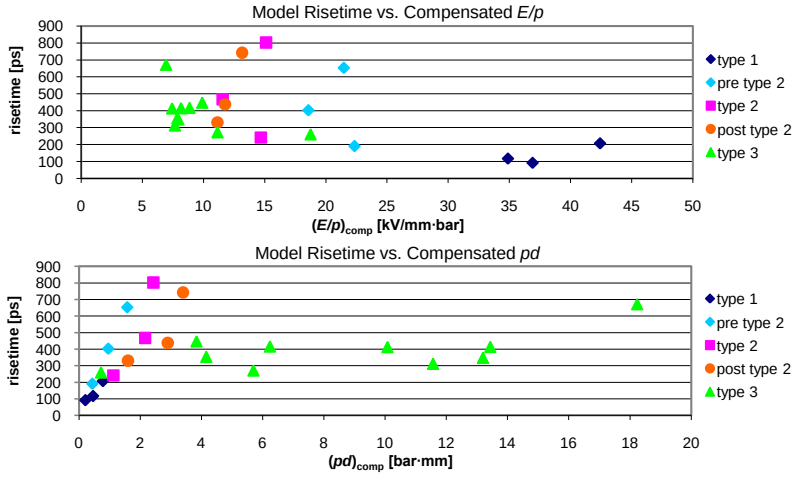

Figure 121. *Risetime as a function of electric field strength (top) and pressure and compensated gap distance (bottom) grouped by pulse type, including subcategories.*

Critical field strength $(E/p)_{crit}$ was observed to be constant only for type III pulses where net ionization $\alpha - \eta = 0$ when $E/p \approx 8.9$ kV/mm·bar as calculated by Townsend's theories. Type II pulses were observed to have critical field strength values ranging from 10 to 25 kV/mm·bar and type I pulses have even higher critical field strengths exceeding 30 kV/mm·bar which agree well with Kuffel's proposed increase in critical field strength of SF_6 for decreasing *pd* values.

Thus, pressure and inter-electrode distance determine the breakdown waveform type and consequently, define the risetime of voltage collapse. Development of breakdown waveforms can be outlined in Table 8.1 and modeled typical *dV/dt* pulses with their respective integral waveforms are shown in Figure 122.

Table 8.1. *Breakdown waveform development*

Type I		For small *pd* values less than 1 bar·mm, critical field strength exceeds 30 kV/mm·bar. Once flashover occurs, voltage collapse is a fast linear phenomenon with risetimes less than 200 ps.
Type II	**Pre**	As the product of pressure and gap distance increases, the critical field strength required for breakdown decreases to values ranging between 15 – 25 kV/mm·bar. At this point voltage collapse is no longer linear. Instead, the initial rapid voltage collapse is followed by a decline in the gradient, after which the remaining portion collapses slightly slower ("Type 2 PRE" in Figure 122).
	Mid	At field strength values of approximately 15 kV/mm·bar, a linear voltage collapse is followed by a short saturation period (slowing of voltage collapse) after which the remaining collapse occurs at the same rate as the initial gradient ("Type 2 MID" in Figure 122).
	Post	Further increasing *pd* to correspond to approximately 10 kV/mm·bar field strength will cause a gradual onset of breakdown until it reaches a point where remaining voltage collapse is significantly faster (Type 2 POST in Figure 122).
		The risetimes for breakdown in the $10 < E/p < 25$ kV/mm·bar range are primarily dependant on gap distance. A larger gap distance equates to a longer linear saturation period where *dV/dt* is constant (*dV/dt* plateau area) which results in a larger risetime. Overall, for $10 < E/p < 25$ kV/mm·bar and $1 < pd < 4$ bar·mm, risetimes range from 250 to 800 ps.
Type III		Increasing *pd* over 4 bar·mm will result in critical electric field strength approaching 8.9 kV/mm·bar. Following a rapid but brief drop in voltage at the onset of breakdown, the remaining collapse decelerates exponentially. Here, risetimes are fairly constant between 250 and 450 ps increasing eventually up to 700 ps as pressure and gap distance in increased to 18 bar·mm.

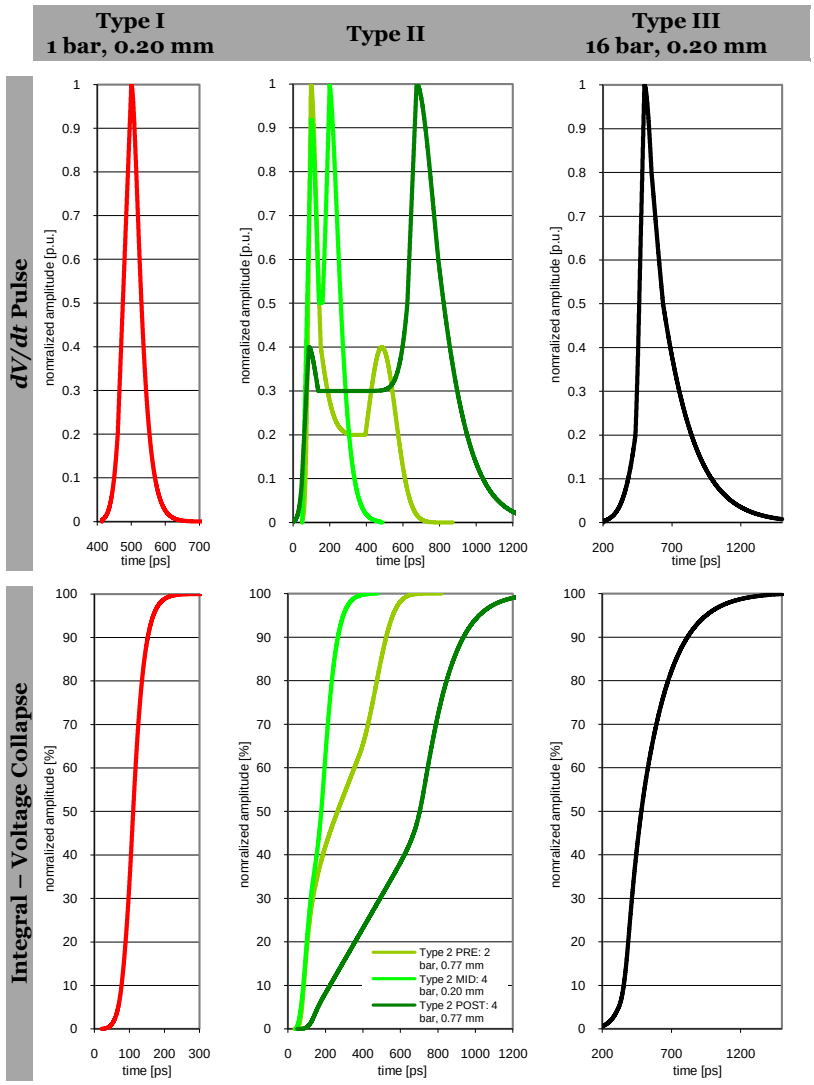

Figure 122. *Schematic of modeled waveforms.*

Based on the theories discussed in Chapter 2, possible physical explanations behind the observed breakdown processes can be hypothesized as follows:

The faster risetimes for type I pulses could be accredited to the lower density of SF_6 present in the gas chamber for small *pd* values. Since less electron-attaching electronegative gas is present, current growth is less obstructed and thus breakdown occurs rapidly over the small gap. Moreover, as explained earlier for smaller *pd* values, electrons may migrate across the gap without a single collision (or insufficient number of collisions), thus increasing the required voltage necessary for breakdown (as was observed during measurements).

In contrast, for type III discharge, the increased gas pressure (higher

density of electronegative gas) contributes to the absence of free electrons. Therefore, once discharge commences and progresses across the gap, charge carriers become scarcer, current decreases, and consequently voltage collapse slows down resulting in larger risetimes compared to type I.

Type II discharge could be characterized by unstable ionization where the initial electron avalanche progresses to a certain point where charge carriers become limited. Distance between electrodes determines the onset of this instability which results in a constant *dV/dt* of varying duration. Possible reasons for scarcity of charge carrier limiting the expansion of voltage collapse could be attributed to decreasing net ionization due to recombination or insufficient energy gained between collisions to further advance current growth. The progression then continues after it has received additional electrons by various secondary processes discussed in 2.2.2 or possibly by streamers connecting secondary avalanches to facilitate the rapid expansion. Furthermore, due to the large volume of gas present in the test gap, additional charge carriers may migrate towards the spark gap under the influence of the electric field. In addition, the inhomogeneity of the electric field may play a role in type II pulses. The ionization coefficient $\alpha = \alpha(E)$ is considered constant for homogeneous fields. As gap distance is increased, the field distribution in the gap becomes less uniform leading to a change in the development of the electron avalanche. However, based on simulation, the fluctuation of electric field in the spark gap is considerable only for inter-electrode distances exceeding c. 0.6 mm as shown in Figure 123. The figure depicts the electric field deviation in the planar region directly at the center of the spark gap.

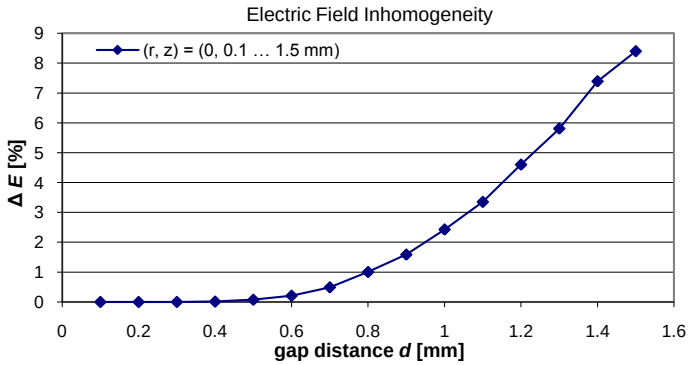

Figure 123. *Variation of electric field at spark gap (difference between minimum and maximum electric field at the center of the HV electrode tip and the ground plate).*

Thus, if increasing inhomogeneity is responsible for the widening saturation between type II *dV/dt* peaks, then this development should only be observed in d = 0.77 mm pulses where electric field varies across the spark gap and waveforms for d = 0.20 mm and d = 0.46 mm should therefore be identical. As this is not the case, a varying ionization

coefficient resulting from electric field inhomogeneity cannot solely contribute to the observed type II development.

Numerous variables and problems affecting the accurate portrayal of breakdown have been discussed throughout this text. In order to confidently measure the fast breakdown phenomenon, one must be able to separate external factors not related to the physical process from the acquired data. Several essential considerations have been accounted for, such as:

Mechanical Expansion. Since gap distance has a significant effect on breakdown characteristics, it is essential to accurately determine the inter-electrode distance and its variation under stress. Large pressurized gas chamber devices experience exceptionally large stresses due to their considerable surface area and thus structural deformation is more than likely. The effect of mechanical expansion is more significant for smaller gaps.

Impedance Matching. Impedance of the transmission line along which the measured signal propagates should be maintained as constant as possible. The signal will reflect and attenuate at each discontinuity boundary thus differentiating the captured waveform from the original pulse. In practice, an ideal system is unattainable as repeated discharge will corrode the electrode surface creating impurities (i.e. surface roughness, by-products, etc.) which influence the breakdown process.

Flashover Point. In addition to maintaining constant impedance, electrode design is key in setting the onset site for breakdown. Any inhomogeneity along the electrode surface will accumulate electric field and cause breakdown in an undesirable location. When measuring with numerous sensors, relative distance from the flashover point, will affect the comparability of measured data.

Breakdown Scatter. Considerable variation between successive breakdown voltages is evident. Therefore, it is necessary to measure numerous samples from which an average value can be calculated. Breakdown voltage values have a considerable impact on post-measurement analysis (i.e. calculating E/p).

Electromagnetic Interference. High breakdown voltages result in considerable disturbances coupling into the measured signal. The efficiency of shielding is a compromise between available resources (cable length, measurement area size, grounding possibilities) and measurement range (smaller applied voltage result in smaller disturbances). Although individual device protection is improving (newer oscilloscopes are able to withstand external noise better), numerous interference coupling possibilities still exist along interconnections between system components (i.e. cables and test equipment, internal noise in the supply source, etc.).

System Bandwidth. Using *D*-dot sensors to evaluate breakdown waveforms requires equipment capable of measuring 30 – 50 ps risetimes

(possibly even faster). This equates to a recommended system bandwidth of at least 35 GHz. Higher measurement resolution using series sampling data acquisition is not recommended due to large scatter between successive pulses. In series sampling, high repetition rates are typically used for attaining sufficient samples within a reasonable timeframe, which in turn further stresses the supply equipment and increases data scatter. One may opt for longer intervals between pulses allowing the insulation gas and equipment to recover, but measurement duration increases significantly. In addition, one must consider the issue where increased bandwidth and sampling also increases the amount of recorded disturbances. As resolution increases, the measurement system will be able to observe any minute oscillations resulting from i.e. surface roughness or impedance discontinuity in greater detail. For this reason, any increase in the system bandwidth of the systems presented in this text would be futile since higher integrity data would require a more detailed electrode design. Thus, the setups are operating at their maximum capacity from both the structural design's and measurement system's point of view.

All the above mentioned factors have a considerable effect on analyzing the breakdown process. However, the most significant impact was observed to be related to the measurer (human error). Once samples have been recorded and displayed by the measurement equipment, it is up to the measurer to decide if the presented data is an accurate representation. Due to the limited amount of samples, a slight deviation in interpreting the appropriate zero level, pulse onset and end point can lead to a large fluctuation in the end result (i.e. risetime). As technological advances increase sampling capability and measurement techniques improve, the ambiguity of measured data will no doubt decrease, enabling a more consistent comparison between different measurement systems and reduce the level of interpretation required by the measurer. Until then, it is essential to utilize the existing equipment as efficiently as possible and account for microscopic level details in test equipment design when striving to measure the ultrafast phenomena of breakdown as accurately as possible.

References

Air11 Air Liquid, Gas Encyclopedia, *SF6 Sulfur hexafluoride CAS Number: 2551-62-4 UN1080*, [cited 02.05.2011] http://encyclopedia.airliquide.com/Encyclopedia.asp?GasID=34

All04 Allen NL 2004, 'Mechanisms of Air Breakdown' in Haddad, A & Warne, DF (eds), *Advances in High Voltage Engineering*, IET, Chp. 1.

And03 Andrews JR 2003, *UWB Signal Sources, Antennas & Propagation*, Application Note AN-14a, Picosecond Pulse Labs.

And66 Andreev SI & Orlov BI 1966, *Development of a Spark Discharge-I*, Sov. Phys. Tech. Phys., Vol. 10, pp. 1097-1101.

Aro03 Aro M, Elovaara J, Karttunen M, Nousiainen K & Palva V 2003, *Suurjännitetekniikka*, Otatieto.

Bla91 Blanchet M 1991, *Production par éclateurs d'impuslion de haute tension brèves dans le domaine de la centaine de picoseconds*, L'onde Électrique, Vol. 71, No. 2.

Bog82 Boggs SA, Chu FY, Fujimoto N, Krenicky A, Plessl A & Schlicht D 1982, *Disconnect Switch Induced Transients and Trapped Charge Gas Insulated Substations*, IEEE Trans. Power Apparatus and Systems, Vol. PAS-101, pp. 3593-3602.

Bra58 Braginskii SI 1958, *Theory of the Development of a Spark Channel*, Soviet Physics JETP, Vol. 34(7), No. 6.

Bur85 Burkhart S 1985, *Coaxial E-Field Probe for High-Power Microwave Measurement*, IEEE Trans. Microwave Theory and Techniques, Vol. MTT-33, No. 3, pp. 262 – 265.

Cig77 CIGRE, 1977, *Breakdown of Gases in Uniform Fields* Working Group 15.03.

Dic02 Dick AR, MacGregor SJ & Pate RC 2002, *Transmission line switch design for the investigation of sub-nanosecond electrical breakdown*, Meas. Sci. Technol. Vol. 13, pp. 539-546.

Dra51 Drabkina SI 1951, *The Theory of the Development of the Channel in the Spark Discharge*, Soviet Physics, JETP 21, p. 473.

Eng89 Engel TG, Donaldson AL & Kristiansen M 1989, *The Pulsed Discharge Arc Resistance and its Functional* Behavior, IEEE Trans. Plasma Sci, Vol. 17, No. 2.

Far04 Farish O, Judd MD, Hampton BF & Peason JS 2004, 'SF6 Insulation Systems and their Monitoring' in Haddad A & Warne DF (eds), *Advances in High Voltage Engineering*, IET, Chp. 2.

Far94 Farish O 1994, *Acting on Impulse: Application of HV pulse technology*, Engineering Science and Educational Journal, December, pp. 277-286.

Fro02 Frost CA, Martin TH, Patterson PE, Rinehart LF, Rohwein GJ, Roose LD, Aurand JF & Buttram MT 1993, *Ultrafast Gas Switching Experiments*, Proc. 9th IEEE Int. Pulsed Power Conf., New York, pp. 491-494.

Gri09 Griffin GD, Sauers I & James DR, Department of Energy's Information Bridge: DOE Scientific and Technical Information, *Evaluation of Possible Biological Effects from Exposure to Gaseous SF_6 Breakdown Products* [cited 26.02.2009], http://www.osti.gov/bridge/servlets/purl/138692-aavEYi/138692.PDF

Hus99 Hussey TW, Davis KJ, Lehr JM, Roderick NF, Pate RC & Kunhardt E 1999, *Dynamics of Nanosecond Spark-Gap Channels*, 12th IEEE Int. Pulsed Power Conf., Monterey CA, pp. 1171-1174.

IEC89 International Electrotechnical Commission, 1989, International Standard 60-1, Second Edition, part 1, p. 61.

Kin85 Kind D & Kärner H 1985, *High-Voltage Insulation Technology*, Vieweg.

Klü07 Klüss JV 2007, *Characteristics of Submillimeter Flashover in Pressurized SF_6*, Master's Thesis, Helsinki University of Technology, Espoo.

Kuf00 Kuffel E, Zaengl WS & Kuffel J 2000, *High Voltage Engineering Fundamentals*, Butterworth-Heinemann, pp. 295-296.

Kus85 Kushner MJ, *et al.* 1985, *Arc Resistance of laser triggered spark* gaps, J. Appl. Phys., Vol. 58, pp.1744–1751.

Lec09 LeCroy, Product Datasheet, *WaveMaster 8 Zi Series*, [cited 26.10.2009], http://www.lecroy.com/tm/products/Scopes/WaveMaster_8_Zi/

Lin07 Lindell I 2007, *Sähkötekniikan Historia*, Sähkömagnetiikan laboratorion oppimateriaalisarja, report 25, Espoo.

Mal87 Malik NH & Qureshi AH, 1987, *Breakdown Mechanisms in Sulphur-Hexafluoride*, IEEE Trans. Electr. Insul., Vol. EI-13, No. 3, pp. 135-145.

Mar81 Martin, JC 1981, 'Solid, Liquid and Gaseous Switches' in *Pulsed Power Lecture Series,* Lecture No. 30, p.9.

Nai96 Naidu MS & Kamaraju V 1996, *High Voltage Engineering 2nd Edition*, McGraw-Hill, Chp 2.1.

Nat09 National Instruments, Developer Zone Tutorial, *Bandwidth, Sample Rate, and Nyquist Theorem*, [cited 20.10.2009], http://zone.ni.com/devzone/cda/tut/p/id/2709

Osm92 Osmokrovic P, Krstic S, Ljevac M & Novakovic D 1992, *Influence of GIS Parameters on the Toepler's Constant*, IEEE Trans. Electrical Insulation, Vol. 27, pp. 214-220.

Péc01 Pécastaing, L, Paillol, J, Gilbert, A & Domens P 2001, *Design and Performance of High Voltage Pulse Generators for Ultra-Wideband Applications*, Meas. Sci. Technol. 12, pp. 1718-1725.

Råd01 Räde L & Westergren B 2001, *Mathematics Handbook for Science and Engineering*, Studentlitteratur, p. 515.

Rom44 Rompe R & Weitzel W 1944, *Uber das Toeplersche Funkengesetz*, Z. fur Phys, pp.122, 636.

Say09 Sayed Saad Amin, Electrical Power Systems and Transmission Network Website, *SF6 Gas Properties*, [cited 26.02.2009], http://www.sayedsaad.com/substation/index_sf6.html

Sin03 Singha S 2003, *Toepler's Spark Law in a GIS with compressed SF6-N2 mixture*, IEEE Transactions on Dielectric and Electrical Insulation, Vol. 10, No. 3.

Sor77 Sorenson, TP & Ristic, VM 1977, *Rise Time and Time Dependant Spark-Gap Resistance in Nitrogen and Helium*, J. Appl. Phys., Vol. 48, No.1, pp.114-117.

Tek10 Tektronix, Technical Brief, *Understanding Oscilloscope Bandwidth, Rise Time and Signal Fidelity*, [cited 3.9.2010], http://www2.tek.com/cmswpt/pidetails.lotr?ct=PI&cs=cpc&ci=3802&lc=EN

Tri80 Trinh NG 1980, *Electrode Design for Testing in Uniform Field Gaps*, IEEE Trans. Power Apparatus and Systems, Vol. PAS-99, No.3, pp. 1235-1242.

Wik09 Wikipedia, Free Encyclopedia, *Pulsed Power*, [cited 11.02.09], http://en.wikipedia.org/wiki/Pulsed_power

Wik09a Wikipedia, Free Encyclopedia, *Sulfur hexafluoride*, [cited 05.02.09], http://en.wikipedia.org/wiki/Sulfur_hexafluoride

Wik10 Wikipedia, Free Encyclopedia, *Electric Arc*, [cited 4.6.2010], http://en.wikipedia.org/wiki/Electric_arc

Wik10a Wikipedia, Free Encyclopedia, *Ion*, [cited 31.8.2010], http://en.wikipedia.org/wiki/Ion

Appendix 1 – Complete Tables

Table 6.3. *Calculated gap distance based on theory.*

d_0 [mm]	p [bar]	E [kV/mm]	$E \cdot p$ [kV·bar/mm]	U_b [kV]	$d = U_b/E \cdot p$ [mm]	Δd [mm]	Δd [%]
0.17	5	8.9	44.5	14.43	**0.32**	0.15	191
0.17	10	8.9	89.0	43.49	**0.49**	0.32	287
0.17	11	8.9	97.9	58.89	**0.60**	0.43	354
0.17	12	8.9	106.8	75.32	**0.71**	0.54	415
0.17	13	8.9	115.7	88.61	**0.77**	0.60	451
0.17	14	8.9	124.6	109.66	**0.88**	0.71	518
0.17	15	8.9	133.5	121.59	**0.91**	0.74	536
0.17	16	8.9	142.4	133.67	**0.94**	0.77	552
0.17	17	8.9	151.3	148.03	**0.98**	0.81	576
0.17	18	8.9	160.2	162.60	**1.01**	0.84	597
d_0	p	E	$E \cdot p$	U_b	*theoretical d*	Δd	Δd
0.2	1	8.9	8.9	7.75	**0.87**	0.67	436
0.2	2	8.9	17.8	9.83	**0.55**	0.35	276
0.2	3	8.9	26.7	13.50	**0.51**	0.31	253
0.2	4	8.9	35.6	16.45	**0.46**	0.26	231
0.2	5	8.9	44.5	17.81	**0.40**	0.20	200
0.2	6	8.9	53.4	21.51	**0.40**	0.20	201
0.2	7	8.9	62.3	25.55	**0.41**	0.21	205
0.2	8	8.9	71.2	32.69	**0.46**	0.26	230
0.2	9	8.9	80.1	41.63	**0.52**	0.32	260
0.2	10	8.9	89.0	53.42	**0.60**	0.40	300
0.2	11	8.9	97.9	63.42	**0.65**	0.45	324
0.2	12	8.9	106.8	74.90	**0.70**	0.50	351
0.2	13	8.9	115.7	84.61	**0.73**	0.53	366
0.2	14	8.9	124.6	98.17	**0.79**	0.59	394
0.2	15	8.9	133.5	122.20	**0.92**	0.72	458
0.2	16	8.9	142.4	126.59	**0.89**	0.69	444
d_0	p	E	$E \cdot p$	U_b	*theoretical d*	Δd	Δd
0.46	1	8.9	8.9	16.05	**1.80**	1.34	392
0.46	2	8.9	17.8	17.82	**1.00**	0.54	218
0.46	3	8.9	26.7	19.70	**0.74**	0.28	160
0.46	4	8.9	35.6	24.98	**0.70**	0.24	153
0.46	5	8.9	44.5	34.10	**0.77**	0.31	167
0.46	6	8.9	53.4	37.99	**0.71**	0.25	155
0.46	7	8.9	62.3	44.83	**0.72**	0.26	156
0.46	8	8.9	71.2	55.26	**0.78**	0.32	169
0.46	9	8.9	80.1	63.62	**0.79**	0.33	173
0.46	10	8.9	89.0	74.12	**0.83**	0.37	181
0.46	11	8.9	97.9	86.24	**0.88**	0.42	191
0.46	12	8.9	106.8	104.76	**0.98**	0.52	213
0.46	13	8.9	115.7	121.10	**1.05**	0.59	228
0.46	14	8.9	124.6	135.56	**1.09**	0.63	237
0.46	15	8.9	133.5	152.55	**1.14**	0.68	248
0.46	16	8.9	142.4	159.71	**1.12**	0.66	244
0.46	17	8.9	151.3	164.16	**1.09**	0.63	236
0.46	18	8.9	160.2	173.20	**1.08**	0.62	235
d_0	p	E	$E \cdot p$	U_b	*theoretical d*	Δd	Δd
0.77	1	8.9	8.9	33.08	**3.72**	2.95	483
0.77	2	8.9	17.8	33.92	**1.91**	1.14	247
0.77	3	8.9	26.7	36.74	**1.38**	0.61	179
0.77	4	8.9	35.6	44.73	**1.26**	0.49	163
0.77	5	8.9	44.5	50.00	**1.12**	0.35	146
0.77	6	8.9	53.4	63.49	**1.19**	0.42	154
0.77	7	8.9	62.3	68.65	**1.10**	0.33	143
0.77	8	8.9	71.2	73.59	**1.03**	0.26	134
0.77	9	8.9	80.1	83.49	**1.04**	0.27	135
0.77	10	8.9	89.0	98.81	**1.11**	0.34	144
0.77	11	8.9	97.9	118.10	**1.21**	0.44	157
0.77	12	8.9	106.8	131.82	**1.23**	0.46	160
0.77	13	8.9	115.7	141.41	**1.22**	0.45	159
0.77	14	8.9	124.6	154.96	**1.24**	0.47	162
0.77	15	8.9	133.5	165.02	**1.24**	0.47	161

Table 6.4. *Compensated gap distance using reference onset.*

d [mm]	*d* (theory) [mm]	Δ*d* [mm]	compensated *d* [mm]	*p* [bar]	*pd* [bar·mm]	U_b [kV]	*E/p* [kV/mm·bar]
0.17	**0.32**	**0.00**	**0.17**	**5**	**0.85**	14.43	16.98
0.17	0.49	0.16	**0.33**	10	3.34	43.49	13.01
0.17	0.60	0.28	**0.45**	11	4.92	58.89	11.97
0.17	0.71	0.38	**0.55**	12	6.61	75.32	11.39
0.17	0.77	0.44	**0.61**	13	7.95	88.61	11.15
0.17	0.88	0.56	**0.73**	14	10.16	109.66	10.79
0.17	0.91	0.59	**0.76**	15	11.35	121.59	10.72
0.17	0.94	0.61	**0.78**	16	12.55	133.67	10.65
0.17	0.98	0.65	**0.82**	17	14.01	148.03	10.57
0.17	1.01	0.69	**0.86**	18	15.49	162.60	10.50
d	***d* (theory)**	**Δ*d***	**compensated *d***	***p***	***pd***	***U_b***	***E/p***
0.20				1	0.20	7.75	38.77
0.20				2	0.40	9.83	24.58
0.20				3	0.60	13.50	22.50
0.20				4	0.80	16.45	20.57
0.20				5	1.00	17.81	17.81
0.20				6	1.20	21.51	17.93
0.20	**0.41**	**0.00**	**0.20**	**7**	**1.40**	25.55	18.25
0.20	0.46	0.05	**0.25**	8	1.99	32.69	16.41
0.20	0.52	0.11	**0.31**	9	2.79	41.63	14.94
0.20	0.60	0.19	**0.39**	10	3.90	53.42	13.69
0.20	0.65	0.24	**0.44**	11	4.82	63.42	13.17
0.20	0.70	0.29	**0.49**	12	5.89	74.90	12.71
0.20	0.73	0.32	**0.52**	13	6.78	84.61	12.49
0.20	0.79	0.38	**0.58**	14	8.09	98.17	12.14
0.20	0.92	0.51	**0.71**	15	10.58	122.20	11.55
0.20	0.89	0.48	**0.68**	16	10.86	126.59	11.65
d	***d* (theory)**	**Δ*d***	**compensated *d***	***p***	***pd***	***U_b***	***E/p***
0.46				1	0.46	16.05	34.88
0.46				2	0.92	17.82	19.37
0.46				3	1.38	19.70	14.27
0.46				4	1.84	24.98	13.58
0.46				5	2.30	34.10	14.83
0.46				6	2.76	37.99	13.76
0.46	**0.72**	**0.00**	**0.46**	**7**	**3.22**	44.83	13.92
0.46	0.78	0.06	**0.52**	8	4.13	55.26	13.37
0.46	0.79	0.07	**0.53**	9	4.81	63.62	13.22
0.46	0.83	0.11	**0.57**	10	5.73	74.12	12.93
0.46	0.88	0.16	**0.62**	11	6.83	86.24	12.62
0.46	0.98	0.26	**0.72**	12	8.65	104.76	12.10
0.46	1.05	0.33	**0.79**	13	10.23	121.10	11.84
0.46	1.09	0.37	**0.83**	14	11.60	135.56	11.69
0.46	1.14	0.42	**0.88**	15	13.25	152.55	11.52
0.46	1.12	0.40	**0.86**	16	13.79	159.71	11.58
0.46	1.09	0.37	**0.83**	17	14.03	164.16	11.70
0.46	1.08	0.36	**0.82**	18	14.79	173.20	11.71
d	***d* (theory)**	**Δ*d***	**compensated *d***	***p***	***pd***	***U_b***	***E/p***
0.77				1	0.77	33.08	42.96
0.77				2	1.54	33.92	22.03
0.77				3	2.31	36.74	15.91
0.77				4	3.08	44.73	14.52
0.77				5	3.85	50.00	12.99
0.77				6	4.62	63.49	13.74
0.77				7	5.39	68.65	12.74
0.77				8	6.16	73.59	11.95
0.77				9	6.93	83.49	12.05
0.77	**0.83**	**0.00**	**0.77**	**10**	**7.70**	98.81	12.83
0.77	0.88	0.05	**0.82**	11	9.00	118.10	13.12
0.77	0.98	0.15	**0.92**	12	11.02	131.82	11.97
0.77	1.05	0.21	**0.98**	13	12.79	141.41	11.06
0.77	1.09	0.26	**1.03**	14	14.35	154.96	10.80
0.77	1.14	0.31	**1.08**	15	16.20	165.02	10.19

= reference

Table 6.5. *Compensated gap distance using linear gradient.*

d_0 [mm]	p [bar]	$d = 0.0546p + 0.05$	Compensated pd [bar·mm]	Measured U_b [kV]	E/p [kV/mm·bar]
0.17	5	0.32	1.62	14.43	8.94
0.17	10	0.60	5.96	43.49	7.30
0.17	11	0.65	7.16	58.89	8.23
0.17	12	0.71	8.46	75.32	8.90
0.17	13	0.76	9.88	88.61	8.97
0.17	14	0.81	11.40	109.66	9.62
0.17	15	0.87	13.04	121.59	9.33
0.17	16	0.92	14.78	133.67	9.05
0.17	17	0.98	16.63	148.03	8.90
0.17	18	1.03	18.59	162.60	8.75
d_0	p	$d = 0.051p + 0.0866$	pd	U_b	E/p
0.2	1	0.14	0.14	7.75	56.35
0.2	2	0.19	0.38	9.83	26.07
0.2	3	0.24	0.72	13.50	18.78
0.2	4	0.29	1.16	16.45	14.15
0.2	5	0.34	1.71	17.81	10.43
0.2	6	0.39	2.36	21.51	9.13
0.2	7	0.44	3.11	25.55	8.23
0.2	8	0.49	3.96	32.69	8.26
0.2	9	0.55	4.91	41.63	8.48
0.2	10	0.60	5.97	53.42	8.95
0.2	11	0.65	7.12	63.42	8.90
0.2	12	0.70	8.38	74.90	8.93
0.2	13	0.75	9.74	84.61	8.68
0.2	14	0.80	11.21	98.17	8.76
0.2	15	0.85	12.77	122.20	9.57
0.2	16	0.90	14.44	126.59	8.77
d_0	p	$d = 0.0395p + 0.4693$	pd	U_b	E/p
0.46	1	0.51	0.51	16.05	31.54
0.46	2	0.55	1.10	17.82	16.25
0.46	3	0.59	1.76	19.70	11.17
0.46	4	0.63	2.51	24.98	9.96
0.46	5	0.67	3.33	34.10	10.23
0.46	6	0.71	4.24	37.99	8.96
0.46	7	0.75	5.22	44.83	8.59
0.46	8	0.79	6.28	55.26	8.80
0.46	9	0.82	7.42	63.62	8.57
0.46	10	0.86	8.64	74.12	8.58
0.46	11	0.90	9.94	86.24	8.67
0.46	12	0.94	11.32	104.76	9.25
0.46	13	0.98	12.78	121.10	9.48
0.46	14	1.02	14.31	135.56	9.47
0.46	15	1.06	15.93	152.55	9.58
0.46	16	1.10	17.62	159.71	9.06
0.46	17	1.14	19.39	164.16	8.46
0.46	18	1.18	21.25	173.20	8.15
d_0	p	$d = 0.0332p + 0.7843$	pd	U_b	E/p
0.77	1	0.82	0.82	33.08	40.46
0.77	2	0.85	1.70	33.92	19.94
0.77	3	0.88	2.65	36.74	13.86
0.77	4	0.92	3.67	44.73	12.19
0.77	5	0.95	4.75	50.00	10.52
0.77	6	0.98	5.90	63.49	10.76
0.77	7	1.02	7.12	68.65	9.65
0.77	8	1.05	8.40	73.59	8.76
0.77	9	1.08	9.75	83.49	8.57
0.77	10	1.12	11.16	98.81	8.85
0.77	11	1.15	12.64	118.10	9.34
0.77	12	1.18	14.19	131.82	9.29
0.77	13	1.22	15.81	141.41	8.95
0.77	14	1.25	17.49	154.96	8.86
0.77	15	1.28	19.23	165.02	8.58

Table 6.5.1. *Compensated gap distance based on measurements.*

d_0 [mm]	p [bar]	measured d [mm]	Compensated pd [bar·mm]	Measured U_b [kV]	E/p [kV/mm·bar]
0.17	5	0.29	1.46	14.43	9.85
0.17	10	0.64	6.45	43.49	6.74
0.17	11	0.73	7.99	58.89	7.37
0.17	12	0.81	9.70	75.32	7.77
0.17	13	0.89	11.54	88.61	7.68
0.17	14	0.96	13.51	109.66	8.12
0.17	15	1.04	15.57	121.59	7.81
0.17	16	1.11	17.72	133.67	7.55
0.17	17	1.17	19.91	148.03	7.43
0.17	18	1.23	22.14	162.60	7.34
d_0	p	d	pd	U_b	E/p
0.2	1	0.21	0.21	7.75	37.59
0.2	2	0.22	0.44	9.83	22.54
0.2	3	0.24	0.72	13.50	18.64
0.2	4	0.28	1.11	16.45	14.87
0.2	5	0.32	1.61	17.81	11.03
0.2	6	0.38	2.28	21.51	9.44
0.2	7	0.45	3.12	25.55	8.20
0.2	8	0.52	4.14	32.69	7.90
0.2	9	0.59	5.35	41.63	7.78
0.2	10	0.67	6.75	53.42	7.91
0.2	11	0.76	8.32	63.42	7.62
0.2	12	0.84	10.06	74.90	7.45
0.2	13	0.92	11.93	84.61	7.09
0.2	14	0.99	13.93	98.17	7.05
0.2	15	1.07	16.02	122.20	7.63
0.2	16	1.14	18.20	126.59	6.96
d_0	p	d	pd	U_b	E/p
0.46	1	0.47	0.47	16.05	34.43
0.46	2	0.48	0.96	17.82	18.64
0.46	3	0.50	1.50	19.70	13.10
0.46	4	0.54	2.15	24.98	11.64
0.46	5	0.58	2.91	34.10	11.70
0.46	6	0.64	3.84	37.99	9.90
0.46	7	0.71	4.94	44.83	9.08
0.46	8	0.78	6.22	55.26	8.89
0.46	9	0.85	7.69	63.62	8.27
0.46	10	0.93	9.35	74.12	7.93
0.46	11	1.02	11.18	86.24	7.71
0.46	12	1.10	13.18	104.76	7.95
0.46	13	1.18	15.31	121.10	7.91
0.46	14	1.25	17.57	135.56	7.72
0.46	15	1.33	19.92	152.55	7.66
0.46	16	1.40	22.36	159.71	7.14
0.46	17	1.46	24.84	164.16	6.61
0.46	18	1.52	27.36	173.20	6.33
d_0	p	d	pd	U_b	E/p
0.77	1	0.78	0.78	33.08	42.62
0.77	2	0.79	1.58	33.92	21.52
0.77	3	0.81	2.43	36.74	15.09
0.77	4	0.85	3.39	44.73	13.21
0.77	5	0.89	4.46	50.00	11.20
0.77	6	0.95	5.70	63.49	11.14
0.77	7	1.02	7.11	68.65	9.66
0.77	8	1.09	8.70	73.59	8.46
0.77	9	1.16	10.48	83.49	7.97
0.77	10	1.24	12.45	98.81	7.94
0.77	11	1.33	14.59	118.10	8.09
0.77	12	1.41	16.90	131.82	7.80
0.77	13	1.49	19.34	141.41	7.31
0.77	14	1.56	21.91	154.96	7.07
0.77	15	1.64	24.57	165.02	6.72

Appendix 2 – Four-Boundary Analysis

In the following analysis, it is assumed that the homogeneous plane on the tip of the electrode is not ideally coupled with its 2 mm curvature. Figure 124 depicts the case where the plane region is not ideally flat (not exactly 90° to the center y-axis). This case assumes that the plane (at an angle of $\theta_1 = 89.90°$) is coupled with the curvature at a slight angle of 1.35° (making the onset of the curvature at an angle of $\theta_2 = 88.55°$ relative to the center y-axis). Using equation (5.1) from Section 5.3.2, the impedance of the plane area $Z_0 = 1.047 \approx 1\ \Omega$ and the onset of the curvature impedance $Z_1 = 1.519 \approx 1.5\ \Omega$.

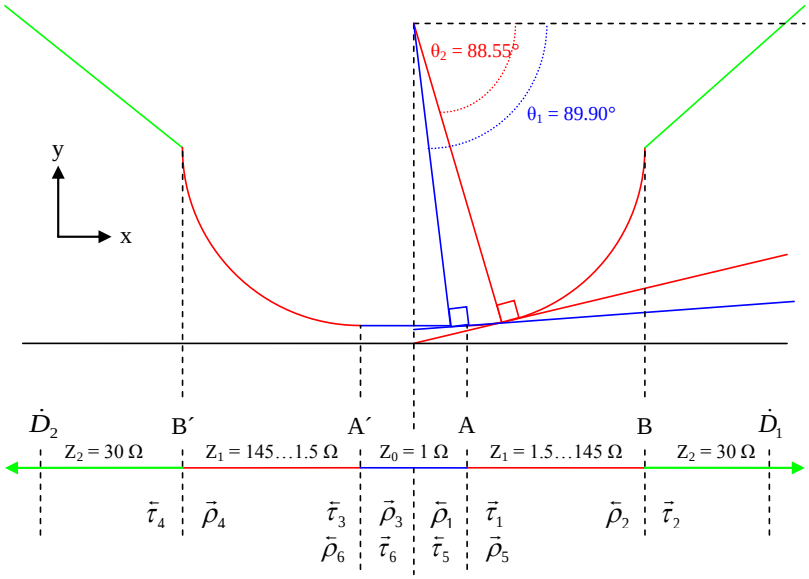

Figure 124. *Non-ideality of the electrode tip. Note: angle in figure is exaggerated.*

Now there are four impendence discontinuity boundaries along the transmission line labeled as A, A´, B and B´. The respective reflection and transmission coefficients for each boundary are shown in Table 1.

Table 1. *Reflection and transmission coefficients of the Four-Boundary Analysis.*

Boundary	Transition	$Z_1[\Omega]$	$Z_2[\Omega]$	τ	ρ
A	$Z_0 \Rightarrow Z_1$ = $Z_1 \Rightarrow Z_0$	1 ⇨ 1.5	1.5 ⇨ 1	$\vec{\tau}_1 = 1.2$ $\overleftarrow{\tau}_5 = 0.8$	$\overleftarrow{\rho}_1 = 0.2$ $\vec{\rho}_5 = -0.2$
B	$Z_1 \Rightarrow Z_2$ =	145 ⇨	30	$\vec{\tau}_2 = 0.34$	$\overleftarrow{\rho}_2 = -0.66$
A´	$Z_0 \Rightarrow Z_1$ = $Z_1 \Rightarrow Z_0$	1 ⇨ 1.5	1.5 ⇨ 1	$\overleftarrow{\tau}_3 = 1.2$ $\vec{\tau}_6 = 0.8$	$\vec{\rho}_3 = 0.2$ $\overleftarrow{\rho}_6 = -0.2$
B´	$Z_1 \Rightarrow Z_2$ =	145 ⇨	30	$\overleftarrow{\tau}_4 = 0.34$	$\vec{\rho}_4 = -0.66$

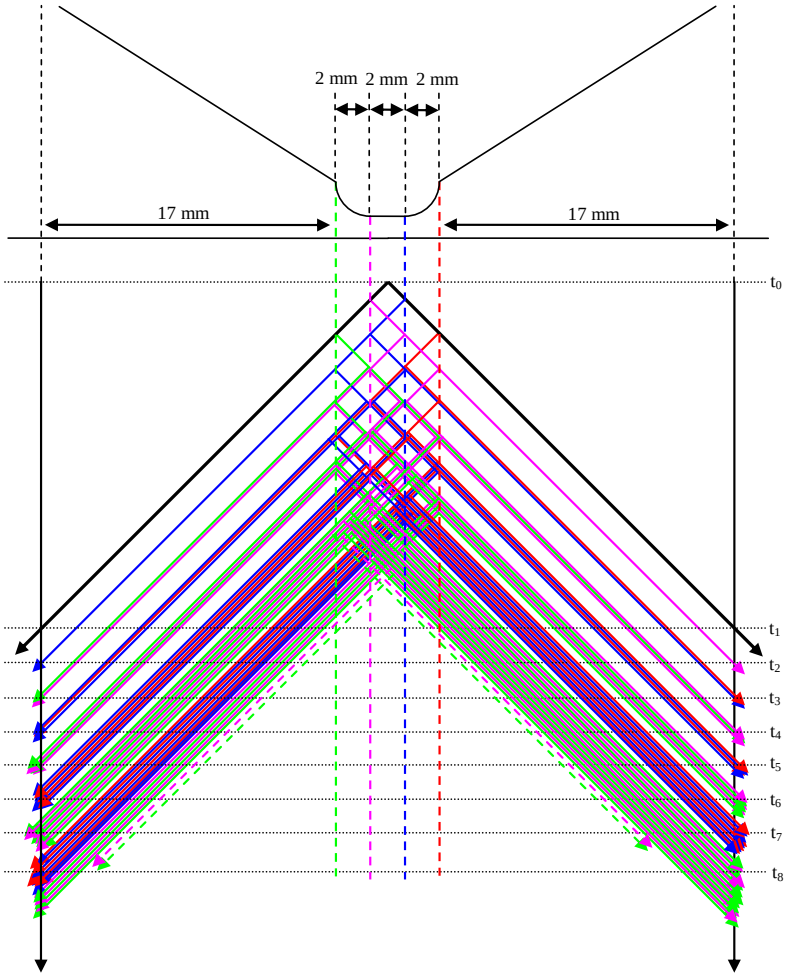

Figure 125. *Lattice diagram visualizing the summation of reflections from four boundaries. Note: not all reflections are shown in the figure.*

As is evident from Figure 125, the additional boundaries lead to a rapid accumulation of propagating signals reflecting and attenuating along the transmission line. Approximately 40 ps after the initial pulse arrives at the sensor 13 reflected signals of varying polarity and amplitude are superimposed onto the original pulse. Corresponding time periods and respective amplitudes are shown in Table 2. These four-boundary amplitude coefficients and propagation time periods are utilized to model waveforms observed by the *D*-dot sensors for symmetrical inputs of varying durations as shown in Figure 126.

Table 2. *Reflections from four boundaries.*

t_i [ps]		$\dot{D}(t_i)$	
t_0	0	0	0
t_1	66.6	$\tau_1 \tau_2$	0.4080
t_2	73.3	$\rho_3 \tau_1 \tau_2 = \rho_1 \tau_1 \tau_2$	0.0816
t_3	79.9	$\rho_1 \rho_3 \tau_1 \tau_2 + \rho_2 \rho_5 \tau_1 \tau_2 = [(\rho_1)^2 + \rho_2 \rho_6] \tau_1 \tau_2$	0.0702
t_4	86.3	$\rho_4 \tau_1 \tau_2 \tau_3 \tau_6 + \rho_3 \rho_1 \rho_3 \tau_1 \tau_2 + \rho_3 \rho_2 \rho_5 \tau_1 \tau_2$ $= [(\rho_1)^3 + \rho_2 (\rho_6 \rho_1 + \tau_1 \tau_6)] \tau_1 \tau_2$	-0.2445
t_5	92.9	$\rho_1 \rho_4 \tau_1 \tau_2 \tau_3 \tau_6 + \rho_1 \rho_3 \rho_1 \rho_3 \tau_1 \tau_2 + \rho_1 \rho_3 \rho_2 \rho_5 \tau_1 \tau_2 + \rho_2 \rho_3 \tau_1 \tau_5 \tau_1 \tau_2 +$ $\rho_2 \rho_5 \rho_2 \rho_5 \tau_1 \tau_2$ $= [(\rho_1)^4 + (\rho_1)^2 \rho_2 \rho_6 + 2(\rho_1 \rho_2 \tau_1 \tau_6) + (\rho_2)^2 (\rho_6)^2] \tau_1 \tau_2$	-0.0935
t_6	99.5	$\tau_3 \rho_4 \tau_6 \tau_1 \rho_2 \rho_5 \tau_2 + \tau_3 \rho_4 \tau_3 \rho_1 \rho_3 \tau_1 \tau_2 + \tau_3 \rho_4 \rho_6 \rho_4 \tau_6 \tau_1 \tau_2 +$ $\rho_3 \rho_1 \tau_3 \rho_4 \tau_6 \tau_1 \tau_2 + \rho_3 \rho_1 \rho_3 \tau_1 \rho_2 \rho_5 \tau_2 + \rho_3 \rho_1 \rho_3 \rho_1 \rho_3 \tau_1 \tau_2 +$ $\rho_3 \rho_2 \rho_5 \rho_2 \rho_5 \tau_1 \tau_2 + \rho_3 \tau_1 \rho_2 \tau_5 \rho_3 \tau_1 \tau_2$ $= [(\rho_1)^5 + (\rho_1)^3 \rho_2 \rho_6 + 3[(\rho_1)^3 \rho_2 \tau_1 \tau_6] + 2[(\rho_2)^2 \rho_6 \tau_1 \tau_6] + (\rho_2)^2 (\rho_6)^2 \rho_1] \tau_1 \tau_2$	-0.0844
t_7	106.1	$\rho_1 \rho_3 \rho_1 \tau_3 \rho_4 \tau_6 \tau_1 \tau_2 + \rho_1 \tau_3 \rho_4 \rho_6 \rho_4 \tau_6 \tau_1 \tau_2 + \rho_1 \tau_3 \rho_4 \tau_6 \tau_1 \rho_2 \rho_5 \tau_2 +$ $\rho_1 \tau_3 \rho_4 \tau_6 \rho_1 \rho_3 \tau_1 \tau_2 + \rho_1 \rho_3 \rho_1 \rho_3 \rho_1 \rho_3 \tau_1 \tau_2 + \rho_1 \rho_3 \tau_1 \rho_2 \rho_5 \rho_2 \rho_5 \tau_2 +$ $\rho_1 \rho_3 \tau_1 \rho_2 \tau_5 \rho_3 \tau_1 \tau_2 + \rho_1 \rho_3 \rho_1 \rho_3 \tau_1 \rho_2 \rho_5 \tau_2 + \tau_1 \rho_2 \tau_5 \tau_3 \rho_4 \tau_6 \tau_1 \tau_2 +$ $\tau_1 \rho_2 \tau_5 \rho_3 \rho_1 \rho_3 \tau_1 \tau_2 + \tau_1 \rho_2 \tau_5 \rho_3 \tau_1 \rho_2 \rho_5 \tau_2 + \tau_1 \rho_2 \rho_5 \rho_2 \tau_5 \rho_3 \tau_1 \tau_2 +$ $\tau_1 \rho_2 \rho_5 \rho_2 \rho_5 \rho_2 \rho_5 \tau_2$ $= [(\rho_1)^6 + (\rho_1)^4 \rho_2 \rho_6 + (\rho_2)^3 (\rho_6)^3 + 4[(\rho_1)^3 \rho_2 \tau_1 \tau_6] + 4[(\rho_2)^2 \rho_1 \rho_6 \tau_1 \tau_6] +$ $(\rho_1)^2 (\rho_2)^2 (\rho_6)^2 + (\rho_2)^2 (\tau_1)^2 (\tau_6)^2] \tau_1 \tau_2$	0.15003
t_8	112.7	*Approximated*	0.0300
t_9	119.4		0.0260
t_{10}	126.0		-0.0950
t_{11}	132.7		-0.0360
t_{12}	139.3		-0.0320
t_{13}	146.0		0.0620
t_{14}	152.7		0.0120
t_{15}	159.3		0.0110
t_{16}	166.0		-0.0390

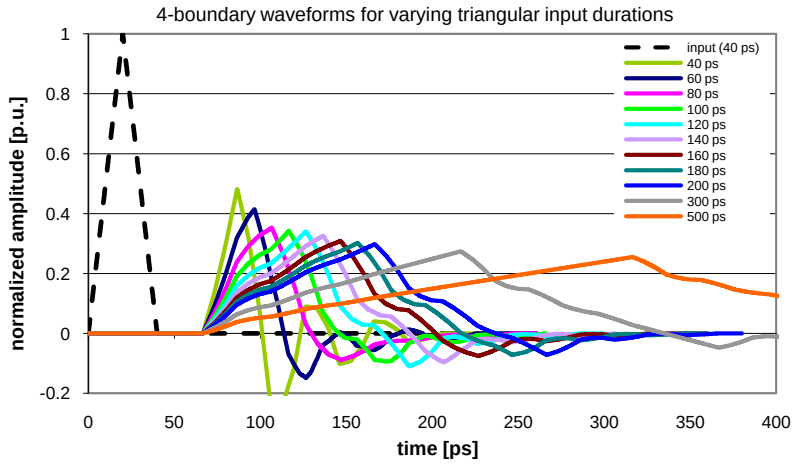

Figure 126. *Waveforms observed by the D-dot sensors for inputs reflecting from four boundaries.*

It is apparent that symmetrical triangular input pulses do not reproduce the measured waveforms. The rising front is a fairly good representation of observed signals. However, the falling tail does not have the appropriate time scale. Therefore, further analysis is required in order to determine the pulse shape of flashover in the gap which coincides with measured data from the sensors.

Appendix 3 – Side Flashover Analysis

To account for side flashover, the lattice diagram is modified to consider the impact of reflections occurring from such discharge (Figure 127). This analysis studies how the closest sensor to the discharge site ($\dot{D}_1$) will record a different waveform than the farthest sensor ($\dot{D}_2$). Amplitudes and reflection periods for each sensor are given in Table 3 and Table 4.

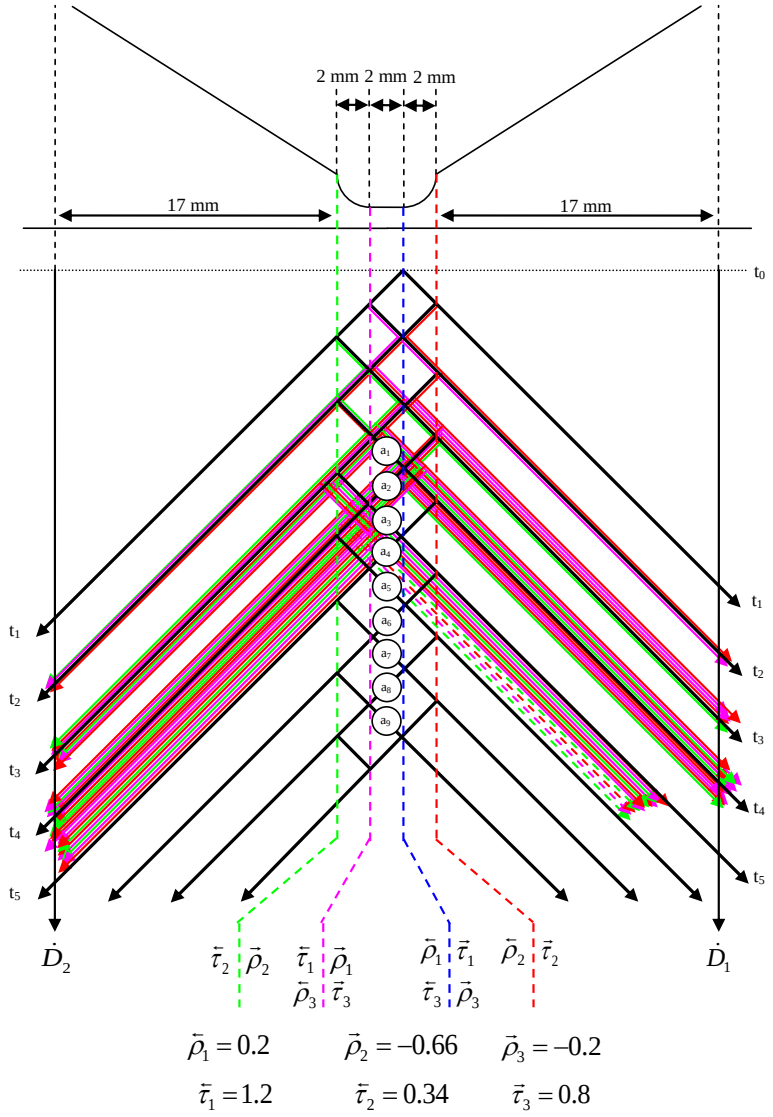

Figure 127. *Lattice diagram for side flashover (flashover along dashed blue line).*

Table 3. *Reflection amplitudes for closest sensor.*

t_i [ps]		$\dot{D}_1(t_i)$	
t_0	0	0	0
t_1	63.3	τ_2	0.3400
t_2	76.3	$\rho_1\tau_1\tau_2 + \rho_2\rho_3\tau_2$ = $[\rho_1\tau_1 + \rho_2\rho_3]\,\tau_2$	0.1265
t_3	89.9	$(\rho_2)^2(\rho_3)^2\tau_2 + \rho_1\rho_2\rho_3\tau_1\tau_2 + (\rho_1)^3\tau_1\tau_2 + \rho_1\rho_2\tau_1\tau_2\tau_3 + \rho_2(\tau_1)^2\tau_2\tau_3$ = $[(\rho_1)^3\tau_1 + (\rho_2)^2(\rho_3)^2 + \rho_1\rho_2\tau_1(\rho_3 + \tau_3) + \rho_2(\tau_1)^2\tau_3]\,\tau_2$	-0.2816
t_4	103.2	$(\rho_2)^3(\rho_3)^3\tau_2 + (\rho_2)^2(\rho_3)^2\rho_1\tau_1\tau_2 + (\tau_1)^2(\rho_2)^2\rho_3\tau_3\tau_2$ $+ (\rho_2)^2\rho_1\rho_3\tau_1\tau_3\tau_2 + (\rho_1)^2(\tau_1)^2\rho_2\tau_3\tau_2 + (\rho_1)^2(\tau_1)^2\rho_2\tau_3\tau_2$ $+ (\rho_1)^3\rho_2\rho_3\tau_1\tau_2 + (\rho_2)^2\rho_1\rho_3\tau_1\tau_3\tau_2 + (\rho_1)^3\rho_2\tau_1\tau_3\tau_2$ $+ (\rho_1)^5\tau_1\tau_2 + (\rho_1)^2(\tau_1)^2\rho_2\tau_3\tau_2 + (\rho_2)^2(\tau_1)^2(\tau_3)^2\tau_2$ $+ (\rho_2)^2(\tau_1)^2\,\rho_3\tau_3\tau_2$ = $[(\rho_1)^5\tau_1 + (\rho_2)^3(\rho_3)^3 + (\rho_1)^3\rho_2\tau_1(\rho_3 + \tau_3) + 3(\rho_1)^2(\tau_1)^2\rho_2\tau_3$ $+ 2(\rho_2)^2(\tau_1)^2\,\rho_3\tau_3 + 2(\rho_2)^2\rho_1\rho_3\tau_1\tau_3 + (\rho_2)^2(\tau_1)^2(\tau_3)^2$ $+ (\rho_2)^2(\rho_3)^2\rho_1\tau_1]\,\tau_2$	0.0329
t_5	116.6	$\left(\dot{D}_1(t_4)\cdot\frac{\rho_2}{\tau_2}\rho_3 + \dot{D}_2(t_3)\cdot\frac{\rho_2}{\tau_2}\tau_1\tau_3 + a_2\rho_1\tau_1\right)\tau_2$	0.0976
t_6	129.9	$\left(\dot{D}_1(t_5)\cdot\frac{\rho_2}{\tau_2}\rho_3 + \dot{D}_2(t_4)\cdot\frac{\rho_2}{\tau_2}\tau_1\tau_3 + a_4\rho_1\tau_1\right)\tau_2$	-0.0968
t_7	143.2	$\left(\dot{D}_1(t_6)\cdot\frac{\rho_2}{\tau_2}\rho_3 + \dot{D}_2(t_5)\cdot\frac{\rho_2}{\tau_2}\tau_1\tau_3 + a_6\rho_1\tau_1\right)\tau_2$	-0.0423
t_8	156.5	$\left(\dot{D}_1(t_7)\cdot\frac{\rho_2}{\tau_2}\rho_3 + \dot{D}_2(t_6)\cdot\frac{\rho_2}{\tau_2}\tau_1\tau_3 + a_8\rho_1\tau_1\right)\tau_2$	0.0567
t_k	t_{k-1} + 13.33	$\left(\dot{D}_1(t_{k-1})\cdot\frac{\rho_2}{\tau_2}\rho_3 + \dot{D}_2(t_{k-2})\cdot\frac{\rho_2}{\tau_2}\tau_1\tau_3 + a_n\rho_1\tau_1\right)\tau_2$ $\begin{cases} n = 2k-8 > 1 \\ a_n = \dot{D}_1(t_{k-2})\frac{\rho_2}{\tau_2}\tau_3 + a_{n-1}\rho_1 \\ a_1 = 0.1570 \end{cases}$	

Table 4. *Reflection amplitudes for farthest sensor.*

t_i [ps]		$\dot{D}_2(t_i)$	
t_0	0	0	0
t_1	69.9	$\tau_1\,\tau_2$	0.4080
t_2	83.3	$\rho_2\tau_1\tau_2\tau_3 + (\rho_1)^2\tau_1\tau_2 + \rho_2\rho_3\tau_1\tau_2$ = $[(\rho_1)^2\tau_1 + \rho_2\tau_1(\rho_3 + \tau_3)]\,\tau_2$	-0.1453
t_3	96.6	$(\rho_1)^4\tau_1\tau_2 + (\rho_1)^2\rho_2\tau_1\tau_2\tau_3 + (\tau_1)^2\rho_1\rho_2\tau_2\tau_3 + (\rho_2)^2\rho_3\tau_1\tau_2\tau_3 + (\rho_2)^2(\rho_3)^2\tau_1\tau_2 + (\rho_1)^2\rho_2\rho_3\tau_1\tau_2 + (\rho_2)^2\rho_3\tau_1\tau_2\tau_3$ = $[(\rho_1)^4\tau_1 + (\rho_2)^2(\rho_3)^2\tau_1 + (\rho_1)^2\rho_2\tau_1(\rho_3 + \tau_3) + 2(\rho_2)^2\rho_3\tau_1\tau_3 + 2(\tau_1)^2\rho_1\rho_2\tau_3]\,\tau_2$	-0.0869
t_4	109.9	$[\,(\rho_1)^3(\tau_1)^2\rho_2\tau_3 + (\rho_2)^3(\rho_3)^2\tau_1\tau_3 + (\rho_2)^2(\tau_1)^2\rho_1\rho_3\tau_3 + (\rho_2)^2(\tau_1)^2(\tau_3)^2\rho_1 + (\rho_2)^2(\tau_1)^3(\tau_3)^2 + (\rho_1)^6\tau_1 + (\rho_1)^4\rho_2\tau_1\tau_3 + 2(\rho_1)^3(\tau_1)^2\rho_2\tau_3 + (\rho_1)^2(\rho_2)^2\rho_3\tau_1\tau_3 + (\rho_1)^3(\tau_1)^2\rho_2\tau_3 + (\rho_2)^2(\tau_1)^2\rho_1\rho_3\tau_3 + (\rho_2)^2(\tau_1)^2(\tau_3)^2\rho_1 + (\rho_2)^3(\rho_3)^2\tau_1\tau_3 + 2(\rho_2)^2(\tau_1)^2\rho_1\rho_3\tau_3 + (\rho_1)^2(\rho_2)^2\,\rho_3\tau_1\tau_3 + (\rho_1)^4\rho_2\rho_3\tau_1 + (\rho_2)^3(\rho_3)^3\tau_1 + (\rho_1)^2(\rho_2)^2(\rho_3)^2\tau_1 + (\rho_2)^3(\rho_3)^2\tau_1\tau_3]\,\tau_2$ = $[\,(\rho_1)^6\tau_1 + (\rho_2)^3(\rho_3)^3\tau_1 + (\rho_1)^4\rho_2\tau_1(\rho_3 + \tau_3) + 4(\rho_2)^2(\tau_1)^2\rho_1\rho_3\tau_3 + 4(\rho_1)^3(\tau_1)^2\rho_2\tau_3 + 3(\rho_2)^3(\rho_3)^2\tau_1\tau_3 + 2(\rho_2)^2(\tau_1)^2(\tau_3)^2\rho_1 + 2(\rho_1)^2(\rho_2)^2\,\rho_3\tau_1\tau_3 + (\rho_1)^2(\rho_2)^2(\rho_3)^2\tau_1 + (\rho_2)^2(\tau_1)^3(\tau_3)^2\,]\,\tau_2$	0.1703
t_5	123.2	$\left(\dot{D}_2(t_4)\cdot\frac{\rho_2}{\tau_2}\rho_3 + \dot{D}_1(t_4)\cdot\frac{\rho_2}{\tau_2}\tau_1\tau_3 + a_3\rho_1\tau_1\right)\tau_2$	0.0203
t_6	136.5	$\left(\dot{D}_2(t_5)\cdot\frac{\rho_2}{\tau_2}\rho_3 + \dot{D}_1(t_5)\cdot\frac{\rho_2}{\tau_2}\tau_1\tau_3 + a_5\rho_1\tau_1\right)\tau_2$	-0.0808
t_7	149.9	$\left(\dot{D}_2(t_6)\cdot\frac{\rho_2}{\tau_2}\rho_3 + \dot{D}_1(t_6)\cdot\frac{\rho_2}{\tau_2}\tau_1\tau_3 + a_7\rho_1\tau_1\right)\tau_2$	0.0448
t_8	163.2	$\left(\dot{D}_2(t_7)\cdot\frac{\rho_2}{\tau_2}\rho_3 + \dot{D}_1(t_7)\cdot\frac{\rho_2}{\tau_2}\tau_1\tau_3 + a_9\rho_1\tau_1\right)\tau_2$	0.0452
t_k	t_{k-1} + 13.33	$\left(\dot{D}_2(t_{k-1})\cdot\frac{\rho_2}{\tau_2}\rho_3 + \dot{D}_1(t_{k-2})\cdot\frac{\rho_2}{\tau_2}\tau_1\tau_3 + a_n\rho_1\tau_1\right)\tau_2$ $\begin{cases} n = 2k-7 > 1 \\ a_n = \dot{D}_2(t_{k-2})\frac{\rho_2}{\tau_2}\tau_3 + a_{n-1}\rho_1 \\ a_1 = 0.1570 \end{cases}$	

Appendix 4 – Side Flashover Coordinates

The side flashover analysis assumes that when flashover occurs on the curvature of the electrode, it is closest to one sensor ($d_1, \dot{D}_1$) while farthest from the opposite probe ($d_2, \dot{D}_2$) as shown in Figure 128 in black. Respective oscilloscopes for each sensor are also identified in the figure.

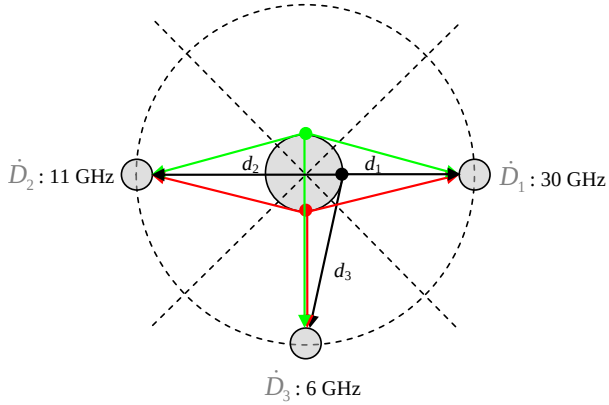

Figure 128. *Side flashover location.*

In this case, where $d_1 < d_3 < d_2$, flashover occurs closest to $\dot{D}_1$ and farthest from $\dot{D}_2$ and therefore enables the comparison of 30 GHz and 11 GHz measured data using the previously presented side reflection analysis (Appendix 3). As for the corresponding 6 GHz measurement, this case would be closest to a center flashover situation with some degree of variation since d_3 is slightly longer than 2 cm (distance from sensor to center). Consequently, measured waveforms should vary from each other as shown in Figure 129, where side flashover (blue) refers to measured 30 GHz and 11 GHz data, while center flashover (pink) refers to 6 GHz data.

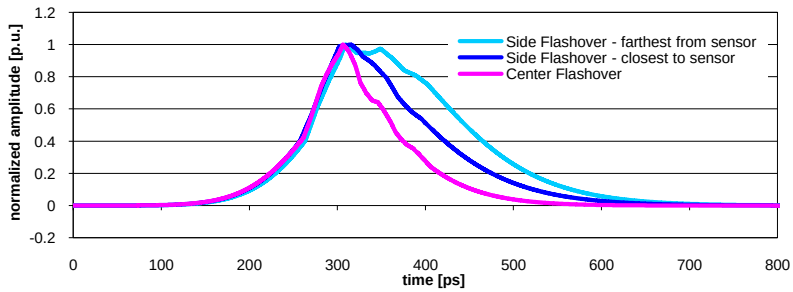

Figure 129. *Modeled side flashover waveforms.*

For the other two presented cases (red and green in Figure 128), distance between sensors $\dot{D}_1$ and $\dot{D}_2$ to the flashover point is equal, $d_1 = d_2$, while flashover in the gap occurs either closest or farthest from $\dot{D}_3$. Thus, 11 GHz and 30 GHz oscilloscopes should measure similar center flashover pulses while the 6 GHz oscilloscope measures one of the side flashover pulses (either closest or farthest). Next, these scenarios are related to measured data (Figure 130 - Figure 132).

Example of Center Flashover

All oscilloscopes measure similar wave shape. However, bandwidth and sampling limitations are evident as the time scale for each pulse is different.

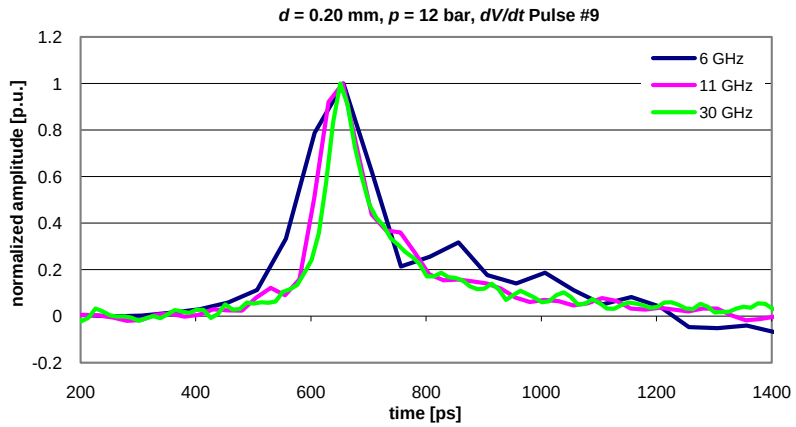

Figure 130. *Center flashover. D_1 = 30 GHz, D_2= 11 GHz, D_3= 6 GHz. Equal distance from flashover point to all probes.*

Example of Side Flashover (red/green case)

11 GHz and 30 GHz oscilloscopes measure a similar center flashover waveform, while the 6 GHz measures side flashover.

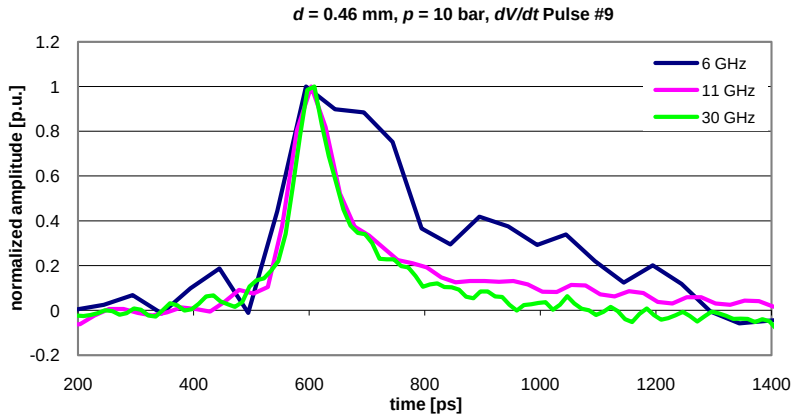

Figure 131. *Side flashover – red/green case. Equal distance from flashover point to 11 GHz and 30 GHz oscilloscope probes.*

Example of Side Flashover (black case)

11 GHz and 30 GHz oscilloscopes measure corresponding side flashover waveform as previously discussed for the "black" case (peak saturation and widening of pulse width), while the 6 GHz oscilloscope measures center flashover. In Figure 132, "30 GHz" represents side flashover closest to its sensor ($\dot{D}_1$) and "11 GHz" represents the farthest side flashover waveform ($\dot{D}_2$).

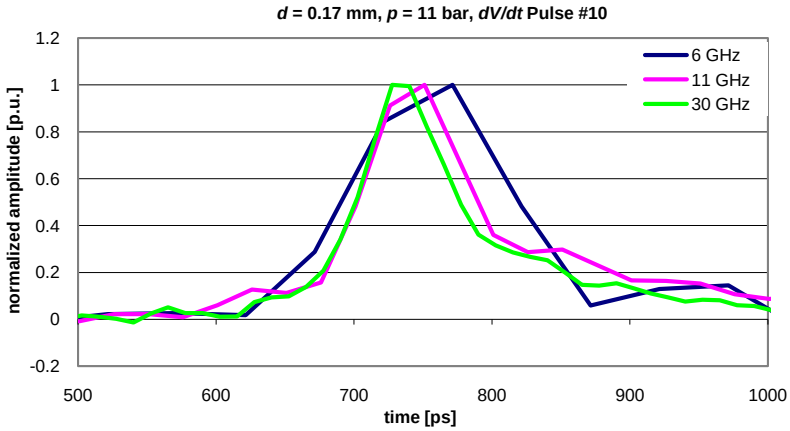

Figure 132. *Side flashover – black case.*

Note that it is impossible to observe an example of this case in practice, as it would require the 6 GHz oscilloscope to measure a faster pulse than the 30 GHz and 11 GHz oscilloscope. As is clearly evident, the bandwidth and sampling of the 6 GHz oscilloscope is not sufficient to capture a waveform representative of the situation depicted in Figure 129 (pink waveform, "Center Flashover") and as such, in Figure 132 the pulse width of the 6 GHz waveform exceeds that of the other measured signals.

The presented cases are ideal as they assume flashover always occurs closest to one sensor. However, there is no way of determining exactly how flashover was distributed along the electrode tip during measurements and which sensor was closest at that instant. From the photos (Figure 93) it is evident that side flashover is scattered along the curvature (some clustered together while others separate) and thus the measured waveform will differ somewhat from those presented in this side flashover analysis as distance fluctuates between flashover point and sensor. In addition, the limitation of bandwidth and sampling also plays a significant role in modifying the observed pulse shape and its dominance over reflections is uncertain. Nevertheless, the general trends (distinct peaks and variations in the falling tail of the *dV/dt* pulse) are observable despite these uncertainties.

Appendix 5 – Measured Waveforms

The following pages present all measured *dV/dt* waveforms along with their respective excitation impulses (applied voltage). Furthermore, integrals of cropped (solid lines) and line-fitted (dashed lines) *dV/dt* pulses are also shown when applicable.

Note:

d = 0.77 mm, p = 4 bar: Trigger level was selected poorly. Thus, the waveform recorded by the 6 GHz and the 30 GHz oscilloscopes is incomplete. 11 GHz oscilloscope captured entire signal.

d = 0.20 mm, p = 15 bar: The hardware measuring breakdown voltage failed. Breakdown voltage value was recorded from the frozen computer screen but applied voltage waveform could not be saved.

d = 0.17 mm, p = 5 bar

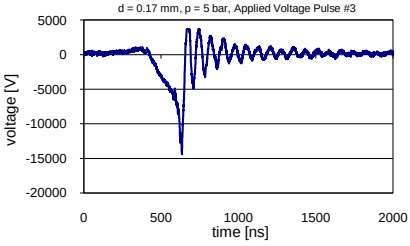

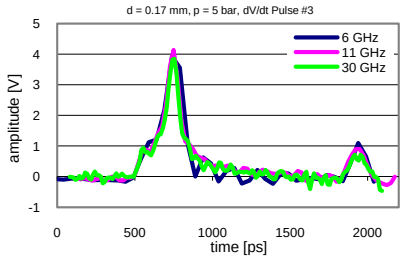

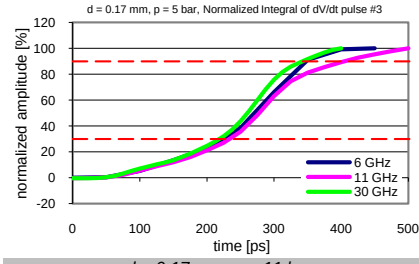

d = 0.17 mm, p = 10 bar

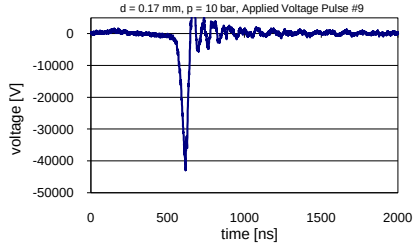

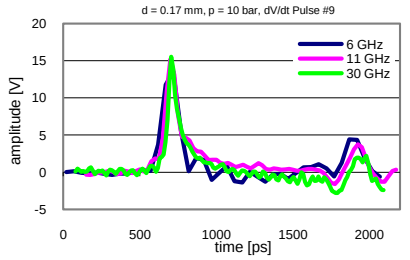

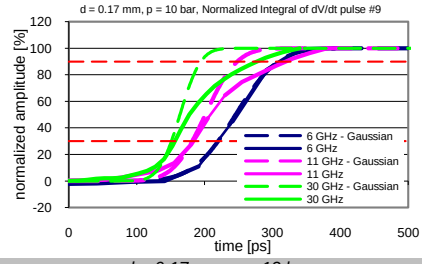

d = 0.17 mm, p = 11 bar

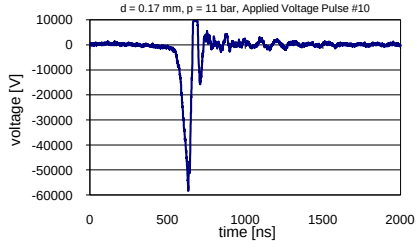

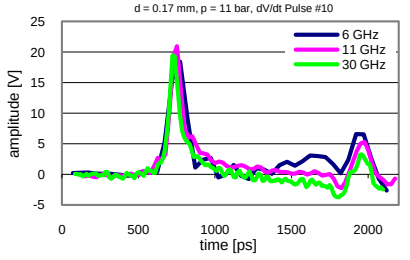

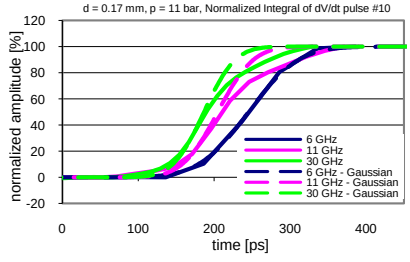

d = 0.17 mm, p = 12 bar

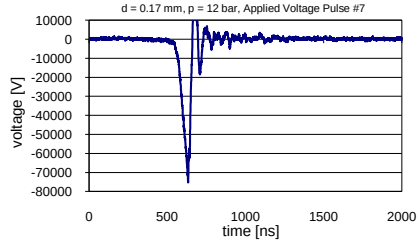

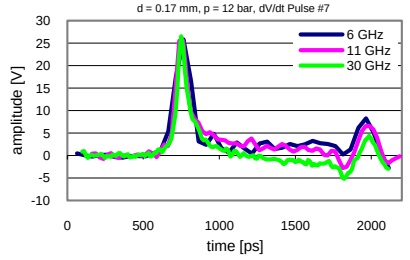

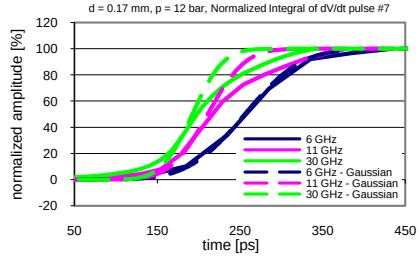

d = 0.17 mm, p = 13 bar

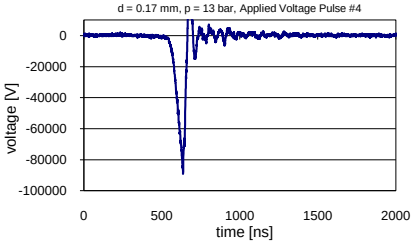

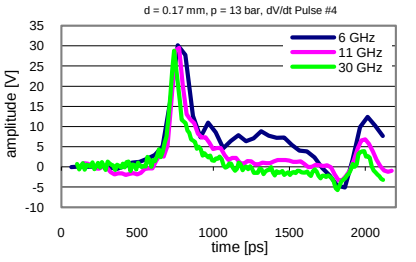

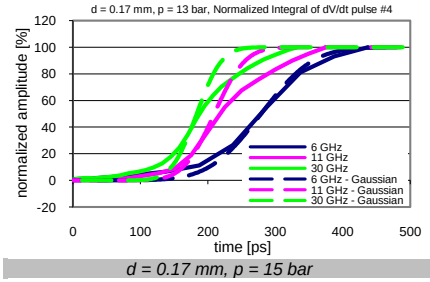

d = 0.17 mm, p = 14 bar

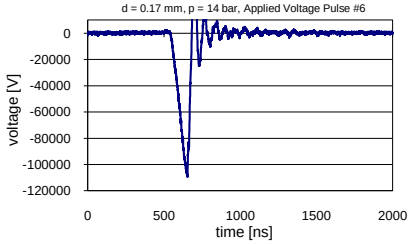

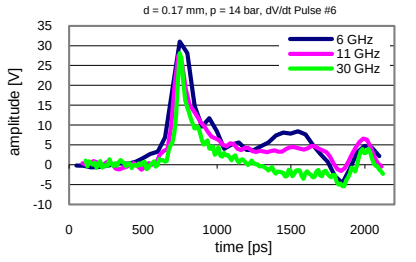

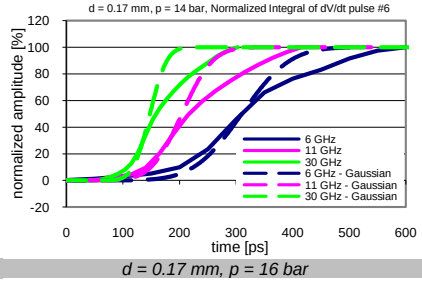

d = 0.17 mm, p = 15 bar

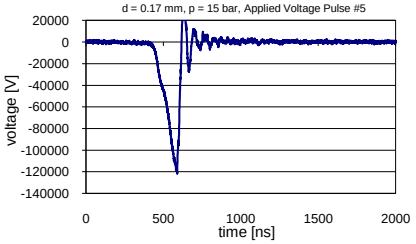

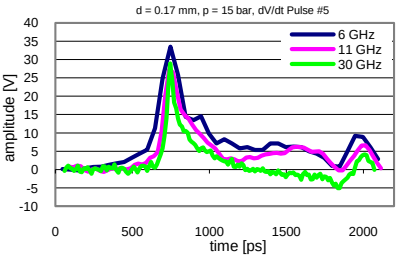

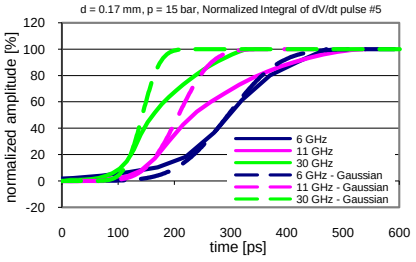

d = 0.17 mm, p = 16 bar

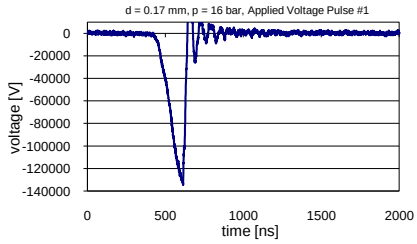

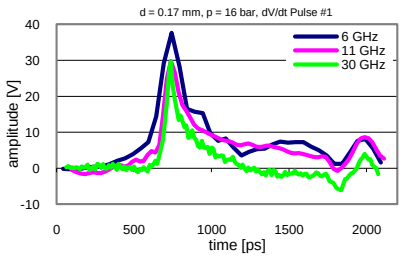

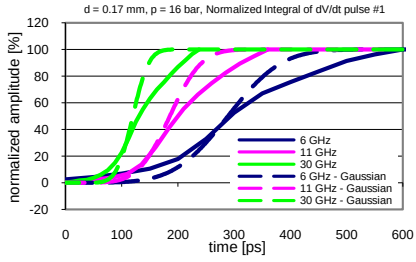

d = 0.17 mm, p = 17 bar

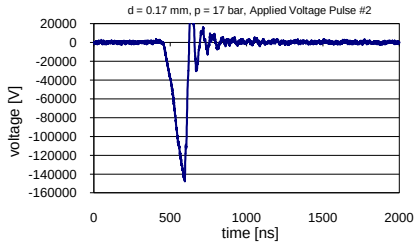

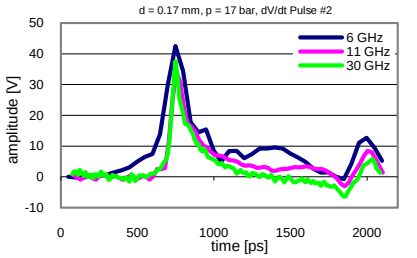

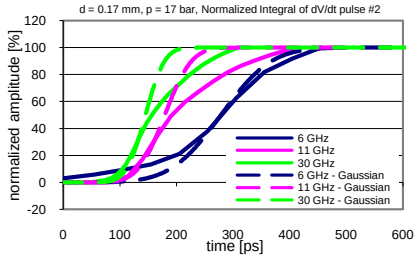

d = 0.17 mm, p = 18 bar

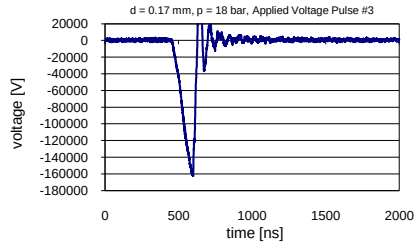

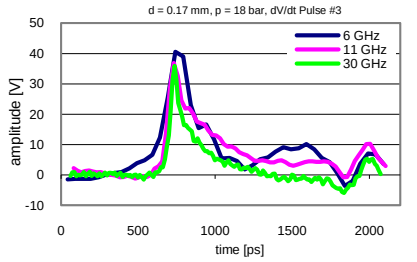

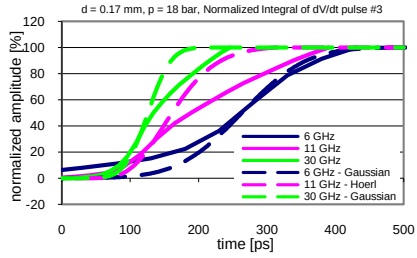

d = 0.20 mm, p = 1 bar

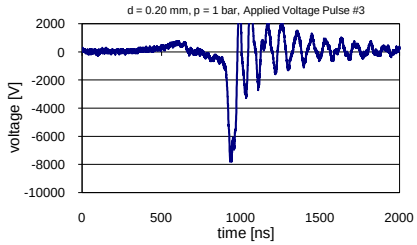

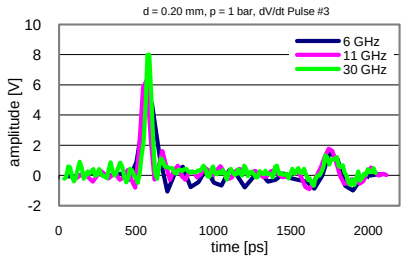

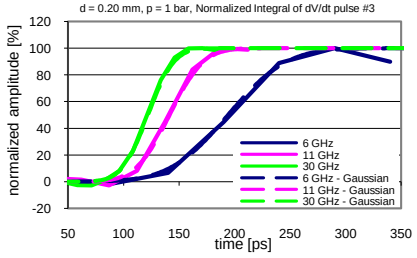

d = 0.20 mm, p = 2 bar

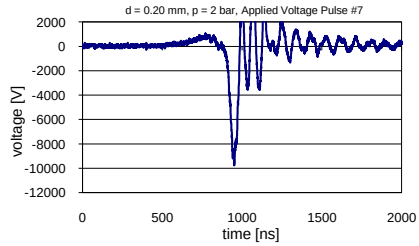

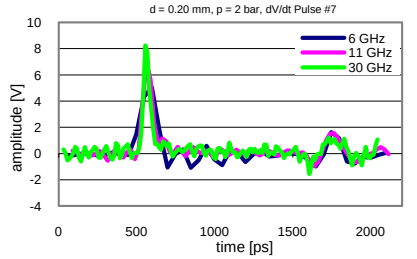

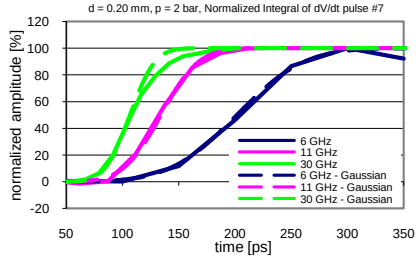

d = 0.20 mm, p = 3 bar

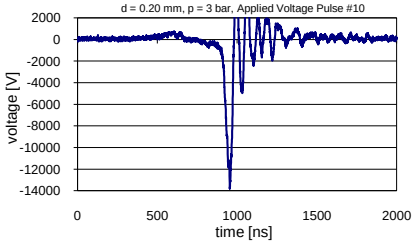

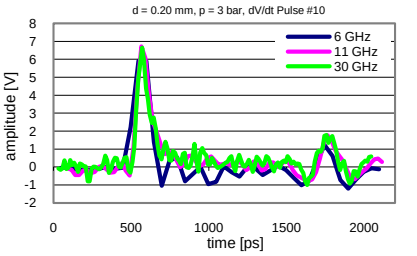

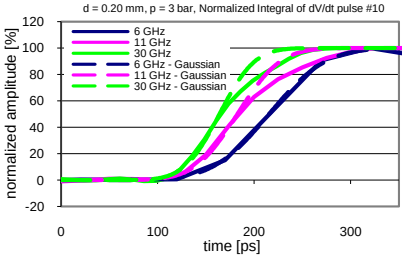

d = 0.20 mm, p = 4 bar

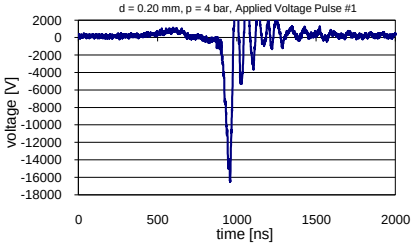

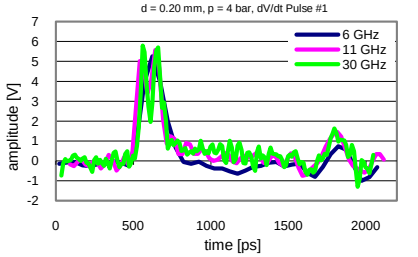

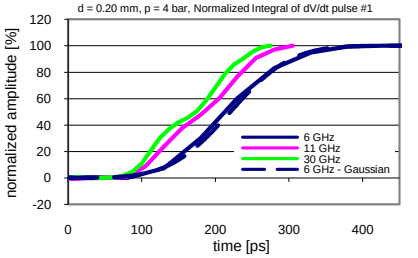

d = 0.20 mm, p = 5 bar

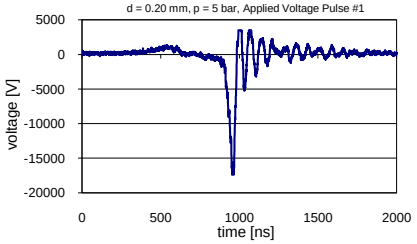

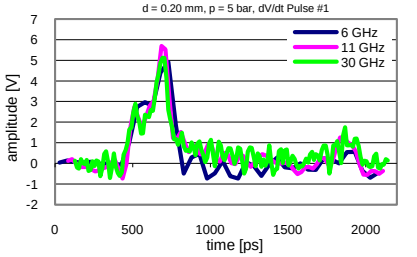

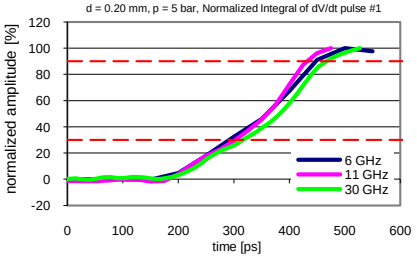

d = 0.20 mm, p = 6 bar

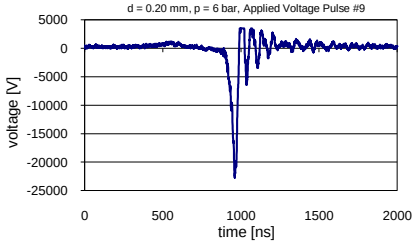

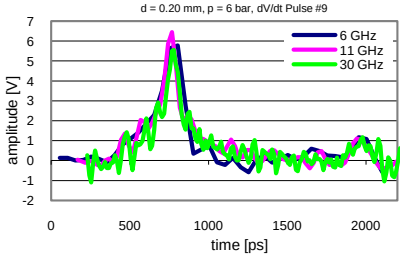

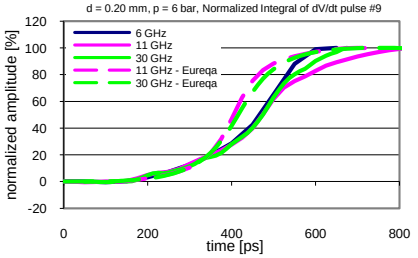

d = 0.20 mm, p = 7 bar

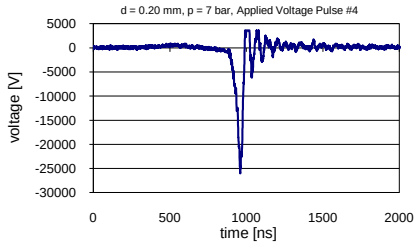

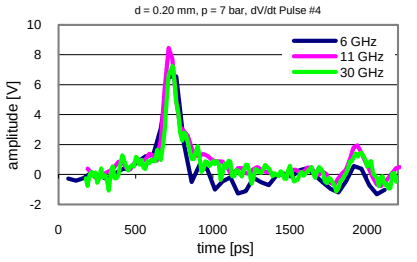

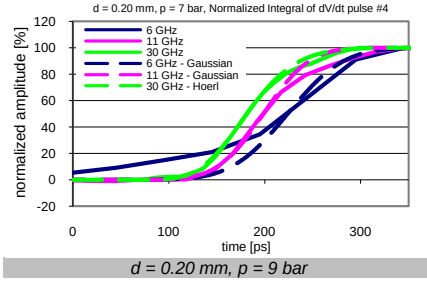

d = 0.20 mm, p = 8 bar

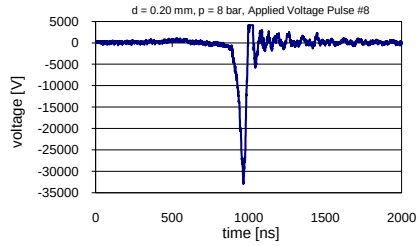

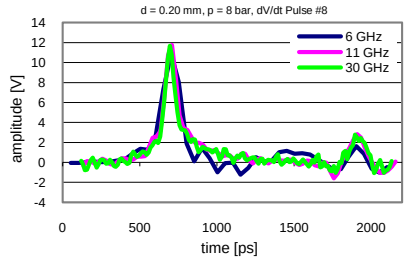

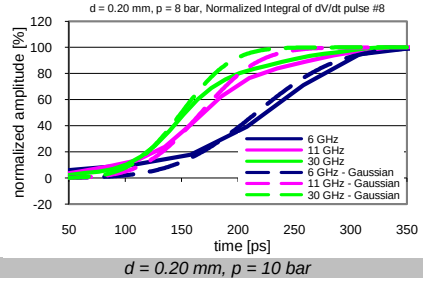

d = 0.20 mm, p = 9 bar

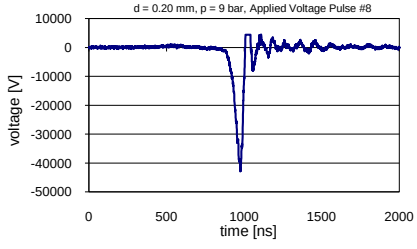

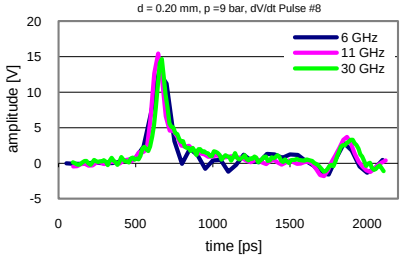

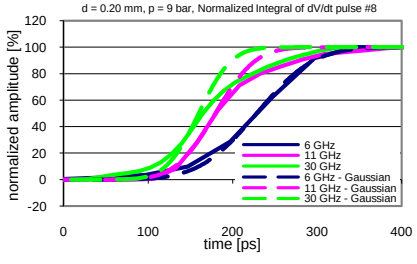

d = 0.20 mm, p = 10 bar

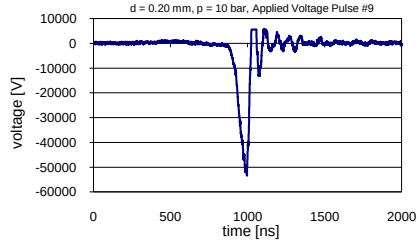

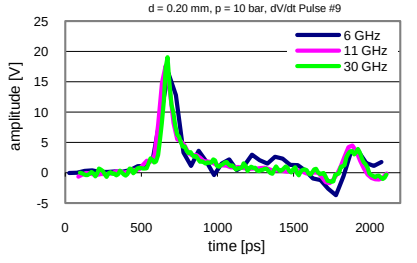

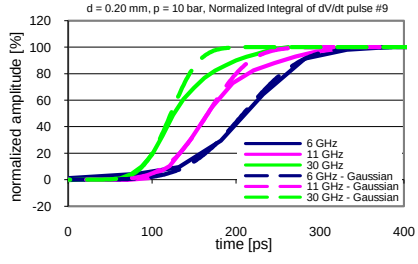

d = 0.20 mm, p = 11 bar

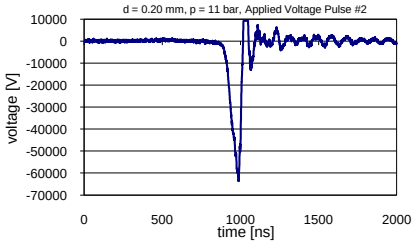

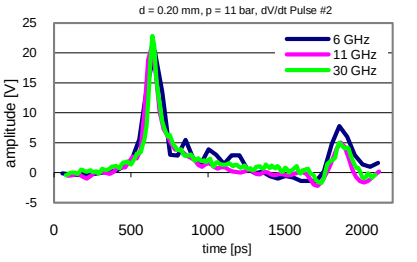

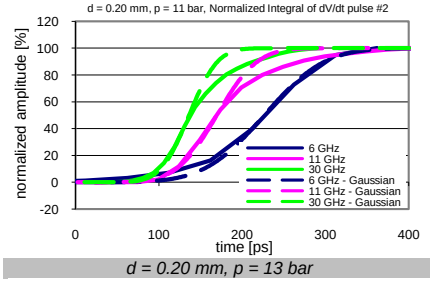

d = 0.20 mm, p = 12 bar

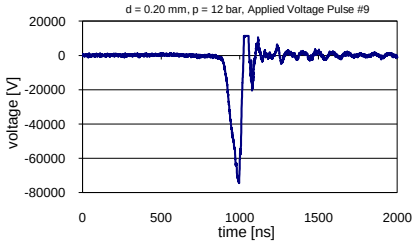

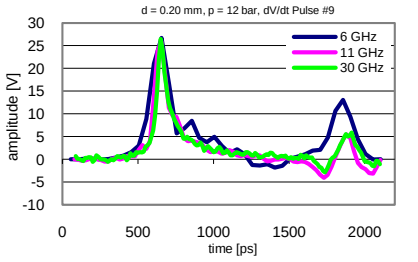

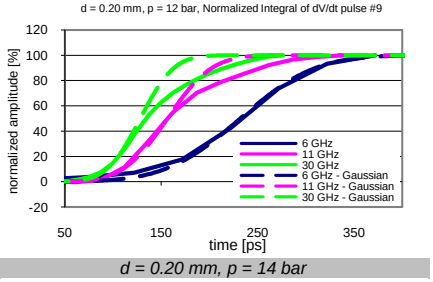

d = 0.20 mm, p = 13 bar

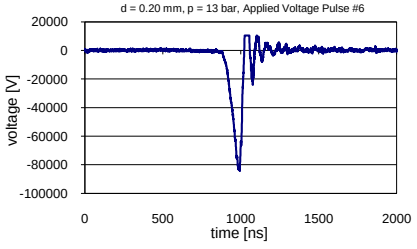

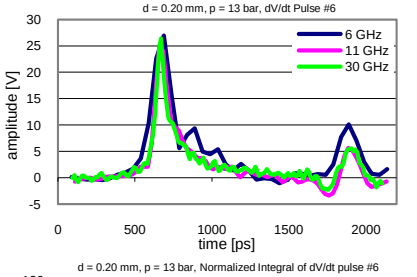

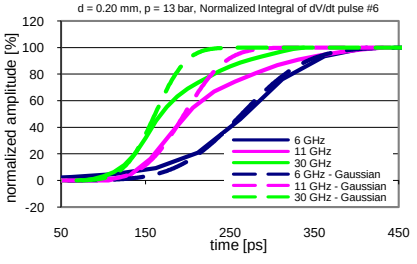

d = 0.20 mm, p = 14 bar

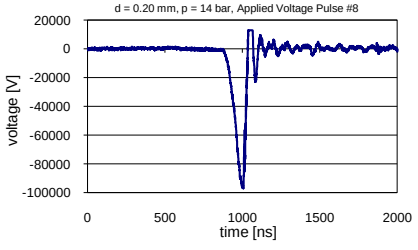

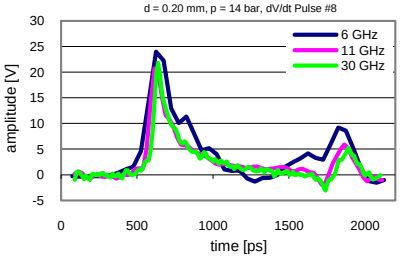

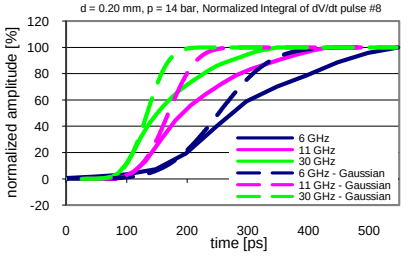

d = 0.20 mm, p = 15 bar

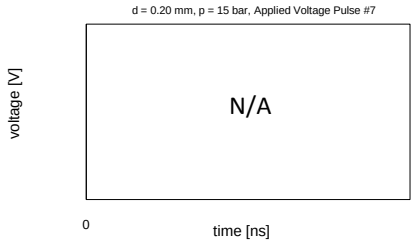

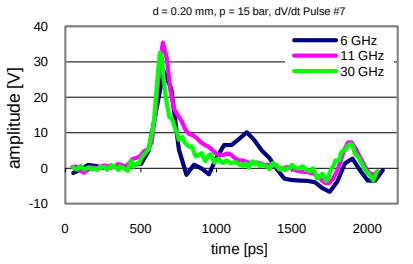

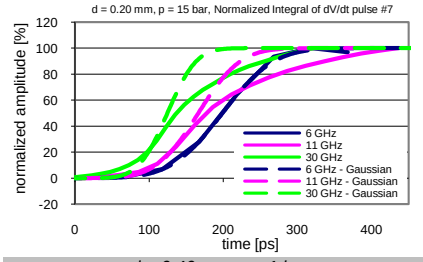

d = 0.20 mm, p = 16 bar

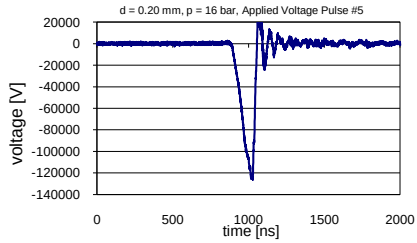

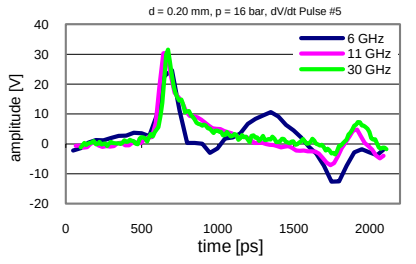

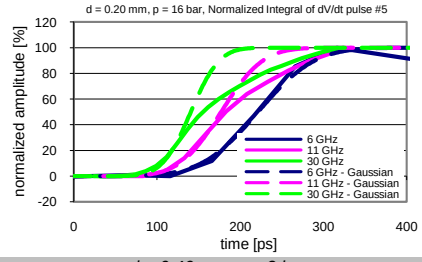

d = 0.46 mm, p = 1 bar

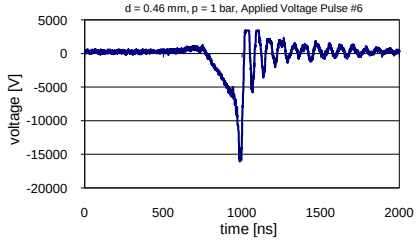

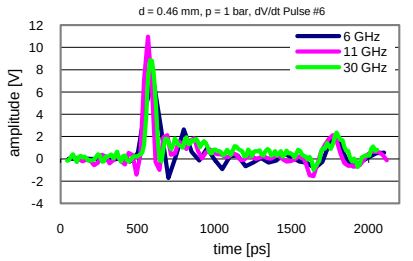

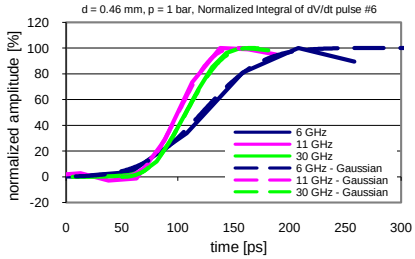

d = 0.46 mm, p = 2 bar

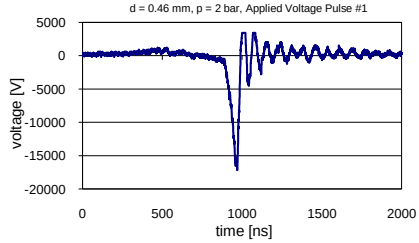

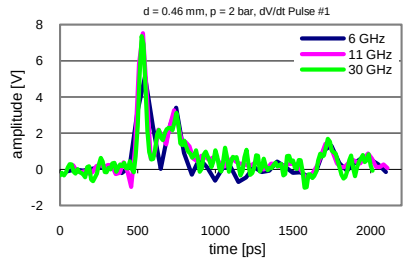

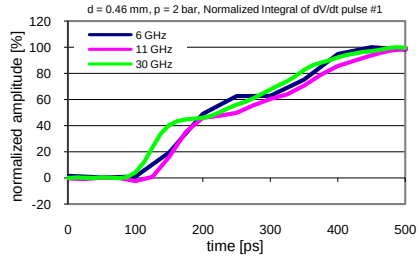

d = 0.46 mm, p = 3 bar

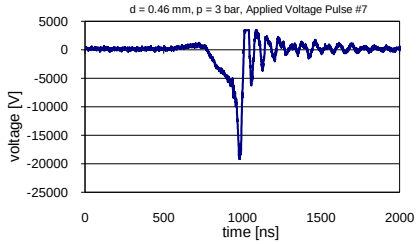

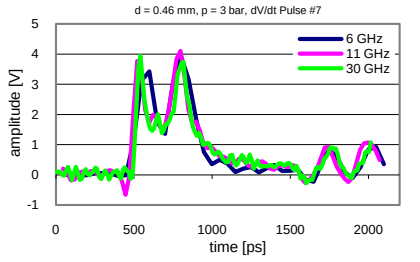

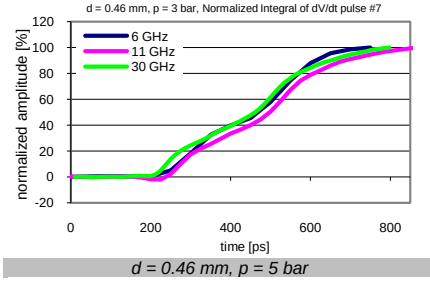

d = 0.46 mm, p = 4 bar

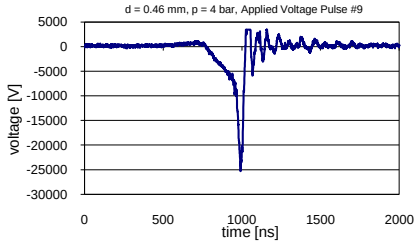

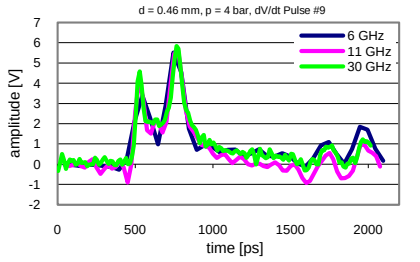

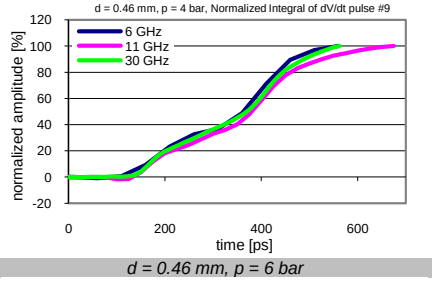

d = 0.46 mm, p = 5 bar

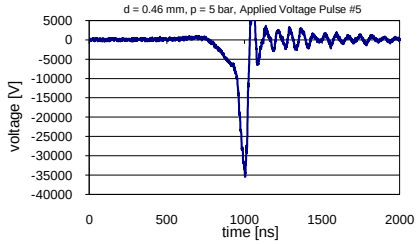

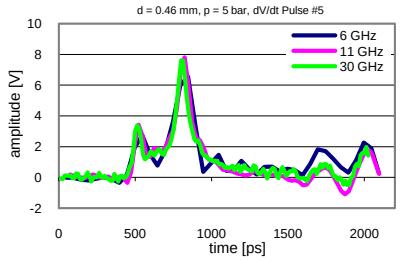

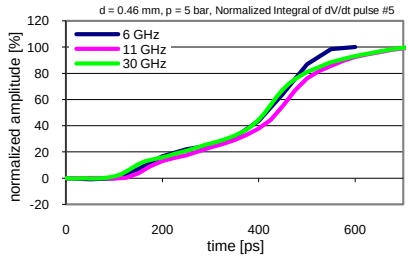

d = 0.46 mm, p = 6 bar

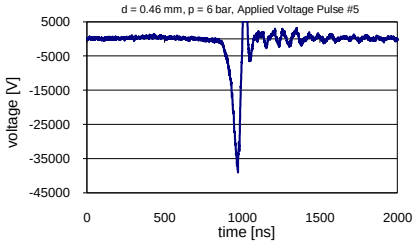

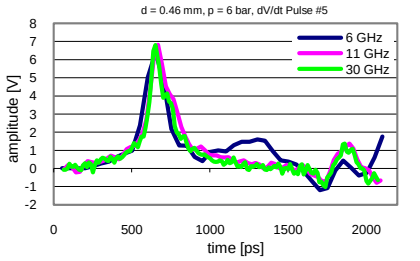

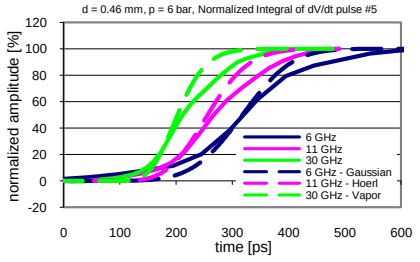

d = 0.46 mm, p = 7 bar

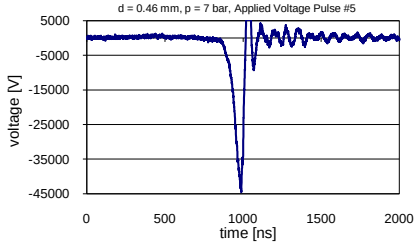

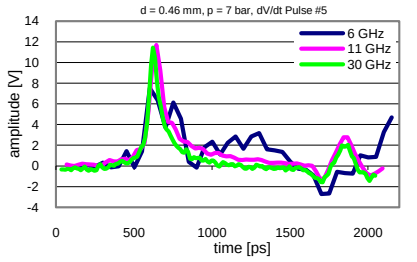

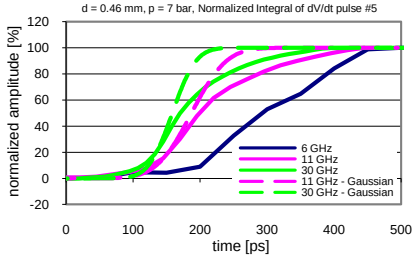

d = 0.46 mm, p = 8 bar

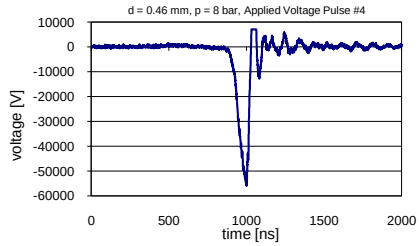

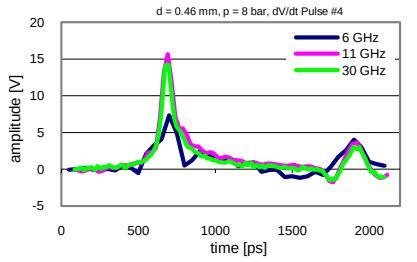

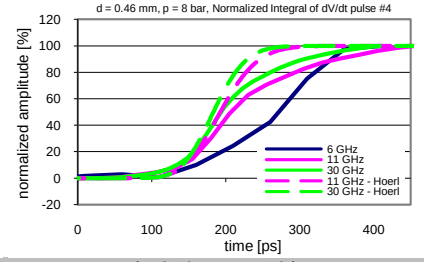

d = 0.46 mm, p = 9 bar

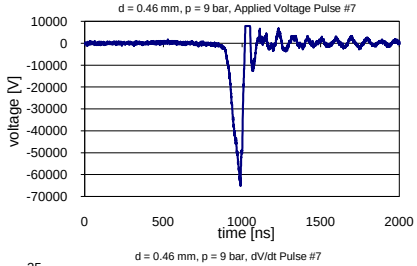

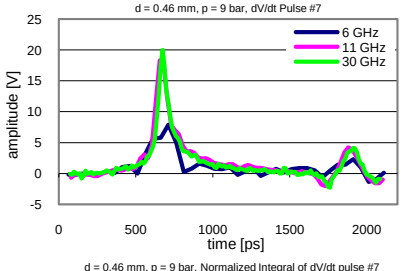

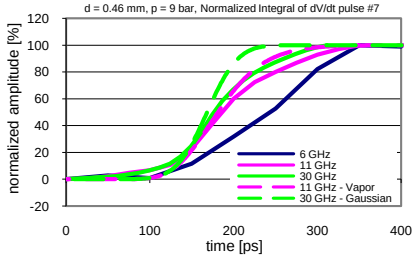

d = 0.46 mm, p = 10 bar

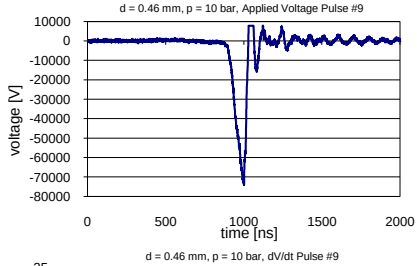

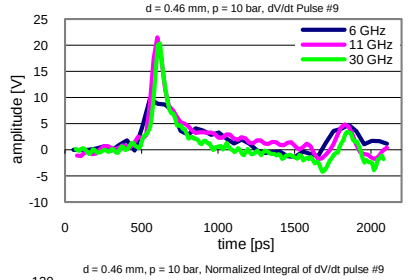

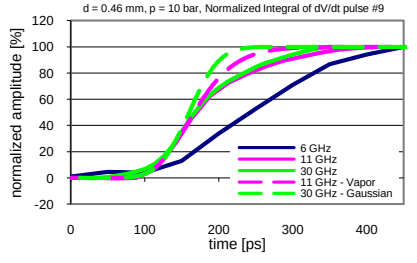

d = 0.46 mm, p = 11 bar

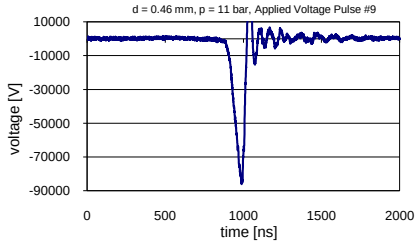

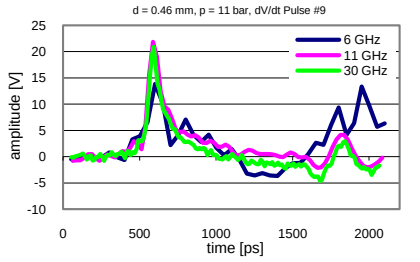

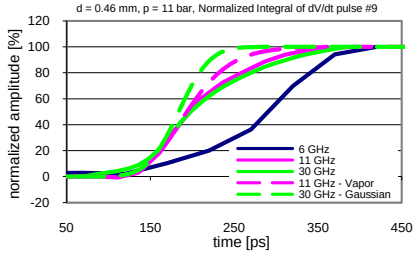

d = 0.46 mm, p = 12 bar

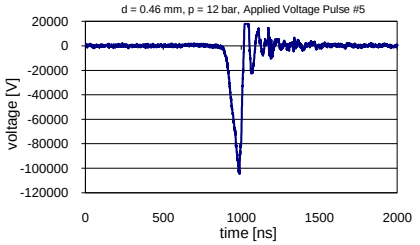

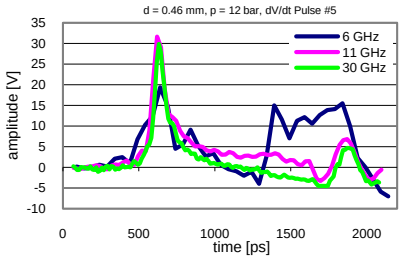

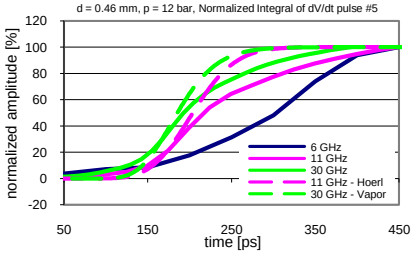

d = 0.46 mm, p = 13 bar

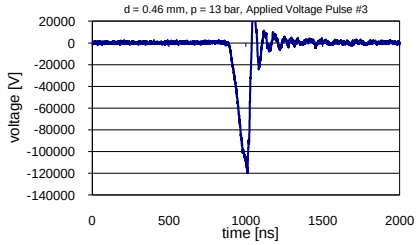

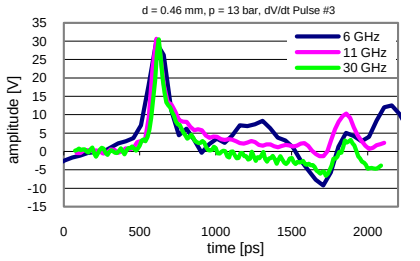

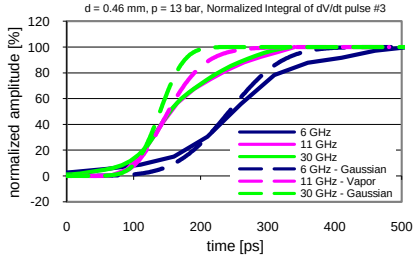

d = 0.46 mm, p = 14 bar

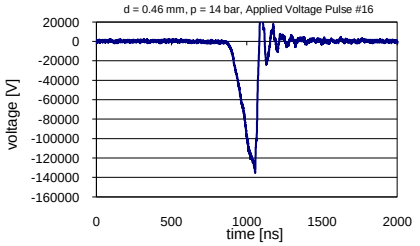

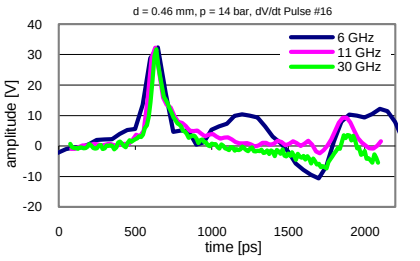

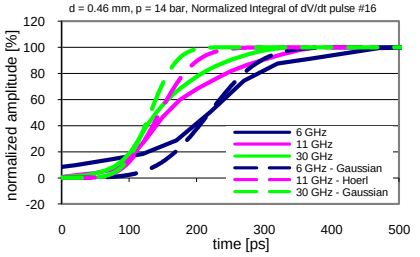

d = 0.46 mm, p = 15 bar

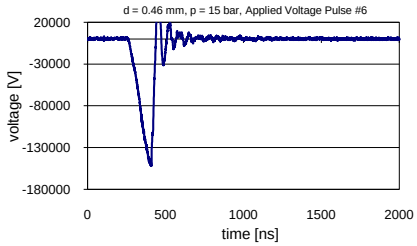

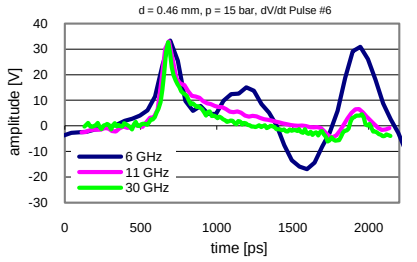

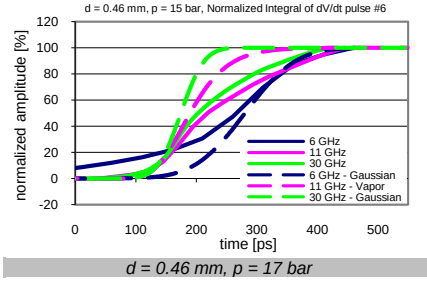

d = 0.46 mm, p = 16 bar

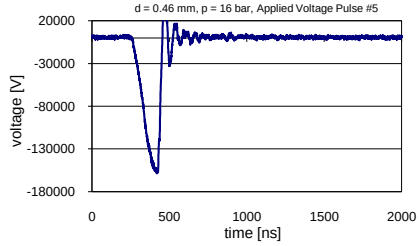

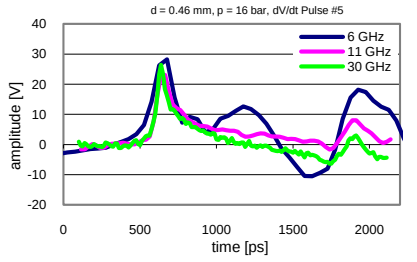

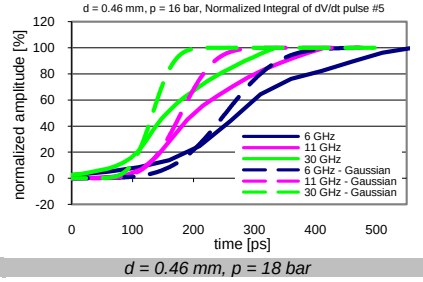

d = 0.46 mm, p = 17 bar

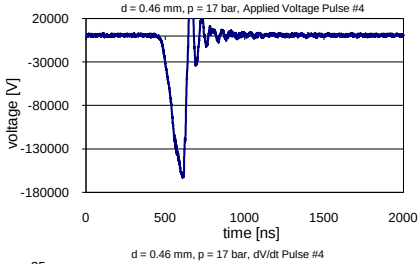

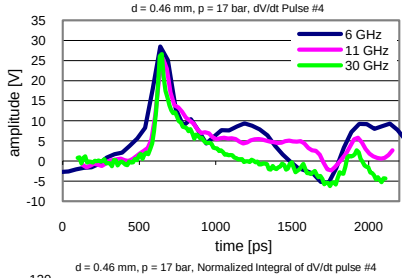

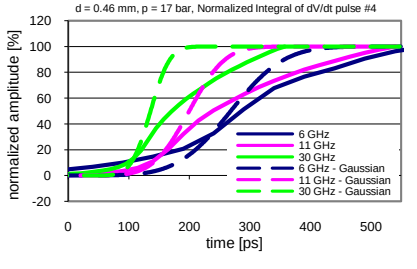

d = 0.46 mm, p = 18 bar

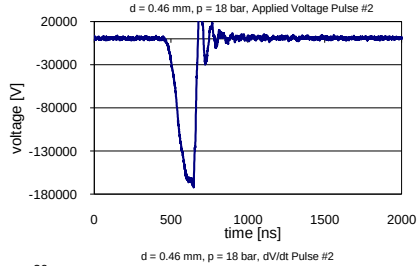

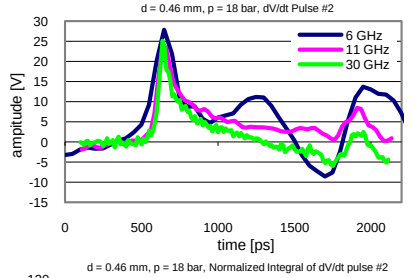

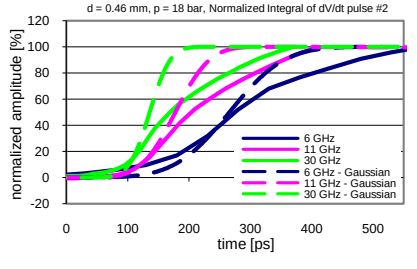

d = 0.77 mm, p = 1 bar

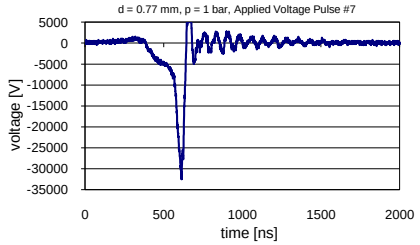

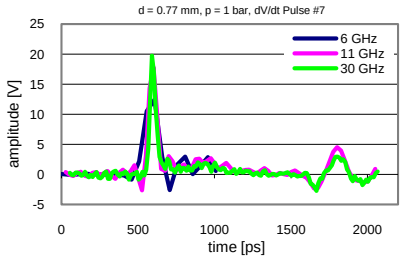

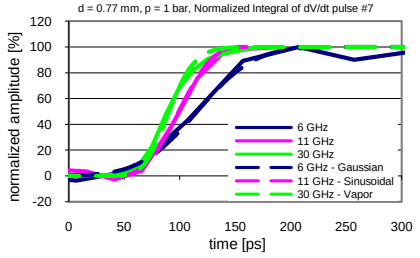

d = 0.77 mm, p = 2 bar

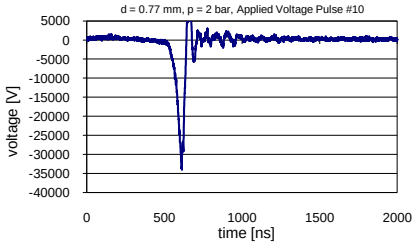

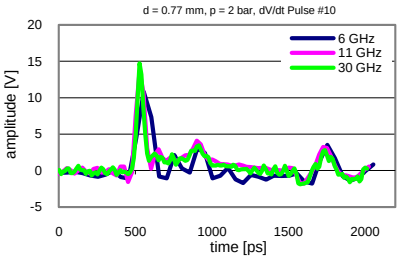

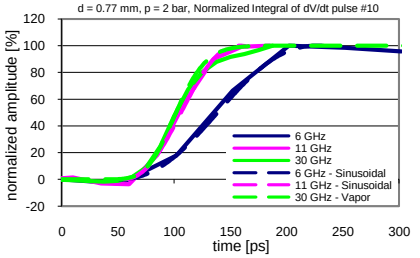

d = 0.77 mm, p = 3 bar

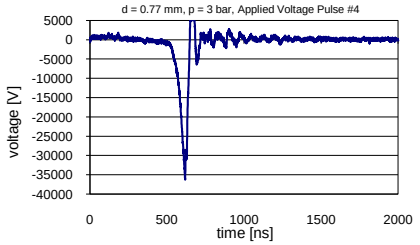

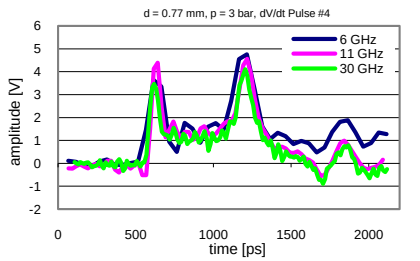

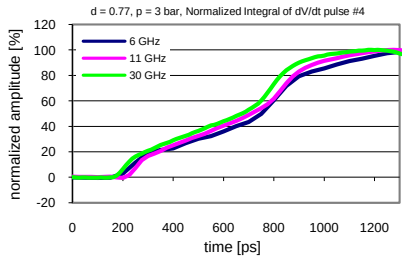

d = 0.77 mm, p = 4 bar

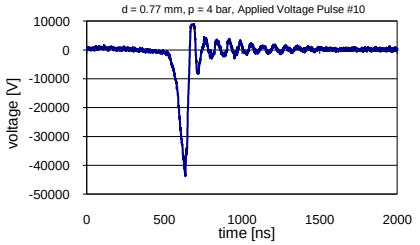

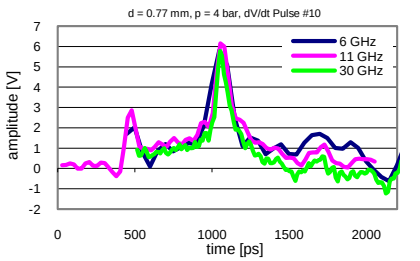

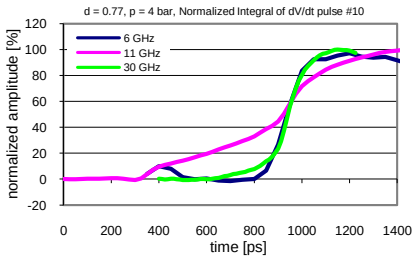

d = 0.77 mm, p = 5 bar

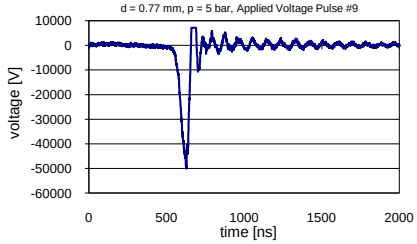

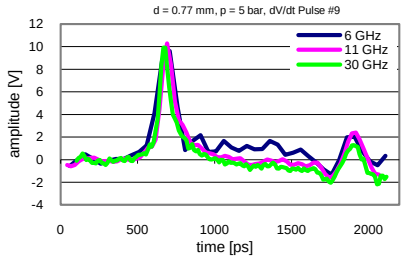

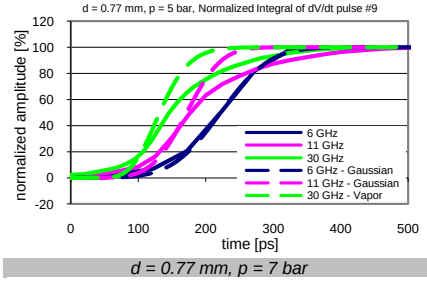

d = 0.77 mm, p = 6 bar

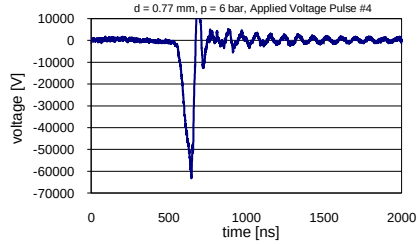

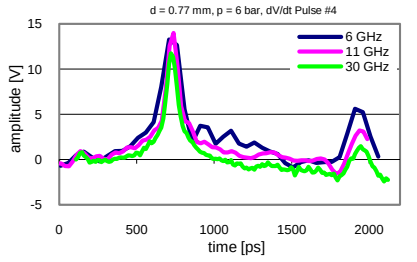

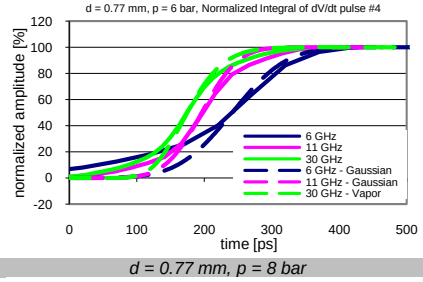

d = 0.77 mm, p = 7 bar

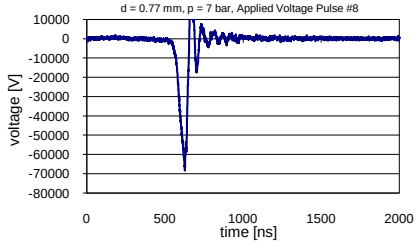

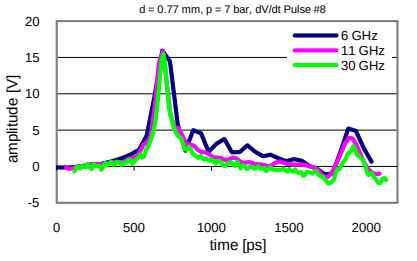

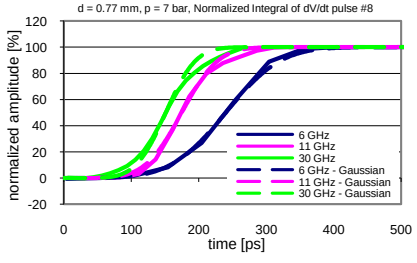

d = 0.77 mm, p = 8 bar

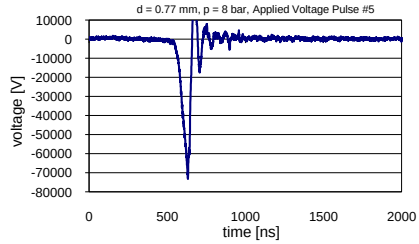

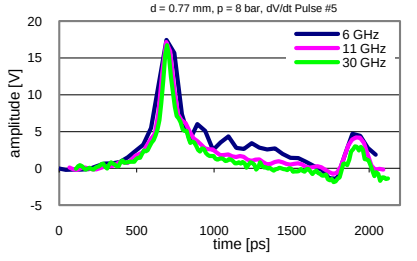

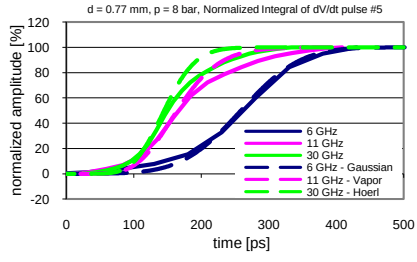

d = 0.77 mm, p = 9 bar

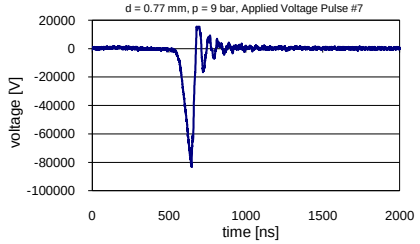

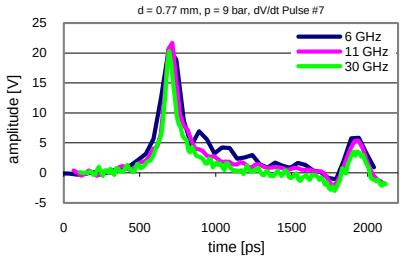

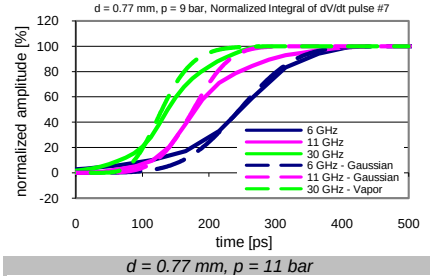

d = 0.77 mm, p = 10 bar

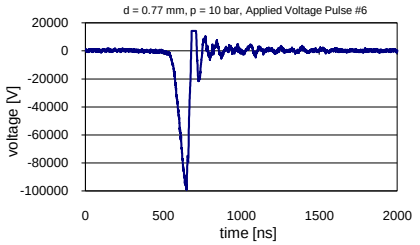

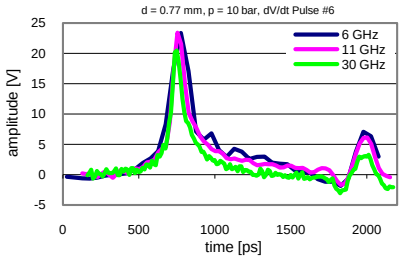

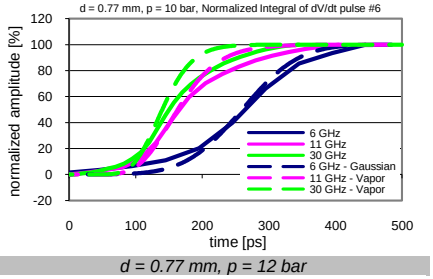

d = 0.77 mm, p = 11 bar

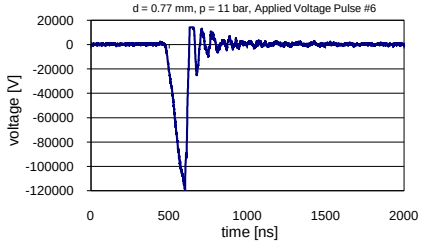

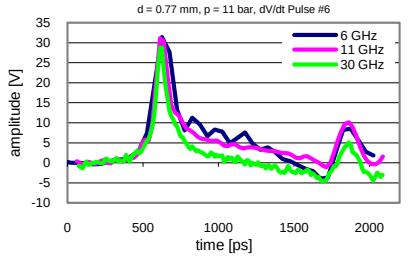

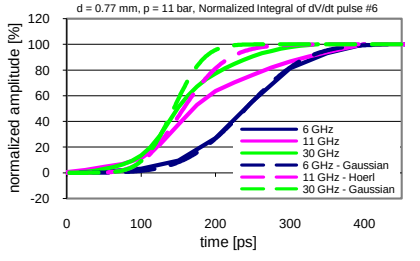

d = 0.77 mm, p = 12 bar

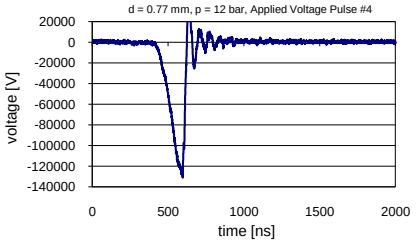

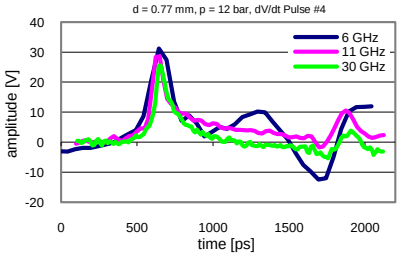

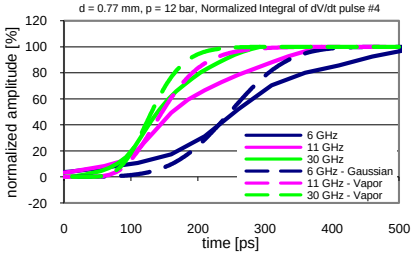

d = 0.77 mm, p = 13 bar

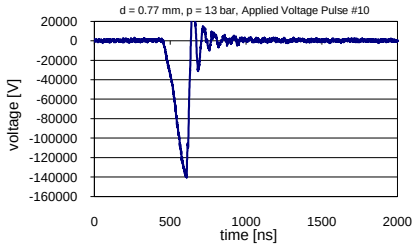

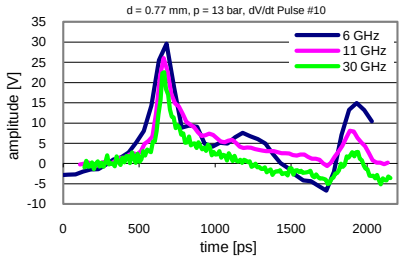

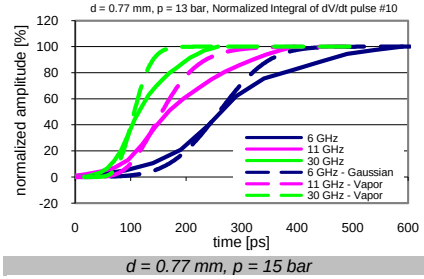

d = 0.77 mm, p = 14 bar

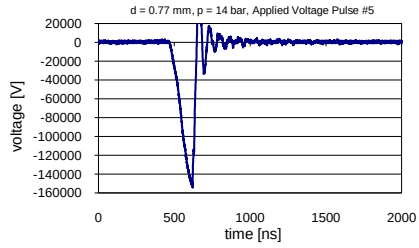

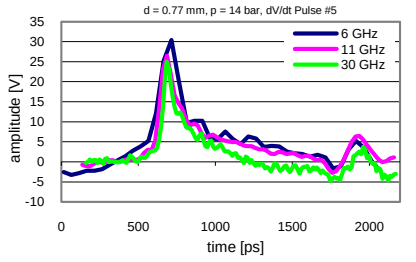

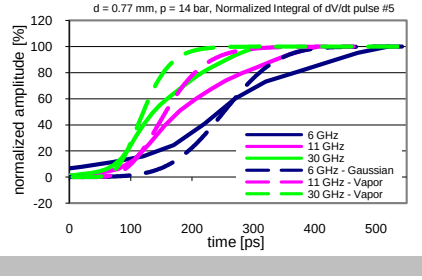

d = 0.77 mm, p = 15 bar

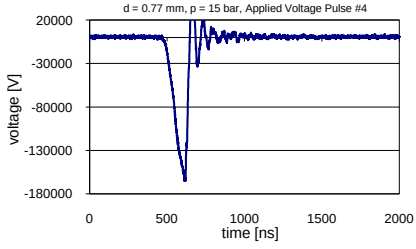

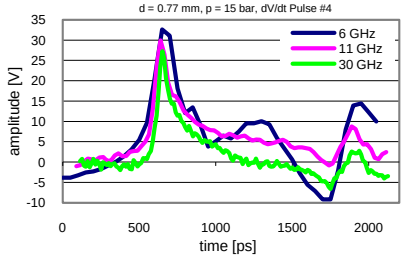

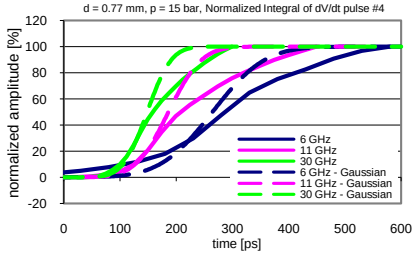

Insight into ultrafast gas breakdown is essential for designing fast plasma switches implemented in applications ranging from UWB radar and particle accelerators to EMP testing and bioelectromagnetic studies. Such rapid breakdown in pressurized submillimeter spark gaps challenges the accurate recording of the observed events. Using state of the art equipment and multiple simultaneous data acquisition systems, breakdown in sulfur hexafluoride (SF6) is studied in high resolution with great data integrity. Measured breakdown voltages reach 180 kV and risetime of voltage collapse is recorded as fast as 50 ps. Inter-electrode distance is varied from 0.1 – 0.9 mm and pressure increased to 19 bar. The influence of these parameters is recorded, identified and categorized. Methods for removing the impact of the measurement system are implemented in efforts to distinguish the physical phenomenon from influential external factors. Ultimately, breakdown characteristics are explained as a function of electric field, pressure and gap distance.

Aalto-DD 53/2011

ISBN: 978-952-60-4170-4 (pdf)
ISBN: 978-952-60-4169-8
ISSN-L: 1799-4934
ISSN: 1799-4942 (pdf)
ISSN: 1799-4934

Aalto University
School of Electrical Engineering
Department of Electrical Engineering
www.aalto.fi

BUSINESS + ECONOMY

ART + DESIGN + ARCHITECTURE

SCIENCE + TECHNOLOGY

CROSSOVER

DOCTORAL DISSERTATIONS